Numerical modeling of turbulent hydrogen combustion for nuclear safety management

Javier Lobato Perez

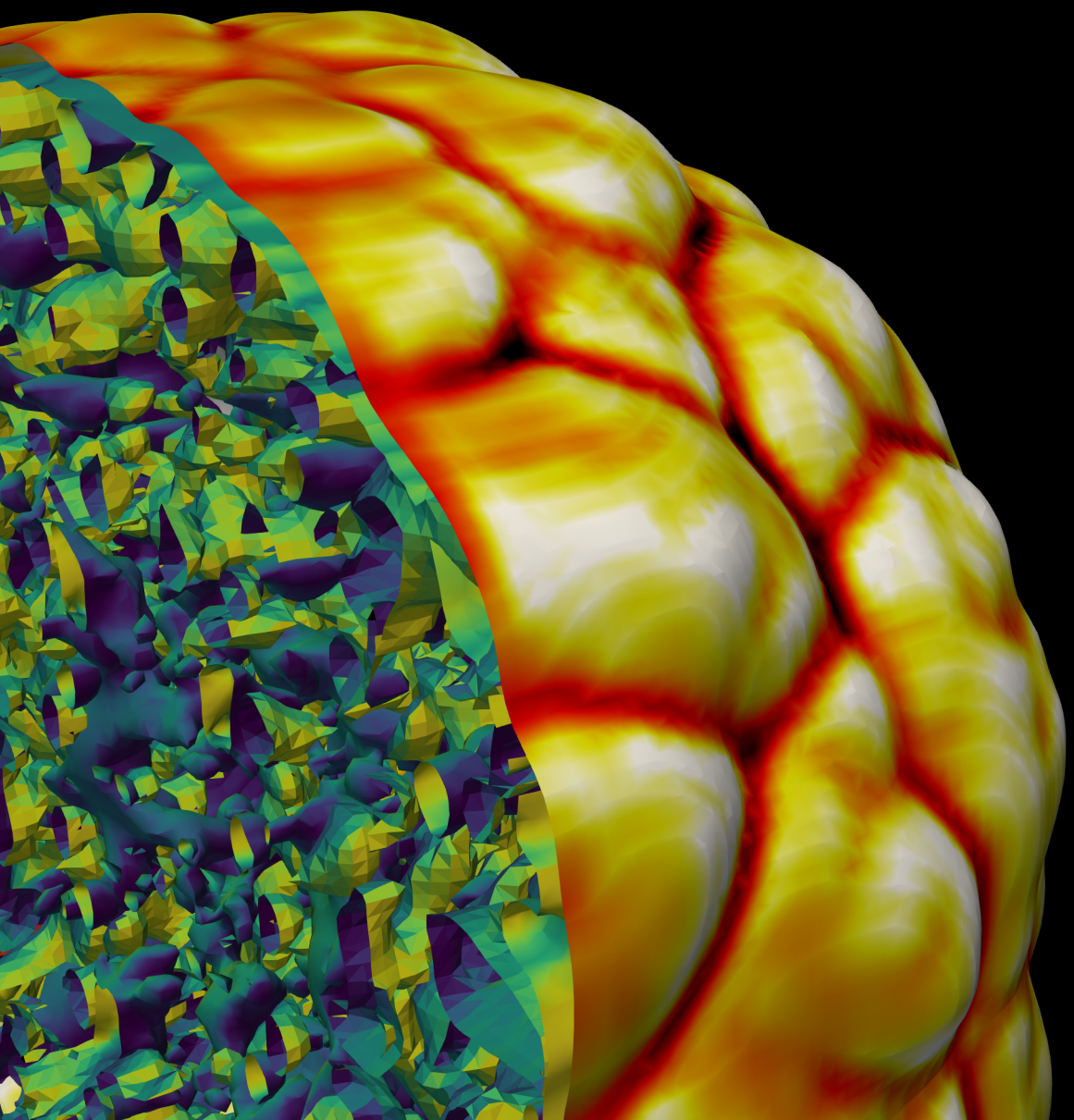

TU Delft

Numerical modeling of turbulent hydrogen combustion for nuclear safety management

by

Javier Lobato Perez

to obtain the degree of Master of Science in Aerospace Engineering

at Delft University of Technology,

to be defended publicly on the 14th of July 2021.

Student number:	4936620	
Project duration:	March, 2020 – July, 2021	
Thesis committee:	Prof. dr. S. Hickel	TU Delft, academic supervisor
	Dr. I. Langella	TU Delft, examiner
	Dr. ir. A.H. van Zuijlen	TU Delft, examiner
	Dr. D. Dovizio	NRG, daily supervisor

The thesis was carried out in collaboration with Nuclear Research & Consultancy Group (NRG).

This document is confidential and cannot be made public until July 2023.

EU Duc = N

Goods labeled with an EU DuC (European Dual-use Codification) not equal to 'N' are subject to European and national export authorization when exported from the EU and may be subject to national export authorization when exported to another EU country as well. Even without an EU DuC, or with EU DuC 'N', authorization may be required due to the final destination and purpose for which the goods are to be used. No rights may be derived from the specified EU DuC or absence of an EU DuC.

Acknowledgments

First and foremost, I would like to thank Dr. D. Dovizio for all the help and support provided during the more than one year that this thesis has taken to completion. For this thesis, I was able to be part of the exciting research that is conducted at NRG, in the intersection of nuclear engineering and computer fluid dynamics, with a topic as challenging as combustion. With his help and frequent discussions, I have been able to understand such a complex phenomena and learn from him, not only of fluid flows. My gratitude towards him goes beyond these lines. I am also grateful to my academic supervisor, Prof. Dr. S. Hickel, for supervising this thesis and for the valuable feedback provided. I want to also thank Dr. ir. A.H. van Zuijlen and Dr. I. Langella for accepting the invitation of being a part of the examination committee.

Being able to keep working on the thesis in such a year, even if remotely due to the pandemic, has been an great opportunity thanks to the incredible people that has surrounded me. I have a lot of gratitude towards Ed Komen for the trust and aid and also to the other team colleagues at NRG, specially to Edo Frederix for the support with OpenFOAM – as he never said no to my more than recurrent questions and always pointed in the right direction. A mention to the other interns whom I had the pleasure to spend time: the combustion guys, Federico and Adrian, and the team *Mojo's*, Salvo and Pablo. Meeting you in Petten and the sporadic futsal games made the situation more bearable. Even if the lockdown forced everyone to stay more at home, luckily in my case that has not been a problem thanks to my amazing housemates in Alkmaar: Mario, who helped me discover inner hobbies as guitar building, taught me home building skills and showed me that life does have another point of view; Lucia, who was the best hater-fit-crazy-clean housemate one can ever wish; Job, whose chess games I will cherish and long talks until very late at night presented the right side of many stories; and Jop, whose passion and life-hints were appreciated and usually right. The weekly *vrijdagmiddagborrel* was a pinch of relax in difficult times.

With this thesis I complete my MSc Engineering studies, so I also want to remember the days at Liszt-straat 117 with Alfredo and Chou and the classes with Adrian, Eric, Enri, Philipp, Uri and Fran. The bioinformatics project with Thomas and Aysun was a wonderful experience – thank you for giving me the chance to being part of it. Finally, my experience in ISAE, Toulouse, will always be happily reminded: to the ML team, Daniel, Ekhi and Antonio, and to the other PhD candidates of the DAEP, specially Dani, Gonzalo and Anais. Even if not directly to this thesis, you contributed to my personal growth and helped me get to where I am currently standing. Finally I have to thank the people who, even if it was through a screen more time than I have wished, are always there: my parents, my sister and Inés.

I learned a lot during these three years, about aerodynamics, physics and mathematics, but more importantly, I learned be a little more confident in my own capabilities. I am sure that these years have been fundamental in my education, as I have been able to study in the outstanding institution as TU Delft, but also personally, as I have been lucky to share my trip with a lot of incredible people that have contributed to who I am today.

Javier Lobato Perez
Alkmaar, July 2021

Abstract

During a severe accident in a water-cooled nuclear power plant, large quantities of hydrogen can be generated in the reactor core. The hydrogen mixed with air presents a potential risk of combustion when the hydrogen concentration reaches flammability limits. If combustion occurs, pressure loads can damage safety systems and even compromise the structural integrity of the nuclear reactor walls. Thus, predicting the pressure loads is an important safety issue to ensure the reliability of critical structures in the event of a severe accident.

Computational Fluid Dynamics (CFD) codes can be used as numerical tools to assess the risks of hydrogen combustion and predict detailed transients of the pressure loads. The scenarios simulated in nuclear safety engineering can be analyzed with low fidelity models based on reduction assumptions of the physical phenomena. Specifically, the flame gradient models are chosen to model the combustion phenomena based on a turbulent flame speed to which the combustion propagates. Different approaches to compute the turbulent flame speed are implemented and compared in this study, including the Turbulent Flame Closure (TFC) and the Extended Turbulent Flame Closure (ETFC). New models are proposed based on new experimental correlations specifically derived for lean mixtures of hydrogen. Other required libraries as flame radius calculation, radiative heat transfer properties determination, and axisymmetric Adaptive Mesh Refinement are implemented and evaluated. A study on the influence of the ignition source term is also carried out.

The implementation of the solver and the models is verified with the analytical solution of a planar one-dimensional premixed flame moving into frozen turbulence. Moreover, three different experimental cases, relevant to nuclear safety, are selected to perform the validation of the solver. The first one is a spherical combustion chamber which was experimentally tested with lean hydrogen mixtures and controlled measured homogeneous isotropic turbulence. The second one is the Thermalhydraulics Hydrogen Aerosol and Iodine (THAI) facility, which is a larger vessel where effects as buoyancy become more relevant. Finally, the third one is a flame acceleration enclosure called ENACCEF-2, where obstacles are placed along a cylindrical tube to promote flame acceleration and the transition from deflagration to detonation.

Numerical results are presented in terms of the flame front location, the flame front velocity, and the pressure rise. The sensitivity of the results to mesh resolution, time discretization, and initial turbulence levels is assessed. The implemented combustion models are simulated with multiple turbulence models, analyzing the results and the influence on one each other. In general, the proposed models represent an approach that provides good predictions in both flame development and pressure dynamics, being more robust than other models previously available.

Contents

List of Figures

List of Tables

List of Symbols

α	Thermal diffusivity coefficient
α_{eff}	Effective thermal diffusivity coefficient
A_e	Efficiency function empirically derived for transport of turbulent eddies
α_L	Laminar (or molecular) thermal diffusivity coefficient
α_p	Unburnt coefficient for the BML model
α_t	Turbulent thermal diffusivity coefficient
α_u	Unburnt mixture thermal diffusivity coefficient
α_w	Wedge angle of axisymmetric geometry
β	Zel'dovich number
β_j	Temperature exponent of the j-th reaction for the Arrhenius law
β_p	Burnt coefficient for the BML model
$\delta(c - c_0)$	Dirac-delta function
$\Delta h^0_{f,k}$	k-th species formation enthalpy
Δt	Timestep
Δt_{max}	Maximum allowable timestep
Δx	Spatial discretization
δ_{coeffs}	Delta coefficients, reciprocal of the center-to-center distance between cells projected over the face normal of the shared face
Δ_f	Analytical flame thickness
δ_L	Laminar flame thickness
δ_{ij}	Kronecker delta
$\dot{Q}$	External heat source term
$\dot{\omega}_c$	Progress variable source term
$\dot{\omega}_k$	k-th species global chemical reaction rate
$\dot{\omega}_k$	Chemical reaction rate of the k-th species
$\dot{\omega}_T$	Temperature source term due to the chemical reaction
$\dot{\omega}_{kj}$	k-th species chemical reaction rate of reaction j
ϵ	Emission (or emissivity) coefficient
ϵ_{tk}	Thermokinetic index for laminar flame speed correction
η	Kolmogorov length scale
γ	Ratio of specific heat capacities
$\Gamma(x)$	Gamma function
Γ_{ign}	Strength of regress variable ignition source term
γ_{ign}	Time-normalized strength of regress variable ignition source term
γ_p	Intermediate mixture for the BML model
$\hat{f}$	Filtered quantity f
κ	Thermal conductivity
κ_c	Local flame curvature
κ_s	Local strain rate
λ	Thermal diffusivity
$b\mathcal{F}$	Blending function
$\mathcal{C}$	Linear anisotropic scattering factor
$\mathcal{D}_{jk}$	Mass diffusion between species j and k, having $\mathcal{D}_{jk} = \mathcal{D}_{kj}$
$\mathcal{F}_1$, $\mathcal{F}_2$	Blending functions of the $k-\omega-$SST
$\mathcal{G}$	Non-reacting scalar variable for the level-set approach
$\mathcal{G}^*$, $\mathcal{R}'$, $\mathcal{G}'$	Coefficients for the transport equation of Ξ
$\mathcal{L}$	Markstein length
$\mathcal{M}$	Markstein number

$\mathcal{Q}_j$	Rate of progress of reaction j
$\mathcal{R}$	Universal gas constant
$\mathcal{R}_c$	Coefficient for the transport equation of S_L
$\mathcal{S}_k$	Symbol for the k-th species
$\mathcal{T}$	Thickness of two-dimensional mesh
μ	Dynamic viscosity
μ_{S_L}	Average value of the laminar flame speed
ν	Kinematic viscosity
ν_t	Turbulent kinematic viscosity
ω	Turbulence specific dissipation rate
ω_{ign}	Ignition source term for the regress variable equation
ω_u	Unburnt domain
$\overline{A}$	Mean flame front area
$\overline{f}$	Reynolds averaged quantity f
∂V	Volume boundary
Φ	Equivalence ratio
ϕ_Ξ	Flux of the wrinkling factor Ξ
$\phi_{i,j}$	Flux of the i-th cell through the j-th face
ψ	Compressibility factor
ρ	Fluid density
ρ_b	Burnt mixture density
ρ_u	Unburnt mixture density
σ_λ	Scattering coefficient of the medium for wavelength λ
σ_{eff}	Effective scattering coefficient
σ_{ext}	Extinction strain rate
σ_s	Total isotropic scattering coefficient
σ_{ij}	Total stress tensor
σ_{rs}	Resolved strain
τ_η	Kolmogorov-scales characteristic timescale
τ_{ign}	Duration of regress variable ignition source term
τ_c	Chemical timescale (or combustion timescale)
τ_L	Lagrangian characteristic timescale
τ_t	Turbulence characteristic timescale
τ_{ij}	Deviatoric stress tensor
Co	Courant number
Co_{CFL}	Courant–Friedrichs–Lewy condition based Courant number
Co_{max}	Maximum allowable Courant number
Co_{St}	Turbulent flame speed based Courant number
Da	Damköhler number
erfc	Complementary error function
Ka	Karlovitz number
Ka_δ	Reaction zone thickness Karlovitzt number
Le	Lewis number
Le_t	Turbulent Lewis number
Pr	Prandtl number
Pr_t	Turbulent Prandtl number
Re	Reynolds number
Re_η	Kolmogorov-scales Reynolds number
Re_t	Turbulent Reynolds number
Sc	Schmidt number
Sc_t	Turbulent Schmidt number
θ_{kj}, θ'_{kj}, θ''_{kj}	Molar stoichiometric coefficients of the k-th species in the j-th reaction
ε	Turbulent kinetic energy dissipation
$\vec{\hat{g}}$	Normalized vector of the gravitational force
$\vec{\Phi}(\vec{s}_i, \vec{s})$	Incident scattering phase function from all possible directions $\vec{s}_i$ in direction $\vec{s}$
$\vec{g}$	Gravitational force

$\vec{g}$	Vector of the gravitational force
$\vec{n}$	Unit vector normal to the flame front
$\vec{n}_f$	Corrected unit vector normal to the flame front
$\vec{n}_r$	Unit vector for flame radius calculation
$\vec{n}_s$	Unit vector normal to a isosurface
$\vec{r}_w$	Wall positioning vector
$\vec{S}_{f,j}$	Vector normal to the cell j-th face with magnitude the cell face area
$\widetilde{f}$	Favre averaged quantity f
Ξ	Wrinkling factor
ξ	Dimensionless normalized distance variable
Ξ^{model}	Wrinkling factor of an specific combustion *model*
Ξ_{eq}	Equilibrium wrinkling factor
Ξ^*_{eq}	Temporal variable for the equilibrium wrinkling factor
Ξ_c	Wrinkling factor coefficient
Ξ_{sc}	Wrinkling factor shape coefficient
ζ	Dimensionless normalized distance variable
ζ, ζ'	Velocity gradient AMR criteria
Z, Z'	AMR metrics based on a normalized velocity gradient criterion
A	TFC model constant
a	Absorption (or absorptivity) coefficient
$a'_{i,j}$	Polynomial fit j-th coefficient for the thermodynamic properties of the i-th species
A_S	Sutherland's law coefficient
A_s	Self-propagating isosurface area
a_s	Velocity of sound
A_T	Wrinkled flame front area
A_{fi}	Arrhenius preexponential constant for the j-th reaction
$a_{p,i,j}$	Polynomial fit j-th coefficient for the pressure normalized absorption coefficient of the i-th species
$a_{p,i}$	Pressure normalized absorption coefficient for the i-th species
AF	Amplification factor
B	FSC model constant
b	Regress variable
BR	Blockage ratio
c	Progress variable
c_P	Specific heat capacity at constant pressure
c_V	Specific heat capacity at constant volume
$CD_{k-\omega}$	Coefficient from the $k-\omega-$SST turbulence model
D	Mass diffusivity coefficient
D_ω	Effective diffusivity for ω
D_{eff}	Effective mass diffusivity coefficient
d_{ign}	Diameter of the regress variable ignition source term
D_ε	Effective diffusivity for ε
D_b	Burnt mixture mass diffusivity coefficient
d_i	i-th coefficient for the default laminar flame speed correlations
D_k	Effective diffusivity for k
D_t	Turbulent mass diffusivity coefficient
D_t^∞	Turbulent mass diffusivity coefficient when $t \to \infty$
D_u	Unburnt mixture mass diffusivity coefficient
$D_{\mathcal{L}}$	Markstein diffusivity coefficient
$D_{t,t}$	Time-dependent turbulent mass diffusivity coefficient
E	Total internal energy
E_c	Emission contribution to the radiative heat transfer process
E_{aj}	Activation energy of equation j
E_a	Activation energy of the main combustion chemical equation
f	Arbitrary quantity or field used for generalized equations
f', f''	Fluctuating component of a given quantity f

$f_{k,j}$	External volume force over the k-th species in the j-th direction
G	(Directionally averaged) Radiative heat transfer intensity
G_{coef}	Gravitational coefficient of the turbulence model
H	Total enthalpy
h	Specific enthalpy
h_u	Unburnt specific enthalpy
$I)$	Turbulent intensity
$I_\lambda(\vec{r},\vec{s})$	Radiation intensity at location $\vec{r}$ in direction $\vec{s}$ for a given wavelength λ
i_b	Black body radiation
K	Kinetic energy
k	Turbulent kinetic energy
k_λ	Absorption coefficient of the medium for wavelength λ
K_{fi}	Forward rate of reaction j
K_{ri}	Reverse rate of reaction j
l_t	Integral length scale
m	Total mass (within a closed system)
m_{t}	Thermal index for laminar flame speed correction
m_k	k-th species mass (within a closed system)
n	Total number of moles (within a closed system)
n_{b}	Baric index for laminar flame speed correction
n_k	k-th species number of moles (within a closed system)
p	Pressure
$P(c),\ P(x_i,t,c)$	Probability density function for the progress variable
p_{ref}	Reference pressure
p_k	k-th species partial pressure
q_i	Heat flux in the i-th direction
q_i^{rad}	Radiative heat flux in the i-th direction
r_{ign}	Radius of the regress variable ignition source term or the initial patching
R_f	Flame radius
R_f^0	Unstrained laminar spherical flame radius
$R_{(i)}$	Specific gas constant (of the i-th species)
S	Stoichiometric mass ratio
S_ε	Source term for the transport equation of ε
s_d	Displacement speed
S_f	Source term
S_k	Source term for the transport equation of k
S_s	Self-propagating isosurface speed
$S_{f,j}$	j-th face normal vector with the cell face area as magnitude
$S_{h,rad}$	Enthalpy equation radiative heat transfer source term
$S_{L,0}$	Unstrained laminar flame speed
$S_{L,0}^{\text{ref}}$	Uncorrected (reference) unstrained laminar flame speed
S_{lpl}	Light path length
S_L	Laminar flame speed
S_L^∞	Strained laminar flame speed
S_t	Turbulent flame speed
S_t^∞	Turbulent flame speed when $t \to \infty$
S_t^{model}	Turbulent flame speed of an specific combustion *model*
SF	Smoothing factor
T	Temperature
t	Time
T_{ref}	Reference temperature
T_b	Burnt mixture temperature
T_u	Unburnt mixture temperature
T_{ad}	Adiabatic flame temperature
u'	Root-mean-square velocity fluctuations
u_l'	u' at the end of linear dependence between S_t and u'

u'_m	u' that provides maximum values of S_t
u'_q	u' for flame quenching
U_∞	Inflow freestream velocity
u_i	Velocity
V	Volume
$V_{k,i}$	k-th species diffusion velocity in the i-th direction
$V_{L,0}$	Unstrained laminar flame velocity
V_L^∞	Strained laminar flame velocity
V_S	Strained smooth velocity
V_T	(Spatial) turbulent flame velocity
W	Mean molecular weight of the mixture
W_k	k-th species molecular weight
X_c	Scalar dissipation rate
x_i	Spatial coordinate in the i-th direction
X_k	k-th species mole fraction
Y_f	Flame front location in the vertical direction
Y'_f	Fuel mass fraction
$Y_{k(,j)}$	k-th species mass fraction (in the j-th mixture state)
Z	Mixture fraction

List of Abbreviations

AEA Activation Energy Asymptotics.

AF Amplification Factor.

AMR Adaptive Mesh Refinement.

BC Boundary Conditions.

BML Bray-Moss-Libby.

BR Blockage Ratio.

BWR Boiling Water Reactors.

CAD Computational Aided Design.

CFD Computational Fluid Dynamics.

CFL Courant–Friedrichs–Lewy.

CFM Coherent Flamelet Model.

CPU Central Processing Unit.

DNS Direct Numerical Simulation.

EBU Eddy-Break-Up.

ENACCEF *Enceinte d'accélération de flamme*.

ETFC Extended Turbulent Flame-speed Closure.

FSD Flame Surface Density.

FSM Flame Speed Models.

GRI Gas Research Institute.

GTFC Goulier Turbulent Flame-speed Closure.

GUI Graphical User Interface.

HD Hydrogen Deflagration.

IACC Isochoric Adiabatic Complete Combustion.

ICARE *Institut de Combustion, Aerothermique, Reactivite et Environnement*.

IRSN *Institut de radioprotection et de sûreté nucléaire*.

JANAF Joint Army-Navy-NASA-Air Force.

LBL Line-By-Line.

LES Large Eddy Simulation.

LP Lumped Parameter.

LWR Light-Water Reactors.

MUSCL Monotone Upstream-centered Schemes for Conservation Laws.

NASA National Aeronautics and Space Administration.

NEA Nuclear Energy Agency.

NPP Nuclear Power Plants.

NRG Nuclear Research & consultancy Group.

OECD Organization for Economic Co-operation and Development.

PAR Passive Autocatalytic Recombiners.

PIMPLE PI(SO) and (SI)MPLE algorithm combination.

PISO Pressure-Implicit with Splitting of Operators.

PIV Particle Image Velocimetry.

PM Photo-Multipliers.

PWR Pressurized Water Reactor.

RANS Reynolds Averaged Navier Stokes.

RDT Rapid Distortion Theory.

RTE Radiative Transfer Equation.

SCWR Supercritical Water Reactor.

SF Smoothing Factor.

SIMPLE Semi-Implicit Method for Pressure Linked Equations.

SLW Spectral-Line Weighted.

SST Shear Stress Transport.

TFC Turbulent Flame-speed Closure.

THAI Thermal-hydraulics, Hydrogen, Aerosol and Iodine.

URANS Unsteady Reynolds Averaged Navier Stokes.

WSGGM Weighted Sum of Gray Gases Model.

1

Introduction

In the context of nuclear safety engineering, hydrogen management is an important component to ensure the reliability and proper functioning of critical systems in the case of a severe accident. The hydrogen release and combustion have received considerable attention after the Fukushima accident, where the pressure loads that resulted from the hydrogen combustion damaged the structural integrity of the nuclear reactor containment. The prediction of the loads through computational models should represent, as faithfully as possible, these complex physical phenomena.

This report is structured in five chapters. The first one presents the thesis project itself together with an introduction to the topic related to nuclear engineering, with the motivation and some background information to understand why the subject is relevant to the community. The problem statement and the research questions that were proposed at the beginning of the thesis project are outlined at the end of the chapter. The second chapter provides an overview of combustion theory: it sets the foundations with the equations derived from basic principles, introducing relevant quantities and concepts. Then, it provides a more phenomenological description of combustion and its interaction with other flow phenomena as well as the different regimes of combustion. The approaches available to model combustion and turbulence are also included. They are put into context by comparing them with the main findings from a literature review with the latest developments in the field and what other research groups are working on. The chapter concludes with a primer on radiative heat transfer, which is another physical mechanism that plays a role in the problem.

The third chapter shows the methodology, transitioning from the physical and phenomenological description of the previous chapter to the numerical implementation of the mathematical set of equations to address the problem. The computer tool used for the project is introduced as well, together with the developments used to expand and customize it to the particular needs of the industry. Chapter four presents the results of the thesis: starting with the verification of the computational model with one analytical case followed by the validation with the results of three experimental facilities. The thesis is wrapped up with chapter five, showing the conclusions and future recommendations to keep developing the numerical model here presented.

1.1. Motivation and background

Nuclear power plants (NPP) are power stations that generate electricity from a self-sustained nuclear fission chain reaction. This reaction relies on heavy-nucleus materials like uranium or plutonium that, when hit by a neutron, generate more new neutrons and release energy. The neutrons promote the chain reaction as they trigger the reaction again and the energy release is used to heat water that, through a steam turbine, is converted into electricity.

The most common reaction is that of uranium-235 [83], an isotope whose main reaction when impacted by a neutron is given by:

$$ {}^{1}_{0}\mathrm{n} + {}^{235}_{92}\mathrm{U} \longrightarrow {}^{236}_{92}\mathrm{U} \longrightarrow 3\,{}^{1}_{0}\mathrm{n} + {}^{141}_{56}\mathrm{Ba} + {}^{92}_{36}\mathrm{Kr} \ . $$

However, this is not the only reaction, given that the unstable ^{236}U isotope may result also in different final products as xenon, iodine, strontium, plutonium, or cesium [83], although with less prevalence, due to different reaction rates:

$$ {}^{1}_{0}\mathrm{n} + {}^{235}_{92}\mathrm{U} \longrightarrow {}^{236}_{92}\mathrm{U} \longrightarrow \begin{cases} 3\,{}^{1}_{0}\mathrm{n} + {}^{137}_{55}\mathrm{Cs} + {}^{96}_{37}\mathrm{Rb} \\ 2\,{}^{1}_{0}\mathrm{n} + {}^{144}_{54}\mathrm{Xe} + {}^{90}_{38}\mathrm{Sr} \\ \ldots \end{cases} \ . $$

Depending on how these reactions are managed, there are many NPP designs and different ways to classify them. Based on how the nuclear reaction is controlled, there are thermal neutron reactors (where neutron moderators are required to reduce the speed of the produced neutrons to facilitate the collision between them and other uranium atoms) and fast neutron reactors (they use special fuels, not requiring neutron moderators). Within the first group, a subclassification is usually made based on the moderator material, having graphite reactors, molten salt reactors, heavy-water reactors, or Light-Water Reactors (shortened as LWR). The last one uses ordinary, usually deionized, water as moderator and as core coolant (to maintain the nuclear core at a manageable temperature). More than 80% of the total nuclear reactors in the world are of the LWR type [63]. Thus, another classification has been devised for LWR, based on the number of closed loops of the water circuit and how they operate.

Boiling Water Reactors (BWR) have just one internal water loop (not taking the condenser loop into account): it pumps the water through the reactor core, evaporating it and directing it first to the turbine and then to a condenser, where the steam is converted into liquid water again and directed to the reactor core (Figure 1.1a). Pressurized Water Reactors (PWR) have two water loops: one pressurized circuit connects the reactor core with a steam generator, where the water in the second closed-loop boils through heat exchange. Water is heated but not converted into steam due to the high pressures in the first loop. The second loop connects the steam generator with the turbine and the condenser (see Figure 1.1b). Even if it is a more complex system, PWR have advantages as an uncontaminated water loop through the turbine and smaller power production as heat increases [27]. There is a third type, the supercritical water reactor (SCWR), which has a similar structure to the PWR but it operates at supercritical pressures (which for water is above 22 MPa), providing higher thermal efficiency. However, this design is still in development. Of these three types, more than 80% are PWR. Thus, even with all these many different designs (and others not mentioned here), almost 70% of the total nuclear energy is produced with PWR.

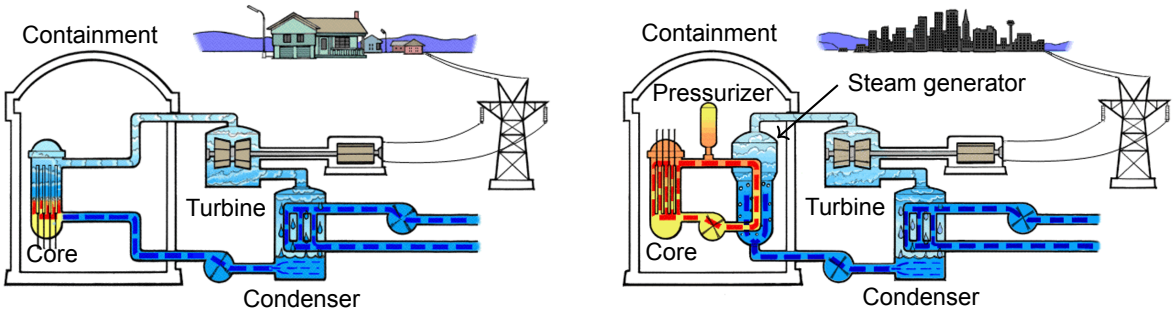

(a) Boiling Water Reactor.

(b) Pressurized Water Reactor.

Figure 1.1: Types of Light-Water Reactor designs, adapted from [26].

The fuel is obtained from the isotope of interest of uranium, converted into uranium dioxide UO_2 powder, which is then compacted into cylindrical pellets to make it more stable and provide structural integrity even at high temperatures [83]. These pellets are then inserted into fuel rods: sealed tubes grouped into fuel assemblies that make the core of a power reactor. The fuel assemblies are introduced in water, which serves the two-fold purpose of cooling and moderating the reaction. There is a space between the pellets and the inner wall of the rods, which is usually filled with helium to improve heat conductivity. The fuel rods are covered with zirconium cladding (mainly in the form of alloys known as Zircaloy, being Zircaloy 2 and Zircaloy 4 the most common ones). This material has been chosen as it is corrosion-resistant, it presents a good thermal conductivity, and most importantly, it has a low neutron absorption cross-section [36] (which means that it allows neutrons to cross between fuel rods, promoting the chain reaction).

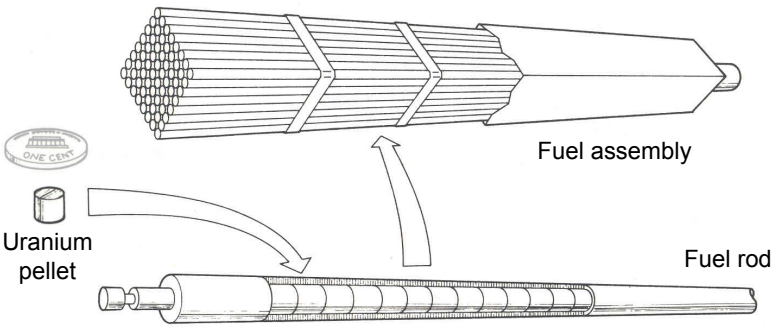

Figure 1.2: Uranium pellet, fuel rod, and fuel assembly, adapted from [94].

During the normal operation of a nuclear power plant, no hydrogen release can lead to any deflagration process. However, in a severe accident, if a loss of coolant occurs, very high temperatures will trigger a reaction between zirconium alloys and water steam, producing hydrogen gas following:

$$Zr + 2\,H_2O \longrightarrow ZrO_2 + 2\,H_2 \ .$$

When this reaction is sustained during long periods of time, the hydrogen percentage can increase, having a maximum generation rate of up to 1 kg/s [41]. Hydrogen, which is a highly flammable gas, represents a main concern for nuclear safety engineering. Other reactions also produce hydrogen in a smaller amount, but this one, in particular, is accompanied by a large energy release, that induces a feedback loop in the reaction. To avoid the associated problems of this reaction due to the use of zirconium, other alternative claddings as steel have been proposed, and even if the hydrogen-producing reaction occurs with a lower energy release (slowing the chain reaction and the hydrogen generation), the properties of zirconium alloys are, so far, unbeatable. Research programs entirely focused on finding a solution to this problem are being carried out [21]. However, until a compromise cladding material is attained, zirconium will still be present in the reactors, and hydrogen should be managed in the event of a severe accident.

In such an event, hydrogen builds up inside the pipes of the reactor core, increasing the inner pressure and leading to breaks and leakages into the containment building, whose geometry should be designed to account for these scenarios. There are methods, as relief valves, that remove excess pressure, but they can suffer mechanical failures (as in the Three Mile Island accident [136], where an unclosed valve led to the complete depressurization of the reactor and a posterior partial disintegration of the core). Other devices, as Passive Autocatalytic Recombiners (PAR), are located in the containment to reduce the risk of hydrogen ignition and combustion [40]. These devices require no energy, have no moving parts, and are automatically activated when the hydrogen concentration goes over a given threshold level (between 1% and 2%). By using platinum or palladium as the catalyzer, these devices reduce the amount of hydrogen by converting it into non-flammable steam. However, the process is relatively slow,

reducing only ~ 10 kg of hydrogen per hour per PAR (see Table 2 in [7]). Even multiple recombiners are not able to handle sudden increases of hydrogen as their performance depends on the temperature and hydrogen concentration.

Another approach to prevent the risks of combustion consists of filling the nuclear core with nitrogen (as in the Fukushima Daiichi power plant [2]), preventing the mixing of hydrogen with oxygen. Even if this removes the oxidizer inside the reactor core, inhibiting the combustion, explosions can still happen during the release of the hydrogen into the containment building and to the atmosphere, as it occurred in the aforementioned plant after an earthquake and posterior tsunami.

1.2. Problem statement and research questions

The risk of these scenarios requires a proper study of the containment structure and the accurate calculation of the peak pressure resulting from the combustion of hydrogen, as this will affect the structural integrity of the containment. There exist two approaches to perform these calculations: Lumped Parameter (LP) codes, also known as system codes, and Computational Fluid Dynamics (CFD) codes [62]. The former type requires few computational resources and has been extensively validated, being a mature technique. However, it suffers from a limited accuracy: as the main interest is to consider very long time evolution, a simplified approach is used for the space discretization, having very coarse mesh (usually between 50 and 100 elements for a full nuclear containment) and lacking turbulence modeling (which clearly affects the results from combustion implementations). Some of the most well-known lumped-parameter codes are CONTAIN [109], ASTEC [77], SPECTRA [127], and MELCOR [61].

Computational Fluid Dynamics (CFD) codes, on the other hand, provide accurate predictions for primary and secondary flows with a local spatial resolution of all the variables of interest, although they usually require a computer cluster to perform the calculations and they add uncertainty in the turbulence modeling and other closure terms. Moreover, they can also handle combustion modeling and other chemically reacting problems. This accurate resolution provides pressure peaks from flame front accelerations that LP codes cannot predict, as they are limited to the isochoric adiabatic complete combustion (IACC) pressure [80]. The most common CFD solvers are ANSYS Fluent [5], STAR-CCM+ [22], and OpenFOAM [68].

Lumped-parameter codes and CFD codes are not competing for the same terrain: there have been suggestions where both approaches can be coupled [80]. LP codes can quickly simulate the whole accident scenario (which takes several hours of physical time). CFD cannot do that, but it returns more accurate results. The coupling would use the LP codes to quickly simulate a large number of possible accident scenarios with limited accuracy, simulating those cases of special interest with CFD codes. The use of more refined spatial discretizations in the CFD codes can then be considered, even for turbulent resolution with techniques as Large Eddy Simulation (LES).

The thesis described in this report has addressed the problem mentioned at the beginning of this chapter from the point of view of CFD codes: simulating hydrogen turbulent combustion scenarios for nuclear safety management. The main combustion reaction, given by :

$$H_2 + 0.5\,O_2 \longrightarrow H_2O \quad ,$$

has been analyzed with different combustion models. Even if radicals are also generated during the chemical process, having, in reality, more than 50 chemical reactions [32] for hydrogen combustion, its presence is not modeled under the framework of this thesis. CFD simulations are being considered as alternatives to LP codes, as they provide more accurate results. However, low-fidelity combustion models are still employed together with Reynolds Averaged Navier Stokes models. High-fidelity models, as transported-pdf for the combustion or Direct Numerical Simulation for the turbulence calculation, are usually not considered [17] for this scenario. Some of the combustion models proposed in the thesis include new experimental correlations developed for nuclear safety, providing improved accuracy in the modeling of combustion phenomena. Therefore, more accurate results are expected, leading to

a better assessment of nuclear facilities under severe accident scenarios. Nevertheless, some problematic areas of the CFD codes used by the community concerning hydrogen combustion modeling for nuclear safety analysis have been identified:

1. Reliable computer modeling is needed to assess the associated residual risks of possible hydrogen deflagrations. Promising results have been obtained in the past with the commercial CFD software Fluent (see [122]). However, this tool is commercially developed, so the source code is protected, being not possible to modify some of the features that it includes.
2. Even with an open-source code, it is often desired to retrieve numerical results in the shortest period of time while still capturing the flow phenomena accurately. To do so, techniques as Adaptive Mesh Refinement and simplifications as axisymmetric grids should be considered. The use of axisymmetric grids allows the reduction of the problem and can be used because most of the geometries present a symmetry around an axis of rotation.
3. The most widely-used and standard combustion models in the community are the Flame Speed Models (FSM), which require a correlation for the turbulent flame speed. These correlations are based on old experimental data. More recent experimental data of the turbulent flame speed for hydrogen are available and should be included to update the combustion model. This correlation, recently proposed by Goulier [47], is obtained for experiments of lean mixtures of hydrogen and a wide range of turbulence scenarios. It is expected to provide improved results for the flame propagation in the mixtures concerning nuclear safety, which usually have low hydrogen concentrations.
4. Regardless of the combustion model, the dependence on the turbulence properties is direct. Thus, the effects of the variables that represent turbulence quantities on the combustion model should be carefully analyzed.
5. In many of the experimental facilities employed to retrieve turbulent flame speed correlations, effects as buoyancy or flame acceleration are not considered, in order to isolate the physical phenomena. However, in real scenarios, flame acceleration and buoyancy may play an important role in the numerical results.

These problems have raised research questions that are listed below to search for solutions or understand the complications that arise in the field:

1. How can the current combustion model formulation be implemented in an open-source platform as OpenFOAM?
    - Can the simulations be less case-dependent, in terms of ignition or other model constants, in this new framework?
    - How can these new combustion models be verified?
2. Can Adaptive Mesh Refinement be implemented for axisymmetric geometries in the open-source CFD code?
3. How should the experimental correlation of Goulier be coupled with classical combustion models as the TFC proposed by Zimont to better predict flame development?
4. What is the effect of different turbulence models in the combustion models? Can some general guidelines be provided?
5. How do the different combustion models perform under conditions such as flame acceleration or buoyancy flows?

The answer to these questions will be provided throughout the thesis and they will be recalled in the last chapter to show an overview of the relevance of the work done and the outcomes of the research.

2

Theoretical background and literature review on modeling approaches

Prior to showing the methodology followed and the obtained results of this thesis, the used framework should be established and some relevant terms have to be clearly defined. By doing this, it is ensured that the assumptions taken can be correspondingly argued and the concepts have an adequate mathematical description, as it will be useful for further chapters of the thesis. This chapter moves from a a general overview to the specific simplifications used and the model on which the combustion equation is built. Thus, two sections make up the chapter: a first one that presents the description of combustion phenomena and a second one that shows the models available to compute the turbulence, combustion and radiative heat transfer, stating the reasons to choose one over the others.

2.1. Theoretical description of combustion

This section presents all the mathematical formalism of combustion as a reaction between different chemical compounds, which is modeled with a set of equations that describe the motion of the flow. Then, turbulence is introduced and a set of dimensionless numbers, commonly used to describe the flow status, is defined. Different classifications and types of combustion are shown, focusing on the one of interest in the last subsections.

2.1.1. Mathematical formulation of a reacting fluid flow

As combustion occurs within a flow, it should be described using a set of partial differential equations that account for the motion of a fluid. They are based on the continuum hypothesis, assuming that the macroscopic quantities define a domain of the fluid volume, regardless of its size (even if on a microscopic scale they are made up of molecules). Based on this continuum, the equations that govern fluid mechanics can be written as [114]:

- **Continuity/Mass conservation**:

$$\frac{\partial}{\partial t}(\rho) + \frac{\partial}{\partial x_i}(\rho u_i) = 0\,, \tag{2.1}$$

  where u_i is the velocity in the i-th direction (denoted as x_i), ρ is the density of the fluid, and t represents time.

- **Momentum conservation**:

$$\frac{\partial}{\partial t}\left(\rho u_j\right) + \frac{\partial}{\partial x_i}\left(\rho u_i u_j\right) = -\frac{\partial}{\partial x_j}\left(p\right) + \frac{\partial}{\partial x_i}\left(\tau_{ij}\right) + \rho \sum_{k=1}^{N} Y_k f_{k,j}\,, \tag{2.2}$$

where the p represents the pressure, τ_{ij} is the deviatoric stress tensor component, given by:

$$\tau_{ij} = -\frac{2}{3}\mu\frac{\partial u_k}{\partial x_k}\delta_{ij} + \mu\left(\frac{\partial u_i}{\partial x_j} + \frac{\partial u_j}{\partial x_i}\right)$$

and $f_{k,j}$ represents the external volume forces applied to each one of the k-th mixture species (denoted with the mass fraction Y_k) in the j-th direction. μ is the dynamic viscosity and δ_{ij} the Kronecker delta.

- **Total enthalpy conservation**:

$$\frac{\partial}{\partial t}\left(\rho H\right) + \frac{\partial}{\partial x_i}\left(\rho u_i H\right) = \dot{\omega}_T + \frac{\partial}{\partial t}\left(p\right) - \frac{\partial}{\partial x_i}\left(q_i\right) + \frac{\partial}{\partial x_j}\left(\tau_{ij} u_i\right) + \dot{Q} + \rho \sum_{k=1}^{N} Y_k f_{k,i}\left(u_i + V_{k,i}\right)\,, \tag{2.3}$$

where:

  - H is the total enthalpy, that can be expressed with the specific heat capacity at constant pressure c_P and temperature T as:

$$H = \int_{T_0}^{T} c_P dT + \frac{1}{2} u_i u_i\,.$$

  - The reaction source $\dot{\omega}_T$ can be expressed individually for each k-th species in terms of the individual source rate $\dot{\omega}_k$ and the formation enthalpy $\Delta h^0_{f,k}$, having:

$$\dot{\omega}_T = -\rho \sum_{k=1}^{N} \Delta h^0_{f,k} \dot{\omega}_k\,.$$

  - q_i is the heat flux from heat diffusion (in terms of the thermal diffusivity λ) and species diffusion (written with the enthalpy of the k-th species and the diffusion velocity $V_{k,i}$):

$$q_i = -\lambda\frac{\partial T}{\partial x_i} + \rho \sum_{k=1}^{N} h_k Y_k V_{k,i}\,.$$

    This term is usually neglected as it is considerably smaller than $\dot{\omega}_T$.
  - $\dot{Q}$ is the external heat source term
  - The last term represents the power produced on the k-th species in the i-th direction by the volume force $f_{k,i}$.

The total enthalpy conservation was used based on previous in-house studies and it was the chosen one for this study. However, total internal energy can also be used to write a balance equation. The temporal derivative of the pressure in Equation 2.3 presents challenges on the formulation of some numerical models, so the accuracy of either approach has to be assessed.

- **Species conservation**:

$$\frac{\partial}{\partial t}\left(\rho Y_k\right) + \frac{\partial}{\partial x_i}\left(\rho\left[u_i + V_{k,i}\right] Y_k\right) = \dot{\omega}_k\,, \tag{2.4}$$

requiring $N-1$ transport equation if mass conservation is being used and N species transport equations otherwise. Equation 2.4 is expressed in terms of the mass fraction Y_k, defined as the ratio between k-th species mass m_k and total mass m:

$$Y_k = \frac{m_k}{m} \qquad \text{where} \qquad \sum_{k=1}^{N} Y_k = 1\,.$$

The equations for species conservation can also be expressed in terms of the mole fraction X_k given as:

$$X_k = \frac{n_k}{n} \qquad \text{where} \qquad \sum_{k=1}^{N} X_k = 1\,,$$

where n is the total number of moles in volume V and n_k is the number of moles of the k-th specie in the volume. These two ways of expressing the species concentration in the mixture can be related to the molecular weight of each specie k, denoted as W_k, and the mean molecular weight of the mixture, W, having:

$$X_k = \frac{W}{W_k} Y_k \qquad \text{where} \qquad W = \sum_{k=1}^{N} X_k W_k\,.$$

The diffusion velocity term, i.e. $V_{k,i}Y_k$, is usually replaced by calling Fick's law in the case of binary diffusion:

$$V_{1i}Y_1 = -\mathcal{D}_{12}\frac{\partial Y_1}{\partial x_i}\,,$$

where $\mathcal{D}_{12}$ is the diffusion between species 1 and 2. This substitution is also done in the energy conservation equation. In the case of multispecies diffusion, the Hirschfelder and Curtiss approximation is usually employed. It is given as:

$$V_{ki}Y_k = V_{ki}\frac{W_k}{W}X_k = -D_k\frac{W_k}{W}\frac{\partial X_k}{\partial x_i} \qquad \text{where} \qquad D_k = \frac{1-Y_k}{\sum_{j\neq k}\frac{X_j}{\mathcal{D}_{jk}}}\,,$$

where $\mathcal{D}_{jk}$ is the mass diffusivity between species j and k.

These $3+N$ conservation equations have to be closed with a thermochemical model. A equation of state that relates the state variables (pressure, temperature, and density) under certain conditions is required. For example, the ideal gas law is usually invoked. It is given for the mixture within a system by:

$$p = \rho\frac{\mathcal{R}}{W}T\,, \tag{2.5}$$

having the temperature T, universal gas constant $\mathcal{R}$, and the mixture molecular weight W related to the total pressure p. This can be related with the partial pressure of the k-th species, denoted as p_k and defined with the relation:

$$p_k = \rho_k\frac{R}{W_k}T \qquad \text{having that} \qquad p = \sum_{k=1}^{N} p_k\,. \tag{2.6}$$

The ideal gas law fails to predict the condensation to liquid and is inaccurate at very high pressures and extremely low temperatures [114]. It is the closure used for the current study as the conditions allow to: no liquid condensation and no extreme pressures nor temperatures. The models used for the state and transport properties (as c_p, c_v, D, μ or λ) are presented in Chapter 3.

The different equations presented are related to the chemical phenomena that is to be analyzed with a system of M chemical reactions and N species, which is described as:

$$\sum_{k=1}^{N}\theta'_{kj}\mathcal{S}_k \rightleftharpoons \sum_{k=1}^{N}\theta''_{kj}\mathcal{S}_k \qquad \text{for} \quad j = 1,\dots,M\,, \tag{2.7}$$

where θ'_{kj} and θ''_{kj} represent the molar stoichiometric coefficients of the k-th species in the j-th reaction and $\mathcal{S}_k$ represents the k-th species. Even if the amount of species and reactions that are modeled

in low-fidelity approaches is usually reduced, it should be kept in mind that the number of chemical reactions that occur and the number implied species is large. Moreover, the double arrow indicates that the reaction occurs in both directions, having two reaction rates for reaction j: the forward rate of reaction K_{fj} and the reverse rate of reaction K_{rj}. With mass and species conservation conservation it is ensured that:

$$\sum_{k=1}^{N} \theta'_{kj} W_k = \sum_{k=1}^{N} \theta''_{kj} W_k \qquad \text{or} \qquad \sum_{k=1}^{N} \theta_{kj} W_k = 0 \qquad \text{for} \quad j = 1, \dots, M\,, \tag{2.8}$$

having that:

$$\theta_{kj} = \theta''_{kj} - \theta'_{kj}\,. \tag{2.9}$$

The chemical rate $\dot{\omega}_k$ of a given species k (source term of Equation 2.4 is the sum of all the chemical reaction rates $\dot{\omega}_{k,j}$ of all possible M reactions:

$$\dot{\omega}_k = \sum_{j=1}^{M} \dot{\omega}_{kj} = W_k \sum_{j=1}^{M} \omega_{kj} Q_j\,. \tag{2.10}$$

The rate of progress of the j-th reaction, Q_j, can be defined with the forward and reverse rates of reaction as:

$$Q_j = \frac{\dot{\omega}_{kj}}{W_k \theta_{kj}} = K_{fi} \prod_{k=1}^{N} \left(\frac{\rho Y_k}{W_k} \right)^{\theta'_{kj}} - K_{ri} \prod_{k=1}^{N} \left(\frac{\rho Y_k}{W_k} \right)^{\theta''_{kj}}\,. \tag{2.11}$$

The determination of the rate constants K_{fi} and K_{rj} represents a central problem of combustion [114]. The forward reaction rates are usually expressed with the empirical Arrhenius law as:

$$K_{fj} = A_{fi} T^{\beta_j} \exp\left(-\frac{E_{aj}}{RT} \right), \tag{2.12}$$

where A_{fi} is the preexponential constant for the j-th reaction, β_j is the temperature exponent and E_{aj} is the activation energy of the j-th reaction. The backward reaction rates are computed with the equilibrium constants as:

$$K_{rj} = \frac{K_{fj}}{\left(\frac{p_a}{RT} \right)^{\sum_{k=1}^{N} \theta_{kj}} \exp\left(\frac{\Delta S_j^0}{R} - \frac{\Delta H_j^0}{RT} \right)}, \tag{2.13}$$

where $p_a = 1$ bar and the increments of enthalpy and entropy, ΔH_j^0 and ΔS_j^0, respectively, refer to the changes between reactants and products. All these coefficients are obtained from the tabulation of chemical kinetic solvers, as values from Q_j obtained experimentally are widely disputed in the chemical kinetics community [114]. As a final remark, the Arrhenius law cannot be used as a closure in numerical models based on Reynolds-averaging due to the nonlinearity of the expression, which would lead to large truncation errors if only a few terms are considered on the expansion. However, increasing the order of the polynomial leads to many unclosed terms that would require extra transport equations.

2.1.2. Turbulence description

Turbulence is the fluid motion characterized by chaotic changes in pressure and flow velocity, increasing dissipation and diffusivity. Even if characterized by irregular motion, it is a deterministic and can be described with the conservation equations shown in Subsection 2.1.1. These flows occur at large Reynolds numbers (see Subection 2.1.3 for a definition of this dimensionless number). Turbulent flows are inherently three dimensional, so two dimensional simplifications incur in deviations from reality. A more detailed explanation of the topic can be found in [116] and [78].

To simplify turbulent flows, it is assumed that turbulence is homogeneous (statistical properties are invariant under coordinate axes translations), isotropic (statistical properties are invariant under rotations and reflections), and statistically stationary (statistical properties are invariant under time shifts). The use of this assumption allows a reduction of turbulence to a simple ensemble of eddies of different velocities and length scales. These eddies have different length scales: ranging from the largest eddies, which are from the size of the order of the flow geometry, to the smallest scales, where dissipation of the energy from the larger scales into heat occurs by viscosity. The transfer of energy occurs through the energy cascade in the inertial range, where large scales with high kinetic energy transfer this energy to the smaller scales, eventually reaching the smallest scales where the viscous stresses transform the kinetic energy into internal energy. These regions and the life cycle of the turbulent energy can be seen in Figure 2.1.

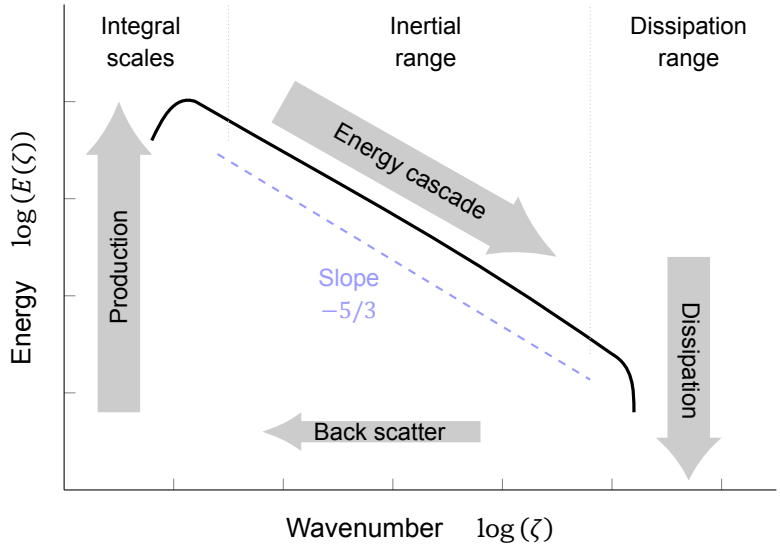

Figure 2.1: Sketch of the turbulence energy cascade with the spectrum of turbulence energy and the life cycle of turbulence energy, adapted from [116].

The different eddy scales and their respective characteristic length, velocity, and time scales are defined by the kinematic viscosity ν, turbulent kinetic energy dissipation ε, and turbulent kinetic energy k. The integral scales have an associated length scale l_t, and its characteristic velocity $u'(l_t)$ and timescale τ_t are computed with k and ε, being them defined as:

$$l_t = \frac{k^{3/2}}{\varepsilon}, \qquad u'(l_t) = \sqrt{\frac{2k}{3}}, \qquad \tau(l_t) = \tau_t = \frac{l_t}{u'(l_t)} = \sqrt{\frac{3}{2}}\frac{k}{\varepsilon}.$$

On the other hand, the Kolmogorov scales, which are the smallest scales in the dissipation range, are defined based on the dissipation ε and viscosity ν, having that:

$$\eta = \left(\frac{\nu^3}{\varepsilon}\right)^{1/4}, \qquad u'(\eta) = (\nu\varepsilon)^{1/4}, \qquad \tau(\eta) = \tau_\eta = \left(\frac{\nu}{\varepsilon}\right)^{1/2}.$$

These results are obtained from dimensional analysis.

2.1.3. Dimensionless numbers

Before proceeding to a description of the combustion phenomena, some relevant dimensionless numbers are presented. These dimensionless numbers will help to classify flow and flame regimes, determining the range of validity of certain hypotheses and assumptions.

- **Reynolds number**: the general definition of the Reynolds number is the ratio of inertial forces to viscous forces:

$$\mathrm{Re} = \frac{\rho U_\infty L}{\mu} = \frac{U_\infty L}{\nu}\,, \tag{2.14}$$

where ρ is the density, U_∞ is the velocity, L is a characteristic length, μ is the dynamic viscosity and ν is the kinematic viscosity. Values of $\mathrm{Re} >> 1$ are associated with turbulent flows while values $\mathrm{Re} < 1$ are associated with laminar flow (also known as creeping or Stokes flow). This Reynolds number is defined based on mean quantities. However, it can also be expressed as a local variable or based on the turbulent quantities. The turbulent Reynolds number Re_t is useful for combustion regimes classification and it is defined as:

$$\mathrm{Re}_t = \frac{\rho u' l_t}{\mu} = \frac{u' l_t}{\nu} \xrightarrow[\nu = S_{L,0}/\delta_L]{\text{which by using}} \mathrm{Re}_t = \left(\frac{l_t}{\delta_L}\right)\left(\frac{u'(l_t)}{S_{L,0}}\right), \tag{2.15}$$

where u' are the turbulent velocity fluctuations, $S_{L,0}$ is the laminar unstrained flame speed, and δ_L is the flame thickness. Values larger than unity are associated with turbulent flames while those smaller than unity are laminar flames.

- **Mach number**: the Mach number is the ratio of flow velocity with the local speed of sound:

$$\mathrm{Ma} = \frac{u}{a_s}\,. \tag{2.16}$$

The velocity of sound a_s is defined as:

$$a_s = \sqrt{\gamma\left(\frac{\partial p}{\partial \rho}\right)_T} \xrightarrow{\text{which for an ideal gas is}} a_s = \sqrt{\gamma R T}\,,$$

where γ is the ratio of specific heat capacities $\gamma = c_P/c_V$ and R is the universal gas constant. The Mach number is a local quantity. Four regimes can be distinguished and used to characterize the flow regime. For $\mathrm{Ma} < 0.8$ the flow is subsonic, for $0.8 < \mathrm{Ma} < 1.2$ the flow is transonic, if $1.2 < \mathrm{Ma} < 5$ the flow is on the supersonic regime and for $5 < \mathrm{Ma}$ the flow is hypersonic. Further assumptions can be made if $\mathrm{Ma} \lesssim 0.2$ (fully incompressible flow) and different number of boundary conditions are required depending on whether $\mathrm{Ma} > 1$ or $\mathrm{Ma} < 1$.

- **Prandtl number**: it is the ratio between the momentum and thermal diffusivity:

$$\mathrm{Pr} = \frac{\nu}{\alpha} = \frac{\mu/\rho}{\kappa/(c_P\rho)}\,, \tag{2.17}$$

where α is the thermal diffusivity, κ is the thermal conductivity and c_P is the specific heat at constant pressure. This value doesn't depend on length values (as the Reynolds number does) and it is approximately constant for a wide range of temperatures and pressures. When $\mathrm{Pr} << 1$ heat diffuses faster compared with momentum (having larger thermal boundary layers) while $\mathrm{Pr} >> 1$ means that the heat diffuses slower than the momentum (having thicker velocity boundary layers). The Prandtl number is specie-dependent in the case of a mixture. For turbulent flows, an analogy to the laminar (or molecular) Prandtl number defined above is used, having:

$$\mathrm{Pr}_t = \frac{\nu_t}{\alpha_t}\,. \tag{2.18}$$

The turbulent Prandtl number is used for the closure of the turbulent energy flux (see Equation 2.70) in a similar way to the eddy viscosity for the Reynolds stresses. Even though momentum and temperature can be unrelated and the use of a constant single value is highly disregarded [74], using Pr_t represents a simple approach to deal with unclosed terms.

- **Schmidt number**: defined as the ratio between momentum and mass diffusivity:

$$\mathrm{Sc} = \frac{\nu}{D}\,, \tag{2.19}$$

where D is the mass diffusivity of a given species (as the Schmidt number is also a specie-dependent value). This number is relevant for species transport. The same turbulent analogy as for the Prandtl number is applied in the Schmidt number, having a turbulent diffusivity D_t:

$$\mathrm{Sc}_t = \frac{\nu_t}{D_t}\,. \tag{2.20}$$

- **Lewis number**: related to the two previous dimensionless numbers, the Lewis number shows the relationship between thermal and mass diffusivity, thus its relevance for combustion studies:

$$\mathrm{Le} = \frac{\alpha}{D} = \frac{\mathrm{Sc}}{\mathrm{Pr}}\,. \tag{2.21}$$

Experimentally determining the laminar Lewis number is not something straightforward. The most classical way to retrieve it [11] uses an effective Lewis number, which is the sum between laminar and turbulent Lewis number. The former is the one presented above and the latter is defined as:

$$\mathrm{Le}_t = \frac{\alpha_t}{D_t}\,. \tag{2.22}$$

Both laminar and turbulent Lewis numbers vary for each individual species. If the Lewis number equals one, the thermal and mass diffusivity have the same rate. Although this is taken as an assumption in many combustion models and implementations, it is not fully true, and the assessment of non-unity Lewis numbers should be kept in mind [18]. The relevance of this dimensionless number is stated elsewhere [114], e.g. the behavior of thermodiffusive instabilities is determined by the Lewis number of the mixture.

- **Damköhler number**: it is defined as the ratio between the mass transport/turbulent timescale τ_t and the chemical/combustion reaction timescale τ_c as:

$$\mathrm{Da} = \frac{\tau_t}{\tau_c} \xrightarrow[\substack{\tau_c = D/(S_{L,0})^2 \\ \delta_L = D/S_{L,0} \\ \tau_t = L/u'(L)}]{\text{which by using}} \mathrm{Da}\,(L) = \frac{L/u'(L)}{\delta_L/S_{L,0}}\,, \tag{2.23}$$

where the chemical timescale is expressed in terms of the flame thickness and the laminar flame speed (quantities defined in Subsection 2.1.5). To invoke the relation $\delta_L = D/S_{L,0}$, a Schmidt number of one in the unburnt gases is required [88]. The mass transport timescale can be either associated with the integral length scales, obtaining:

$$\mathrm{Da}\,(l_t) = \frac{\tau(l_t)}{\tau_c} = \frac{l_t/u'(l_t)}{\delta_L/S_{L,0}} = \left(\frac{l_t}{\delta_L}\right)\left(\frac{u'(l_t)}{S_{L,0}}\right)^{-1}\,, \tag{2.24}$$

or with the Kolmogorov scales:

$$\mathrm{Da}\,(\eta) = \frac{\tau(\eta)}{\tau_c} = \frac{\eta/u'(\eta)}{\delta_L/S_{L,0}}\,. \tag{2.25}$$

Usually, the preferred definition is the one based on the integral length scale. The meaning of this dimensionless number is explained in Subsection 2.1.7, as it is used to classify the different combustion regimes.

- **Karlovitz number**: is the ratio between the chemical timescale τ_c and the Kolmogorov timescale τ_η, having:

$$\mathrm{Ka} = \frac{1}{\mathrm{Da}\,(\eta)} = \frac{\tau_c}{\tau\,(\eta)} = \left(\frac{\delta_L}{\eta}\right)^2 = \frac{\delta_L/S_{L,0}}{\eta/u'(\eta)}\,, \tag{2.26}$$

where the same expressions as before have been used to rewrite the chemical and Kolmogorov timescales. Some authors prefer to use a reaction zone thickness Karlovitz number given as $\mathrm{Ka}_\delta = \delta_L^2 \mathrm{Ka}$. The Karlovitz number can also be expressed as:

$$\mathrm{Ka} = \left(\frac{l_t}{\delta_L}\right)^{-1/2} \left(\frac{u'(l_t)}{S_{L,0}}\right)^{3/2}, \tag{2.27}$$

by using Equation 2.15 and the fact that the ratio of integral timescale to Kolmogorov timescale is the square root of the turbulent Reynolds number $\mathrm{Re}_t^{1/2} = \tau\left(l_T\right)/\tau\left(\eta\right)$, where the timescale of L can be computed as $\tau\left(L\right) = L/u'\left(L\right)$. The following relation between turbulent Reynolds number, Damkholer number and Karlovitz number can be constructed:

$$\mathrm{Re}_t = \mathrm{Da}^2 \mathrm{Ka}^2 . \tag{2.28}$$

- **Markstein number**: this number characterizes the heat release with respect to the variation of the flame surface topology:

$$\mathcal{M} = \frac{\mathcal{L}}{\delta_L}, \tag{2.29}$$

where $\mathcal{L}$ is the Markstein length and δ_L is the laminar flame thickness. If $\mathcal{M} < 0$, an increase in the stretch corresponds to an increase of flame front propagation (while $\mathcal{M} > 0$ describe flames with stable responses to stretch).

- **Zeldovich number**: measures the activation energy of a chemical reaction:

$$\beta = \frac{E_a}{RT_b} \cdot \frac{T_b - T_u}{T_b}, \tag{2.30}$$

where E_a is the activation energy of the reaction defined in the Arrhenius equation, T_u is the unburnt mixture temperature, and T_b is the burnt mixture temperature. This dimensionless number is not a ratio between magnitudes. Indeed, its typical value in combustion scenarios lies between $\beta \approx 8$ and $\beta \approx 20$ [88].

2.1.4. Combustion phenomena and types of combustion

Combustion is a reduction-oxidation exothermic reaction that occurs at high temperatures. It requires a fuel and an oxidizer that, after the reaction is completed, produce oxidized, usually gaseous, products. In order to start the combustion process, heat is required (forming what is known as the fire triangle: fuel, oxidizer, and heat [100]). The high-temperatures produced by the reaction create a chain reaction, triggering a self-sustainable reaction.

Combustion is a complex phenomenon that involves multiple physical mechanisms that are interrelated with each other: chemistry, mass diffusion and mass transfer, turbulent mixing, convection due to forces as buoyancy, solid particle transport, radiation, thermodynamics, fluid mechanics... The study of a combustion scenario requires either the modeling of each one of the components or the justified simplification based on the validity of a given assumption in each specific case of study. During the modeling, and as for any other chemical flow, the Navier-Stokes equations should include the combustion reaction and/or any other chemistry-related phenomena, apart from the fluid dynamics that they represent. Moreover, and given that the mixture is made up of multiple species, heat capacities and transport coefficients should be tracked individually (as their value significantly changes with temperature), requiring the calculation of the mixture composition.

The combustion process can be classified depending on multiple criteria. Some of them can directly be related to the flow regime (as it is the case of laminar combustion or turbulent combustion) while others are useful for the propulsive industry (complete or incomplete combustion). Two relevant classifications for this project are introduced:

- **Based on the reactants mixing**: combustion, as any other reaction, occurs between reactants and products, having that two reactants are required: fuel and oxidizer. In the combustion of gaseous species there is no multiphase phenomena involved, so the degree to which the mixing between these two reactants occurs, determines the physical mechanisms that control the combustion [88].

  - **Non-premixed combustion**: the oxidizer and the fuel enter the domain where combustion happens through two different streams. It is also known as diffusion combustion, given that the mechanism that controls the combustion is the rate at which the fuel and oxidizer mix. This makes modeling more straightforward [88]. In this combustion regime, there is an intense chemical reaction zone and the flame front is determined by the stoichiometric value of the mixture, separating the oxidizer and the fuel. The flame is convected and deformed by the local flow field. The simplest example is a lighter: it exhausts a stream of fuel that gets mixed with the air (oxidizer) that surrounds the lighter, creating a non-premixed flame.
  - **Premixed combustion**: the oxidizer and the fuel enter the combustion domain mixed and through the same stream. Thus, both species are, in the simplest case, in a homogeneous mixture of fuel and oxidizer. Once the mixture is ignited, the flame front separates the reactants and the products with the flame propagating towards the reactants mixture. One example is a gas stove: the natural gas (fuel) and ambient air (oxidizer) are mixed before arriving at the flame front, where the reaction takes place.
  - **Partially-premixed combustion**: this regime is in between the previous two and comes from a more realistic point of view, given that the existence of a purely premixed or non-premixed flame in an uncontrolled scenario is complicated. Flame lift-off, stratification, or incomplete mixing are some of the situations that lead to partially-premixed combustion. In nuclear safety, hydrogen goes up in the containment, so stratification will occur. Although some authors separate stratified from partially-premixed combustion (see Figure 4 of [111]), in the majority of the cases stratified combustion is considered as one way in which partially-premixed combustion may occur [88]. Partially-premixed combustion has regions with different concentrations of fuel, oxidizer, and products, having different stoichiometric values and showing features from diffusion flames in some zones and from premixed flames in others. This makes that the characteristic velocities from premixed combustion are not guaranteed. The most classical example of a partially-premixed flame is a triple flame [42], where a gradient in the stoichiometric ratio appears in the stream, having three flame fronts that coalesce in a point: a rich premixed flame, a diffusion flame, and a lean premixed flame.

- **Based on the combustion propagation mechanism**: when the hydrogen concentration is within the flammability limits, there are two ways in which the premixed reactants mixture can be heated [62]. If there is too much or too little hydrogen volume, combustion does not occur. These regimes are usually characterized by Saphiro diagrams that show the type of combustion for a given mixture of hydrogen, steam, and air (see Figure 2.2). The main two modes are:

  - **Deflagration**: these flames travel slower than the velocity of sound with respect to the unburnt gas mixture. The propagation is, in the absence of strong body forces as buoyancy, limited by heat transfer from the hot burnt gases to the unburnt gases, raising the temperatures, and promoting the exothermic reaction in the unburnt gases. The reaction zone where the chemical combustion occurs progresses through the medium by mass and heat diffusion. If the concentration of hydrogen is very low ($< 8\%$ in volume), the mixture will burn without a drastic increase in pressure.
  - **Detonation**: when the combustion wave moves faster than the velocity of sound with respect to the unburnt gas, the compression of the pressure wave increases the temperature of the unburnt gases above the autoignition temperature, initiating the combustion. There are empirical criteria (sigma- and lambda-criterion) to determine whether detonation will occur. Direct initiation of detonation requires a high energy source (multiple orders of magnitude larger than the energy for a deflagration) so it is unlikely that it occurs in reactor accidents. However, deflagration flames can accelerate, eventually leading to a detonation wave. Flame acceleration is mainly caused by turbulence, obstacles in the flame

path, flame interface instabilities, confinement effects, and acoustic/shock wave interactions. Deflagration-to-detonation transition involves a variety of instabilities and mixing processes that transform a deflagration front into a detonation wave.

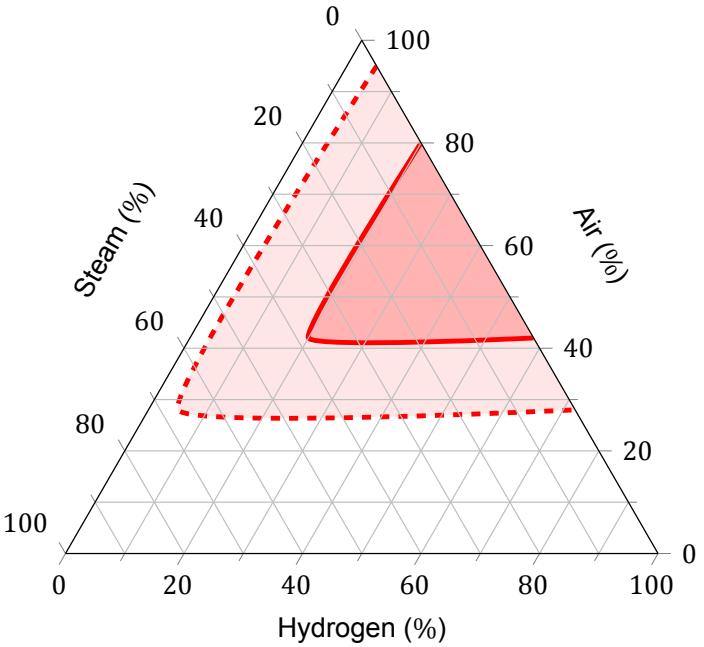

Figure 2.2: Shapiro flammability diagram for a hydrogen-steam-air mixture at 1 bar and 300 K, adapted from [123]. Two regions are presented: one bounded by the detonation limit — and the other by the deflagration limit - - .

2.1.5. Premixed combustion

Before introducing turbulence effects, a laminar one-dimensional premixed flame is considered. Premixed flames can be simplified with a combustion chemical reaction between two reactants and the products (which encompass all combustion products):

$$\theta'_F \, \mathrm{F} + \theta'_O \, \mathrm{O} \longrightarrow \mathrm{Products}\,, \tag{2.31}$$

where F stands for fuel and O for oxidizer. The reaction is under stoichiometric conditions when the ratio of mole fractions is given by the molar stoichiometric coefficients θ'_F and θ'_O multiplied by the molecular weight of the specie W_i, obtaining the stoichiometric mass ratio S:

$$S = \left(\frac{Y_O}{Y_F}\right)_{st} = \frac{\theta'_O W_O}{\theta'_F W_F}\,. \tag{2.32}$$

The equivalence ratio is a dimensionless parameter given as the ratio of mole (or mass) fractions with respect to the stoichiometric ratio of mole (or mass) fractions:

$$\Phi = \frac{(X_F/X_O)}{(X_F/X_O)_{st}} = \frac{(Y_F/Y_O)}{(Y_F/Y_O)_{st}} = S \cdot \frac{Y_F}{Y_O}\,. \tag{2.33}$$

If $\Phi < 1$ the mixture is lean (there is an excess in the oxidizer) and when $\Phi > 1$ the mixture is rich (having an excess of fuel). When $\Phi \approx 1$, the mixture is called stoichiometric. In nuclear safety engineering, the mixtures are always characterized by a lean equivalence ratio.

Activation-Energy-Asymptotic theory

The Activation-Energy-Asymptotic (AEA) described by Zel'dovich [149] is usually employed as a starting point to describe premixed flamed, as it presents a one dimensional premixed flame in order to define many of the quantities that are referred later on. An unperturbed laminar planar premixed flame can be analyzed as a one-dimensional adiabatic stationary front that propagates in a fuel-air mixture flow. This theory doesn't model detonations but only deflagrations. It is worth recalling that in premixed combustion, the flame front separates the homogeneous mixture of the reactants (left-hand side of the chemical reaction) of the products (right-hand side of the equation). A single step irreversible chemical reaction is considered, where, by knowing one state, the other is automatically defined. The simplified theory requires strong assumptions as a reaction unity constant Lewis number and a constant specific heat capacity between burnt and unburnt gases. However, it has to be stressed out that these assumptions are not present in the numerical model and are used here to detail the structure of premixed flames. Finally, the asymptotic case of large Zeldovich numbers ($\beta >> 1$) is being considered in this theory. As only one chemical equation is considered, the progress variables c is commonly used to denote the reaction progress:

$$c = \frac{Y_f' - Y_{f,u}}{Y_{f,b} - Y_{f,u}} \xrightarrow[\text{Le=1}]{\text{when}} c = \frac{T - T_u}{T_b - T_u}\,, \tag{2.34}$$

where Y_f' is the fuel mass fraction and the subscripts b and u represent the burnt and unburnt states, so that c ranges between 0 and 1 denoting unburnt and burnt mixtures respectively. The regress variable b is an alternative way to describe the state in the chemical reaction, being defined as $b = 1 - c$ and taking values of 0 and 1 in the burnt and unburnt mixture respectively.

The equations that define a one-dimensional laminar premixed flame are obtained after simplifying Equation 2.1, 2.2, and 2.3 (this last is rewritten in terms of the progress variable with Le $= 1$), having:

$$\frac{d}{dx}(\rho u) = 0\,, \tag{2.35}$$

$$\frac{d}{dx}\left(\rho u^2\right) = \frac{d}{dx}\left(\frac{4}{3}\mu\frac{du}{dx}\right) - \frac{dp}{dx}\,, \tag{2.36}$$

$$\frac{d}{dx}(\rho u c) = \frac{d}{dx}\left(\rho D\frac{dc}{dx}\right) + \dot{\omega}_c\,. \tag{2.37}$$

Even if the pressure drop is small when compared with the pressure itself (by integrating Equation 2.36, $\Delta p/p = \mathcal{O}((\rho_u/\rho_b - 1)\left(S_{L,0}\right)^2 p/\rho_u) << 1$) and the assumption of $p =$ cst across the flame is justified [88], it can be seen that the pressure gradient term is preserved in the momentum conservation given that the distance throughout which the drop occurs is very small.

A laminar premixed flame can be divided into three main different domains (see Figure 2.3) having the unburnt gas region (where the mixture is composed of unburnt reactants at low-temperature T_u), the laminar flame and the burnt gas region (where the mixture is composed of burnt products at high temperature T_b). The laminar flame region is subdivided into a preheat zone, where the temperature starts to rise but the reaction rate is still negligible) and a reaction zone (where the majority of the reaction takes place).

Two properties define a laminar premixed flame: the laminar flame speed, $S_{L,0}$, and the laminar flame thickness, δ_L. The first one is represented as the velocity of the incoming unburnt gases in Figure 2.3 (given that flame is considered to be steady). If the flame is moving in a steady medium, $S_{L,0}$ is the speed at which the flame propagates. The AEA theory predicts [88] that $S_{L,0} \propto \sqrt{D/\tau_c}$, where τ_c is the characteristic flame time, combustion time, or chemical timescale.

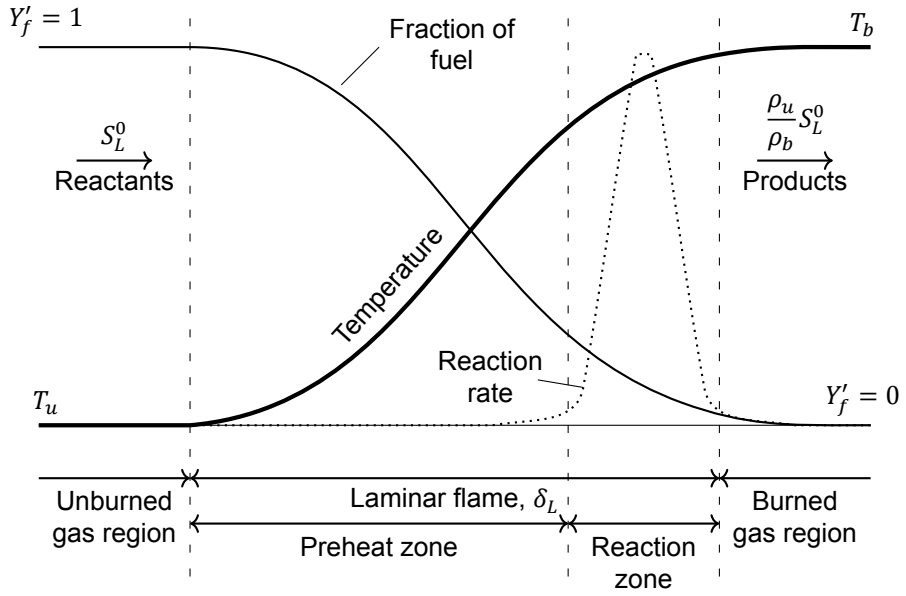

Figure 2.3: One-dimensional laminar premixed flame schematics (modified from [88]). The reaction zone is thinner than the one here drawn [114].

The second parameter represents the thickness of the flame and there are different methods to compute it (having that usually they yield different results):

- Thermal thickness: although it requires knowing the temperature profile, this is the best definition and most accurate method:

$$\delta_L = \frac{\max(T) - \min(T)}{\max\left|\frac{\partial T}{\partial x}\right|}. \tag{2.38}$$

- Progress-variable based thickness: similarly to the previous method, there is an approach based on the gradient of the progress variables [88] which should yield the same results as the thermal-thickness if $\mathrm{Le} = 1$ and close results as Le approaches unity:

$$\delta_L = \frac{1}{\max\left|\frac{\partial c}{\partial x}\right|}. \tag{2.39}$$

  An alternatively formulation based on the distance between $c = 0.01$ and $c = 0.99$ exists [114], although it is deemed as not useful by the author later in the same reference.

- Mixture properties method: by using the properties of the fluid, the *diffusive* thickness (as it is based on the thermal diffusivity coefficient α) can be computed as [88]:

$$\delta_L = \frac{\alpha_u}{S_{L,0}}, \tag{2.40}$$

  or with the corrected version of [114]:

$$\delta_L = 2\frac{\alpha_u}{S_{L,0}}\left(\frac{T_b}{T_u}\right)^{0.7}. \tag{2.41}$$

2.1.6. Effects of turbulence in combustion (and viceversa)

When the aforementioned laminar flame starts to curve (without turbulence being required), there are strain effects that should be taken into account. A laminar flame can also propagate spherically and not planarly, having that the previous discussion is no longer valid because the curved flame front is now, at least, two dimensional. Moreover, large strain values may lead to local flame extinction. The strained laminar flame speed S_L^∞ (although sometimes simply denoted as S_L) is related to the unstrained laminar flame speed $S_{L,0}$ to account for the flame strain and extinction (see Equation 5.88 of [88]):

$$S_L^\infty = S_{L,0}\left(1 - \left(\frac{\rho_b}{\rho_u}\right)^2 \frac{D_b}{D_u}\tau_c \kappa_s\right), \tag{2.42}$$

where the diffusivities of the burnt D_b and unburnt D_u mixture have been separated (although in most cases $\rho_b^2 D_b = \rho_u^2 D_u$ [88]) and the local strain rate κ_s is generally given for an infinitely thin self-propagating surface as [20]:

$$\kappa_s = \frac{1}{A_s}\frac{dA_s}{dt} = n_{s,j} n_{s,k} \frac{\partial u_j}{\partial x_k} - \frac{\partial u_k}{\partial x_k} + S_s \frac{\partial n_{s,k}}{\partial x_k}, \tag{2.43}$$

where A_s is the area of the self-propagating surface, S_s is the surface self-propagation speed and $\vec{n}_s$ is the unit normal vector to the surface, which if defined in terms of the progress variable yields:

$$\vec{n}_s = -\frac{\nabla c}{|\nabla c|}. \tag{2.44}$$

When the surface is assumed to be a sphere of radius R_f, the local strain rate can be expressed as:

$$\kappa_s = \frac{1}{A}\frac{dA}{dt} \longrightarrow \kappa_s = \frac{2}{R_f}\frac{dR_f}{dt}. \tag{2.45}$$

Moreover, the spherically unstrained propagating flame front can be assumed to be defined with a flame radius R_f^0 (the superscript here denotes unstrained laminar spherical flame) that is no longer moving with the unstrained laminar flame speed $S_{L,0}$ but the unstrained laminar flame velocity [46], which is defined as:

$$V_L^0 = \frac{dR_f^0}{dt} \longrightarrow V_L^0 = \frac{\rho_u}{\rho_b} S_{L,0}. \tag{2.46}$$

Defining which isosurface is the one that represents the flame radius is somehow tricky (as different isosurfaces have different speeds) and it will be discussed in Subsection 3.2. Similarly to the unstrained laminar flame speed, there is a strained laminar flame speed V_L^∞ (or simply V_L):

$$V_L^\infty = \frac{\rho_u}{\rho_b} S_L^\infty. \tag{2.47}$$

When a premixed flame front is moving in a turbulent medium, its propagation speed presents an intricate physical definition, and sometimes lacks a mathematical formalization, even if many authors have tried to characterize it (see [89] and [114]). In a 1D turbulent statistically stationary case, the local flame speed is equal to the local mean flow velocity towards the mean flame position. However, extrapolating this definition to an arbitrary three-dimensional turbulent flow is complicated: choosing the flame surface may be ambiguous and the local flow velocity varies depending on the isosurface chosen. This is especially complicated in some combustion regimes where the flame front is spread and the combustion and turbulence are interrelated (namely the well-stirred reactor, see Section 2.1.7 and Figure 2.8). The flamelet regime (which is the one mainly concerning nuclear safety applications) assumes that the turbulent flame front is composed of many infinitesimally small laminar flames (see Figure 2.5), and that every part moves at the laminar flame speed. The flame front is thin and their fluctuations can be confined in a region (known as flame brush), having that the turbulent flame speed

S_t is the velocity at which that bounded region advances. The spatial turbulent flame velocity V_T for a spherically propagating flame front of radius R_f can be expressed as:

$$V_T = \frac{dR_f}{dt} = \frac{\rho_u}{\rho_b} S_t \,. \tag{2.48}$$

The turbulent flame speed can also be defined in terms of the reaction rate and the mass flux through the wrinkled flame front area A_T and mean flame front area $\overline{A}$ [114], leading to:

$$\frac{S_t}{S_{L,0}} = \frac{A_T}{\overline{A}} \,. \tag{2.49}$$

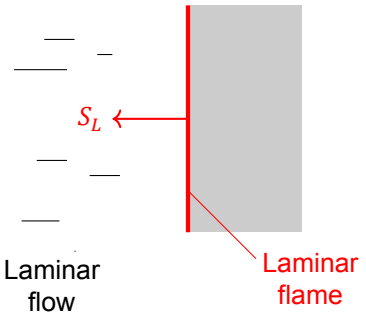

Figure 2.4: Laminar flame, where S_L is the laminar flame speed.

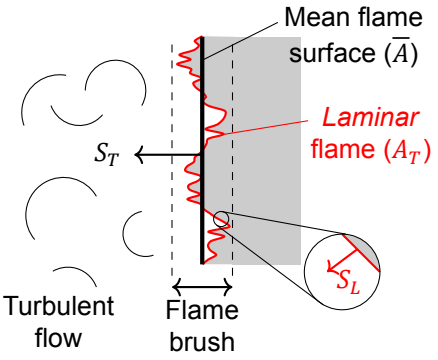

Figure 2.5: Turbulent flame with the flamelet approach depicted in the zoomed detail, S_t is the turbulent flame speed.

However, as the turbulent flame speed is used in many combustion models, its dependence on different variables has been thoroughly studied (for a review check Chapter 4 of [88] , where it is discussed the dependence of S_t on diffusivity, pressure, temperature,...). One of the most notable influences on the turbulent flame speed is its dependence on the root mean square of the velocity fluctuations u' (see Figure 2.6). When there is no turbulence ($u' = 0$), the turbulent flame speed should match the laminar flame speed $S_t = S_L$. When $u' \neq 0$ there are three different regions in this diagram, having a linear dependence region for $u' < u'_l$ (although some authors prefer to restrict the linear region up to $u' < S_L$ [73]), the bending regions between $u'_l < u' < u'_m$ (where the slope decreases until it reaches the maximum S_t) and the quenching region between $u'_m < u' < u'_q$ (having that at u'_q the turbulence is so high that the combustion is stopped and if $u'_q < u'$ combustion doesn't happen anymore).

The clearest effects that turbulence has on the flame front are the wrinkling and the possible break up of the flame front in pockets of combustion that move following the flow field. The wrinkling is usually accompanied by local stretching that occurs in curved expanding flames, which may lead to premature quenching. Moreover, there are flame instabilities that, even if they can also happen in laminar flames, are enhanced by turbulent flows. The two main ones are:

- **Hydrodynamic instability**: also known as the Darrieus-Landau instability. The thermal expansion of the combustion products (i.e. the fact that the burnt gases have a lower density than the reactants $\rho_b < \rho_u$) makes that the flame fronts are unstable to perturbations of any wavelength, see [87]. The outcomes of this instability are that the flame front tends to form cusps and crests (see Figure 2.7a compared with Figure 2.7b). This can clearly be seen in in Bunsen burner flames that, even if $U_\infty = S_L$, the flame front is not completely planar but curved.

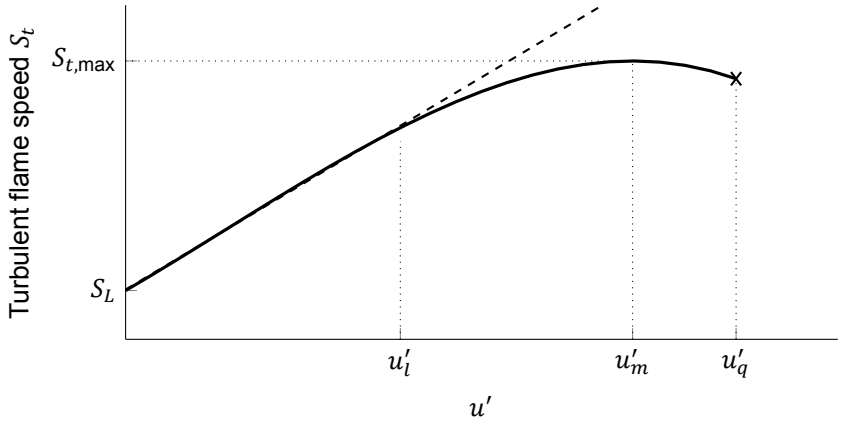

Figure 2.6: Sketch of the typical dependence of the turbulent flame speed on the root mean square of the velocity fluctuations, based on [88].

- **Thermodiffusive instability**: it is based on the preferential diffusion of the limiting mixture component, i.e. when the mixture is not stoichiometric and the mass diffusivity of the deficient d reactant is higher than that of the excess e reactant $D_d > D_e$. This is the case in lean hydrogen-air mixtures (directly concerning nuclear safety applications), causing a turbulent flame speed decrease in the downstream pointing parts of a curved flame front. The preferential diffusion effects occur as well if the mixture molecular diffusivity is higher than the mixture thermal diffusivity (i.e. Le < 1). In this case, the reactants diffuse towards the burnt gases faster than the heat of the reaction is transferred to the fresh gases. This is opposed to Le > 1, where the heat is transferred faster to the reactants than the reactants are diffused to the product regions, having a stable regime. A detailed explanation of this phenomenon can be found in [114]. This instability can be seen in the appearance of cellular structures in the flame front (see Figure 2.7c compared with Figure 2.7b).

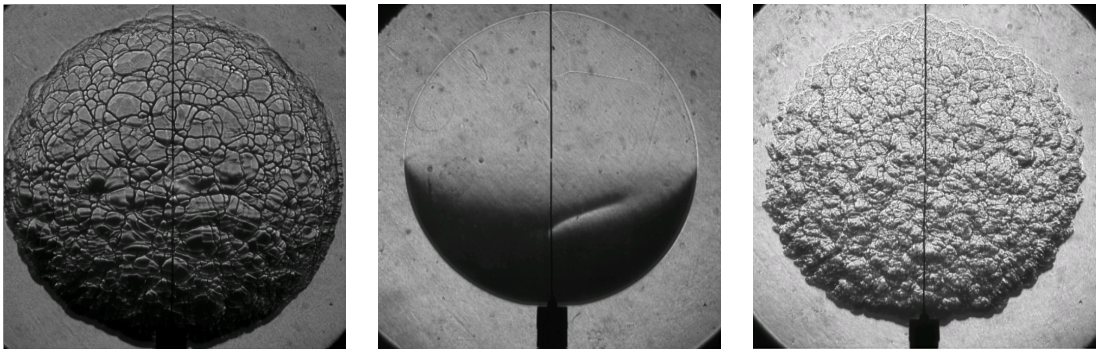

(a) Hydrodynamic instability ($\Phi = 4.0$, $p = 20$ atm, $t = 3.0$ ms).

(b) No instabilities ($\Phi = 4.0$, $p = 5$ atm, $t = 4.5$ ms).

(c) Thermodiffusive instability ($\Phi = 0.6$, $p = 5$ atm, $t = 3.5$ ms).

Figure 2.7: Intrinsic flame instabilities of hydrogen-air spherical flames, obtained from [99].

As the two effects can appear simultaneously, the response of the flame to these perturbations largely depends on the mixture properties. In the case where Le > 1 and/or $D_d < D_e$, the diffusive-thermal instability can cancel the effects of the hydrodynamic instability, such that the flame front tends to be planar.

The strained smooth velocity V_S is the flame propagation velocity when the thermodiffusive instabilities and the wrinkling of the flame front (which indeed causes an increase in the flame propagation velocity) are not considered. It is defined as (see Equation 99 in [46]):

$$V_S = V_L^0 - \mathcal{L}\kappa_s\,, \tag{2.50}$$

where $\mathcal{L}$ is the Markstein length (which is mixture dependent) and κ_s is the local stretch rate previously defined. $\mathcal{L}$ represents the linear relationship between the flame speed and the flame stretch that can be observed both theoretically and experimentally. Depending on whether $\mathcal{L}$ is positive or negative, an increase on the stretch rate will decrease or increase V_S with respect to V_L^0.

The turbulent field is also affected by combustion and by the flame front itself. The clearest example is the countergradient scalar transport, whose discussion is reserved for Subsection 2.2.2. Another effect occurs due to the temperature change between the two sides of the flame, which leads to a change in the kinematic viscosity, affecting the local Reynolds number. For gases, kinematic viscosity increases with temperature, which leads to a lower value of the local Reynolds number in the burnt region, possibly causing flow relaminarization. Through the flame front, there is also an increase in speed, which depends on the density ratio and the laminar flame speed. This speed increase is relevant given that it occurs in a very thin region of space, modifying the turbulent flow field and the vorticity field, leading to flame-generated turbulence. Finally, the importance of turbulent stretching should not be underestimated in combustion modeling [88].

The last effect discussed here is buoyancy. It also affects laminar flames, but when considering combustion as a reaction with two mixtures separated by a flame front (emulating a *two-phase flow* where one domain consists of a burnt mixture and the other of an unburnt mixture), buoyancy effects play a critical role. Fresh heavy cold unburnt gases are separated from burnt light hot gases by a surface that can quench and is conditioned by turbulence. External forces (e.g. gravity) and pressure gradients affect each domain of the fluid differently [114]. Even if most of the flames are not affected by gravity (as they occur in confined and small spaces), most of them are affected by pressure gradients (given that they are enclosed in ducts). However, in nuclear safety, the size of large containments makes also that gravity plays a non-negligible role through thermal convection and buoyancy.

2.1.7. Turbulent premixed combustion regimes

As it has been shown, coupling turbulence with combustion causes physical interactions. This has led to the creation of a diagram to, phenomenologically, classify the flame regimes. There are authors [114] that are against this classification as it is based on orders of magnitudes and the actual limits are not well-defined. Even so, this diagram is widely used and many improvements have been proposed [33], as it is recurrently employed to classify premixed combustion flames. This diagram was proposed originally by Borghi [15] so it has kept his name, although it has been improved and modified by many other authors [88]. The axis of the chart (see Figure 2.8) are dimensionless ratios of length and velocity in logarithmic scale, having in the horizontal axis l_t/δ_L (ratio of integral length scale over flame thickness) and in the vertical axis $u'/S_{L,0}$ (turbulent velocity fluctuations over unstrained laminar flame speed).

Three of the previously defined dimensionless numbers were carefully crafted into expressions of these two ratios (see Equations 2.15, 2.27, and 2.24). It should be noted that to determine those expressions, the assumption of constant unity Schmidt number was made. However, this assumption should be reconsidered, as it has been shown that the Schmidt number varies depending on the mixtures [50]. The intersection between these dimensionless numbers define four different types of premixed flames:

- **Laminar flames**: these flames are restricted to low turbulent Reynolds numbers $\mathrm{Re}_t < 1$. All the following regimes are turbulent flames.
- **Well-stirred reactor**: this region is enclosed by $\mathrm{Da} < 1$, which means that $\tau_t < \tau_c$, so the chemistry is slower than the turbulent diffusion. Moreover, when $l_t/\delta_L < 1$, the largest turbulent eddies are smaller than the thickness of the flame, so they influence the chemical reactions that occur in the flame front, cause local extinction and thicken the flame front. Sometimes an alternative domain is given for $\mathrm{Ka} > 100$, named broken reaction zones, that overlaps with the well-stirred reactor.
- **Thickened wrinkled flames**: this regime is also known as distributed combustion or thin reac-

tions zones. The regime is bounded for values of Ka > 1 and Da > 1, which means that on the one hand $\tau_c > \tau(\eta)$ while on the other $\tau(l_t) > \tau_c$ (as the integral length scale based Damkholer number is used). This means that the chemical timescale is of the order of the timescale of all the intermediate turbulent structures. Thus, the flame structure is large enough to allow small Komogorov-size eddies penetrate it and make it thicker. However, it is assumed that the reaction region is still thin and only the preheat region is affected by the turbulence.

- **Flamelets**: bounded by Ka < 1, i.e. $\tau_c > \tau(\eta)$. This means that not even the smallest eddies can penetrate the flame front, leading to the laminar flamelet assumption. This model states that the turbulent flame front can be thought of as an ensemble of stretched laminar flames, so the flame structure is locally the same as that of a laminar flame. This allows separating chemical and turbulent effects, using the laminar flame theory to determine reaction rates. In this case, neither the preheat nor the reaction regions are affected by turbulence. Most of the developed computational models lay in this regime, given that the assumption of fast chemistry is relatively accurate in this region. Moreover, there is another division depending on whether $S_{L,0} > u'$ or $S_{L,0} < u'$, having two sub-regimes inside the flamelet regime:
  - **Corrugated flamelets**: if $u' > S_{L,0}$, then large eddies can advect the flame front, distorting it and even creating pockets of the unburnt mixture inside the burnt domain (being eventually consumed by the flame front).
  - **Wrinkled flamelets**: the flame propagation is faster than the flame wrinkling by turbulence, so the laminar flame speed governs the regime. These flamelets are considerably similar to a laminar flame, as turbulence effects are small.

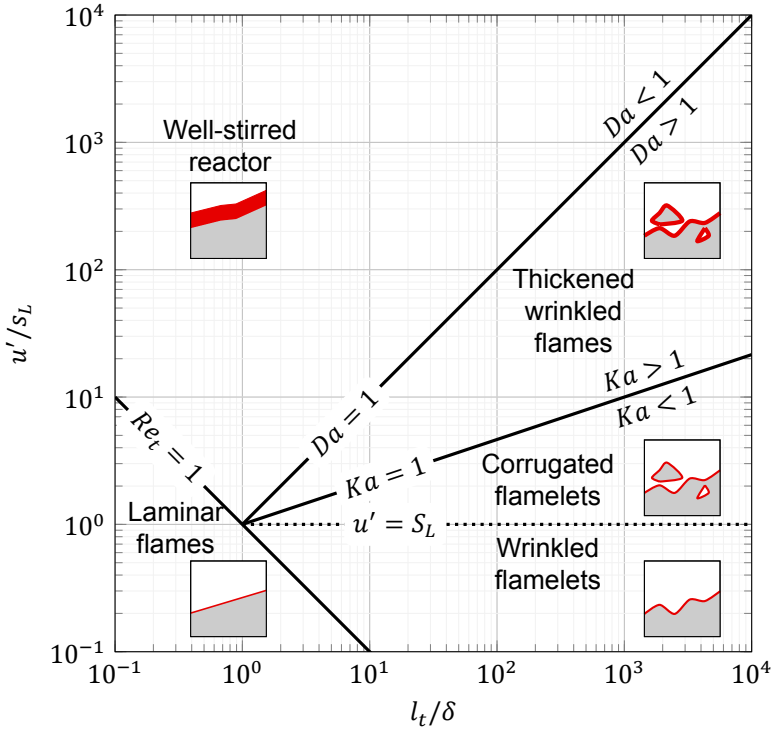

Figure 2.8: Borghi diagram for premixed combustion regimes, adapted from multiple sources [12, 15].

2.2. Modeling of turbulent premixed combustion and other involved phenomena

The mathematical formulations and a phenomenological description have been presented in the previous section. These equations need to be simplified and modeled in order to make them computable.

Two main blocks make up the problem that is to be analyzed: turbulence modeling and combustion modeling. Thus, the first subsection deals with the approaches available to model turbulence in fluid flows. The second subsection describes the methods and models that have been historically described for premixed combustion. Finally, the last subsection includes the modeling approaches for radiative heat transfer, as it plays a relevant role in some combustion scenarios.

2.2.1. Computational modeling of turbulence

To analyze real combustion scenarios where the fluid flow cannot be simplified with one-dimensional rules (as done for the one dimensional laminar flame), computer modeling is required. Computational Fluid Dynamics (CFD) has classically relied on three levels of turbulence modeling, depending on the available computational resources and the required accuracy. These three categories of turbulence modeling are (based on [133] and [114]):

- **DNS** (Direct Numerical Simulation): the full instantaneous Navier-Stokes are solved without any turbulence model, capturing all turbulent scales. This requires powerful computer facilities and it is limited to low Reynolds numbers. However, it provides the most accurate results, so it is used to isolate the effects of combustion models from the effects of turbulence.
- **LES** (Large Eddy Simulation): the large scales are computed explicitly while the smaller ones are modeled with subgrid-scale closure rules. Coarser grids than the DNS can be used as the turbulence below the smallest cell size is accounted for by the subgrid model. This allows for an accurate description of the turbulence and its interactions with combustion. It includes unsteady effects and, although it requires turbulence modeling, its impact on the results is limited. 3D domains are required and the numerical costs are still too high for some cases of the industry.
- **RANS** (Reynolds Averaged Navier Stokes): all turbulent scales are modeled. Although originally developed for mean flow fields, unsteady RANS (known as URANS) simulations are nowadays also widely spread. The models allow coarser numerical grids (compared to DNS) and simplifications such as 2D flow or symmetry are commonly used to reduce the geometrical dimensions. The greatest advantage is the lower computational demand, which comes associated with a lower accuracy when compared to DNS and LES.

RANS is the most used engineering approach for turbulent flows but it imposes a barrier on the accuracy that can be expected from the results. Although it can be argued that when dealing with combustion models, the most relevant part is not the modeling of the turbulence but the modeling of combustion, it cannot be neglected the interaction between combustion and turbulence. Moreover, many combustion models strongly rely on the turbulence parameters. Thus, moving from RANS to LES should improve the results, at the expense of increased computational requirements. However, and given that both models are interconnected, it is not clear at which point it is required to improve the turbulence model (moving to higher accuracy RANS models or even LES) or the combustion model (going from a simple to a more detailed approach), as a combination of both may be required to achieve more realistic results. Thus, and as a first step, RANS will be used to create a baseline for combustion modeling.

Reynolds averaging is used in the RANS codes to obtain a manageable version of the instantaneous balance equations presented from Equation 2.1 to Equation 2.4. Reynolds averaging of a given quantity f is defined for constant density flows as:

$$f = \overline{f} + f' ,$$

where f is split into a mean component $\overline{f}$ and a fluctuating component f'. This decomposition is combined with time averaging that reduces the fluctuating part. However, this process produces unclosed quantities that require modeling assumptions.

For density variable flows, the Favre-averaged decomposition is often invoked, defining the mass-weighted averages for any given quantity f as:

$$f = \widetilde{f} + f'' ,$$

where now the mean component is defined in terms of

$$\widetilde{f} = \frac{\overline{\rho f}}{\overline{\rho}},$$

(having that the mean fluctuations are still $\widetilde{f''} = 0$). The relation between Favre-averaged and Reynolds-averaged quantities is not straightforward unless other assumptions are performed, as this requires either the knowledge or the modeling of the density fluctuation correlations, that are not readily available. Moreover, comparing Favre-averaged quantities with experimental data is not obvious, given that most experimental techniques can't provide Favre mass-averaged values (e.g. temperatures from a thermocouple are either instantaneous or Reynolds averaged values). From a simple model (see for example Section 5.1 from [114]) it can be shown that the differences between $\overline{f}$ and $\widetilde{f}$ are significant and they depend on the ratio of burnt and unburnt densities.

When this decomposition is introduced in the set of equations that describe reacting flows (i.e. from Equation 2.1 to 2.4), the obtained equations are given as:

- **Favre-averaged continuity/Mass conservation**:

$$\frac{\partial}{\partial t}\left(\overline{\rho}\right) + \frac{\partial}{\partial x_i}\left(\overline{\rho}\widetilde{u}_i\right) = 0. \tag{2.51}$$

- **Favre-averaged momentum conservation**:

$$\frac{\partial}{\partial t}\left(\overline{\rho}\widetilde{u}_j\right) + \frac{\partial}{\partial x_i}\left(\overline{\rho}\widetilde{u}_i\widetilde{u}_j\right) = -\frac{\partial \overline{p}}{\partial x_j} + \frac{\partial \overline{\tau}_{ij}}{\partial x_i} - \frac{\partial}{\partial x_i}\left(\overline{\rho}\widetilde{u_i'' u_j''}\right) + \overline{\rho}\sum_{k=1}^{N}\widetilde{Y_k f_{k,j}}. \tag{2.52}$$

- **Favre-averaged enthalpy conservation**:

$$\frac{\partial}{\partial t}\left(\overline{\rho}\widetilde{H}\right) + \frac{\partial}{\partial x_i}\left(\overline{\rho}\widetilde{u}_i\widetilde{H}\right) = \overline{\dot{\omega}}_T + \frac{\partial \overline{p}}{\partial t} + \widetilde{u}_i\frac{\partial \overline{p}}{\partial x_i} + \overline{u_i''\frac{\partial p}{\partial x_i}} + \frac{\partial}{\partial x_i}\left(\overline{\lambda\frac{\partial T}{\partial x_i}} - \overline{\rho}\sum_{k=1}^{N}\widetilde{h_k Y_k V_{k,i}} - \overline{\rho}\widetilde{u_i'' H''}\right) + \ldots$$
$$\ldots + \widetilde{\dot{Q}} + \overline{\tau_{ij}\frac{\partial u_i}{\partial x_j}} + \overline{\rho}\sum_{k=1}^{N}\widetilde{Y_k f_{k,i}\left(u_i + V_{k,i}\right)}. \tag{2.53}$$

- **Favre-averaged species conservation**:

$$\frac{\partial}{\partial t}\left(\overline{\rho}\widetilde{Y}_k\right) + \frac{\partial}{\partial x_i}\left(\overline{\rho}\widetilde{u}_i\widetilde{Y}_k\right) + \frac{\partial}{\partial x_i}\left(\overline{\rho}\widetilde{u_i'' Y_k''} + \overline{V_{k,i}Y_k}\right) = \overline{\dot{\omega}}_k. \tag{2.54}$$

The term $\overline{\tau}_{ij}$ can be approximated with $\tilde{\tau}_{ij}$ in Equation 2.52 as the value of the fluctuation $\overline{\tau_{ij}''}$ is really small compared with the Favre-averaged value $\tilde{\tau}_{ij}$. The set of Favre averaged Navier Stokes equations are not closed and have undefined terms that require modeling and closure approaches. Three different terms have to be closed:

- **Reynolds stresses**: to close this term, the Boussinesq eddy viscosity approximation is often used, having:

$$\overline{\rho u_i'' u_j''} = \overline{\rho}\widetilde{u_i'' u_j''} \approx -\mu_t\left(\frac{\partial \widetilde{u}_i}{\partial x_j} + \frac{\partial \widetilde{u}_j}{\partial x_i} - \frac{2}{3}\delta_{ij}\frac{\partial \widetilde{u}_k}{\partial x_k}\right) + \frac{2}{3}\overline{\rho}k\delta_{ij}. \tag{2.55}$$

  The turbulent dynamic viscosity μ_t (or its counterpart turbulent kinematic viscosity ν_t, related as $\mu_t = \overline{\rho}\nu_t$) should be computed with an additional model. Multiple models can be used, although these models have been developed for constant density flows (replacing the Reynolds averages

with Favre averages) and for non-reacting flows (so the direct applicability to reacting flows is still an open question). Some preliminary studies [35] show that the results are largely dependent on the turbulence model, being necessary a comparison study to determine the best one. Four already-implemented turbulence models are used in this thesis:

– $k-\varepsilon$ [86]: two transport equations are used to close the turbulence model: one for the turbulent kinetic energy k and another for the turbulent kinetic energy dissipation rate ε:

$$\frac{\partial}{\partial t}(\rho k)+\frac{\partial}{\partial x_i}(\rho u_i k)-\frac{\partial}{\partial x_i}\left(\frac{\partial}{\partial x_i}(\rho D_k k)\right) = \rho P_k-\left(\frac{2}{3}\rho\frac{\partial(u_i k)}{\partial x_i}\right)-(\rho\epsilon)+S_k\,, \quad (2.56)$$

$$\frac{\partial}{\partial t}(\rho\varepsilon)+\frac{\partial}{\partial x_i}(\rho u_i \varepsilon)-\frac{\partial}{\partial x_i}\left(\frac{\partial}{\partial x_i}(\rho D_\varepsilon \varepsilon)\right) = C_1\rho P_k\frac{\varepsilon}{k}-\left(\left(\frac{2}{3}C_1-C_{3,RDT}\right)\rho\frac{\partial(u_i\varepsilon)}{\partial x_i}\right)-\left(C_2\rho\frac{\varepsilon}{k}\varepsilon\right)+S_\varepsilon\,, \quad (2.57)$$

where P_k is the turbulent kinetic energy production rate due to the anisotropic part of the Reynolds-stress tensor, defined as:

$$P_k = 2\nu_t\left[\frac{1}{2}\left(\frac{\partial u_i}{\partial x_j}+\frac{\partial u_j}{\partial x_i}\right)\right]^2 = \nu_t\frac{\partial u_i}{\partial x_j}\left(\frac{\partial u_i}{\partial x_j}+\frac{\partial u_j}{\partial x_i}\right).$$

S_ε and S_k are the internal source terms for ε and k respectively, and D_ε and D_k are the effective diffusivities for ε and k, respectively. For the standard version of the $k-\varepsilon$, the source terms have a zero value $S_\varepsilon = S_k = 0$. The standard coefficients were used: $C_1 = 1.44$, $C_2 = 1.92$ and $C_{3,RDT} = 0.0$. The turbulent viscosity is then computed as:

$$\nu_t = C_\mu\frac{k^2}{\varepsilon}\,, \quad (2.58)$$

where the coefficient $C_\mu = 0.09$.

– Buoyant-$k-\varepsilon$: the inclusion of the buoyancy term in the transport equations for $k-\varepsilon$ model is considered by the developers as a different turbulence model. The source terms that before had a zero value are defined as:

$$S_k = -G_{\text{coeff}}k\,, \quad (2.59)$$

and

$$S_\varepsilon = -C_1\tanh\left(\frac{|\hat{g}_i u_i|}{|u_j-\hat{g}_j(\hat{g}_i u_i)|}\right)G_{\text{coeff}}\varepsilon\,, \quad (2.60)$$

where G_{coeff} is defined as:

$$G_{\text{coeff}} = C_\mu\frac{k}{\varepsilon}\left(g_i\cdot\frac{\partial\rho}{\partial x_i}\right),$$

and the gravitational term is defined with the vector g_i (that has a direction given with the normalized vector $\hat{g}_i = g_i/(g_j g_j)$). The calculation of the turbulent viscosity is performed the same way as before (see Equation 2.58).

– $k-\omega$ [140]: an alternative approach is to solve for the turbulent kinetic energy k and the turbulence specific dissipation rate ω having:

$$\frac{\partial}{\partial t}(\rho k)+\frac{\partial}{\partial x_i}(\rho u_i k)-\frac{\partial}{\partial x_i}\left(\frac{\partial}{\partial x_i}(\rho D_k k)\right) = \rho P_k-\frac{2}{3}\rho k\frac{\partial u_i}{\partial x_i}-C_\mu\rho\omega k\,, \quad (2.61)$$

$$\frac{\partial}{\partial t}(\rho\omega) + \frac{\partial}{\partial x_i}(\rho u_i \omega) - \frac{\partial}{\partial x_i}\left(\frac{\partial}{\partial x_i}(\rho D_\omega \omega)\right) = C_\gamma \rho \frac{P_k}{\nu} - \frac{2}{3} C_\gamma \rho \omega \frac{\partial u_i}{\partial x_i} - \rho C_\beta \omega^2 , \quad (2.62)$$

where D_ω represents the effective diffusivity for ω and the standard coefficients were used: $C_\mu = \beta^* = 0.09$, $C_\beta = 0.072$ and $C_\gamma = 0.52$. The turbulent viscosity is computed as:

$$\nu_t = \frac{k}{\omega} , \quad (2.63)$$

from which it can be inferred that the relation between the turbulent kinetic energy dissipation rate ε and the turbulent specific dissipation rate ω can be expressed as:

$$\omega = \frac{\varepsilon}{\beta^* k} . \quad (2.64)$$

– $k-\omega$–SST [102]: in order to overcome some deficiencies of the $k-\omega$ regarding freestream values and to be able to capture flow separation, the $k-\omega$ model has been extended to get the $k-\omega$–SST. Two equations are still being solved for the turbulent kinetic energy k and the turbulence specific dissipation rate ω having:

$$\frac{\partial}{\partial t}(\rho k) + \frac{\partial}{\partial x_i}(\rho u_i k) - \frac{\partial}{\partial x_i}\left(\frac{\partial}{\partial x_i}(\rho D_k k)\right) = \rho P_k - \frac{2}{3}\rho k \frac{\partial u_i}{\partial x_i} - C_\mu \rho \omega k , \quad (2.65)$$

$$\frac{\partial}{\partial t}(\rho\omega) + \frac{\partial}{\partial x_i}(\rho u_i \omega) - \frac{\partial}{\partial x_i}\left(\frac{\partial}{\partial x_i}(\rho D_\omega \omega)\right) = C_\gamma \rho \frac{P_k}{\nu} - \frac{2}{3} C_\gamma \rho \omega \frac{\partial u_i}{\partial x_i} - \rho C_\beta \omega^2 - \rho\,(\mathcal{F}_1 - 1)\,CD_{k\omega} , \quad (2.66)$$

where

$$CD_{k\omega} = \frac{2\sigma_{\omega 2}}{\omega}\left(\frac{\partial k}{\partial x_i} \cdot \frac{\partial \omega}{\partial x_i}\right) ,$$

having the default coefficients as $\sigma_{\omega 2} = 0.856$ (the remaining not included coefficients have the same value as for the $k-\omega$). The turbulent viscosity is computed as:

$$\nu_t = \frac{a_1 k}{\max(a_1\omega, b_1 \mathcal{F}_2 S)} . \quad (2.67)$$

The two blending functions that have been invoked in the model are defined as:

$$\mathcal{F}_1 = \tanh\left(arg_1^4\right) \quad \text{where} \quad arg_1 = \min\left[\max\left(\frac{\sqrt{k}}{\beta^*\omega y}, \frac{500\nu}{y^2\omega}\right), \frac{4\sigma_{\omega 2} k}{CD_{k\omega} y^2}\right] , \quad (2.68)$$

and as:

$$\mathcal{F}_2 = \tanh\left(arg_2^2\right) \quad \text{where} \quad arg_2 = \max\left(\frac{2\sqrt{k}}{\beta^*\omega y}, \frac{500\nu}{y^2\omega}\right) , \quad (2.69)$$

(even if the function $\mathcal{F}_{23}$ is also available, combining $\mathcal{F}_2$ with another blending function).

There are other approaches don't require the eddy-viscosity hypothesis and they compute the Reynolds stress tensor components directly [85]: either with an Algebraic Stress Model (that provides each component as a function of known quantities) or with a Reynolds Stress Model (based on extra transport equations).

- **Turbulent energy flux**: it is closed based on the gradient hypothesis:

$$\overline{\rho}\widetilde{u_i''H''} = -\frac{\mu_t}{\mathrm{Pr}_t}\frac{\partial \widetilde{H}}{\partial x_i}\,, \tag{2.70}$$

  where Pr_t is an analogy to the laminar Prandtl number for turbulent flow conditions. As it was be described, this number is usually taken as constant (ranging between $\mathrm{Pr}_t = 0.75$ and $\mathrm{Pr}_t = 1$), although this is erroneous and can lead to inaccurate results (see Subsection 2.1.3).

- **k-th species turbulent mass flux**: again, the gradient hypothesis is used:

$$\overline{\rho}\widetilde{u_i''Y_k''} = -\frac{\mu_t}{\mathrm{Sc}_{kt}}\frac{\partial \widetilde{Y}_k}{\partial x_i}\,, \tag{2.71}$$

  where the turbulent Schmidt number of the k-th species is given by Sc_{kt}. It should be kept in mind that in some cases this gradient assumption is not accurate and counter-gradient turbulent transport can also be observed.

2.2.2. Modeling of premixed combustion

The effects of combustion in the Favre-averaged equations presented before (see from 2.51 to 2.54) is achieved through the source term in the species equation $\overline{\dot{\omega}}_k$. The averaged reaction rate cannot be straightforwardly expressed as a function of the mean quantities on which it depends (i.e. $\widetilde{Y}_k$ and $\widetilde{T}$). Equation 2.54 has to be solved for every species present in the combustion process. Although this number may seem reduced for hydrogen combustion in air, the mechanism developed at San Diego University [4] consists of 57 species and involves more than 250 equations. Moreover, the thermophysical, chemical, and transport coefficients are usually tabulated for reactions in the laminar regime, not being directly applicable to turbulent flames. Even if the coefficients can be expressed as functions of species mass fractions or temperature, this increases the computational time if the number of chemical reactions is large. However, this provides more accurate non-constant coefficients. Finally, chemical reactions occur under a wide range of chemical time scales, which cannot be handled with a single timescale as done in the common implementations of combustion models.

Therefore, for premixed combustion modeling, a simplification is usually carried out with respect to the number of species in the model, having a simple irreversible reaction between fuel (F) and oxidizer (O) to get some products P given by Equation 2.31, which can be recast as:

$$\mathrm{F} + \mathrm{S}\,\mathrm{O} \longrightarrow (1 + \mathrm{S})\,\mathrm{P}\,, \tag{2.72}$$

which for hydrogen with air is given as:

$$\mathrm{H_2} + 0.5\,(\mathrm{O_2} + 3.770\,\mathrm{N_2}) \longrightarrow \mathrm{H_2O} + 1.885\,\mathrm{N_2}\,,$$

The previous equation can be further simplified into a chemical reaction equation that presents just two states:

$$\text{Reactants} \longrightarrow \text{Products}\,.$$

Thus, the progress variable c can be re-introduced to achieve a single transport equation that determines in which state of the chemical reaction a given location is. For the case of $\mathrm{Le} \neq 1$, the progress variables was given by:

$$c = \frac{Y_f' - Y_{f,u}}{Y_{f,b} - Y_{f,u}}\,. \tag{2.73}$$

The use of c allows to obtain a single species transport equation for the progress variable:

$$\frac{\partial}{\partial t}(\rho c) + \frac{\partial}{\partial x_i}(\rho u_i c) - \frac{\partial}{\partial x_i}\left(\rho D \frac{\partial c}{\partial x_i}\right) = +\dot{\omega}_c\,. \tag{2.74}$$

However, when implementing this equation into a CFD solver, it should be Favre-averaged so it is consistent with the other quantities computed by the solver, having:

$$\frac{\partial}{\partial t}\left(\overline{\rho}\tilde{c}\right)+\frac{\partial}{\partial x_i}\left(\overline{\rho}\widetilde{u_i}\tilde{c}\right)-\frac{\partial}{\partial x_i}\left(\overline{\rho}\overline{D}\frac{\partial\tilde{c}}{\partial x_i}-\overline{\rho}\widetilde{u_i''c''}\right)=\overline{\dot{\omega}}_c\,. \tag{2.75}$$

The turbulent scalar transport is usually modeled with the standard gradient diffusion hypothesis (cf. Equation 2.71) as:

$$\overline{\rho}\widetilde{u_i''c''}=\overline{\rho u_i''c''}=-\overline{\rho}\frac{\overline{\nu_t}}{\mathrm{Sc}_t}\frac{\partial\tilde{c}}{\partial x_i}=-\overline{\rho}\overline{D_t}\frac{\partial\tilde{c}}{\partial x_i}\,, \tag{2.76}$$

where Sc_t is the mixture turbulent Schmidt number. Although this choice is mainly for practical reasons (as the term can be implemented as D_t plus the laminar molecular transport term D, usually ignoring the latter as $D_t >> D$), there are DNS and theoretical studies (see Section 5.3.8 of [114] for a review on them) that show the appearance of a counter-gradient transport effect that becomes relevant in some scenarios. Other closures that don't involve the gradient assumption have been suggested, e.g.

$$\overline{\rho u_i''c''}=\overline{\rho}\tilde{c}\left(1-\tilde{c}\right)\left(\tau_c S_L-2\mathrm{A}_e u'\right)\,, \tag{2.77}$$

where A_e is an efficiency function defined to account for different turbulent eddy sizes (derived from experimental studies [101]). Another solution is to construct a transport equation for $\overline{\rho u_i''c''}$, although this leads to new unclosed terms. The turbulent scalar transport term closure or modeling remains a controversial topic and the limitations of the gradient transport approach should be kept in mind.

Before presenting the most well-known combustion models, a theoretical framework in which some of them are based is introduced. The Bray-Moss-Libby (BML) approach is one of the most simplified yet powerful methods. It assumes an infinitely thin flame front (smaller than the smallest Kolmogorov scale) where the possibility of finding intermediate combustion species other than reactants or products is small. It also considers a unity Lewis number and an adiabatically and isobarically combustion. It is based on a bimodal probability density function (pdf) that has no state in between $c=0$ and $c=1$:

$$P(c)=\alpha_p\delta(c)+\beta_p\delta(1-c)\qquad\text{where}\qquad\alpha_p+\beta_p=1\,, \tag{2.78}$$

where $\delta(c-c_0)$ is the Dirac-delta function, given as:

$$\delta(c-c_0)=\begin{cases}\infty & \text{for } c=c_0\\ 0 & \text{elsewhere}\end{cases}\qquad\text{so that}\qquad\int_{-\infty}^{\infty}g(c)\delta(c-c_0)dc=g(c_0)\,.$$

The closure of the turbulent scalar transport term provides the expression on which Equation 2.77 is based on:

$$\overline{\rho}\widetilde{u_i''c''}=\overline{\rho}\tilde{c}\left(1-\tilde{c}\right)\left(\overline{u}_{i,b}-\overline{u}_{i,u}\right)\,.$$

This expression is always either zero or positive, in contrast to the gradient assumption (see Equation 2.76) usually applied to the turbulent transport, which is either zero or negative. Other fluctuation terms can be estimated with the BML approach as:

$$\overline{\rho}\widetilde{c''^2}=\overline{\rho\left(c-\tilde{c}\right)^2}=\overline{\rho}\left(\widetilde{c^2}-\tilde{c}^2\right)=\overline{\rho}\tilde{c}\left(1-\tilde{c}\right)\,. \tag{2.79}$$

This model can't close the mean source term of Equation 2.75 because the reaction occurs neither on the burnt nor unburnt states, having:

$$\overline{\dot{\omega}}_c = \int_0^1 \dot{\omega}_c P(c) dc \Rightarrow \overline{\dot{\omega}}_c = \alpha_p \omega(0) + \beta_p \omega(1) = 0\,.$$

To solve this issue, alternatives have been proposed. One of them is to include a probability of finding intermediate states of combustion between $c = 0$ and $c = 1$, redefining the pdf as:

$$P(c) = \alpha_p \delta(c) + \beta_p \delta(1-c) + \gamma_p f(c, x_i) \qquad \alpha_p + \beta_p + \gamma_p = 1\,, \tag{2.80}$$

where γ_p represents the probability of finding intermediate mixture species between burnt and unburnt states. Although more advanced approaches are preferred to model the source term, the BML provides a foundation for many other combustion models that will be presented next.

Most of the combustion community has been developing models to characterize the flame behavior in the source term. Due to the large number of combustion models available, grouping them is tricky, especially as every author follows his own guidelines to make a classification. Therefore, a considerable effort has been made to reach (as much as possible) an agreement between the different literature sources (see [33], [88], [105], [114], [134]). The different groups of premixed combustion modeling are:

- **Algebraic mixing models**: many different approaches can be included in this category. Most of them assume that chemical timescales are shorter than turbulent timescales (i.e. $Da >> 1$), so the reaction rate can be controlled by the turbulent mixing rate. The *scalar dissipation rate formulation* is one recurrent way to close the source term by using a proportionality rule with respect to the scalar dissipation rate X_c, having:

$$\overline{\dot{\omega}}_c = \frac{1}{2c_m - 1}\left(2\overline{\rho D \frac{\partial c}{\partial x_i}\frac{\partial c}{\partial x_i}}\right) = \frac{\overline{\rho}\widetilde{\mathrm{X}}_c}{2c_m - 1} \quad \text{where} \quad c_m = \frac{\overline{c\dot{\omega}_c}}{\overline{\dot{\omega}}_c} = \frac{\int_0^1 c\dot{\omega}_c f(c) dc}{\int_0^1 \dot{\omega}_c f(c) dc}\,. \tag{2.81}$$

  A balance equation can be derived for X_c [97], but simpler, usually algebraic, approaches can be used:

$$\overline{\dot{\omega}}_c = \frac{\overline{\rho}\widetilde{\mathrm{X}}_c}{2c_m - 1} = \frac{\overline{\rho}}{2c_m - 1}\frac{\varepsilon}{k}\tilde{c}\,(1-\tilde{c})\,. \tag{2.82}$$

  To obtain this last equation, $c^2 \approx c$ has been assumed with the use of Equation 2.79 (as intermittency appears between fresh and burnt gases) and the turbulent mixing time scale τ_t has been estimated with the ratio between turbulent kinetic energy k and dissipation rate ε. This expression is the theoretical foundation of a phenomenological model known as the *Eddy-Break-Up* (EBU) model, for which the chemical source term is given by:

$$\overline{\dot{\omega}}_c = C_{\mathrm{EBU}}\overline{\rho}\frac{\epsilon}{k}\tilde{c}\,(1-\tilde{c})\,, \tag{2.83}$$

  where C_{EBU} is a highly case-dependent parameter. The EBU model assumes two species (reactants and products), treated as ideal gases with constant c_p, and with a single step irreversible chemical reaction, not accounting for thermal/pressure diffusion nor pressure fluctuations, and having a Lewis number of unity between both species. The EBU model has been improved by different authors, as the original formulation overestimates the value of the reaction rate in highly strained regions due to the large ratio of ε/k. However, as most of these models are based on the turbulent time, the burning velocity always scales with the thickness of a hypothetical monodimensional transient flame. Another limitation of these models is that the *constants* are case-dependent and no algebraic model has been validated to provide well-defined conditions for arbitrary flames. Moreover, it has not yet been proved that an algebraic model can accurately reproduce the self-similarity structure of a developing flame.

- **pdf-based models**: two large groups arise based on whether *a priori* assumptions are made with respect to the pdf used, having the presumed-pdf methods or the transported-pdf methods.

  The first category defines two transport equations to determine the pdf shape: one for the first pdf moment (expected value or mean) and the other one for the second pdf moment (central moment or variance). This requires an assumption of fast chemical kinetics (high Da number), whose coefficients can be tabulated before the simulation (so the solver is fully decoupled from the chemical process). The moments for the presumed pdf provide the source term of the progress variable equation as:

$$\overline{\dot{\omega}}_c(x_i,t) = \int_0^1 \dot{\omega}_c(c')P(x_i,t,c')dc' .$$

  The value of $\dot{\omega}_c(c')$ is usually obtained through the calculation of a one-dimensional steady flame or from tabulated libraries [110]. The Favre-averaged probability density function is usually defined as $\overline{\rho}\widetilde{P}(c) = \rho P(c)$, where the most-common shape for the pdf $\widetilde{P}(x_i,t,c)$ is the beta distribution, which is given by:

$$\widetilde{P}(c) = \frac{c^{a-1}(1-c)^{b-1}}{\int_0^1 c^{a-1}(1-c)^{b-1}dc} = \frac{\Gamma(a+b)}{\Gamma(a)\Gamma(b)}c^{a-1}(1-c)^{b-1} ,$$

  where the gamma function $\Gamma(x)$ is defined as:

$$\Gamma(x) = \int_0^{+\infty} e^{-t}t^{x-1}dt .$$

  The choice of this pdf is not based on physical principles [59] but it has been proved to be a robust method that covers the whole domain of premixed turbulent combustion (from the flamelet to the well-stirred reactor regime). However, there are situations (as tri-modal combustion processes) that cannot be represented with the typical bimodal-beta distributions. Although this pdf is not directly defined in terms of the first two moments of the progress variable ($\tilde{c}$ and $\widetilde{c''^2}$), the coefficients a and b can be expressed as a function of those:

$$a = \tilde{c}\left[\frac{\tilde{c}\,(1-\tilde{c})}{\widetilde{c''^2}} - 1\right] \qquad b = \frac{a}{\tilde{c}} - a .$$

  The first moment can be retrieved from Equation 2.75, while the transport equation for the second moment is usually obtained by deriving a balance equation for $\widetilde{c''^2} = \widetilde{c^2} - \tilde{c}^2$, having:

$$\frac{\partial}{\partial t}\left(\overline{\rho}\widetilde{c''^2}\right) + \frac{\partial}{\partial x_i}\left(\overline{\rho}\widetilde{u}_i\widetilde{c''^2}\right) = \frac{\partial}{\partial x_i}\left(\overline{\rho D\frac{\partial c''^2}{\partial x_i}}\right) + \overline{2c''\frac{\partial}{\partial x_i}\left(\rho D\frac{\partial \tilde{c}}{\partial x_i}\right)} - \frac{\partial}{\partial x_i}\left(\overline{\rho u_i'' c''^2}\right)$$
$$- 2\overline{\rho u_i'' c''}\frac{\partial \tilde{c}}{\partial x_i} - 2\overline{\rho D\frac{\partial c''}{\partial x_i}\frac{\partial c''}{\partial x_i}} + 2\overline{c''\dot{\omega}_c} . \quad (2.84)$$

  The derivation of this expression and different closure terms can be found in [114]. The presumed pdf modeling is a simple yet (generally) accurate model, although the source term may diverge (not for numerical reasons) if the state probability values are small [88].

  The second category (also known as balance equation for pdf) doesn't solve transport equations for the moments of a presumed pdf but solves a transport equation for either the joint scalar pdf or the joint velocity-scalar pdf. The chemical source term requires no modeling, directly including finite rate chemistry effects. This model was first derived for turbulent reactive flows [115] and for non-premixed flames (see literature review of [112]), but it has been expanded to premixed flames.

  Transported pdf models still face two challenges [23]: account for the small-scale structure of turbulence (the chemical reaction rate can be assumed as a one-point pdf but the diffusion component requires spatial information) and the feasibility of the computational implementation (given that the sampling of many pdf is done with Monte Carlo methods). Other approaches have been described by Valiño [130] and Sabel'nikov and Soulard [121] to avoid Monte Carlo methods by using the pdf equation with stochastic fields.

- **Flame surface density models**: the models under the FSD acronym are usually based on the Coherent Flamelet Model (CFM) of Marble and Broadwell [98]. Both the FSD and the CFM are valid under the flamelet assumptions, and they express the mean reaction rate as a function of the flame surface area. This value can be theoretically expressed as the product of flame surface density Σ (which is the ratio between flame surface area and unit volume) multiplied by the local consumption rate per unit of flame area $\rho_u \langle s_c \rangle_s$, obtaining:

$$\overline{\dot{\omega}}_c = \rho_u \langle s_c \rangle_s \overline{\Sigma},$$

where $\langle s_c \rangle_s$ is the average flame consumption speed along the surface. Although this expression may not seem to introduce any new physical insight, it is separating chemical kinetic features (included in the average flame consumption speed) from interactions between turbulence and combustion (accounted for in the flame surface density).

This expression includes two terms that should be modeled to obtain the reaction rate: $\langle s_c \rangle_s$ and Σ. The first one is expressed in terms of known flame quantities: either local stretch rate (which cannot be fully resolved with RANS modeling):

$$\langle s_c \rangle_s \simeq s_c \overline{\kappa}.$$

or the unstrained laminar flame speed $S_{L,0}$:

$$\langle s_c \rangle_s = I_0 S_{L,0},$$

(although the second approach introduces the stretch factor I_0, which is usually approximated from experimental [1] or DNS data [58]). It has been shown that the value of $I_0 \simeq 1$, so the main modeling effort is put on the flame surface density Σ. The community has proposed a variety of solutions and models to compute this value, which range from algebraic models to transport equations for the mean flame surface density. In Table 5.3 of [114], there is a comparative of the different models proposed by the different researchers. However, there are few comparative studies of the accuracy of these models [88] (where it is pointed out also non-physical terms in the transport equations). Finally, and as a brief remark to show the entanglement that occurs between the different combustion models, the FSD model coupled with a transport equation for Σ where the sink and source terms are balanced produces an EBU-type of model [88].

- **Isosurface models**: the main model is based on a level-set of a non-reacting scalar variable $\mathcal{G}$ for which a balance equation is constructed [113]. This mathematical construction replaces the progress variable equation with the $\mathcal{G}$-equation (levering the complexities of modeling the conter-gradient diffusion and reaction rate source terms). However, this model is originally restricted to wrinkled flamelets [141]. The aforementioned equation for the local, instantaneous flame element is given by:

$$\rho \frac{\partial \mathcal{G}}{\partial t} + \rho u_i \frac{\partial \mathcal{G}}{\partial x_i} = \rho_u s_d \left| \frac{\partial \mathcal{G}}{\partial x_i} \right|, \tag{2.85}$$

where s_d is the displacement speed of the flame element. The flame front is identified with a isosurface given by $\mathcal{G} = \mathcal{G}_0$. The displacement speed is expressed in terms of quantities that can be either computed or modeled [113], obtaining:

$$s_d = S_{L,0} - S_{L,0}\mathcal{L}\kappa_c - \kappa_s \mathcal{L} = S_{L,0} - S_{L,0}\mathcal{L}\frac{\partial n_i}{\partial x_i} - n_i \frac{\partial n_i}{\partial x_j} n_j \mathcal{L},$$

where the strain rate κ_s and the flame curvature κ_c have been expressed in terms of the flame normal vector, given by $\vec{n} = -\nabla\mathcal{G}/|\nabla\mathcal{G}|$, and $\mathcal{L}$ is the Markstein length (which combined with the unstrained laminar flame speed produces the Markstein diffusivity $D_{\mathcal{L}} = S_{L,0}\mathcal{L}$). The displacement speed is designed to handle the regime of thin reaction zones, although a common set of equations has been developed to, in theory, extend the range of applicability [113]. The Favre averaged equation for the variable $\widetilde{\mathcal{G}}$ is then described as:

$$\overline{\rho}\frac{\partial}{\partial t}\widetilde{\mathcal{G}} + \overline{\rho}\widetilde{u}_i \frac{\partial}{\partial x_i}\widetilde{\mathcal{G}} = \overline{\rho} S_t \left| \frac{\partial \widetilde{\mathcal{G}}}{\partial x_i} \right| - \overline{\rho} D_t \widetilde{\kappa} \left| \frac{\partial \widetilde{\mathcal{G}}}{\partial x_i} \right|, \tag{2.86}$$

where the strain rate effects have been introduced into the turbulent flame speed S_t. Two of the main drawbacks of this model are the tendency to form flame cusps (requiring a diffusive term) and the fact that coupling this mathematical construction with the physical Favre-averaged fluid flow equations may not be straightforward [114].

- **Flame gradient models**: these models are also known as self-similarity models, as they try to extract the mean structure of the development of a premixed flame, or as flame speed correlation models, given that they define the speed at which the flame front moves. Some authors [114] group the iso-surface models, the FSD approach, and the flame gradient models under a single group named geometry-based models (as the flame front is associated with a surface that moves from the burnt gases towards the fresh gases), either with the $\mathcal{G}$-equation, flame surface density or an instantaneous isosurface of a progress variable. This highlights the parallelism between different models that may be derived from different principles. Moreover, and especially interesting, the $\mathcal{G}$-equation model has been compared with some flame-gradient models, obtaining similar constructions with different levels of physical and mathematical formalism [152]. The flame gradient (or flame normal) models can be derived from the balance equation of a 1D flame by accounting for the different phenomenological observed terms [88]. From these principles, the source term for Equation 2.75 is computed based on these different assumptions. One advantage of these models is that they are simple enough to couple new correlations and see what effects they have. Two wide-spread models exist in the literature:

  – *Turbulent Flame-speed Closure* (TFC) model: it was described by Zimont in [150]. The model assumes that small eddies enter in the preheat zone and enhance mixing (so the thickness and burning rate are increased) while large eddies increase the burning rate by wrinkling the thickened flamelets (which contrasts with the classical Activation Energy Asymptotics (AEA) theory [88]). Based on these assumptions, the range of applicability is restricted to the domain of $\mathrm{Re} >> 1$, $\mathrm{Da} >> 1$ and $\mathrm{Ka} > 1$. The model proposes a joint closure reaction for both the diffusive term and the source term (instead of providing only the source term closure) given by:

$$-\frac{\partial}{\partial x_i}\left(\overline{\rho}\widetilde{u_i''c''}\right)+\overline{\dot{\omega}}_c=\frac{\partial}{\partial x_i}\left(\overline{\rho}D_t\frac{\partial\tilde{c}}{\partial x_i}\right)+\rho_u S_t\left|\frac{\partial\tilde{c}}{\partial x_i}\right|, \tag{2.87}$$

  (which indeed uses the gradient assumption for the turbulent scalar transport term, with the drawbacks previously explained). The turbulent diffusivity is evaluated based on the turbulent coefficients (some authors classify the TFC as an algebraic model), having:

$$D_t=D_t^{\infty}=\frac{C_\mu}{\mathrm{Pr}_t}\frac{\widetilde{k}^2}{\tilde{\varepsilon}}. \tag{2.88}$$

  On the other hand, the turbulent flame speed has been experimentally approximated based on a dependence on the Da, having:

$$S_t=S_t^{\infty}=Au'\mathrm{Da}^{1/4}=Au'\left(\frac{l_t}{u'\tau_c}\right)^{1/4}, \tag{2.89}$$

  where the chemical timescale of a corresponding laminar flame is usually computed as:

$$\tau_c=\frac{\kappa_u}{\left(S_{L,0}\right)^2}. \tag{2.90}$$

  There are other approaches to compute τ_c based on the equivalence ratio that may be interesting for partially-premixed combustion [90]. The author of the TFC model has proposed an improved version to compensate for the drawbacks of using the gradient diffusion approximation in the model [153] by using an expression based on the Bray-Moss-Libby approach. There are formulations of the turbulent flame speed that include effects related to the critical stretch rate (quenching effects) and preferential diffusion (caused, amongst others, by temperature variations) [122]. The constant A is usually taken to be $A \approx 0.52$ or $A \approx 0.40$.

Although the TFC has been extensively used, it has some limitations [90]. The model cannot capture the transition from laminar to turbulent, imposing boundary conditions based on the gradient of $\tilde{c}$ causes problems with the source term (which is based on its derivative), the linear growth of the flame thickness with the flame development time is not predicted (as the burning velocity doesn't have a dependence on the flame width nor on time) and the turbulent flame speed correlation produce more accurate results for $u'/S_L > 4$. The correlation returns a value of $S_t \to 0$ when no turbulence is present (i.e. if $u' \to 0$, then Equation 2.89 returns $S_t \to 0$ while it should tend to the laminar flame speed $S_t \to S_L$, see Figure 2.6).

– *Extended Turbulent Flame-speed Closure* (ETFC) model (also known as *Flame Speed Closure* model): to solve some of the problems of the TFC, Lipatnikov and Chomiak [89] proposed a new model that includes a time dependence in the turbulent flame speed and in the turbulent diffusivity and also a laminar term to account for $u' \to 0$ (that vanishes when turbulence is high, leading to the TFC model with time-dependent diffusivity and laminar flame speed). The laminar source term was originally given based on theoretical and phenomenological descriptions, but given that the calculation may be computationally expensive, the practical alternative source term is given by:

$$-\frac{\partial}{\partial x_i}\left(\overline{\rho}\widetilde{u_i''c''}\right)+\overline{\dot{\omega}}_c=\frac{\partial}{\partial x_i}\left(\overline{\rho}D_{t,t}\frac{\partial\tilde{c}}{\partial x_i}\right)+\rho_u S_t\left|\frac{\partial\tilde{c}}{\partial x_i}\right|+\frac{\rho_u\left(S_{L,0}\right)^2}{4\left(D_u+D_{t,t}\right)}\tilde{c}(1-\tilde{c})\,. \tag{2.91}$$

The D_u refers to the mass diffusivity computed based on the unburnt mixture. The time dependent turbulent diffusivity is given by:

$$D_{t,t}=D_t^{\infty}\left[1-e^{-t/\tau_L}\right]=\frac{C_\mu}{\mathrm{Pr}_t}\frac{\widetilde{k}^2}{\tilde{\varepsilon}}\left[1-e^{-t/\tau_L}\right], \tag{2.92}$$

and the time dependent turbulent flame speed is described by:

$$S_t=S_t^{\infty}\left[1+\frac{\tau_L}{t}\left(e^{-t/\tau_L}-1\right)\right]^{1/2}=Bu'\mathrm{Da}^{1/4}\left[1+\frac{\tau_L}{t}\left(e^{-t/\tau_L}-1\right)\right]^{1/2}, \tag{2.93}$$

The constant B may differ from the constant A of the TFC model, but it is usually taken as the same. In these two equations, the time dependence is included through two variables, namely t (which is the flame development time, equal to the time from ignition) and τ_L (which is the Lagrangian time scale). From dimensional analysis, it was shown that this latter timescale is computed as:

$$\tau_L=\frac{D_t^{\infty}}{u'^2}=\frac{1}{u'^2}\frac{C_\mu}{\mathrm{Pr}_t}\frac{\widetilde{k}^2}{\tilde{\varepsilon}}\,.$$

Both the TFC and ETFC are based on the velocity fluctuations u' which, according to some authors [114], are tricky to generalize for cases with unknown conditions. For RANS simulations, the interpretation of u' inside a flame front is still an open question. The issue is that turbulence quantities are controlled by u' and, with these models, they control the mean reaction rate of the combustion process. By using a model based on u', it should be kept in mind that:

– Using u' to characterize the velocity fluctuations of a flame doesn't have theoretical foundations. In fact, $\widetilde{k}$ can only be accurately defined far from the flame front. These turbulence values are given for the fresh mixture in experiments, however, they are volume fields in a CFD code for both unburnt and burnt mixture.

– When implementing combustion models and validating against experiments, there are occasions [47] where the value of u' is truly homogeneous in the domain at the beginning of the deflagration. This can be used to separate the effects of combustion and turbulence models at the early stages. When these values are not available, the influence of the turbulence model is something that should be taken into account.

Before detailing the approach followed for the thesis, the ones followed by different nuclear research institutes for the studied problematic are presented. As a reminder for the introduction, it should be stressed that the large size of the geometry (nuclear reactor containment) and the physical time to be simulated (with an order of magnitude of several hours) make that most of the literature has been based on LP codes. Lately, more CFD simulations are being performed but complex models (as transported pdf or Direct Numerical Simulation) are not usually considered [17] due to the increase in computational demand.

Most of the researchers focus on low-fidelity approaches for combustion, modeling the mean chemical reaction source term directly (with an eddy break-up model for example). It can be pointed out the work of some pioneers in the field, [119] and [81] where it can be seen that the recurrent EBU model appears as the cornerstone for combustion modeling in the field. Although it can be argued that these papers date from more than 20 years ago, in the nuclear safety community these models are preferred to complex high-fidelity models. The Molkov algebraic model for the flame surface density has also been used to incorporate wrinkling, fractal evolution, leading point development, and turbulence effects into Ξ [6]. Sometimes two-step chemical reaction equations [143] or flame surface density models with auto-ignition terms [57] (or [56] from the same research group) are used, but a large part of the community still relies on the TFC [54, 122] or similar flame gradient models based on in-house correlations with some extra correction terms [131]. The TFC has proved to, under the aforementioned conditions, be a successful model that has been applied in multiple scenarios with acceptable results (from Bunsen burners [151] to spark ignition combustion engines [137]), being even coupled with LES turbulence modeling (e.g. [38] or [79]). In the field of nuclear safety, the different models presented before have been under improvement with new correlations, based on experimental estimations.

2.2.3. Radiative heat transfer modeling

There are three mechanisms of heat transfer: conduction, convection, and radiation. The first one is solved by considering the diffusion equation in solids and boundaries and the second one with the Navier-Stokes equations (including the corresponding term in the energy equation). However, thermal radiation is caused by energy emission in the form of electromagnetic waves, radiating with a spectral distribution where the maximum energy is located at the wavelength of the source temperature.

The wavelength is related to the temperature, having infrared wavelengths for most engineering systems and visible light if the temperature goes above 1000 K. This is the case for combustion temperatures, where the radiative heat fluxes may be of similar order than the convection heat transfer [133]. Moreover, the products of combustion (mainly CO_2 and H_2O) are absorbers/emitters of radiation while soot and other solid particles may cause scattering. Thus, the fluid is a participating medium in the heat transfer process. Radiation redistributes the energy within the flow and through exchanges between boundary surfaces (via flow interactions).

One of the issues of including radiative heat transfer in CFD calculations is the different scales in which it operates. Thermal radiation propagates at the speed of light which is around 3×10^8m/s, being many orders of magnitude larger than the speed of sound. Thus, the radiation process can be modeled in a quasi-steady state, i.e. radiation propagates sufficiently fast to instantaneously adapt to variations in flow conditions and/or boundary conditions. Even so, there is a strong indirect coupling between flow field properties and radiation through the medium properties and the source term of the energy equation. Moreover, the level of heat losses, especially the radiative ones, modifies and affects the flame response and development [114], having that scattering can even quench flames.

The gases resulting from combustion are not relevant scatters of radiation but they are strong absorbers and emitters of energy. Although not explicitly stated throughout this subsection, the radiative properties and coefficients depend on the wavelength λ. Therefore there are (mainly) four models [103] that can be used to obtain the properties of a given medium mixture:

- Line-by-line (LBL) approach: it is the most accurate numerical method, as it relies on the calculation for each wavenumber of the lines of interest (which entails detailed quantum-state infor-

mation). Doing this process for a large number of lines in each database (around 10^5 lines) is prohibitive, especially because radiation is just a part of the whole combustion modeling process.

- Narrow-band model: it is constructed from averaged-spectral absorption-emission lines of molecular gases from a small number of lines. This is based on the idea that for a narrow range of wavenumbers, the Planck function is nearly constant. This model is still quite computationally expensive and it is not straightforward to apply it in the scenario of inhomogeneous fluids at runtime. Different tools, such as RADCAL [49], are based on a Narrow Band Model and can be used to compute mean absorption coefficients.
- Wide-band model: it is spectrally coarser than the narrow band model, averaging the properties over a larger wavenumber range. The absorption or emission of these bands can have a box, triangular, or exponential profile.
- Global models: these models, also known as total absoptivity-emissivity models, are based on Hottel's charts, which show the radiative properties as functions of temperature, pressure, and species concentration. The main assumption of these charts is that all boundaries are black and the medium is non-scattering. The most common model of this group is the Weighted Sum of Gray Gases Model (WSGGM). From the data of these charts, the range of applicability can be extended based on the idea that the total emissivity and absorptivity of a non-gray gas can be represented as a weighted sum of the emissivities/absorptivities of a finite number of gray gases. There are other approaches, as the even more simplified Grey Gas model (where just a single gray gas is used) or an improved WSGGM, known as Spectral-Line Weighted sum of gray gases (shortened as SLW and that has shown more accurate than the WSGGM in homogeneous and isothermal media, as it obtains its polynomial coefficients directly from the line-by-line model [37]).

Once the properties of a mixture are known, the actual radiative heat transfer should be solved. There are mainly two theories developed to analyze electromagnetic radiation propagation into matter and interacting with matter: the classical electromagnetic wave theory and the radiative transfer theory. Both describe the same process, but the former does so from a microscopic point of view and the latter from a macroscopic one. Thus, the radiative transfer theory is the one that should be pursued in CFD studies [133]. It is based on the radiative transfer equation (RTE): a conservation principle applied to a bundle of monochromatic radiation. The RTE can be obtained from many viewpoints [103], the Eulerian point of view is being the one presented here. The general relationship that governs the changes in intensity along a radiation ray due to the different radiation phenomena is:

$$\underbrace{\frac{dI_\lambda(\vec{r},\vec{s})}{ds}}_{\substack{\text{rate of change}\\ \text{of intensity}\\ \text{per unit path length}}} = \underbrace{k_\lambda I_{b,\lambda}(\vec{r})}_{\substack{\text{emitted}\\ \text{intensity}}} - \underbrace{k_\lambda I_\lambda(\vec{r},\vec{s})}_{\substack{\text{absorbed}\\ \text{intensity}}} - \underbrace{\sigma_\lambda I_\lambda(\vec{r},\vec{s})}_{\substack{\text{out-scattered}\\ \text{intensity}}} + \underbrace{\frac{\sigma_\lambda}{4\pi}\int_{4\pi} I_\lambda(\vec{r},\vec{s}_i)\vec{\Phi}(\vec{s}_i,\vec{s})d\Omega_i}_{\substack{\text{in-scattered}\\ \text{intensity}}}, \tag{2.94}$$

where $I(\vec{r},\vec{s})$ represents the radiation intensity at the location $\vec{r}$ in the direction $\vec{s}$, the integral accounts for the incident scattering from all possible directions $\vec{s}_i$, and the subscript λ indicates the wavelength dependence (see [34]). The derivation of this equation can be found in Chapter 10 of [103]. This equation can be further simplified by using the non-dimenisonal optical coordinates [133]. Regardless of that, the RTE equation is an integro-differential equation (where intensity appears inside an integral and a derivative) in three spatial dimensions and two-directional coordinates. This makes the equation extremely difficult to solve, so methods and simplifications are required to analyze the equation.

The P1 model (see [44] and [103]) is based on the idea that the intensity of a participating medium behaves as a rapidly converging series based on orthogonal spherical harmonics constructed over a Fourier series. The P1 model is a member of the P-N family (which are methods accurate only in isotropic radiation intensity [147]) obtained by truncating after the first element. The model is based on a gray (radiation coefficients don't depend on the wavelength) and diffusive (no dependence of the coefficients on the propagation direction) medium enclosed between opaque (incident rays on the walls are absorbed) and grey diffusive (no surface reflection is considered) surfaces. The full derivation of

the P1 model can be found in Chapter 16 of [103], having two different spatial differential equations, one for the gradient of the directionally averaged intensity G:

$$q_i^{rad} = -\frac{1}{3\epsilon + \sigma_{\text{eff}}} \frac{\partial G}{\partial x_i}\,, \tag{2.95}$$

and another for the gradient of the radiative heat flux:

$$\frac{\partial q_i^{rad}}{\partial x_i} - \epsilon G = -4 i_b - E_c\,, \tag{2.96}$$

where i_b is the black body radiation (which can be computed with the Stefan Boltzmann law) and E_c is the emission contribution of the model. These two equations can be coupled obtaining a second-order elliptic partial differential equation:

$$\frac{\partial}{\partial x_i}\left(\frac{1}{3\epsilon + \sigma_{\text{eff}}} \frac{\partial G}{\partial x_i}\right) - \epsilon G = -4\epsilon\sigma_S T^4 - E_c\,, \tag{2.97}$$

where σ_{eff} is the effective scattering coefficient, usually computed by:

$$\sigma_{\text{eff}} = 3\sigma_s - \sigma_s \mathcal{C}\,, \tag{2.98}$$

where the σ_s is the total isotropic scattering coefficient (units $1/\text{m}$) and $\mathcal{C}$ is the linear anisotropic scattering factor (dimensionless and bounded in $\mathcal{C} \in \{-1, 1\}$ having backward scattering if $\mathcal{C} = -1$, isotropic behavior if $\mathcal{C} = 0$ or forward scattering if $\mathcal{C} = 1$). This equation has as boundary condition the Marshak BC, which is described as [25]:

$$\frac{\partial}{\partial \vec{n}} G(\vec{r}_w) = \epsilon \frac{3\epsilon + \sigma_{\text{eff}}}{2(2-\epsilon)} \left[G(\vec{r}_w) - 4\sigma_S T^4(\vec{r}_w)\right]\,, \tag{2.99}$$

where $\vec{r}_w$ is the wall positioning vector and the BC accounts for the radiation that is either being emitted or absorbed at the boundaries. Once Equation 2.97 is solved, the source term for the energy equation can be computed. The source term that is included in the right-hand side of the enthalpy equation is given as [25]:

$$S_{rad} = \epsilon G - E_c - 4\epsilon\sigma_S T^4\,, \tag{2.100}$$

which is the divergence of the radiative heat flux defined in Equation 2.95. Although other more accurate approaches are available, the chosen one for this thesis is the P1 model. The P1 model is limited to cases where the optical depth is high. This value is defined as the product $\epsilon \cdot L$, where ϵ equals the absorption coefficient and L is a typical length scale of the case. The threshold varies between authors, being the most restrictive $\epsilon \cdot L > 1$. The main drawbacks are that it cannot be used unless all surfaces are diffuse and can lead to inaccurate results if the geometry is complex, the optical thickness is not high enough or radiative fluxes are coming from localized heat sources or sinks. The main advantage of the P1 model is that CPU cost is low maintaining a reasonably high accuracy (even when compared with more detailed approaches as the Discrete Ordinates Method).

3

Methodology

Once the motivation and research questions have been introduced and the mathematical foundations to tackle them have been presented, this chapter will show the methodology followed and the implementations carried out to achieve the different objectives. First, the numerical tool that has been used is described, with the approach already available in the software to handle fluid flows. Then, the implementations performed in this thesis are presented grouped by category, as many of them were already similarly coded but they had been modified and customized for the requirements of the industry. Thus, for each one of them, first, a motivation is presented, followed by the description of the code already available and the performed implementation. For each library, a comparison between the performance of the already implemented and the customized libraries is shown, to either further present the improvements or support the need for the new library.

3.1. Numerical modeling approach

OpenFOAM is based on the Finite Volume Method [68], which is used to analyze partial differential equations with some initial and boundary conditions discretizing the equation in a grid. The details on how the tool operates and how the user can interact with it can be found in Appendix A. Transport equations can be generally written for a given quantity f as [133]:

$$\underbrace{\frac{\partial}{\partial t}(\rho f)}_{\substack{\text{Temporal}\\ \text{derivative}}} + \underbrace{\frac{\partial}{\partial x_i}(\rho u_i f)}_{\substack{\text{Convective}\\ \text{term}}} - \underbrace{\frac{\partial}{\partial x_i}\left(\rho D \frac{\partial f}{\partial x_i}\right)}_{\substack{\text{Diffusion}\\ \text{term}}} = \underbrace{S_f(f)}_{\substack{\text{Source}\\ \text{term}}} .$$

The equation can be integrated over individual volumes or cells (differential volume dV) of the domain as:

$$\iiint \frac{\partial}{\partial t}(\rho f)\, dV + \iiint \frac{\partial}{\partial x_i}(\rho u_i f)\, dV - \iiint \frac{\partial}{\partial x_i}\left(\rho D \frac{\partial f}{\partial x_i}\right) dV = \iiint S_f(f) dV .$$

The convective and diffusive terms of the equation can be reformulated to be based on the convective and diffusive fluxes through the faces that enclose the volume of the cell.

$$\iiint_V \frac{\partial f}{\partial x_i} dV = \oiint_{\partial V} dS_i\, f ,$$

by using the Gauss divergence theorem expressed for a volume field f in a volume V with a boundary ∂V, described with infinitesimal surface elements dS_i that point outwards of ∂V. Using OpenFOAM

means that all these steps have wrappers that perform the vast majority of the operations without user intervention.

The pressure-velocity coupling is another CFD problem that is handled by the OpenFOAM tool. The system given from Equation 2.51 to Equation 2.53 (i.e. any fluid flow where the energy equation is being considered), can be solved in two ways: coupled (where all the equations are solved at the same time) or segregated (solving iteratively the equations and correcting with updated properties). Most OpenFOAM solvers are constructed in a pressure-based segregated algorithm that can use different approaches to couple momentum and mass conservation equations, namely SIMPLE (Semi-Implicit Method for Pressure Linked Equations), PISO (Pressure-Implicit with Splitting of Operators), or PIMPLE (a merge between PISO and SIMPLE that applies a SIMPLE iteration for each timestep until convergence is achieved, presenting better stability than the PISO algorithm) [133]. SIMPLE was developed for steady-state cases, while the other two were developed for transient unsteady cases. The PIMPLE algorithm is the one used for the thesis and its full description with detailed flow charts can be found in [146] and in [108].

The time advancing performed within the PIMPLE algorithm is based on a time increment Δt, whose value can either be fixed or based on the Courant–Friedrichs–Lewy condition [29]. The CFL condition is generally described for a 1D case as:

$$\mathrm{Co}_{\mathrm{CFL}} = \frac{u\Delta t}{\Delta x} \leq \mathrm{Co}_{\mathrm{max}}\,, \tag{3.1}$$

where u is the velocity in the direction x and Δx is the cell size in that direction. For explicit time-marching techniques (as the ones available in OpenFOAM), the largest allowable value is $\mathrm{Co}_{\mathrm{max}} = 1$. The velocity-based Courant number is implemented in OpenFOAM for a general three-dimensional compressible case as:

$$\mathrm{Co}_{\mathrm{CFL}} = 0.5 \max_i \left(\frac{1}{V_i} \sum_j \left\| \phi_{i,j} \right\| \right) \Delta t\,, \tag{3.2}$$

where V_i is the volume of the i-th cell, and $\phi_{i,j}$ denotes the flux of the i-th cell through the j-th face. The factor 0.5 is used to take the mean of all 6 faces in the case of a hexahedral cell.

However, the combustion model is also defined in terms of the flame velocities, namely S_L and S_t. Thus, another timestep based on the turbulent flame speed (as $S_t > S_L$) is defined as:

$$\mathrm{Co}_{St} = \max_j \left(\delta_{\mathrm{coeffs},j} \frac{\rho_{u,j} S_{t,j} (S_{f,j,k} \cdot n_{j,k})}{\rho_j \left\| S_{f,j} \right\|} \right) \Delta t\,,$$

where the flame normal vector of the j-th face n_j is defined in Equation 3.36, $S_{f,j}$ is the j-th face normal vector with magnitude the cell face area, and $\delta_{\mathrm{coeffs},j}$ is the reciprocal of the center-to-center distance projected over the face normal of the shared face between two cells, with an additional stabilization factor. This has a two-folded objective: firstly, to control the maximum timestep based on combustion, and secondly, to avoid large timesteps due to low flow velocities that may prevent a correct flame expansion. The final timestep Δt for the time advancing is obtained as

$$\Delta t \leftarrow \left(\min \left[\min \left(\frac{\mathrm{Co}_{\mathrm{max}}}{\max\left(\mathrm{Co}_{St}, \mathrm{Co}_{\mathrm{CFL}}\right)}, 1 + 0.1 \frac{\mathrm{Co}_{\mathrm{max}}}{\max\left(\mathrm{Co}_{St}, \mathrm{Co}_{\mathrm{CFL}}\right)} \right), 1.2 \right] \Delta t, \Delta t_{\mathrm{max}} \right)\,,$$

where Δt_{max} is a maximum timestep, which is also user-supplied. Other criteria can be found in the literature to determine the best timestep to advance numerical simulations of combustion phenomena. For example, in [69] another criteria constructed around diffusivities, viscosities, and conductivities is defined as:

$$\max \left(\frac{D\Delta t}{\Delta x^2}, \frac{\mu \Delta t}{\Delta x^2}, \frac{\lambda \Delta t}{\Delta x^2} \right)\,.$$

This criteria hasn't been implemented but it should improve the determination of the Δt, making the solution process more stable.

The baseline solver used for this thesis is `XiFoam`, which is constructed over `pimpleFoam` (whose algorithm was already introduced) to include premixed combustion. The main differences between `XiFoam` and `pimpleFoam` are:

1. The combustion model is included in `XiFoam` with the regress variable $\tilde{b}$ as:

$$\frac{\partial}{\partial t}\left(\overline{\rho}\tilde{b}\right)+\frac{\partial}{\partial x_i}\left(\overline{\rho}\widetilde{u}_i\tilde{b}\right)-\frac{\partial}{\partial x_i}\left(\overline{\rho}D_{\text{eff}}\frac{\partial\tilde{b}}{\partial x_i}\right)=-\overline{\rho}_u S_L\Xi\left|\frac{\partial\tilde{b}}{\partial x_i}\right|. \tag{3.3}$$

   The derivation of this equation, as well as the meaning of each one of its terms, has a dedicated Section given its importance for this thesis (see Section 3.7.1).

2. Apart from the enthalpy transport equation usually considered, `XiFoam` includes also another enthalpy transport equation, having that one equation is used for the enthalpy H transport while the other solves the unburnt enthalpy H_u transport [64] (even if they can be automatically adapted to be expressed in terms of the internal energy):

$$\frac{\partial}{\partial t}\left(\rho H\right)+\frac{\partial}{\partial x_i}\left(\rho u_i H\right)+\frac{\partial}{\partial t}\left(\rho K\right)+\frac{\partial}{\partial x_i}\left(\rho u_i K\right)-\frac{\partial p}{\partial t}-\frac{\partial}{\partial x_i}\left(\rho\alpha_{\text{eff}}\frac{\partial H}{\partial x_i}\right)=S_f\,, \tag{3.4}$$

$$\frac{\partial}{\partial t}\left(\rho H_u\right)+\frac{\partial}{\partial x_i}\left(\rho u_i H_u\right)+\left[\frac{\partial}{\partial t}\left(\rho K\right)+\frac{\partial}{\partial x_i}\left(\rho u_i K\right)-\frac{\partial p}{\partial t}\right]\frac{\rho}{\rho_u}-\frac{\partial}{\partial x_i}\left(\rho\alpha_{\text{eff}}\frac{\partial H_u}{\partial x_i}\right)=S_f\,, \tag{3.5}$$

   where K is the kinetic energy computed as $K=0.5u_i^2$ and S_f includes all the source terms shown in Equation 2.53. The original `XiFoam` solver is based on the `psiuReactionThermo` library, which uses the values of H_u to determine the local unburnt temperature T_u (employed to correct the laminar flame speed) and density ρ_u (present in the source term of the regress variable transport equation). However, and as done previously in the literature [122], these two variables can be reformulated to not depend on the unburnt temperature or density with the use of isentropic relations:

$$\omega_{\tilde{b}}=\rho_u S_t\left|\nabla\tilde{b}\right| \longrightarrow \omega_{\tilde{b}}=\left[\rho_{u,0}\left(\frac{p}{p_0}\right)^{1/\gamma}\right]S_t\left|\nabla\tilde{b}\right|, \tag{3.6}$$

$$S_{L,0}=S_{L,0}^{\text{ref}}\left(\frac{T_u}{T_{\text{ref}}}\right)^{m_{\text{t}}}\left(\frac{p}{p_{\text{ref}}}\right)^{n_{\text{b}}} \longrightarrow S_{L,0}=S_{L,0}^{\text{ref}}\left(\frac{p}{p_{\text{ref}}}\right)^{m_{\text{t}}\frac{\gamma-1}{\gamma}+n_{\text{b}}}, \tag{3.7}$$

   where the subscript 0 represents the uniform initial values of the fields and γ is the heat capacity ratio ($\gamma=c_P/c_V$). As no other argument has been found in any of the papers related to the solver `XiFoam` that support the use of the unburnt mixture equation (partly because the energy equations are usually not detailed, see [65], [75], or [82]), it is decided to remove it from the solver, achieving a reduction in the computational time of around $\sim 15\%$.

Sod's problem

In order to test that the `XiFoam` solver is capable of solving supersonic cases with shockwaves, while still being a pressure-based segregated solved, the Sod's problem is considered [126]. As no combustion is involved, the $\tilde{b}$ equation is not solved (so $\tilde{b}=1$ in all the domain), although the energy equation is. The problem is stated as a membrane in a one-dimensional tube separating two different states of the same mixture (see Figure 3.1): the left state is defined with ρ_1, p_1 and $u_1=0$ m/s while the right state is defined by $\rho_5<\rho_1$, $p_5<p_1$ and $u_5=0$ m/s (so both states were initially at rest). After the membrane is broken, a contact discontinuity and a expansion fan moves to the left and a shockwave move to the right. Thus, the analytical solution consists of five states, from which states 1 and 5 have known properties (the initial ones). The properties of the remaining states can be obtained as:

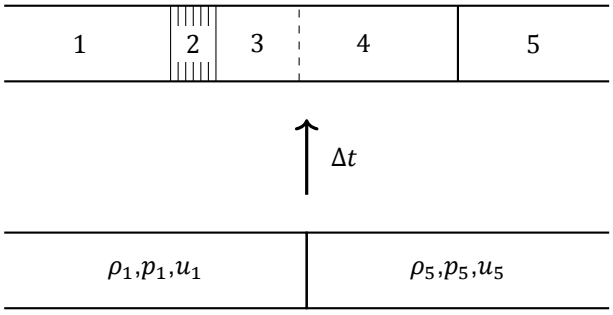

Figure 3.1: Sod's problem description.

- **State 4**: the pressure in this state has to be computed by solving an equation numerically as is it not possible to express it explicitly:

$$p_4 \leftarrow \left[1 - \frac{\gamma-1}{2\gamma}\sqrt{\frac{p_5\rho_1}{p_1\rho_5}}\left(\frac{p_4}{p_5}-1\right)\left(\sqrt{1+\frac{\gamma+1}{2\gamma}\left(\frac{p_4}{p_5}-1\right)}\right)^{-1/2}\right]^{(2\gamma)/(\gamma-1)} = \frac{p_4}{p_1}.$$

  Once the pressure p_4 is known, the velocity and density can be computed as:

$$u_4 = \frac{\sqrt{\frac{\gamma p_5}{\rho_5}}\left(\frac{p_4}{p_5}-1\right)}{\gamma\sqrt{1+\frac{\gamma+1}{2\gamma}\left(\frac{p_4}{p_5}-1\right)}},$$

$$\rho_4 = \rho_5\frac{\left[1+\frac{\gamma+1}{2\gamma}\left(\frac{p_4}{p_5}-1\right)\right]}{\left[1+\frac{\gamma-1}{2\gamma}\left(\frac{p_4}{p_5}-1\right)\right]}.$$

- **State 3**: the only different values through the contact discontinuity are those of density, having the same pressure and velocity of state 4:

$$u_3 = u_4,$$
$$p_3 = p_4,$$
$$\rho_3 = \rho_1\left(\frac{p_3}{p_1}\right)^{1/\gamma}.$$

- **State 2**: within the expansion fan, the three considered properties vary spatially. Thus, they have a dependence on the horizontal coordinate x, the time t, and the initial location of the diaphragm x_{id}:

$$u_2(x,t) = \frac{2}{\gamma+1}\left(\sqrt{\frac{\gamma p_1}{\rho_1}} + \frac{x-x_{id}}{t}\right),$$

$$p_2(x,t) = p_1\left(1-\frac{\gamma-1}{2}u_2(x,t)\sqrt{\frac{\rho_1}{\gamma p_1}}\right)^{(2\gamma)/(\gamma-1)},$$

$$\rho_2(x,t) = \rho_1\left(1-\frac{\gamma-1}{2}u_2(x,t)\sqrt{\frac{\rho_1}{\gamma p_1}}\right)^{2/(\gamma-1)}.$$

The location of each one of the states depends of time and can be computed as:

$$x_{1-2}(t) = x_{id} - t\sqrt{\frac{\gamma p_1}{\rho_1}},$$
$$x_{2-3}(t) = x_{id} + t\left(u_3 + \sqrt{\frac{\gamma p_3}{\rho_3}}\right),$$
$$x_{3-4}(t) = x_{id} + u_3 t,$$
$$x_{4-5}(t) = x_{id} + t\left(\sqrt{\frac{\gamma p_5}{\rho_5}}\sqrt{1 + \frac{\gamma+1}{2\gamma}\left(\frac{p_4}{p_5} - 1\right)}\right).$$

The numerical domain was defined as a prism of 1.00 m $\times 0.10$ m $\times 0.10$ m and discretized with $600\times1\times1$ cells. The pressure and density jumps were imposed through `setFields`, obtaining the step in density with a jump in the temperature. The values chosen were $\gamma = 1.4$, $\rho_5 = 0.125$ kg/m^3, $p_5 = 10$ kPa, $\rho_1 = 1.0$ kg/m^3 and $p_1 = 100$ kPa. Solutions are presented in Figure 3.2 at $t = 0.0005$ s. Four different divergence schemes were used, having used all of them at the same time for all the divergence terms (its mathematical formulation can be seen in [66]):

- **Upwind**: first-order bounded scheme, assigns face value according to upstream value.
- **Limited Linear**: based on the Sweby limiter modified to accommodate central differences [128], blended first/second order, unbounded scheme.
- **Limited Cubic**: total variation diminishing limiter for a centred-cubic differencing scheme.
- **MUSCL**: it stands for Monotone Upstream-centered Schemes for Conservation Laws, second order and unbounded scheme.

The results for these four divergence discretization schemes can be seen in Figure 3.2. It can be seen that all profiles are properly resolved, being the worse one the density gradient across the contact discontinuity (see Figure 3.2a). From the different schemes, there is not much difference, being the limited linear and MUSCL schemes the ones that better performed in the aforementioned density jump. Thus, it can be stated that the solver is capable of resolving problems with shockwaves.

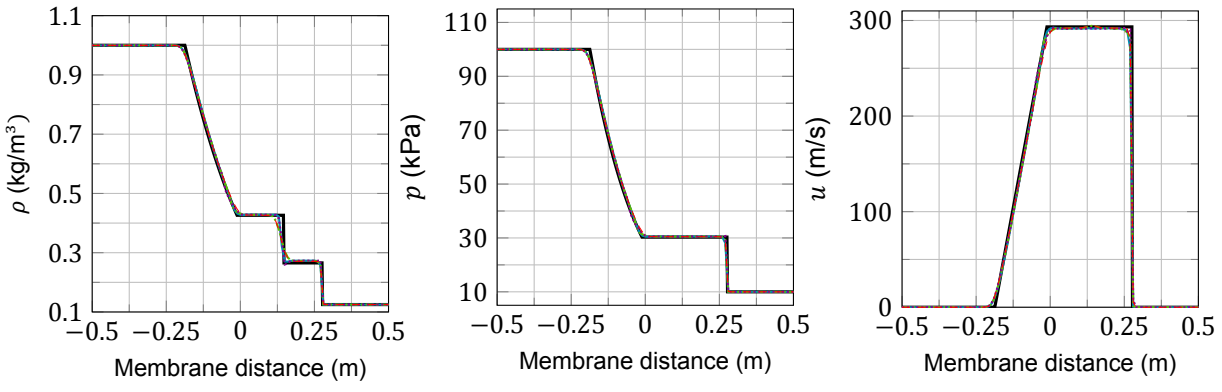

(a) Density at $t = 0.0005$ s.

(b) Pressure at $t = 0.0005$ s.

(c) Velocity at $t = 0.0005$ s.

Figure 3.2: Numerical and analytical solution to Sod's problem. —— is the analytical solution, —— is the limited linear scheme, -·-·- is the limited cubic scheme, ····· is the MUSCL scheme, and - - - is the upwind scheme.

3.2. Flame radius calculation methods

One of the metrics that is extracted from the experimental facilities is the flame radius (or flame front location along a given axis in the case that the flame front doesn't present a spherical shape during the whole experiment). To get this flame radius numerically at runtime, three different methods have been implemented and validated in OpenFOAM:

- `volIntegrated`: the $\tilde{b}$ field can be volume-integrated in the domain (using the density as a correcting term for normalization). Two cases have been implemented, depending on whether the case is three or two dimensional:

$$\text{3D:} \qquad R_f = \left[\frac{3}{4\pi\rho_b}\left(\frac{2\pi}{\alpha_w}\cdot 2^{\mathrm{sym}}\iiint \rho(1-\tilde{b})\,dV\right)\right]^{1/3},$$

$$\text{2D:} \qquad R_f = \left[\frac{1}{\mathcal{T}\pi\rho_b}\left(2^{\mathrm{sym}}\iiint \rho(1-\tilde{b})\,dV\right)\right]^{1/2}.$$

  The three-dimensional case integrates the domain and considers that the shape of the volume is a part of an equivalent sphere. Thus, the integrated volume is corrected with the number of symmetry planes (exponent `sym`) and the angle of the wedge α_w (for axisymmetric geometries). Then, the total volume is related to the flame radius through the volume equation of a sphere. The two-dimensional case follows the same procedure, being the differences that no α_w angle can be corrected and that the volume is assumed to follow the shape of a cylinder (where the depth $\mathcal{T}$ can be retrieved from the mesh).

- `surfAveraged`: the radius is the averaged distance between the ignition location and each one of the cells where $\tilde{f}_{low} < \tilde{f} < \tilde{f}_{up}$, being $\tilde{f}$ any given field and $\tilde{f}_{low}$, $\tilde{f}_{up}$ the lower, upper limit of the variable respectively. OpenFOAM cannot compute isosurfaces at runtime, so the code loops through the cells and checked to see whether they are within bounds for the selected variable and, if they are, the distance from that cell to the ignition location is averaged:

$$R_f = \frac{\sum_i^N \left\|\vec{x}_i - \vec{x}_{\mathrm{ign}}\right\|}{N} \qquad \text{for all } i \text{ such that } \tilde{f}_{low} < \tilde{f}\,(\vec{x}_i) < \tilde{f}_{up}\,.$$

  Instead of a smooth surface, this returns a grid-like isosurface that may span multiple cells. Its use in other cases where the flame front is highly distorted and doesn't present similar development in all directions can return erroneous values, as it will average these cell distances.

- `axialBased`: the flame front location is computed as the maximum coordinate along one axis direction ($\vec{n}_r$) of the grid-like isosurface described as $\tilde{f}_{low} < \tilde{f} < \tilde{f}_{up}$. From the flame front location, and by taking the distance to the ignition location, the flame *radius* can be computed:

$$R_f = \left\|\vec{x}_i - \vec{x}_{\mathrm{ign}}\right\| \qquad \text{where } \vec{x}_i \text{ is } \begin{cases} \tilde{f}_{low} < \tilde{f}\,(\vec{x}_i) < \tilde{f}_{up} \\ \max\left(\vec{x}_i \cdot \vec{n}_r\right) \end{cases}.$$

The `axialBased` and `surfAveraged` methods are, compared to the `volIntegrated` method, computationally slower as they have to loop over all cells of the domain while the volume integration is performed vectorially. Moreover, the `axialBased` and `surfAveraged` methods require the choice of a variable $\tilde{f}$ as well as two limits to define the isosurface (even when they are defined to be symmetric around a given value $\tilde{f}_{low} = \tilde{f}_0 - \epsilon$ and $\tilde{f}_{up} = \tilde{f}_0 + \epsilon$). This choice cannot be arbitrary and it is not exempt from discussion in the literature [114]: it can be thought that $\tilde{b} = 0.5$ represents a mixture with half burnt and half unburnt, although the Favre averaging masks the true meaning of b. The mixture where half is burnt and half is unburnt is given by $\overline{b} = 0.5$, and depending on the density ratio [88], the corresponding Favre-average value ranges $\tilde{b} = (0.8 - 0.9)$. Moreover, from experiments, the regress variable is, of course, not a measurable quantity: temperature profiles are employed to define flame fronts, as they are the information that can be retrieved from capturing devices.

To compare the behavior of the three methods to compute the flame radius, a simple case with a laminar expanding spherical flame was considered. A wedge-type geometry of 1 m ×1 m was discretized with 500×500 cells and with a symmetry plane in the lower face. All fields but the pressure (which had a `fixedValue` Dirichlet-type boundary condition) used a `zeroGradient` Neumann-type boundary condition. Five different configurations were tested to compute the flame radius: the `volIntegrated` method, the `surfAveraged` method with $\tilde{b} = 0.10\left(^{+0.10}_{-0.05}\right)$, $\tilde{b} = 0.50\left(^{+0.10}_{-0.10}\right)$ and $\tilde{b} = 0.90\left(^{+0.05}_{-0.10}\right)$, and the `axialBased` method with $\tilde{b} = 0.50\left(^{+0.10}_{-0.10}\right)$ combined with $\vec{n} = (1, 0, 0)$ or with $\vec{n} = (0, 1, 0)$. When $\tilde{b} = 0.1$ and $\tilde{b} = 0.9$ different values of ϵ had to be chosen for the upper and lower limit to avoid reaching $\tilde{b} = 0$ and $\tilde{b} = 1$, respectively. In Figure 3.3a can be seen three different trends with respect to the flame radius (which gets translated into three different groups of values in the flame velocity in Figure 3.3b). Both `axialBased` approaches give close results between them (being the difference the direction on which the distance is computed) and with the `surfAveraged` method of the same bounds for iso surface selection. The value of `volIntegrated` follows that of `surfAveraged` with $\tilde{b} = 0.90\left(^{+0.05}_{-0.10}\right)$ showing that the integration in the whole domain is similar as taking the outermost part of $\tilde{b}$ (which for the selected density ratio value corresponds to $\overline{b} \simeq 0.5$). Finally `surfAveraged` with $\tilde{b} = 0.10\left(^{+0.10}_{-0.05}\right)$ underpredicts the flame development as that isosurface is largely influenced by the flame diffusion. Cases with smaller diffusivity values would have closer values between the different methods for unbounded geometries (as well as cases where the diffusivity values are larger there would be a more significant spread between the methods).

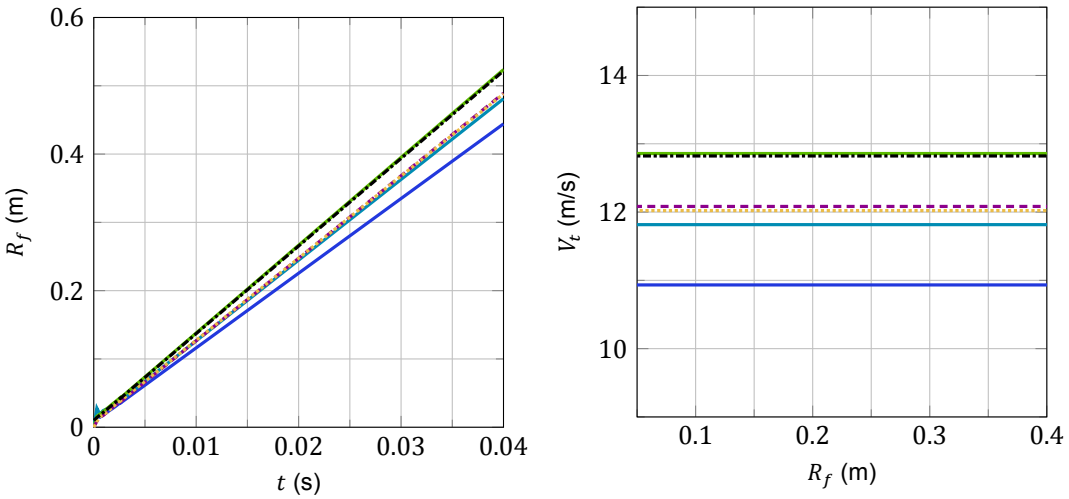

(a) Flame front development.

(b) Turbulent flame velocity.

Figure 3.3: Comparison of different flame-radius calculation methods for unbounded cases: ---- is `axialBased` with $\vec{n}_r = (1, 0, 0)$, ····· is `axialBased` with $\vec{n}_r = (0, 1, 0)$, —— is `surfAveraged` with $\tilde{b} = 0.1$, —— is `surfAveraged` with $\tilde{b} = 0.5$, —— is `surfAveraged` with $\tilde{b} = 0.9$, and -·-·- is `volIntegrated`.

Another simple test case was run to check the behavior of constrained geometries. All the experimental facilities are enclosed within walls (unless the region of interest is restricted to far from the walls) so the walls will modify the flame front development. To analyze how would this affect the different flame radius calculation methods, a domain of $0.10\,m \times 4.0\,m$ was discretized with 50×2000 cells, using a symmetry plane for the lower face and a wall boundary for the outer face (constraining this way the flame development). Only three methods were tested: `volIntegrated`, `surfAveraged` with $\tilde{b} = 0.50\left(^{+0.10}_{-0.10}\right)$ and `axialBased` with $\tilde{b} = 0.50\left(^{+0.10}_{-0.10}\right)$ and $\vec{n}_r = (0, 1, 0)$. In Figure 3.4 can be seen the behavior of the three models, which has been split into three phases depending on time (as the simulation was performed with the same parameters in all the cases, the only difference is the flame radius calculation method):

1. $t < 0.005$ s: the three methods return the same values as the flame is still expanding with a spherical flame front.

2. $0.005\text{s} < t < 0.020\text{s}$: when the flame radius reaches the wall at 0.10 m, the three methods start to return different values, as the flame stops being spherical and looks like an oblate spheroid, with one increasing axis and the other two bounded by the wall. Thus, the integrated volume of the burnt domain is still being referred to a sphere volume, having a smaller radius than the length of the increasing axis. The other two methods also provide different values: the `axialBased` returns the length of this increasing spheroid axis while the `surfAveraged` method presents a transition point when the flame front merges with the wall, having always a smaller radius than the `axialBased` method (because it is taking into account the whole flame front and not just the most advanced location).

3. $0.020\text{ s} < t$: as the flame front transitions to an almost-flat flame front propagating in the unconstrained direction, only two trends appear: the `volIntegrated` method, which still underestimates the flame radius as the reference sphere has a smaller volume than the actual burnt domain which is cylinder-shaped, and the `axialBased`-`surfAveraged` methods, which return the same behavior of flame expanding in the pipe.

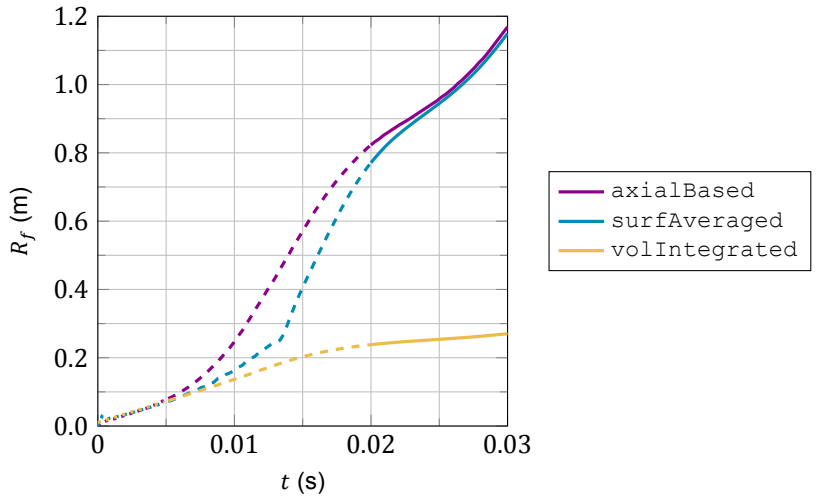

Figure 3.4: Comparison of different flame-radius calculation methods in constrained geometries.

With these results, it can be stated that the calculation procedure to obtain the flame radius has been validated and the adequate choice of method for a case can be argued with these two small examples. For unbounded geometries, the approaches return similar results, depending only on the flame brush diffusion. The one recommended for such cases is the `volIntegrated`, as it is the computationally fastest. However, the `volIntegrated` approach is not suited for constrained geometries. In those cases, the use of the `axialBased` is recommended as it is not influenced by effects like the flame interacting with the wall.

3.3. Ignition methods

Ignition is a complex phenomenon to model with RANS turbulence models and the combustion models described in this thesis. To capture the physical mechanisms that occur during the ignition phase of mixture (where an electrical device is introduced in the volume and discharges an electrical current creating an energy source), an extremely refined temporal and spatial resolution is required. As ignition cannot be properly modeled with the current approach, other alternatives exist to start the combustion. Ignition occurs at the beginning of the combustion process, but the development of the flame largely depends on the way the mixture is ignited. Thus, particular attention must be paid to this step and is extensively discussed below.

3.3.1. Ignition approaches available in OpenFOAM

In the default `XiFoam` solver there are two approaches already implemented that can be used to ignite certain mixture of $\tilde{b} = 1$. The first one is a source term [107] that is added to some cells in the right-hand side of the regress variable transport equation (Equation 3.27):

$$\tilde{b}_i \mathrel{+}= \left(\frac{\Gamma_{\text{ign}}}{\tau_{\text{ign}}}\right) V_i \frac{\rho_u}{\tilde{b}_i + 0.001} = \gamma_{\text{ign}} V_i \frac{\rho_u}{\tilde{b}_i + 0.001}, \tag{3.8}$$

where V_i is the cell volume, ρ_u is the unburnt density, Γ_{ign} is the ignitor strength, and τ_{ign} is the duration of the ignition (even if the ignitor properties can be rewritten together as γ_{ign}). The cells that get the source term added are those whose centers lay within a given diameter d_{ign}. To account for the difference between a spherical flame front and the straight edges of the cells, a correction parameter $S_{t,\text{corr}}$ is used in Equation 3.29 during the time that ignition is activated. The source term makes the diagonal more dominant, so its use results in a more stable solution process. However, the source term itself depends on three variables: Γ_{ign}, τ_{ign}, and d_{ign} (although the two first can be combined in γ_{ign}). The correction parameter $S_{t,\text{corr}}$ requires even more variables (four to be exact, namely `ignitionSphereFraction`, `ignitionThickness`, `ignitionCircleFraction` and `ignitionKernelArea`). The choice of all those parameters (as stated by the developers themselves) is done by trial and error. Moreover, it has been seen that the results obtained with different parameters are not necessarily consistent. Some simple tests were carried out with a 2D unbounded domain by keeping all the properties the same and just modifying one at a time. As it can be seen in Figure 3.5a, the value of the strength radically changes the flame development, which can go from an non-ignited flame if the strength is too low to a quickly expanding flame if the strength increases three orders of magnitude. The main problem of the strength value is that it cannot be determined in any other way than by trial and error, so its use can modify the way a flame develops and tune the results. Moreover, by looking at Figure 3.5b, it can be seen that even with the same strength γ_{ign} and diameter d_{ign} values, the grid resolution can also change the flame front development. A baseline grid V_i^0 was largely coarsened and refined, obtaining different flame front developments (and therefore velocities).

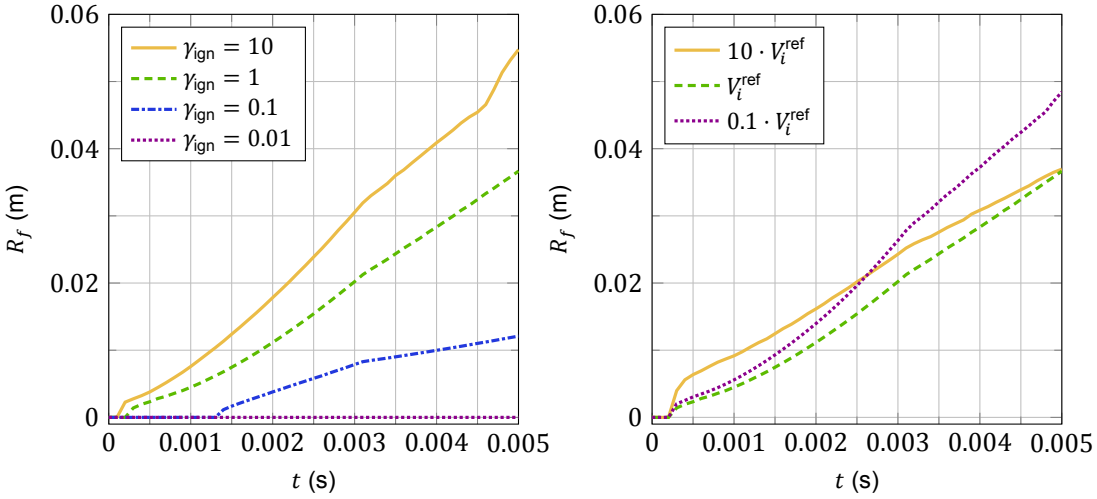

(a) Flame radius evolution for different ignition strengths. Other properties remain constant.

(b) Flame radius evolution for different grid resolutions. Other properties remain constant.

Figure 3.5: Ignition source term implemented in the default version of `XiFoam`.

The second method available in OpenFOAM consists of specifying the initial conditions in the ignition region with $\tilde{b} = 0$ and with the adiabatic flame temperature T_{ad} by using `setFields`. It only depends on the patching radius, as the adiabatic flame temperature at constant volume can be computed for a given mixture before running the numerical simulation. Two different grid resolutions and three patched regions (a 1×1 square, a domain of three cells in L-shape and a 2×2 square) were considered, presenting its flame radius development in Figure 3.6a. As long as the ignition is larger than 1×1

(so that gradients are properly computed) the flame development is consistent, presenting just a time shift consistent with previous studies [122]. For too small patching regions the flame front spreads without combusting, having that $\min\left(\tilde{b}\right) > 0.05$ (see the red region in Figure 3.6b). It can be seen that increasing the ignition volume logarithmically reduces the final smallest value of $\tilde{b}$.

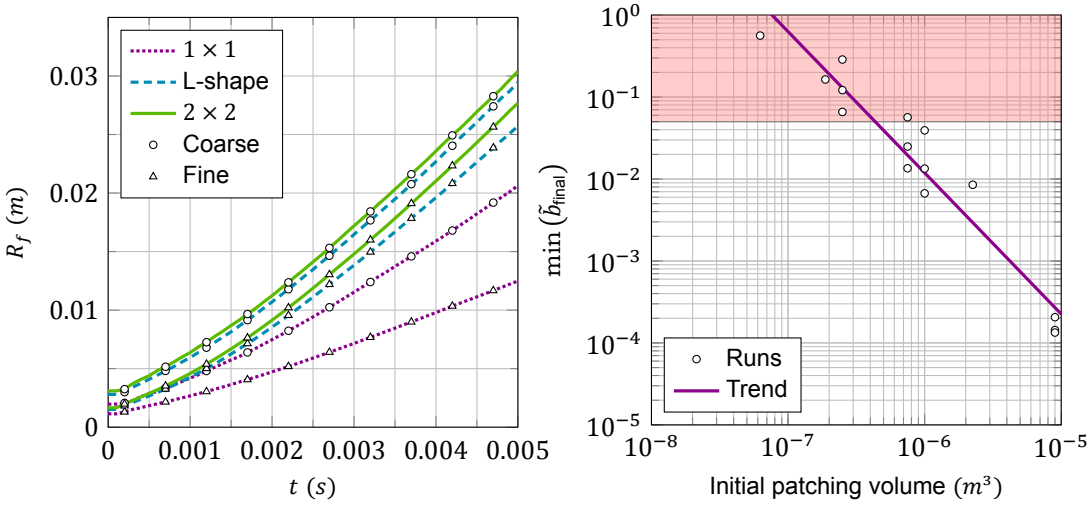

(a) Flame front development for different combinations of ignition shape and grid.

(b) Minimum value at the end of the simulation of $\tilde{b}$ for different ignited volumes.

Figure 3.6: Study of the `setFields` ignition procedure.

3.3.2. Additional ignition implementations

To fully be consistent with the TFC and ETFC combustion models, the source term proposed for each one of these models was also implemented:

- TFC's ignition source term [72]:

$$\omega_{\text{ign}}^{TFC} = \overline{\rho}\Gamma_{\text{ign}} \exp\left(-\left[\left(\frac{r}{r_{\text{ign}}}\right)^2 + \left(\frac{t-t_0}{\tau_{\text{ign}}}\right)^2\right]\right)\tilde{b}\,.$$

- ETFC's ignition source term [60]:

$$\omega_{\text{ign}}^{ETFC} = \overline{\rho}\Gamma_{\text{ign}} \exp\left(-\left[\left(\frac{r}{r_{\text{ign}}}\right)^2 + \mathcal{H}\left(t_0 - t\right)\left(\frac{t-t_0}{\tau_{\text{ign}}}\right)^2\right]\right)\tilde{b}\,.$$

where r is the cell center distance to the ignition location. It can be seen that these source terms are applied globally (as opposed to the `XiFoam` source term) although they are still proportional to a strength value Γ_{ign}. Both ignition terms depend on 4 terms: the source strength Γ_{ign}, the radial spread r_{ign}, the temporal spread τ_{ign} and the source peak location t_0. The only difference between them is the inclusion of the Heaviside function in the temporal term of the ETFC ignition source term, which makes that this source term is completely engaged for $t > t_0$. However, it can be seen that the results for the TFC's source term (see Figure 3.7a) and the ETFC's source term (see Figure 3.7b) are similar between them - although truly inconsistent and parameter-dependent. The same two-dimensional case as before was simulated with a set of parameters (labeled as Original) and used as a reference to compare with each one of the other three main parameters (leaving t_0 out): strength $W_{0,\text{stronger}} > W_{0,\text{original}} > W_{0,\text{weaker}}$, radial spread $\sigma_{r,\text{larger}} > \sigma_{r,\text{original}} > \sigma_{r,\text{smaller}}$ and temporal spread $\sigma_{t,\text{longer}} > \sigma_{t,\text{original}} > \sigma_{t,\text{shorter}}$ (varying just one parameter at a time). It can be seen that the flame development and, consequently, the flame speed are not consistent and the results cannot simply be explained with a temporal shift.

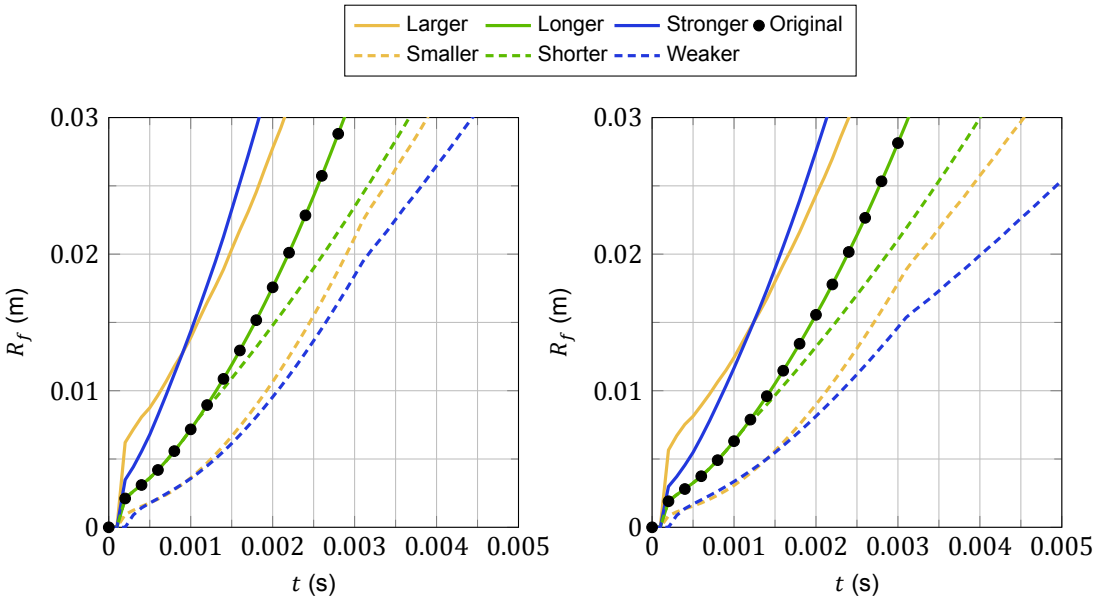

(a) Results for the TFC's ignition source term.

(b) Results for the ETFC's ignition source term.

Figure 3.7: Results for the new implementations of ignition source terms.

The same way the source term in `XiFoam` is not consistent, the source terms defined for the TFC and ETFC models are also parameter dependent. Thus, the chosen way to ignite the mixture is patching with `setFields` with $\tilde{b}$ and T_{ad} a region as small as possible while obtaining small values of $\tilde{b}$ (to ensure flame expansion). Moreover, two other techniques to promote flame expansion were included: turbulent diffusion prevents flame expansion [60] (so it was forced that $D_t = 0\ m^2/s$ during $t < 0.0005\ s$) and the temperature in the burnt region should be enforced [144] (when less than 5% of the domain has been burnt, $\tilde{T} = T_u\tilde{b} + T_b(1-\tilde{b})$ was used). The time during which $D_t = 0\ m^2/s$ and the percentage for the fixed temperature were chosen based on [60] and no sensitivity study was performed, as it is a small percentage of the domain for a short time.

3.4. Adaptive mesh refinement

Gradient-based premixed combustion models rely on the gradient calculation inside the cells where the flame front is located. Even if it is not expected to have cells of the size of the flame reaction zone in RANS simulation, it is preferably to have a flame surface resolved as much as possible (i.e. the cell size closer to the flame front thickness). As it is neither practical nor viable to have a nuclear containment vessel (on the order of hundreds of meters) discretized with scales of the order of millimeters or even less, the use of adaptive mesh refinement (AMR) is the only acceptable tradeoff solution. AMR has been extensively used for a wide variety of problems where the accurate resolution of certain regions of the fluid domain is required. These problems involve not only flame fronts, but also shock waves or fluid interfaces in multiphase flow. Adaptive mesh refinement consists of refining selected cells when the value of a given quantity inside that cell is between the values of a range. The most classical approach is the octree method: each hexahedral cell is divided into 8 new hexahedral cells keeping a hierarchy tree for each level of refinement in a tree structure [39]. A quick remark about adaptive mesh refinement is the necessity of including dynamic load balancing schemes [120] that can balance the number of cells between processors. This is important given that the number of cells in a given region can increase exponentially. For example, if a cube is divided isotropically with one level of refinement, it will become 8 new cubes. If the level of refinement is 2, the amount of obtained cubes is 64 (having a series that follows as 8^{L_R} where L_R is the number of levels of refinement). The number of cells when running multiprocessor simulations should be balanced between the cores so that the simulation time is the same between them and there are no bottlenecks on the process. Thus, redistributing the refined cells between processors is required to maintain high computational efficiency.

3.4.1. Available dynamic mesh motion models in OpenFOAM

The chosen version of OpenFOAM (`v1812`) has already implemented models for dynamic mesh functionalities [67]. In general, there are two approaches to deal with time-varying meshes: automatic mesh motion and topological changes. The first group encompasses those cases where the surface motion is small: the motion of the cell points (i.e. a deformation from the initial grid shape) is enough to account for the change in geometry. The approach is valid as long as the mesh quality is high during the whole duration of the simulation, being the interpolation between deformed steps one of the largest sources of errors.

The second group performs topological changes of the mesh connectivity in order to accommodate larger deformations or motions of the domain boundary. The specific dynamic-mesh objects are based on topological mesh modifiers, and these are based on primitive mesh operations. The primitive mesh operations are nine simple mesh operations (e.g. removing a point) that are tedious to use as they cannot ensure mesh validity when used on their own. Topological mesh modifiers are easier to use, as they are composed of different primitive mesh operations that generate a new valid mesh. Some topological mesh modifiers include cell layer addition and removal, attaching and detaching boundary into internal faces, sliding interfaces and their connectivity, and oct-tree refinement for hexahedral cells. Finally, the dynamic-mesh objects are sets of many topological mesh modifiers that group a recognizable action over a grid (to improve the user-friendliness), as piston-valve coupling or vessel mixing.

Different libraries are included to deal with the dynamic mesh motion, being the most well known `dynamicMotionSolverFvMesh`, `dynamicMotionSolverTopoFvMesh`, `dynamicMultiMotionSolverFvMesh` and `dynamicRefineFvMesh`. The last one is the Adaptive Mesh Refinement. However, it performs the refinement by subdividing one hexahedral cell into eight new ones, without modifying the prism cells. Doing so poses a problem for the 2D axisymmetric meshes that were planned for this thesis due to two reasons. The first one is that the code is not able to divide prism cells (neither general polyhedra) and the cell that shares an edge with the axis of symmetry is a triangular prism (see Figure 3.8a). Thus the cells in the edge of an axisymmetric wedge, which are a prism and thus a polyhedra, are not refined accordingly and they will always present the same size. The second drawback of the original version is that it also refines in the azimuthal direction creating one face per refinement level (see also Figure 3.8a). However, when the solver is used with axisymmetric assumptions, it cannot handle more than one cell in the azimuthal direction. Thus, the solver crashes as soon as the AMR refines the azimuthal direction, which happens when any given cell is refined.

3.4.2. Axisymmetric adaptive mesh refinement implementation

In order to overcome these limitations, the `dynamicRefineFvMeshAxi` library was implemented based on previous work [8]. The published library mainly required to be linked with the current mesh topology classes and data structures so it could be used with the current solver version (as it was written for `v2.0.1` and the version used for this thesis is `v1812`), as well as other minor adjustments to ensure compliance with the industry requirements and further compatibility. Moreover, the differences between the solvers with dynamic-motion and the identical version without it were updated into the custom combustion solver (so it can work with and without adaptive mesh refinement). To achieve a case without refinement, either bounds outside the variable range can be set (e.g. refine cells where $2.0 < \tilde{b} < 3.0$) or the `staticFvMesh` library can be used. As the new axisymmetric library was generated independently of the solver, no dependencies were required during the compilation process, being necessary to include the library within the `controlDict` of those cases where the axial refinement is desired. This also allows the user to refine with other solvers that are not related to combustion.

The library in action can be seen in Figure 3.8b, compared to the same case refined with the default OpenFOAM library in Figure 3.8a. It can be seen that the two main drawbacks presented before have been successfully solved: the prism layer most close to the axis of symmetry is being refined in the radial and longitudinal directions (as opposed to the default library that doesn't refine it) and the azimuthal direction is not being refined (not introducing extra faces and keeping just one cell in this direction).

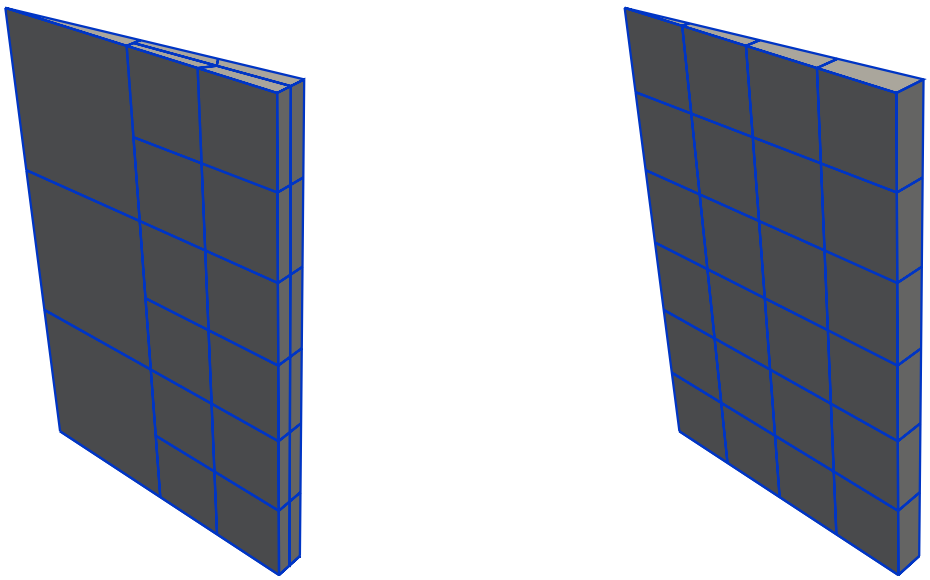

(a) Default `dynamicRefineFvMesh`. **(b)** Implemented `dynamicRefineFvMeshAxi`.

Figure 3.8: Different Adaptive Mesh Refinement libraries handling an axisymmetric wedge.

Even if the main drawbacks of the default version of OpenFOAM have been overcome, there is still room for improvements of the Adaptive Mesh Refinement model. One of the main drawbacks of either formulations is that the `cellLevel` is not read from the time folders but generated when the solver is started. Therefore, if the initial mesh presents a region with a higher level of refinement where it is not desired further refinement from the AMR, the current library will anyhow refine it. This could easily be avoided if the `cellLevel` was read from the initial timestep folder. Another drawback is the inability to refine polyhedra. If the grid is not conformal because a region has been already defined to have an increased cell level throughout the simulation (i.e. the boundary layer may be more refined than the freeflow), the custom library cannot refine the polyhedra that exists in the interface between refinement levels. Even if they look like hexahedra, the cells in between levels are polyhedra given that they have more than 6 faces. Finally, AMR cannot be activated at the beginning of the simulation as it doesn't promote flame expansion. Thus, it is activated once the flame has already expanded (the times at which this happens are presented individually for each experimental facility).

Refinement criteria study

A brief description is presented about the different parameters that define the AMR for the axisymmetric case. The dictionary for the `dynamicRefineFvMeshAxi` library is contained in the `constant/dynamicMeshDict` file and it is composed of (at least) the following items:

- `axis`: controls the direction that is not refined, if the wedge faces are perpendicular to the axis x it should have a value of `0` (having a value of `1` for the y axis and a value of `2` for the z axis).
- `axisVal`: it provides a value between the minimum and maximum coordinates along the `axis` in the geometry.
- `refineInterval`: number of timesteps between refinements, i.e. a value of `1` refines each timestep (being computationally expensive and modifying the mesh too fast when the timestep is small). A value of `5` was used.
- `maxRefinement`: maximum refinement level, it is important to keep in mind that 1 level means dividing a given cell into 8 new cells.

- `maxCells`: number of maximum cells in the domain, the refinement process will stop if this limit is reached.
- `field`: the variable that is used to perform the AMR based on whether the cell values are within bounds.
- `unrefineLevel`: if the `field` value in a given cell is below this value, the cell is coarsened (although the cell cannot be coarser than the initial one).
- `lowerRefineLevel`: lower bound value to trigger cell refinement.
- `upperRefineLevel`: upper bound value to refine any given cell if its value goes below it. This means that the cells that will be refined are those whose `field` is between `unrefineLevel` and `upperRefineLevel`.
- `nBufferLayers`: number of buffer (transition) layers between levels of refinement (as long as `maxRefinement` is larger than one).
- `nBufferLayersR`: the same as `nBufferLayers` but for the unrefinement direction.
- `correctFluxes`: correct the fluxes when dividing the cells, quite undocumented flag, default value is `(phi none)`.
- `dumpLevel`: save a field with the refinement level of each individual cell in every timestep.

One of the main concerns of the user side is on which variable should the refinement be based. In combustion, as it has already been described, the choice of flame front variable is not trivial and there is a discussion on which is the best value to define it. In experimental studies, quantities as the progress variable are not clearly defined, so the researchers use the mass fraction of certain species or temperature to define the flame front. After extrapolating these metrics to CFD calculations, some studies suggest the use of variables such as the mass fraction of species as CH_4 [84]. The heat flux has also been proposed as a good alternative to select the regions where refinement is required [132]. In Flame Surface Density combustion models, the value of Σ has also been successfully used as a refinement criterion [107]. However, in a formulation based on the flame front gradient with a single step irreversible reaction, individual species mass fractions are not available. There are formulations of heat release for progress variable models, as the ones of [104], [96], and [9], but they are always expressed in terms of $\tilde{b}$: either the gradient or a function as $\tilde{b}\left(1-\tilde{b}\right)$. Thus, the refinement for these models is usually based on an expression of $\tilde{b}$ [122] or the gradient of the progress variable [54]. To determine whether there is a better criterion, a cube of $80 \times 80 \times 80$ was run without AMR and then the same physical domain was run with the same properties using a $20 \times 20 \times 20$ baseline grid and AMR with five different criteria:

- $\tilde{b}$ (see Figure 3.9a) refined within $(0.20, 0.85)$.
- $\tilde{b}(1-\tilde{b})$ (see Figure 3.9b): although just a mapping of the previous one, it was used in previous studies for other software tools [117], refined for the values between $(0.20, 0.25)$.
- $\left\|\nabla\tilde{b}\right\| / \max\left(\left\|\nabla\tilde{b}\right\|\right)$ (see Figure 3.9c): normalized gradient of $\tilde{b}$ refined within $(0.20, 1.00)$.
- $\zeta = |\nabla|\widetilde{u}_i|| / \max_{\Omega_u}(|\nabla|\widetilde{u}_i||)$ (see Figure 3.9d): this metric [56], which is based on a normalized velocity gradient criterion, has been proposed to refine ahead of the flame and where Ω_u denotes the unburnt domain. It was refined in the range $(0.10, 10.0)$.
- $\zeta' = \zeta\tilde{b}(1-\tilde{b})$ (see Figure 3.9e): resulted from the combination of two metrics to obtain an improved behavior (as preliminary tests of the AMR with ζ show that it refines also in freestream and spurious regions). It was refined between $(0.02, 10.0)$.

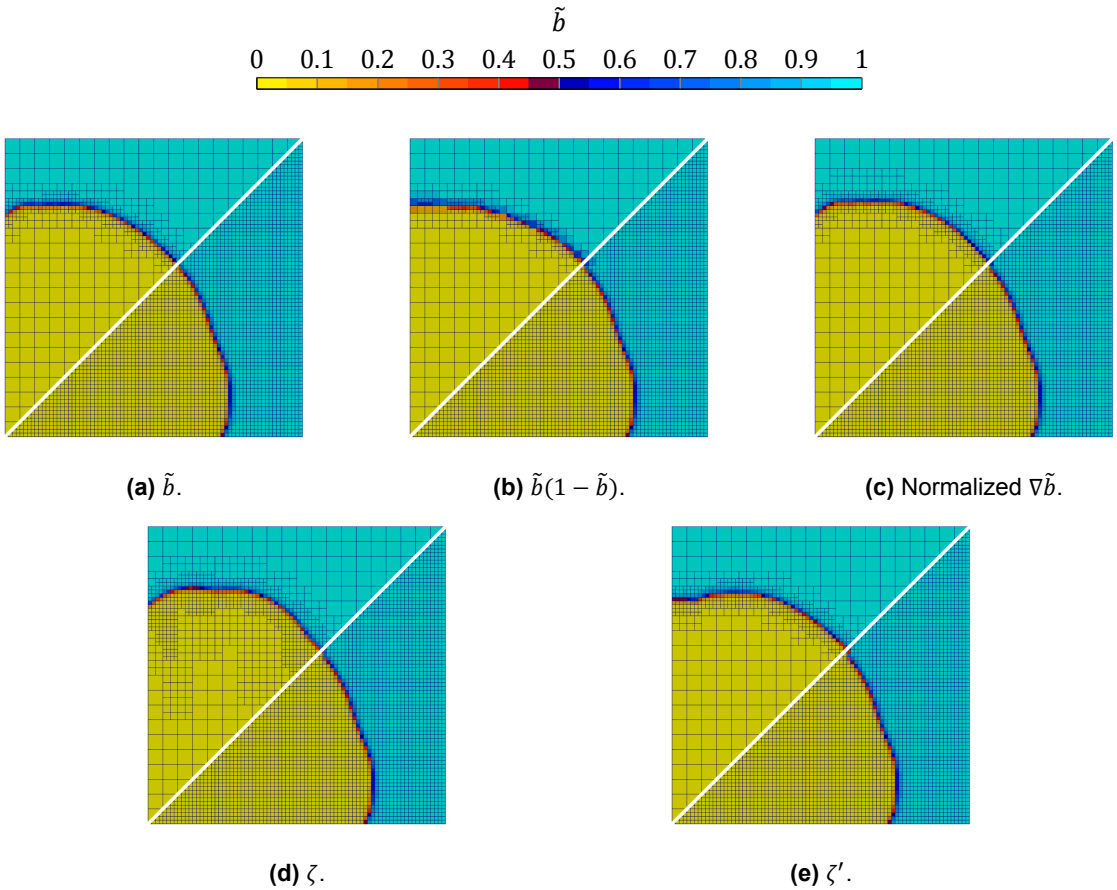

(a) $\tilde{b}$. **(b)** $\tilde{b}(1-\tilde{b})$. **(c)** Normalized $\nabla\tilde{b}$.

(d) ζ. **(e)** ζ'.

Figure 3.9: Resulting fields for different criteria of the AMR, the upper left triangle represents each AMR criterion applied over the coarse unrefined mesh and the lower right triangle is the most refined grid. Time-shifting has been applied so that both flame fronts match as close as possible.

The reference grid has a resolution of $80 \times 80 \times 80$, having that the AMR only refines to a level equal to that of the reference grid (two levels). Moreover, there is a temporal shift (see Figure 3.10) between the different methods that has been accounted for when plotting the radius. The shape of the flame front is similar in all of them and the subtle differences between them get compensated when computing the flame front location. By inspecting Figure 3.10, it can be seen that the flame development of all the AMR criteria follows the same slope (which is that of the reference grid). $\tilde{b}(1-\tilde{b})$ has a larger shift (although this doesn't affect the flame front turbulent velocity, which is the derivative of the flame position in time).

The different cases presented here only show a preliminary study about the different criteria but no insights have been gained in the optimal limit ranges of the AMR or the number of buffer layers. As the results, all the different AMR are similar and no significant outperforming criterion has been found. In particular, this thesis uses $\tilde{b}(1-\tilde{b})$ refined within $(0.20 \sim 0.25)$ to be consistent with previous studies [122]. Even if ζ and ζ' are supposed to perform better, their behavior is not robust. $\tilde{b}(1-\tilde{b})$ ensures that the flame front is refined symmetrically from $\tilde{b} = 0.5$.

3.5. Radiative heat transfer

As described in Section 2.2.3, radiative heat transfer is an important mechanism that plays a relevant role in combustion. Even if in some cases its effect can be neglected and not modeled, there are cases with slower flames and longer runtimes where the energy dissipated by radiation affects important metrics, such as the maximum pressure or pressure gradients. There are two parts to compute the

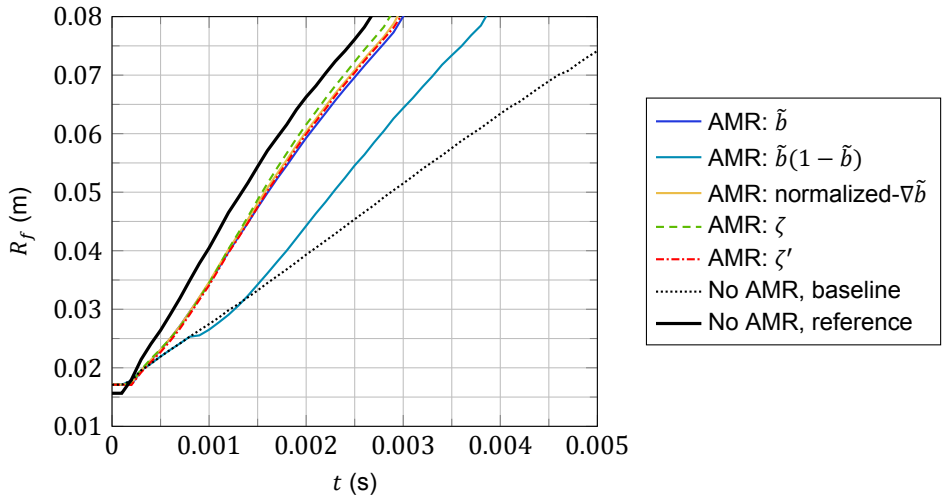

Figure 3.10: Flame radius evolution in time for different AMR refinement criteria.

radiative heat transfer: the transport equations and the calculation of the coefficients.

3.5.1. Available radiative heat transfer models in OpenFOAM

There are implementations of different models for the Radiative Transfer Equation:

- `fvDOM`: it is based on the Finite Volume Discrete Ordinates Method, which solves the RTE equation for n directions in participating media. It doesn't include scatter nor reflective walls.
- `opaqueSolid`: it doesn't add a source term to the energy equation but creates `absorptionEmissionModel` and `scatterModel`.
- `P1`: solves the transport equation for the radiation intensity, presenting good behavior in combustion problems.
- `solarLoad`: used to model the radiation caused by the solar radiation hitting a surface, considering reflective fluxes and diffusive sky radiative fluxes.
- `viewFactor`: uses the shape angles to compute which amount of a given surface is viewed from another, as the sum of all view factors must be conserved.

In past internal studies [122] the Finite Volume Discrete Ordinates Method was used with another simulation software. However, the implementation of the fvDOM in OpenFOAM struggles when dealing with axisymmetric wedges: as the code is inherently three-dimensional and all meshes have three dimensions, the number of vectorial directions for radiation is the same in all axis. This is is problematic with wedge meshes, where just one cell is present in the azimuthal direction. Thus, the `P1` model is the one used for the relevant cases of this thesis. The main advantages of the `P1` model over the `fvDOM` is that the radiation is solved with little computational overhead. However, the main limitation is that all surfaces are assumed to be diffuse and the accuracy depends on the optical thickness value.

The main equation of the model (see Equation 2.97) is solved accordingly to the original formulation, having only the fact that `gamma` includes `a0`$= 1 \times 10^{-18}$ to avoid a division by zero when there is no scattering and no absorptivity:

$$\nabla \cdot (\texttt{gamma}\, \nabla G) - aG = -4(e\sigma_S T^4) - E_c \qquad \text{where} \qquad \texttt{gamma} = \frac{1}{3a + \sigma_{\text{eff}} + \texttt{a0}}.$$

The source term used for the enthalpy equation is separated into different variables to achieve more numerical stability, although Equation 2.100 can be retrieved exactly:

$$\texttt{Sh()} = \texttt{Ru()} - 4\texttt{Rp()}\frac{T^3 h}{c_P} - T^3\texttt{Rp()} * \left(T - 4\frac{h}{c_P}\right) \xrightarrow{\text{where}} \begin{cases} \texttt{Rp()} & = 4\epsilon\sigma \\ \texttt{Ru()} & = aG - E_c \end{cases} .$$

One extra model has to be defined in OpenFOAM to compute the absorption-emission coefficients (the scatter and soot models have not been considered, having that $\sigma_{\text{eff}} = 0$). There are many absorption-emission models to choose, having for example the `binaryAbsorptionEmission`, the simplified `constantAbsorptionEmission`, the `greyMeanAbsorptionEmission` or some more detailed models as the `multiBandAbsorptionEmission`. These models give value to three coefficients based on different assumptions and flow quantities:

a	$\left(m^{-1}\right)$	Absorption (or absorptivity) coefficient
ϵ	$\left(m^{-1}\right)$	Emission (or emissivity) coefficient
E_c	$\left(W\,m^{-3}\right)$	Emission (or emissivity) contribution

The values for the absorptivity and emissivity coefficients of the domain boundaries are provided boundaries in `/constant/boundaryRadiationProperties`. The values for the metal walls of the experimental vessels used are $a_{\text{BC}} = 0.8\,\text{m}^{-1}$ and $\epsilon_{\text{BC}} = 0.001\,\text{m}^{-1}$. Kirchhoff's law of radiation [103] is usually invoked in the fluid flow, having thermodynamic equilibrium as it is emitting and absorbing thermal radiation so that:

$$\epsilon = a\,. \tag{3.9}$$

The advantage of using such an assumption is that only one of the two coefficients has to be computed, being the other one immediately obtained. The value of $E = 0$ W m^{-3}, because the combustion model cannot predict heat fluxes and the energy transport equation is written in terms of the total enthalpy. The model that was used for the thesis is the `greyMeanAbsorptionEmission` model, which is based on the Grey-Gas model, that combines the properties of each gas based on its partial pressure. It is a robust method with an acceptable accuracy.

3.5.2. Absorption and emission coefficient calculation

The default implementation of the `greyMeanAbsorptionEmission` model describes the total absorptibity (and with the use of Equation 3.9 also the emissivity) of a given cell based on the partial pressure of the N species present in the mixture as:

$$a = \sum_{i=0}^{N} a_{p,i}(T) \cdot p_i = \sum_{i=0}^{N} a_{p,i}(T) \cdot P \cdot X_i = \sum_{i=0}^{N} a_{p,i}(T) \cdot \frac{P \cdot Y_i}{W_i \cdot \sum_s \frac{Y_s}{W_s}}\,, \tag{3.10}$$

where i represents the index of each one of the domain species and p_i is the i-th gas partial pressure, which can be computed in terms of the total mixture pressure P and the mole fraction of the i-th gas X_i. The absorption coefficients for each mixture $a_{p,i}(T)$ are computed with a fifth-order (inverse) polynomial of temperature. The polynomial is defined in two intervals (thus requiring 12 coefficients): one polynomial goes from a low temperature bound (`Tlow`) to the matching point of both polynomials (`Tcommon`) and the other one from `Tcommon` to the upper temperature bound (`Thigh`). The polynomial is split at `Tcommon`, that is chosen to have accurate polynomial fits for both $T <$ `Tcommon` and `Tcommon` $> T$. Each one of these polynomial intervals is given as:

$$a_{p,i}(T) = \sum_{j=0}^{5} \frac{a_{p,i,j}}{T^j} = a_{p,i,0} + \frac{a_{p,i,1}}{T} + \frac{a_{p,i,2}}{T^2} + \frac{a_{p,i,3}}{T^3} + \frac{a_{p,i,4}}{T^4} + \frac{a_{p,i,5}}{T^5}\,. \tag{3.11}$$

Just for comparison, the total emissivity computed with the WSGGM model can be expressed as:

$$a = \sum_{i=0}^{N} a_{p,i}(T)\left[1 - e^{-a_{p,i}(T)\cdot PS_{lpl}}\right], \tag{3.12}$$

where k_i represents the gray gas emissivity of the i-th gas, P is the local pressure of the gas and S_{lpl} is the light path length [125]. The Grey Gas model is a more simplified and convenient approach as it doesn't require quantities like the light path length. However, it should be kept in mind that the Grey Gas model approach is usually less accurate than the WSGGM, especially when computing heat fluxes as it overpredicts the flux values [106].

The coefficients $a_{p,i,j}$ can be obtained by interpolating Hottel charts that can be found elsewhere (see [125] or [28]). However, tools as RADCAL [49] provide more accurate values for specific temperatures and mixture compositions, that can be fit with a fifth-order polynomial to be used in OpenFOAM (which is an advantage compared to Hottel charts, because only some chemical mixtures are shown in the charts). A verification of the calculation procedure to get the polynomial fit coefficients was performed. The results, in Figure 3.11a, show the coefficients provided in different tutorial cases of OpenFOAM (which indeed come from correlations provided by the Sandia National Laboratories) compared with the values of a_p provided by RADCAL. It can be seen that there is a clear agreement between the trend and the values. Thus, it can be stated that the pipeline of RADCAL with the different scripts for fitting is validated and it can be used with mixtures that appear in the experimental facilities considered (see Figure 3.11b, where the fit of the two polynomials is provided).

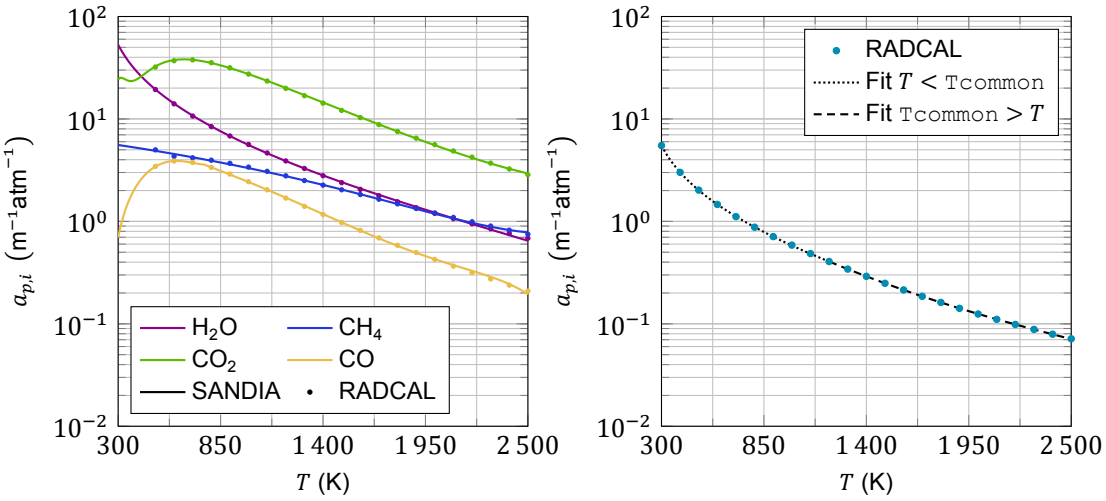

(a) Radiation coefficient pipeline validation with SANDIA polynomials.

(b) Radiation properties fit for a mixture of air and steam.

Figure 3.11: Calculation of the temperature-dependence of the radiation properties.

Nevertheless, the default implementation presents a problem when dealing with the regress variable mixture properties. The mixture described in OpenFOAM with the regress variable presents two states: the unburnt and the burnt one (having a linear function between them). Other properties (as thermodynamics or transport) are computed taking the mixture composition into account. However, for the radiation coefficients only one species is considered, so the equations don't depend on the mixture properties:

$$a = a_{p,\tilde{b}}(T) \cdot P\,, \tag{3.13}$$

where

$$a_{p,\tilde{b}}(T) = \sum_{j=0}^{5} \frac{a_{p,\tilde{b},j}}{T^j} = a_{p,\tilde{b},0} + \frac{a_{p,\tilde{b},1}}{T} + \frac{a_{p,\tilde{b},2}}{T^2} + \frac{a_{p,\tilde{b},3}}{T^3} + \frac{a_{p,\tilde{b},4}}{T^4} + \frac{a_{p,\tilde{b},5}}{T^5}\,.$$

By comparing Equation 3.10 and Equation 3.13 it can be seen that a relevant part of the information is lost, especially when considering the presence of steam, which is as a radiative heat absorber. Thus, a new library, named `bGreyMeanAbsorptionEmission`, was implemented to account for the mixture composition of both burnt and unburnt domains and also the flame brush, having:

$$a = \sum_{i=0}^{1} a_{p,i}(T) \cdot p_i = a_{p,b}(T) \cdot p_b + a_{p,u}(T) \cdot p_u = a_{p,b}(T) \cdot P \cdot X_b + a_{p,u}(T) \cdot P \cdot X_u \,, \tag{3.14}$$

where the b represents the burnt and u the unburnt. The absorption coefficients for the unburnt and burnt regions, $a_{p,u}(T)$ and $a_{p,b}(T)$, respectively, are computed with Equation 3.11, requiring now 12 polynomial coefficients for the unburnt mixture and another 12 coefficients for the burnt one. To verify the implementation of the species dependence, the same simple case was considered: one with the `greyMeanAbsorptionEmission` (see Figure 3.12a) and another with the `bGreyMeanAbsorptionEmission` (see Figure 3.12b). In both scenarios, the temperature dependence was artificially neglected by imposing $a_{p,i,j} = 0$ for all the i-th species and for all $j \geq 1$, so that $a_{p,i,j} = a_{p,i,0}$. In the `greyMeanAbsorptionEmission` case, the value $a_{p,\tilde{b},0} (= 2.1 m^{-1}\text{atm}^{-1})$ appears in all the domain while in the `bGreyMeanAbsorptionEmission`, there is a smooth transition between $a_{p,b,0} (= 2.1 m^{-1}\text{atm}^{-1})$ and $a_{p,u,0} (= 4.1 m^{-1}\text{atm}^{-1})$.

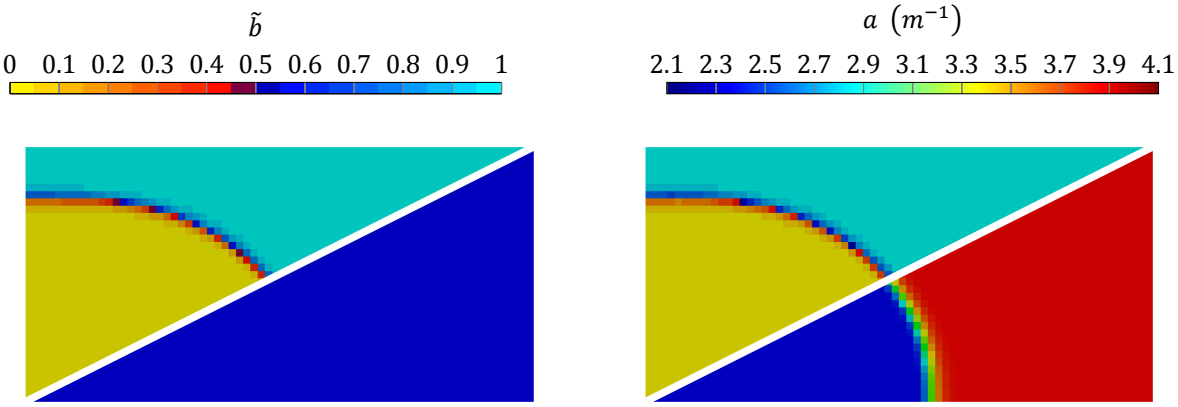

(a) `grayMeanAbsorptionEmission` model. **(b)** `bGrayMeanAbsorptionEmission` model.

Figure 3.12: Dependence between the absorption coefficient (lower right triangle of each image) and regress variable (upper left triangle of each image). No temperature coefficients are imposed for this case ($a_{p,i,j} = 0, \forall i \geq 0, j \geq 1$) to isolate the species-dependence.

3.6. Thermodynamics properties calculation

Another set of properties that has to be computed at runtime based on the mixture properties consists of the thermodynamic and transport properties. It can be seen that neither the enthalpy transport equation (see Equation 3.4), nor the unburnt enthalpy transport equation (see Equation 3.5) include a source term to account for the heat release of the combustion reaction. This is because OpenFOAM uses absolute enthalpy values that already include both the sensible enthalpy and the enthalpy of formation at a standard reference state. OpenFOAM starts the simulation with a temperature field and a regress variable field, from which the enthalpy values are computed based on a set of coefficients that depend spatially on both the regress variable and temperature (having an enthalpy jump across the flame front and higher absolute values in the burnt region). After the first iteration, the transport equation for enthalpy is solved for each timestep and the resulting enthalpy field is used to, inversely and with the use of the regress variable field, get the temperature field. There are four different enthalpy models that relate energy properties-regress variable-temperature:

- Constant heat coefficients: two models appear in this category: `hConst` (used when solving

transport equation for enthalpy, the specific heat capacity at constant pressure is held constant) and the `eConst` (used for the internal energy transport equation maintaining the specific heat capacity at constant volume fixed). For either model two values are required for each specie (products mixture and reactants mixture), namely the specific heat capacity at either constant pressure c_P or constant volume c_V and the heat of formation Δh_f. Given that enthalpy was considered for the energy equation in this thesis, only the `hConst` is further detailed. Even if the specific heat capacity at constant pressure is kept constant, the enthalpy still depends on the temperature as:

$$h = c_P T + \Delta h_f \longrightarrow T = \frac{h - \Delta h_f}{c_P}\,. \tag{3.15}$$

It can be seen that an inverse algorithm is not required to solve the temperature from the enthalpy. Thus, it was the method of choice for simple cases because it is considerably faster and more stable than the models that require inverse solutions. Two pairs $(c_P, \Delta h_f)$ define the model, one for the reactants and another for the products.

- Temperature-dependent heat coefficients: the other two models consider that the specific heat capacity at constant pressure depends on temperature , having the `janaf` model (which stand for Joint Army-Navy-NASA-Air Force) and the `hPolynomial` (where a polynomial of arbitrary order can be used to fit c_P to temperature values). The first one was used, as it is widely reported in the literature. As these methods include a temperature dependence on the c_P coefficients, an iterative Newton-Raphson method is used to determine the temperature from the enthalpy obtained from the transport equation. This requires the use of limiters of the values, which are usually defined to bound negative temperatures that may occur during the solution process of the inverse calculation. However, and given that in combustion the range of temperatures is known, the unburnt (initial) temperature is provided as lower bound and the burnt (adiabatic flame) temperature is used as the maximum value. The JANAF approach [19] is the one used in this thesis for the experimental facilities: it defines a set of 14 coefficients divided in two ranges of temperature similarly to the `greyMeanAbsorptionEmission` (having one range from `Tlow` to `Tcommon` and the other one from `Tcommon` to `Thigh`). However, as opposed to the default implementation of the absorption-emission coefficient calculation, there is also a dependence on the mixture components, requiring 14 coefficients for the products and another 14 for the reactants. The value of the enthalpy, specific heat capacity at constant pressure, and entropy can be computed at runtime with a fifth-order polynomial and using the mole fraction as:

$$\begin{aligned}
\frac{hM}{\mathcal{R}T} &= \sum_{i=0}^{N}\left(\left[\frac{Y_i}{M_i}\sum_s \frac{M_s}{Y_s}\right]\frac{H_i}{\mathcal{R}T}\right) \\
&= \sum_{i=0}^{N}\left(\left[\frac{Y_i}{M_i}\sum_s \frac{M_s}{Y_s}\right]\left[a'_{i,1} + \frac{a'_{i,2}}{2}T + \frac{a'_{i,3}}{3}T^2 + \frac{a'_{i,4}}{4}T^3 + \frac{a'_{i,5}}{5}T^4 + \frac{a'_{i,6}}{T}\right]\right), \qquad (3.16)\\
\frac{c_P M}{\mathcal{R}} &= \sum_{i=0}^{N}\left(\left[\frac{Y_i}{M_i}\sum_s \frac{M_s}{Y_s}\right]\left[a'_{i,1} + a'_{i,2}T + a'_{i,3}T^2 + a'_{i,4}T^3 + a'_{i,5}T^4\right]\right), \qquad (3.17)\\
\frac{sM}{\mathcal{R}} &= \sum_{i=0}^{N}\left(\left[\frac{Y_i}{M_i}\sum_s \frac{M_s}{Y_s}\right]\left[a'_{i,1}\log(T) + a'_{i,2}T + \frac{a'_{i,3}}{2}T^2 + \frac{a'_{i,4}}{3}T^3 + \frac{a'_{i,5}}{4}T^4 + a'_{i,7}\right]\right), \qquad (3.18)\\
& \qquad (3.19)
\end{aligned}$$

where N is the number of species (two in this case), R is the universal gas constant and M is the mixture mean mass.

The thermodynamic calculation has been combined with the `perfectGas` equation of state given by:

$$\rho = \frac{1}{RT}p = \frac{1}{\frac{\mathcal{R}}{M}T}p = \psi p\,,$$

where $\mathcal{R}$ is the universal gas constant and ψ is the compressibility factor that is used to relate pressure and density; and with the `homogeneousMixture` model, which describes a mixture state as:

$$\text{mixture} = \begin{cases} \text{products} & \text{if} \quad \tilde{b} < 0.001 \\ \tilde{b} \cdot \text{reactants} + (1 - \tilde{b}) \cdot \text{products} & \text{if} \quad 0.001 < \tilde{b} < 0.999 \\ \text{reactants} & \text{if} \quad 0.999 < \tilde{b} \end{cases}$$

The thermophysical model also require the calculation of the fluid transport coefficients. The transport models are mainly concerned with the calculation of the dynamic viscosity μ. Even if there are four models (namely `const` with a constant dynamic viscosity, `sutherland` which includes Sutherland's law, and `polynomial` and `logPolynomial` which include polynomial fits of arbitrary order), only the two relevant ones are presented:

- Constant dynamic viscosity (`const`): the dependence of the dynamic viscosity on temperature is neglected. Thus, this model is constructed based on just two values: the constant dynamic viscosity μ and the Prandtl number Pr (which is also assumed constant). From the Prandtl number definition, and based on the specific heat capacity at constant pressure obtained from one of the previous approaches, the thermal conductivity κ can be computed as:

$$\text{Pr} = \frac{c_P \mu}{\kappa} \longrightarrow \kappa = \frac{c_P \mu}{\text{Pr}}\,. \tag{3.20}$$

  Combining the constant dynamic viscosity model with constant heat coefficients (i.e. `hConst`) neglects the dependence of the thermal conductivity on temperature. The effective thermal diffusivity α_{eff} is used for the transport equation of the enthalpy and it is defined as the sum of laminar and turbulent thermal diffusivities:

$$\alpha_{\text{eff}} = \alpha_L + \alpha_t\,. \tag{3.21}$$

  The laminar (or molecular) thermal diffusivity α_L is defined as:

$$\alpha_L = \frac{\kappa}{\rho c_P} \tag{3.22}$$

- Sutherland's law (`sutherland`): when the dependence of temperature in the dynamic viscosity is considered, the most classical approach is Sutherland's law. It proposes a relation between μ and T based on a coefficient A_S computed at a reference temperature T_{ref} (requiring only these two coefficients to define the correlation for a specific mixture composition). These two coefficients can be obtained by performing a regression to values obtained from Cantera. Different authors express Sutherland's law in different forms, having that the one implemented in OpenFOAM is given as:

$$\mu = \frac{A_S \sqrt{T}}{1 + T_{\text{ref}}/T} = \frac{A_S T^{3/2}}{T + T_{\text{ref}}}\,. \tag{3.23}$$

  The calculation of the thermal conductivity is done based on the Eucken approximation, given as:

$$\kappa = \mu c_V \left(1.32 + 1.77 \frac{R}{c_V}\right). \tag{3.24}$$

  where R is the specific gas constant and the specific heat capacity at constant volume c_V can be computed as $c_V = c_P - R$. Finally, the laminar thermal diffusivity can be computed as done before (see Equation 3.22). From the laminar thermal diffusivity and the viscosity, the value of the Prandtl number can be retrieved.

The values used for each one of the cases can be seen in Appendix B. The turbulent thermal diffusivity has not been defined even if its contribution to the effective thermal diffusivity is considerably larger than the laminar thermal diffusivity ($\alpha_t >> \alpha_L$). The use of a laminar flow analogy is recurrent, so the turbulent Prandtl number $\mathrm{Pr}_t = \nu_t/\alpha_t$ is used to get α_t. If the turbulent Prandtl number is known (assuming commonly a value of $\mathrm{Pr}_t = 1$), and combined with the fact that ν_t is obtained from the turbulence model, the turbulent thermal diffusivity can be computed as:

$$\alpha_t = \frac{\nu_t}{\mathrm{Pr}_t}\,. \tag{3.25}$$

The use (and even the mere definition) of the turbulent Prandtl number can be easily debated [74]: the use of $\mathrm{Pr}_t = \mathrm{cst} = 1$ has been multiple times deemed as an erroneous approach, having that many correlations have been proposed both experimentally and phenomenological (for a comparison see [148] or [55]). However, it was used for this thesis at it is the approach usually followed for the used models [88]. Moreover, it was already discussed that if the Lewis number Le is known, the value of the mass diffusivity can also be retrieved to replace the coefficient of the diffusion terms in the combustion model. The density calculation available in OpenFOAM is prone to a better implementation for fully premixed combustion [145] but it wasn't modified for this thesis. In [145], the TFC and ETFC were implemented in `XiFOAM` but many of the problems here stated were avoided. For example, no enthalpy equation was solved as adiabatic conditions with known T_u and T_b were considered.

Any given mixture thermophysical properties can be simply defined based on Δh_f, c_P, M_i, μ, and Pr. These properties can be computed with tools like Cantera [45], which is an open-source tool for chemical kinetics (including thermodynamics and transport modeling). By specifying the initial mixture contents of air and hydrogen (either by mole or mass fractions), the GRI-Mech 3.0 mechanism [124] can be used to equilibrate the reaction and obtain the products. The equilibrium is achieved by keeping the enthalpy and pressure constant, as it is usually assumed that the pressure increment across a flame front is zero. However, when computing the properties for a closed vessel where the peak pressure is of interest, equilibrium should be achieved by keeping the specific volume constant (which also provides the adiabatic flame temperature to be used in the ignition patch as well as for the bounding of the inverse procedure to get the temperature from enthalpy).

Obtaining a fit for the Sutherland law to get A_S and T_{ref} is straightforward with the custom Cantera scripts. Using the Sutherland law should provide better results in the cases where there are diluent species in the reactants (and if they are inert, also in the products). If the reactants mixture also contains diluents, the coefficients for the calculation of the different thermodynamics and absoption-emission properties have to be updated (but no extra transport equation is required). By doing so, the implementation could be assessed against mixtures with diluents (as steam) that are common in the nuclear safety community. However, these cases are beyond the scope of this thesis.

Alternatively $a'_{i,1}, \ldots, a'_{i,7}$ can be used to describe the dependence of the thermodynamic properties on temperature. OpenFOAM includes a precompiled utility named `adiabaticFlameT` which computes the adiabatic flame temperature for a given fuel over a range of equivalence ratios. The output shows the coefficients $a'_{i,1}, \ldots, a'_{i,7}$ for the two temperature ranges and the two species (reactants denotes as `reactants` and products denoted as `products`, as the `burntProducts` represent the part of the products that has undergone combustion, e.g. extra oxidant is not included in the case of lean mixtures). Moreover, the adiabatic flame temperature can be used to validate the Cantera procedure described before. From these equivalence ratios, equally-spaced $\Delta\Phi = 0.01$, the closest value to the equivalence ratio of the study case can be selected. The `adiabaticFlameT` utility doesn't support diluents so another approach is proposed (although not carried out for this thesis). The mixture of Cantera can be set at different temperature values to get a list of $(T_i, c_{P,i}, h_i, s_i)$ that can be then interpolated to get the coefficients of a polynomial with the correct shape desired by OpenFOAM. The validation can be performed with the coefficients obtained from `adiabaticFlameT` for cases without diluent and then extrapolate the validated Cantera code to mixtures that include it.

3.7. Combustion models

The previous discussion presented in this chapter helps to construct a framework on which the combustion phenomena can be studied. The main topic of the thesis here presented is the modeling of turbulent flames with the so-called flame gradient methods. This section is divided into different subsections: first, the current implementation of `XiFoam` (application used as a baseline to develop the custom solve) is introduced; second, the models proposed in this thesis are detailed, showing the motivation before different design choices when compared to other classical models; and third, the changes performed in the solver as well as the implementations of new models are presented and described for Chapter 4.

3.7.1. Default combustion model implemented in OpenFOAM

The combustion modeling in `XiFoam` is based on the work of Weller [138], where a flame surface density model is presented. As already stated, the classification of combustion models is intricate given that many models have similar components. Some authors classify this model as a flame wrinkling model [134] while others consider it an improvement of the Eddy Break-Up model [113], but it has also been regarded as a flame gradient model, similar to the TFC model [105]. Regardless of the classification, one of the most notable differences between the formulation of this model and that of most combustion models is that `XiFoam` is built based on the regress variable $\tilde{b}$ instead of the progress variable $\tilde{c}$ to describe the state of the combustion. Although mainly an implementation choice, it is claimed that it also provides higher numerical stability in the flame propagation process [43]. The equation given in the original paper of the combustion model is:

$$\frac{\partial}{\partial t}\left(\overline{\rho}\tilde{b}\right)+\frac{\partial}{\partial x_i}\left(\overline{\rho}\widetilde{u}_i\tilde{b}\right)-\frac{\partial}{\partial x_i}\left(\overline{\rho}\left[\overline{D}+\frac{\nu_t}{Sc_t}\right]\frac{\partial\tilde{b}}{\partial x_i}\right)=-\left[\overline{\rho}\Xi+\left(\overline{\rho}_u-\overline{\rho}\right)\min\left(\Xi,\Xi_{\text{eq}}\right)\right]\widehat{S_L}\left|\frac{\partial\tilde{b}}{\partial x_i}\right|, \tag{3.26}$$

where Ξ is the flame wrinkling factor defined as the ratio between the flame wrinkled area over the flame normal projected area. This can be formally related to the flame area density with $\Sigma=\Xi\left|\nabla\overline{b}\right|$. Moreover, in the equilibrium case, the flame wrinkling factor is equal to the ratio of turbulent to laminar flame speed, having $\Xi_{\text{eq}}=S_t/S_{L,0}$ (which comes from Equation 2.49, assuming equilibrium case for all the implemented models). In order to simplify the implementation, the original model has been rewritten by taking that $\Xi<\Xi_{\text{eq}}$, as done in [139]:

$$\frac{\partial}{\partial t}\left(\overline{\rho}\tilde{b}\right)+\frac{\partial}{\partial x_i}\left(\overline{\rho}\widetilde{u}_i\tilde{b}\right)-\frac{\partial}{\partial x_i}\left(\overline{\rho}D_{\text{eff}}\frac{\partial\tilde{b}}{\partial x_i}\right)=-\overline{\rho}_u S_L\Xi\left|\frac{\partial\tilde{b}}{\partial x_i}\right|, \tag{3.27}$$

where the effective mass diffusivity D_{eff} has already been defined as $D_{\text{eff}}=D+D_t$ (where $D_{\text{eff}}\approx D_t$ as $D_t>>D$). The model is implemented in `XiFoam` as:

```
fvScalarMatrix bEqn
(
    fvm::ddt(rho, b)
    + mvConvection->fvmDiv(phi, b)
    + fvm::div(phiSt, b)
    - fvm::Sp(fvc::div(phiSt), b)
    - fvm::laplacian(turbulence->alphaEff(), b)
  ==
    fvOptions(rho, b)
);
```

Listing 3.1: `bEqn.H` snippet of the regress variable equation.

It can be seen that the combustion model equation is quite readable from the code listing itself. The term `fvOptions()` allows the user to include new source terms to the equation without the need to modify

and compile the original solver code. It should be noted that the mass diffusivity D_{eff} has been replaced in the diffusive term with the effective thermal diffusivity `alphaEff()`. Although the motivation to do so was mainly pragmatic to have an easier implementation and to require fewer parameters, it implies a value of $\text{Le}_{\text{eff}} = \alpha_{\text{eff}}/D_{\text{eff}} = 1$. Finally, the source term from Equation 3.27 has been reordered to make it fully implicit (as opposed to explicit with the $\tilde{b}$ within the module of the gradient). The source term has been implemented in the left-hand side of the equation with the constructor `fvm::Sp(rho,phi)`, which introduces the corresponding coefficients of `rho` in the matrix of the linear system (instead of including it on the right-hand side vector). By using differential operator properties and the fact that the flame unit vector $n_{f,i}$ normal vector points in the direction of the gradient so:

$$n_{f,i} = \frac{\partial\tilde{b}/\partial x_i}{\left|\partial\tilde{b}/\partial x_i\right|} \longrightarrow n_{f,i}\cdot n_{f,i}\left|\frac{\partial\tilde{b}}{\partial x_i}\right| = n_{f,i}\cdot\frac{\partial\tilde{b}}{\partial x_i} \longrightarrow \left|\frac{\partial\tilde{b}}{\partial x_i}\right| = n_{f,i}\frac{\partial\tilde{b}}{\partial x_i},$$

a fully implicit equation in $\tilde{b}$ can be constructed, achieving stable solutions even in large timesteps [43], by rewriting the source term as:

$$\overline{\rho}_u S_L \Xi \left|\frac{\partial\tilde{b}}{\partial x_i}\right| = \left(\overline{\rho}_u S_L \Xi\, n_{f,i}\right)\cdot\left(\frac{\partial\tilde{b}}{\partial x_i}\right) = \frac{\partial}{\partial x_i}\left(\overline{\rho}_u S_L \Xi\tilde{b}\, n_{f,i}\right) - \tilde{b}\frac{\partial}{\partial x_i}\left(\overline{\rho}_u S_L \Xi\, n_{f,i}\right). \tag{3.28}$$

The quantity referred to as `phiSt` through the code is the flux of turbulent flame speed normal to the cell faces, being defined as:

$$\texttt{phiSt} = \overline{\rho}_u S_{t,\text{corr}} S_L \Xi\left(S_{f,i}\cdot n_{f,i}\right) = \overline{\rho}_u S_{t,\text{corr}} S_L \Xi\, n_f, \tag{3.29}$$

where S_f represents the face normal vector and $S_{t,\text{corr}}$ is a correction factor for the ignition term already presented. The multiplication of the face normal with the flame front vector returns the flux, which is just summed over the cell faces internally by the solver. With this derivation, it can be seen how the regress variable equation is implemented in the solver.

Before discussing the other terms of the combustion model, the calculation of the flame normal vector is discussed. Although it may seem like a simple normalized gradient calculation, it is implemented with a correction to account for coarse flame front resolution. OpenFOAM stores the values in the cell centers, so the gradient can be computed in two different ways: either by taking the difference between cell centers and having the gradient directly defined in the face (having $\nabla\tilde{b}|_f$) or by interpolating the cell-center values in the faces (obtaining $\tilde{b}_f$), computing the gradient in the cell centers and then interpolating back into the faces. The correction term (shown between the parentheses) should be zero in an ideal case with no interpolation nor discretized-gradient calculation errors. The flame normal vector is expressed as follows (not showing a term that is included to avoid divisions by zero):

$$n_{f,i} = \frac{\dfrac{\partial\tilde{b}_f}{\partial x_i} + \dfrac{S_{f,i}}{|S_f|}\cdot\left(\left.\dfrac{\partial\tilde{b}}{\partial x_i}\right|_f - \dfrac{S_{f,i}}{|S_f|}\cdot\dfrac{\partial\tilde{b}_f}{\partial x_i}\right)}{\left\|\dfrac{\partial\tilde{b}_f}{\partial x_i} + \dfrac{S_{f,i}}{|S_f|}\cdot\left(\left.\dfrac{\partial\tilde{b}}{\partial x_i}\right|_f - \dfrac{S_{f,i}}{|S_f|}\cdot\dfrac{\partial\tilde{b}_f}{\partial x_i}\right)\right\|}. \tag{3.30}$$

The first term of Equation 3.28 that has to be modeled is the laminar flame speed S_L which in the code is denoted as `Su`. Before describing how this value is computed, the calculation of $S_{L,0}$ (or `Su0`) is presented. The unstrained laminar flame speed is computed by calling the `unstrainedLaminarFlameSpeed()()` library. It can be either kept constant from the initial conditions (specified with the flag `laminarFlameSpeedCorrelation constant` in the combustion dictionary) or obtained through a correlation. There are two implemented correlations, given by:

- Gulder [51]: the unstrained laminar flame speed is given by:

$$S_{L,0} = S_{L,0}^{\text{ref}}(\Phi)\left(\frac{T_u}{T_{\text{ref}}}\right)^{d_1}\left(\frac{p_u}{p_{\text{ref}}}\right)^{d_2}(1 - Y_{\text{res}}d_3)$$
$$= \left[d_4 \cdot \Phi^{d_5} - e^{-d_6(\Phi-1.075)^2}\right]\left(\frac{T_u}{T_{\text{ref}}}\right)^{d_1}\left(\frac{p_u}{p_{\text{ref}}}\right)^{d_2}(1 - Y_{\text{res}}d_3)\,, \quad (3.31)$$

  where the coefficients d_i are tabulated for different fuels. The value of Y_{res} is the mass fraction of diluents.

- Ravi-Petersen [118]: originally determined for hydrogen, it is given as:

$$S_{L,0} = \left[d_7 + d_8\Phi + d_9\Phi^2 + d_{10}\Phi^3 + d_{11}\Phi^4\right]\left(\frac{T_u}{T_{\text{ref}}}\right)^{\left(d_{12}+d_{13}\Phi+d_{14}\Phi^2+d_{15}\Phi^3\right)}\,. \quad (3.32)$$

  Similarly, d_i are the different experimentally-determined parameters that are required for each different fuel.

Moreover, there are correlations specially designed for hydrogen combustion and nuclear safety [13] that have been used for consistency with previous studies. These correlations require correction terms to account for the unburnt temperature and pressure, which increases in a closed vessel. It was already shown that the unburnt temperature correction can be coupled with the pressure correction term. Once the value of the unstrained laminar flame speed $S_{L,0}$ is computed, the value of the strained laminar flame speed S_L should be obtained. There are three default implemented models to do so:

- Unstrained (`SuModel unstrained`): simply make both unstrained and laminar flame speeds the same:

$$S_L = S_{L,0}\,. \quad (3.33)$$

- Equilibrium (`SuModel equilibrium`): strain effects are accounted for with the calculation of σ_{rs} and an user-defined value of the maximum strain rate σ_{ext}, ideally leading to (almost) local extinction:

$$S_L = S_L^{\infty} = S_{L,0}\max\left(1 - \frac{\sigma_{rs}}{\sigma_{\text{ext}}}, 0.01\right), \quad (3.34)$$

  where the resolved strain σ_{rs} is computed as:

$$\sigma_{rs} = \left[n_i n_i \frac{\partial u_j}{\partial x_j} - n_i \frac{\partial u_j}{\partial x_i} n_j\right]\frac{1}{\Xi} + \left[n_i n_i \frac{\partial S_L n_j}{\partial x_j} - n_i \frac{\partial S_L n_j}{\partial x_i} n_j\right]\frac{(\Xi+1)}{2\Xi}\,, \quad (3.35)$$

  by using the uncorrected flame normal vector defied with:

$$\vec{n} = \frac{\nabla\tilde{b}}{\left\|\nabla\tilde{b}\right\|}\,. \quad (3.36)$$

  The equilibrium approach can be related to laminar flame theory (see Equation 2.42), assuming that the laminar flame speed is in local equilibrium with a linear response of the local components of the resolved strain σ_{rs} (which may not be properly resolved in a coarse RANS simulation). The extinction σ_{ext} should be provided by the user.

- Transport (`SuModel transport`): a transport equation for S_L can be constructed with heuristic arguments (based on the time scale of strain and the strain-rate value at extinction, the full derivation can be found in [138] and in [139]), having the following transport equation:

$$\frac{\partial}{\partial t}(\rho S_L) + \frac{\partial}{\partial x_i}\left(\left(\rho u_i + \phi_\Xi\right) S_L\right) - S_L\frac{\partial}{\partial x_i}(\phi_\Xi) = -S_L\left(-\rho\mathcal{R}_c\frac{S_{L,0}}{S_L}\right) - S_L\left(\rho\left(\sigma_s + \mathcal{R}_c\right)\right)\,, \quad (3.37)$$

where the flux ϕ_Ξ definition is given by:

$$\phi_\Xi = \overline{\rho}_u S_{t,\text{corr}} S_L \Xi \left(S_{f,i} \cdot n_{f,i}\right) - \left[\frac{1}{\left|\partial \tilde{b}/\partial x_i\right|} \cdot \frac{\partial}{\partial x_i}\left(\alpha_{\text{eff}} \frac{\partial b}{\partial x_i}\right)\right]\left(S_{f,i} \cdot n_{f,i}\right) + \rho\left[S_L\left(\frac{1}{\Xi} - \Xi\right)\right]\left(S_{f,i} \cdot n_{f,i}\right), \tag{3.38}$$

and the coefficient $\mathcal{R}_c$ is computed as:

$$\mathcal{R}_c = \frac{\sigma_s S_L^\infty \left(S_{L,0} - S_L^\infty\right) + \left(0.01\mu_{S_L}\right)^2 \sigma_{\text{ext}}}{\left(S_{L,0} - S_L^\infty\right)^2 + \left(0.01\mu_{S_L}\right)^2}, \tag{3.39}$$

where μ_{S_L} is the mean of the laminar flame speed values from the previous iteration and it is used mainly for numerical reasons (to avoid zero divisions). Solving a transport equation requires initial and boundary conditions and, although it is expected to be more precise for strain-sensitive cases, it entails longer computational runs. Preliminary results shown no differences in the results but required longer computational runs.

The second parameter is the area wrinkling factor, denoted as Ξ. Again, there are different flame wrinkling models, having:

- Fixed (`XiModel fixed`): the value of Ξ from the initial conditions is kept constant during the simulation. It is useful for debugging and simulating laminar flames with S_L (achieved by using $\Xi = 1$).
- Algebraic (`XiModel algebraic`): based on a correlation (see Eq 10 in [52]) that has shown good agreement with both experimental and spectral results. The wrinkling factor is obtained as:

$$\Xi = 1 + \left(1 + 2\Xi_{sc}\left(0.5 - b\right)\right)\Xi_c\left(\sqrt{\frac{u'}{S_L + 0.01\mu_{S_L}}}\right)\text{Re}_\eta, \tag{3.40}$$

  where Re_η is the Kolmogorov scale Reynolds number (which is computed with the turbulence properties as $\text{Re}_\eta = u'/\sqrt{\varepsilon\tau_\eta}$), $\Xi_c = 0.62$ is the wrinkling factor coefficient and $\Xi_{sc} = 1$ is the winkling factor shape coefficient.
- Transport (`XiModel transport`): the flame wrinkling factor can also be obtained through a transport equation [138], having:

$$\frac{\partial}{\partial t}\left(\rho\Xi\right) + \frac{\partial}{\partial x_i}\left(\left(\rho u_i + \phi_\Xi\right) S_L\right) - \Xi\frac{\partial}{\partial x_i}\left(\phi_\Xi\right) = \rho\mathcal{R}' - \Xi\rho\left(\mathcal{R}' - \mathcal{G}'\right) - \Xi\rho\max\left(\sigma_t - \sigma_s, 0\right), \tag{3.41}$$

  where the model coefficients are given as [56]:

$$\mathcal{G}^* = \frac{0.28}{\tau_\eta}, \qquad \mathcal{R}' = \frac{\mathcal{G}^*\Xi_{\text{eq}}^*}{\Xi_{\text{eq}}^* - 1}, \qquad \mathcal{G}' = \frac{\mathcal{R}'\left(\Xi_{\text{eq}} - 1.001\right)}{\Xi_{\text{eq}}},$$

  where τ_η is the Kolmogorov timescale (defined in Subsection 2.1.2) and different equilibrium flame wrinkling factors are defined as:

$$\Xi_{\text{eq}}^* = 1.001 + \Xi_c\left(\sqrt{\frac{u'}{S_L + 0.01\mu_{S_L}}}\right)\text{Re}_\eta,$$

$$\Xi_{\text{eq}} = 1.001 + \left(1 + 2\Xi_{sc}\left(0.5 - \min\left[\max\left(b, 0\right), 1\right]\right)\right)\left(\Xi_{\text{eq}}^* - 1.001\right),$$

  Apart from the expected increase on accuracy, the main difference between the transport equation for Ξ and the algebraic correlation is that, even if both are based on Gulder's turbulent flame speed model, the transport equation includes strain effects. It is documented throughout the code that more work has to be done to also account for the enhanced removal rate caused by the flame compression.

Both the transport and the algebraic correlations for Ξ have been used in this work (having them denoted as *XiFoamT* and *XiFoamA*).

3.7.2. GTFC: parameter study analysis and wall bounding

One of the main objectives of this thesis was to test the recently-obtained experimental correlation for lean hydrogen flames (which is especially relevant for nuclear safety management). Two correlations were provided from the experiments (see Equations 115 and 116 of [46]) for the ratio of the turbulent flame velocity, V_T, with the unstrained laminar flame velocity, $V_{L,0}$, (see Equation 3.42) and the turbulent flame velocity, V_T, with the strained smooth velocity, V_S (see Equation 3.43):

$$\frac{V_T}{V_{L,0}} = \frac{S_t^{GTFC}}{S_{L,0}} = (1.613 \pm 0.010) \cdot \left(\frac{R_f}{l_T}\right)^{0.333\pm0.002} \cdot \left(\frac{u'}{S_{L,0}}\right)^{0.526\pm0.002} \cdot (\mathrm{Le})^{-0.140\pm0.005}, \tag{3.42}$$

$$\frac{V_T}{V_S} = (1.696 \pm 0.007) \cdot \left(\frac{R_f}{l_T}\right)^{0.393\pm0.020} \cdot \left(\frac{u'}{S_{L,0}}\right)^{0.530\pm0.002}. \tag{3.43}$$

These correlations were obtained from experiments at different hydrogen concentrations and turbulence intensities, also including multiple runs for each configuration to account for scattering of the results. The coefficient of determination R^2 is around 0.90 for both correlations. It can be seen that one of the main differences between the two correlations is the presence of the Lewis number in Equation 3.42. The coefficients are similar between both correlations. In fact, Equation 3.42 was also fit without including the Lewis number dependence, having also similar coefficients [46]. However, the correlation with the Lewis number dependence was preferred as it provided a slightly better R^2 value. In order to use Equation 3.43, a relationship between V_S and $V_{L,0}$ is required. To do so, Equation 2.45, Equation 2.50 and Equation 2.48 (rewritten for the R_f of a smooth flame and V_S instead of V_T) are combined, obtaining the *smoothing factor*, SF, defined as:

$$SF = \frac{V_S}{V_{L,0}} = \frac{1}{1 + \frac{2\mathcal{L}}{R_f}}. \tag{3.44}$$

V_S can also be expressed with the Amplification Factor AF (whose definition can be found in [48]) in terms of the laminar flame velocity V_L. Equation 3.44 can be exactly retrieved from Equation 4 in [48], although it is not called smoothing factor. With the use of Equation 3.44, the correlation presented in Equation 3.43 can be rewritten to obtain:

$$\frac{S_t^{\mathrm{GTFCp}}}{S_{L,0}} = \frac{V_T}{V_{L,0}} = \frac{V_T}{V_S}\frac{V_S}{V_{L,0}} = (1.696 \pm 0.007) \cdot \left(\frac{R_f}{l_T}\right)^{0.393\pm0.020} \cdot \left(\frac{u'}{S_{L,0}}\right)^{0.530\pm0.002} \left(1 + \frac{2\mathcal{L}}{R_f}\right)^{-1}. \tag{3.45}$$

Both Equation 3.42 and 3.45 approximate the experimental values of the spherical vessel, but its behavior in larger vessels had not been tested. The double presence of the flame radius R_f in Equation 3.45 can make that the correlation overpredicts the turbulent flame speed for large flame radius values. Thus, it is expected that Equation 3.42 provides more consistent results.

To fully understand the differences between Equation 3.42 and classical premixed combustion models, the TFC is used as a reference (given that it is one of the most common models for flame gradient models). It was previously introduced in Equation 2.89, but it is also rewritten in Equation 3.46 in terms of the wrinkling velocity ratio for convenience:

$$\frac{S_t^{\mathrm{TFC}}}{S_{L,0}} = \frac{Au'\mathrm{Da}^{1/4}}{S_{L,0}} = \frac{Au'}{S_{L,0}}\left(\frac{l_t}{u'\tau_c}\right)^{1/4}, \tag{3.46}$$

where the coefficient $A = 0.40$ as previous studies [117].

The first difference that can be seen between both correlations (Equation 3.42 and Equation 3.46) is that the former includes a dependence on the flame radius whereas the latter doesn't. Time dependence is something that models, as the ETFC model (cf. Equations 2.89 and 2.93), include in order to improve the TFC model. The TFC was derived for fully-developed turbulent flame speeds. The temporal component ETFC model (Equation 2.93) asymptotically approaches 1 (having that the $S_t^{\text{ETFC}} \rightarrow S_t^{TFC}$ when $t \rightarrow \infty$). However, in the GTFC model (Equation 3.42), the temporal evolution implicitly stated in terms of the flame radius is unbounded. This yields that $S_t^{\text{GTFC}} \rightarrow \infty$ when $R_f \rightarrow \infty$. Nevertheless, the dependence of the flame speed ratio on the flame radius follows a power of 0.333, so the asymptotic trend is slow: for $R_f = 2$ m the contribution of $R_f^{0.333} = 1.2596$, for $R_f = 4$ m it is of $R_f^{0.333} = 1.5866$ and for $R_f = 8$ m just $R_f^{0.333} = 1.9986$. Criticism may arise for the use of the correlation outside the experimental bounds, as it was developed for a vessel of $0.563\ m$ of diameter and it will be used in vessels up to $9\ m$. However, correlations as the TFC model, are obtained from vessels of reduced size for general mixtures, with hopes of providing the turbulent flame speed for any given fuel at any given equivalence ratio. Meanwhile, the correlation of Equation 3.42 has been developed specifically for lean hydrogen mixtures with the nuclear safety scenarios in mind.

In really large vessels (check for example the containment AP1000 in [95], with a height of 66 m and 40 m in diameter), choosing an asymptotic value for the correlation at large flame radius seems more appropiate than leaving it unbounded (even if for $R_f = 60$ m, the flame radius contribution is $R_f^{0.333} < 4.0$). A bounding based on the flame radius at which Equation 3.42 equals Equation 3.46 was considered, switching from the GTFC correlation to the TFC correlation once the R_f was too large. Even if it seems like a feasible good option in theory, it present problems in practice. The turbulence properties (as it will be discussed later) give different trends for each model. This makes that the critical radius where Equation 3.42 should be bounded to match Equation 3.46 is too small to even use the approach, as the vast majority of the time the velocity ratio was bounded to match the TFC.

One limitation of both correlations (when compared with the default models implemented in `XiFoam`) is that the turbulent flame speed may not always be larger than the laminar flame speed: both Equation 3.42 and Equation 3.46 return values that can be below one (meaning that the laminar flame speed is larger than the turbulent flame speed). To further support this claim, the Borghi diagram presented in Figure 2.8 has been updated with new information (see Figure 3.13). The line denoted as $\Xi^{\text{TFC}} = 1$ has been obtained by manipulating Equation 3.46 to express it in the variables of the Borghi diagram as:

$$\frac{S_t^{\text{TFC}}}{S_{L,0}} = \frac{Au'}{S_{L,0}} \left(\frac{l_t}{u'\tau_c} \right)^{1/4} \xrightarrow[\tau_c = \delta / S_{L,0}]{} \Xi^{\text{TFC}} = \frac{S_t^{\text{TFC}}}{S_{L,0}} = A \left(\frac{u'}{S_{L,0}} \right)^{3/4} \left(\frac{l_T}{\delta} \right)^{1/4} . \tag{3.47}$$

This line ($\Xi^{\text{TFC}} = 1$) separates two domains: where $\Xi^{\text{TFC}} < 1$ (red shaded area) and where $\Xi^{\text{TFC}} > 1$ (elsewhere). The red shaded area implies that $S_{L,0} > S_t^{\text{TFC}}$, which is a nonphysical behavior that should be corrected in the computational formulation of the model. The discussion of this topic is further detailed in Subsection 4.1.2, where numerical proofs of this behavior are presented. Expressing Equation 3.42 in terms of the variables of the Borghi diagram is non-trivial, as there is no dependence on the flame thickness and there is a dependence on the flame radius. Nevertheless, the experimental data from [47] (on which Equation 3.42 is constructed) has been included. Moreover, a blue-shaded area represents the region where the hydrogen flames that appear in the nuclear safety scenarios are located within the Borghi diagram (as depicted in [46]). The good match between the blue region and the experimental data confirms that the experiments cover the region of interest. However, Equation 3.42 still provides turbulent flame speeds smaller than the laminar flame speed in some scenarios. In fact, as Equation 3.42 depends on the flame radius, the value of the correlation tend to zero when $R_f \rightarrow 0$ m. Moreover, there are cases where, even if $R_f >> 0$ m, the turbulence, and mixture properties can make that the correlation predicts values $S_t^{\text{GTFC}} < S_{L,0}$. This only happens for the correlation, as the experimental data for that same case gives indeed $V_T > V_L^0$. These results are presented in Subsection 4.2.4 with more detail.

Another interesting aspect of Equation 3.42 when compared to the behavior of Equation 3.46 (which is

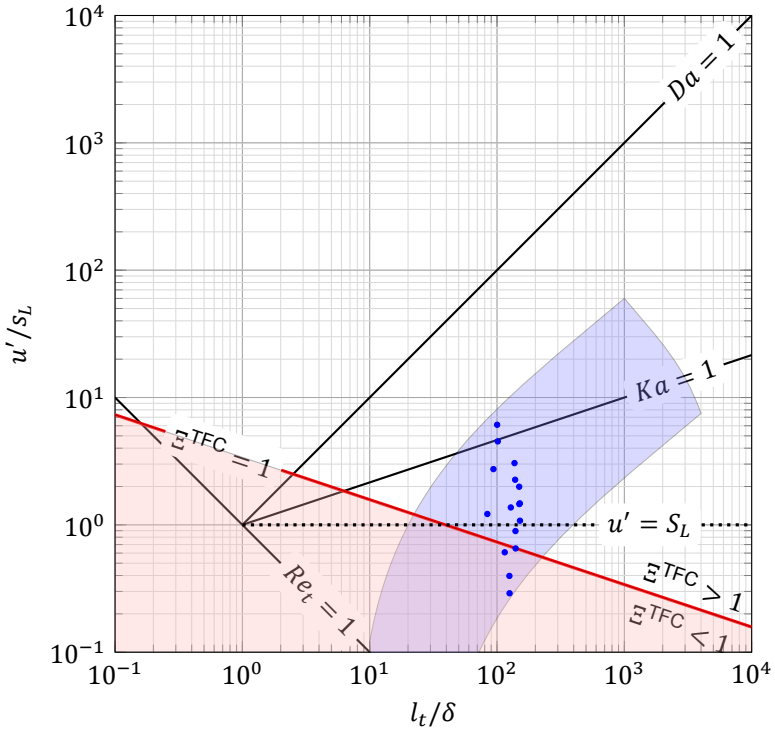

Figure 3.13: Borghi diagram with the TFC turbulent flame speed correlation — (Equation 3.46) and the experimental data, • , from [47] used to determine Equation 3.42, which lays within the region ■ where nuclear accidents happen.

designed for combustion modeling) is the dependence on turbulence. Both equations can be written in terms of the turbulence properties k and ε (together with other variables), obtaining:

$$\frac{S_t^{\text{TFC}}}{S_{L,0}} = \frac{A\left(\sqrt{2k/3}\right)}{S_{L,0}} \left(\frac{\left(0.2014k^{3/2}/\varepsilon\right)}{\left(\sqrt{2k/3}\right)} \cdot \frac{S_{L,0}^2}{\alpha_u} \right)^{1/4}, \tag{3.48}$$

$$\frac{S_t^{\text{GTFC}}}{S_{L,0}} = 1.613 \left(\frac{R_f}{\left(0.2014k^{3/2}/\varepsilon\right)} \right)^{0.333} \left(\frac{\left(\sqrt{2k/3}\right)}{S_{L,0}} \right)^{0.526} (\text{Le})^{-0.140}. \tag{3.49}$$

The coefficient 0.2014 is used based on [30] and on [116] to obtain the local value of the integral length scale, l_t, based on the local turbulence properties of k and ε. To analyze the behavior of these correlations for different combinations of k and ε, some common values are used for the non-turbulence related variables (using $R_f = 0.1\ m$, Le $= 1.0$, $S_{L,0} = 0.1\ m/s$ and $\alpha_u = 1 \times 10^{-5}\ m^2/s$). The sensitivity of the correlations to these parameters is presented at the end of the subsection. In Figure 3.14, the value of the flame speed ratio is plotted in the range $1 < S_t/S_{L,0} < 20$ to show the direction on which the turbulent flame speed increases and how do k and ε globally affect the correlation.

Firstly, it can be seen on Figure 3.14 that the growth direction of $S_t/S_{L,0}$ for each correlation is different. The turbulent flame speed value of the TFC model (Figure 3.14a) increases for higher values of k and decreases it for higher values of ε. The turbulent flame speed of the GTFC model (Figure 3.14b) decreases for higher values of k and increases for higher ε. The fact that $S_t^{\text{GTFC}}/S_{L,0}$ decreases for higher k is contradictory with some theoretical derivations (as Figure 2.6). However, the non-turbulent properties remain fixed in Figure 3.14, which is something that doesn't occur on a real CFD simulation (e.g., increasing k occurs for larger flame radius). Secondly, the slopes of the isolines are also different,

having $S_t^{\text{TFC}}/S_{L,0} \propto k^{3/4}\varepsilon^{-1/4}$ and $S_t^{\text{GTFC}}/S_{L,0} \propto k^{-0.237}\varepsilon^{1/3}$. The region covered within $1 < S_t/S_{L,0} < 20$ is larger in the GTFC model, providing a more robust behavior for low turbulence conditions. The range of possible (k, ε) that lay in the range $1 < S_t/S_{L,0} < 20$ is therefore larger in the GTFC than in the TFC.

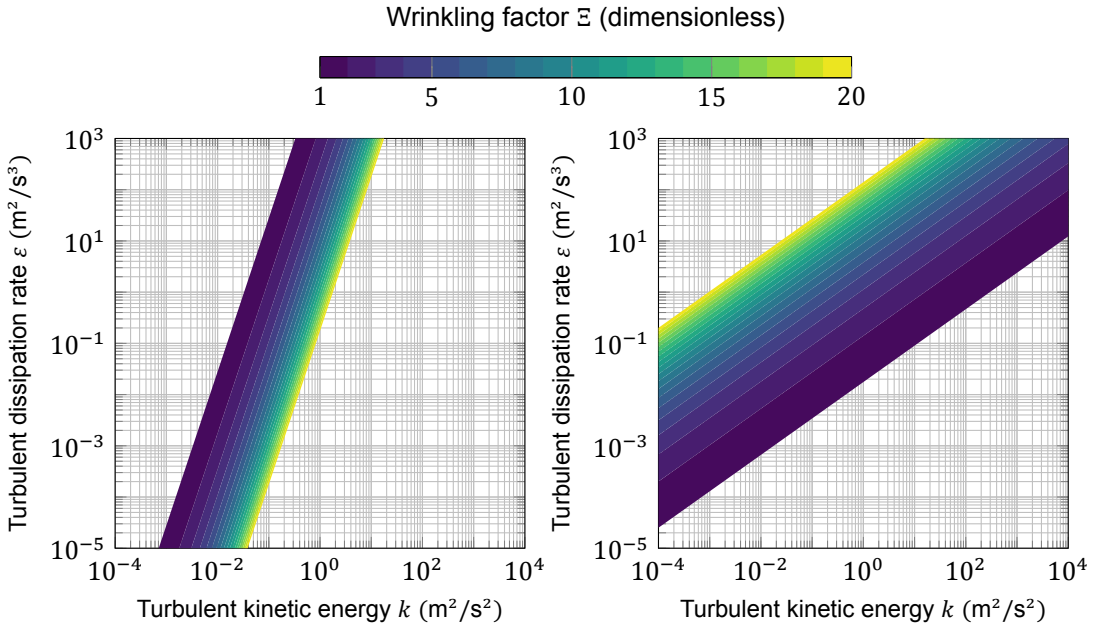

(a) TFC model (see Equation 3.48). **(b)** GTFC model (see Equation 3.49).

Figure 3.14: Flame speed ratio dependence on turbulence properties (k, turbulent kinetic energy and ε, turbulent kinetic energy dissipation) for the TFC and the GTFC correlations.

Two consequences arise from the different dependence on turbulence. First, the TFC provides values within $1 < S_t^{\text{TFC}}/S_{L,0} < 20$ for a smaller region in the turbulence map of (k, ε) when compared to the GTFC. Thus, the GTFC model is less sensitive to initial conditions related to low turbulence. As it was observed when running numerical simulations, the GTFC provides higher S_t values than the TFC model for lean hydrogen mixtures in quiescent initial turbulent conditions, as supported by the experiments on which the model is based. Second, and as it will be described at the end of this subsection, the values of $S_t^{\text{GTFC}}/S_{L,0}$ are large near the wall due to its dependence on the turbulence properties. Thus, unrealistically large flame front speeds appear at the wall, requiring special treatment to bound the model close to walls.

To generate Figure 3.14, the non-turbulence related parameters were fixed based on common lean hydrogen mixture values. However, the dependence of the correlations on these properties should also be considered. For the TFC correlation, the unburnt thermal diffusivity α_u and the unstrained laminar flame speed $S_{L,0}$ were fixed to 1×10^{-5} m^2/s and 0.1 m/s, respectively. In Figure 3.15a the isoline of $S_t^{\text{TFC}}/S_{L,0} = 1$ is plotted for different α_u values (separated two orders of magnitude between each). In Figure 3.15b three isolines represent the effect of $S_{L,0}$. It can be seen that the larger α_u and $S_{L,0}$, the larger the k and the lower the ε are to obtain $S_t^{\text{TFC}}/S_{L,0} = 1$. The effect of the unstrained laminar flame speed is larger than that of the unburnt thermal diffusivity.

The same procedure was followed for the GTFC model, having three non-turbulence related parameters: flame radius R_f (which had a value of 0.1 m before, see Figure 3.15c), unstrained laminar flame speed $S_{L,0}$ (having 0.1 m/s previously, see Figure 3.15d), and Lewis number Le (which took a value of 1.0, see Figure 3.15e). The effect of the Lewis number is more contained than that of the other two variables, being consistent with the variability range caused by the α_u in the TFC and the previous discussion to support the low value of the Lewis number exponent. The growth direction of the unstrained laminar flame speed $S_{L,0}$ is opposed in the TFC and GTFC (cf. Figure 3.15b and Figure 3.15d, respectively). The GTFC presents an interesting coupling that may improve the behavior of flames

propagating within closed vessels: the larger the flame radius, the *lower* the isoline $S_t^{\text{GTFC}}/S_{L,0} = 1$ is, whereas the larger the unstrained laminar flame speed, the higher the isoline is. When the flame propagates in a closed vessel, the flame front expands and causes a flow compression and an increase in pressure. The pressure increase is usually accounted for with a correction term on the laminar flame speed, with higher laminar flame speeds at higher pressures.

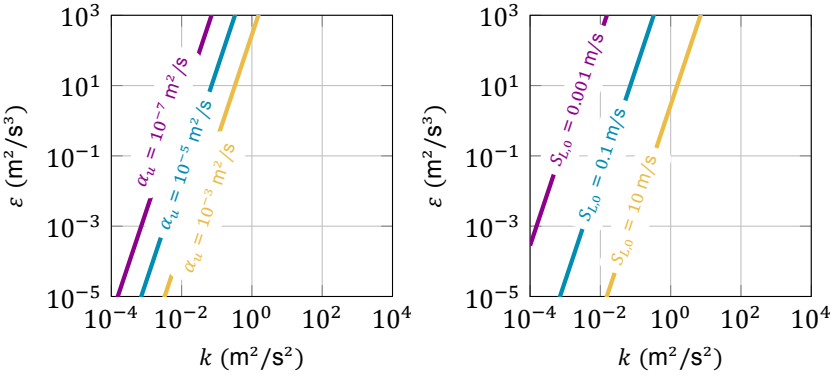

(a) TFC correlation (Eq. 3.48); unburnt thermal diffusivity α_u.

(b) TFC correlation (Eq. 3.48); laminar flame speed $S_{L,0}$.

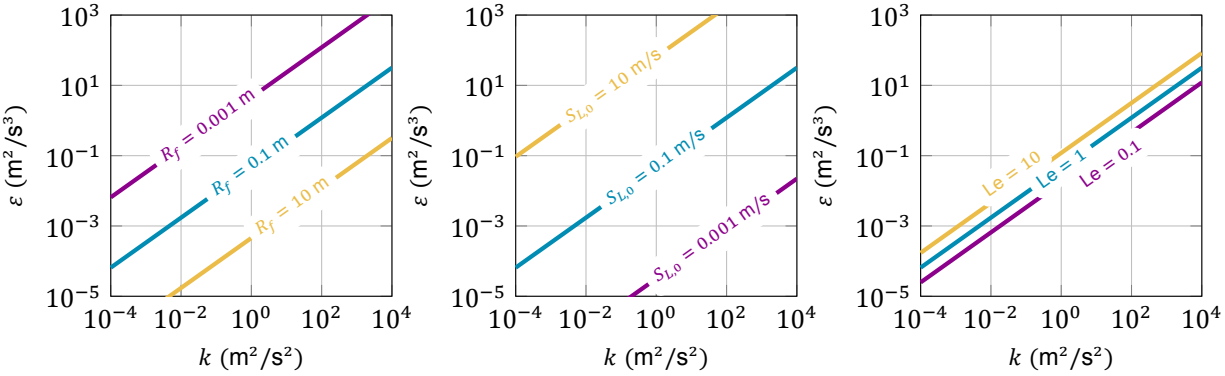

(c) GTFC correlation (Eq. 3.49); flame radius R_f.

(d) GTFC correlation (Eq. 3.49); laminar flame speed $S_{L,0}$.

(e) GTFC correlation (Eq. 3.49); Lewis number Le.

Figure 3.15: TFC and GTFC flame speed ratio sensitivity for the non-turbulence based quantities, showing the isoline of $S_t/S_{L,0} = 1$ for different values of these properties.

As briefly introduced before, it was observed that the GTFC predicts larger values of the flame speed ratio near the wall. In RANS turbulence the treatment of the wall is done with crude models whose accuracy is questionable. Even if the wall is a source term of turbulence, the flame should undergo some quenching at the wall (or at least not expand faster). However, the GTFC predicts faster flame front propigation near walls. To avoid that, the GTFC model has been bounded near the walls to correct for an unrealistic increase in turbulence speed predicted by the definition of model. To make Equation 3.42 as general as possible, a blending function similar to the one used in the $k-\omega$−SST turbulence model has been used. The function has been defined so that it range between 0 (freestream) and 1 (wall), with a smooth transition between the correlation of the GTFC in the freestream (Equation 3.42) and the correlation of the TFC at the wall (Equation 3.46). The GTFC-wb (which stands for GTFC wall-bounded) model can be described as:

$$\frac{S_t^{\text{GTFC-wb}}}{S_{L,0}} = \frac{S_t^{\text{GTFC}}}{S_{L,0}} + b\mathcal{F}\left(\frac{S_t^{\text{TFC}}}{S_{L,0}} - \frac{S_t^{\text{GTFC}}}{S_{L,0}}\right), \tag{3.50}$$

where the blending function has been redefined in terms of ε (given that the turbulence class in OpenFOAM doesn't have an attribute for ω):

$$b\mathcal{F} = \tanh\left(\left[\max\left(\frac{k^{3/2}}{\varepsilon y}, \frac{500\nu\beta^* k}{y^2\varepsilon}\right)\right]^4\right). \tag{3.51}$$

The distance to the closest wall y can be computed with different methods in OpenFOAM, such as the `meshWave` approach, used in the current work. Some results of the unbounded combustion model GTFC compared with the wall-bounded GTFC-wb are presented in Section 4.3.

3.7.3. Modifications and new model implementations

Once the different models have been presented, as well as the original combustion model which is already available in OpenFOAM, the solver `NRGXiFoam` with a description of all its implemented features is presented. As it is based on the `XiFoam` version and many of the models have already been presented and included (i.e. flame radius calculation, adaptive mesh refinement, thermodynamics, radiation...), the main focus of this subsection is to explain the combustion model (whose code is included in the `bEqn.H` file).

For debugging purposes and the verification and validation phases, an optional flag has been implemented, called `fixedTurbValues`, which allows the user to freeze the initial turbulence fields and use them as the turbulence fields for the combustion model throughout the simulation. By doing so, the simulation can isolate turbulence and combustion in the case that turbulence conditions are well-known and defined. The turbulence equations are still being solved and updated in the momentum and energy closures.

The turbulent diffusivity was defined as:

$$D_t = D_t^{\infty} = \frac{C_\mu}{\mathrm{Pr}_t}\frac{\widetilde{k}^2}{\widetilde{\varepsilon}}, \tag{3.52}$$

where the constant $C_\mu = 0.09$ (as described in [60]). However, the implementation uses Equation 2.21 to include a dependence of the Lewis number on all the models (as explicitly it is only included in the GTFC-based models), having:

$$D_t = D_t^{\infty} = \frac{C_\mu}{\mathrm{Sc}_t/\mathrm{Le}}\frac{\widetilde{k}^2}{\widetilde{\varepsilon}}. \tag{3.53}$$

Two extra considerations are required in the turbulent diffusion calculation. First, when $t < 0.0005$ s, the value is enforced to be very small ($D_t = \mathtt{SMALL} = 1.0 \times 10^{-15}$ m^2/s) to promote flame ignition and laminar front expansion. The correction was done for all models but the ETFC (as the diffusive term starts already from zero in the original formulation) and in the XiFoamA model (because inconsistent behavior was observed in the non-smooth transition between the enforced small value and the real D_t value). Secondly, all the models but the TFC use the $D_{t,t}$ described in Equation 2.92 to implement a temporal dependence of the diffusivity in time. Moreover, the diffusivity terms are not corrected for temperature nor pressure when compared to the initial conditions.

Even if different models for the laminar flame speed had been described in Subsection 3.7.1, a pressure correction approach has been hardcoded in the solver to be consistent with previous studies [117, 122]. The laminar flame speed is taken from the initial conditions (taking an average in case there is a non-uniform initial field) to create a scalar $S_{L,0}^{\mathrm{ref}} = \mathtt{Su0}$, having that the unstrained laminar flame speed is constant throughout the field and no spatial variations are accounted for. As only the average pressure is used to correct $S_{L,0}^{\mathrm{ref}}$ (see Equation 3.7, rewritten below for convenience), there is no need to have a field variable for the unstrained laminar flame speed and no dependence on the unburnt temperature:

$$S_{L,0} = S_{L,0}^{\mathrm{ref}}\left(\frac{p_{\mathrm{avg}}}{p_{\mathrm{ref}}}\right)^{m_{\mathrm{t}}\frac{\gamma-1}{\gamma}+n_{\mathrm{b}}} = S_{L,0}^{\mathrm{ref}}\left(\frac{p_{\mathrm{avg}}}{p_{\mathrm{ref}}}\right)^{\epsilon_{\mathrm{tk}}}.$$

The average pressure is computed by taking the mean in the whole field, although approaches that only consider the unburnt mixture should be implemented for higher accuracy (even if deflagration flames have a constant pressure across the flame front). The term ϵ_{tk} is the thermokinetic index, which couples the baric index n_{b} and thermal index m_{t}, which has been interpolated based on the data provided by [135] (that can also be found in [10]) to obtain a correlation based on the volume fraction of hydrogen. The third-order polynomial used is:

$$\epsilon_{\text{tk}} = 1.122417 x_{H_2}^3 + 0.53640717 x_{H_2}^2 - 1.26073921 x_{H_2} + 0.85232708\,,$$

where the volume fraction of hydrogen can be obtained with:

$$x_{H_2} = \frac{0.42\Phi}{0.42\Phi + 1} = \frac{2\Phi}{2\Phi + 4.77}$$

by assuming a mixture with only air (21% of oxygen, the rest being inert nitrogen) and hydrogen, and using the equivalence ration Φ. The laminar flame speed has been made equal to the unstrained laminar flame speed, having simply $S_L = S_{L,0}$.

The different combustion models have been implemented as *flame wrinkling models* to be consistent with the definition of all the other models in the `XiFoam` solver. Thus, the different models were expressed as the ratio of turbulent flame speed over the (unstrained) laminar flame speed, obtaining the wrinkling factor in the equilibrium case $\Xi = \Xi_{\text{eq}} = S_t / S_{L,0}$. From that, the source term of the regress variable equation can be computed for all the models in the same fashion.

One relevant comment should be made about the implementation of the ETFC model. It can be seen in Equation 2.91 that there is an extra term included to model the laminar (i.e. when $u' \to 0$) flame development. The term has not been included so far in the combustion model implementation in the OpenFOAM solver, leading to the truncated ETFC model [88]. The reasons not to do so were the inability to retrieve accurate solutions for low values of $u'/S_{L,0}$, which returned better results without the term than when the term was included. Previous studies [117, 122] that used the ETFC model with the extra laminar source term had a reaction time so small that the effects of the term were negligible. Even if it is the truncated-ETFC version, it will be presented throughout the rest of the thesis simply as the ETFC model. Moreover, and as opposed to previous studies [117, 122], the preferential diffusion (F) and quenching effects (G) have not been included in the turbulent flame speed model. The first ones are included implicitly in the correlation that the GTFC-based models use [46]. These details should be kept in mind when trying to compare the results of different studies, even if other factors are expected to play a larger role (such as having a coupled density-based solved with implicit time marching schemes). Finally, and to conclude both the section and the chapter, a detailed description with the differences between the implemented combustion models is included in Table 3.1.

Table 3.1: Description of the two main characteristics of each one of the combustion models implemented in `NRGXiFoam`: effective diffusivity term D_{eff} and wrinkling factor Ξ. The description of the remaining variables is presented throughout the previous discussion.

Combustion model	Effective diffusivity	Wrinkling factor
ETFC (Lipatnikov's correlation)	$D_{\text{eff}} = \frac{C_\mu}{\text{Sc}_t/\text{Le}}\frac{\widetilde{k}^2}{\widetilde{\varepsilon}}\left[1-e^{-t/\tau_L}\right]$	$\Xi = \frac{Au'}{S_{L,0}}\left(\frac{\tau_t}{\tau_c}\right)^{0.25}\left(1+\frac{\tau_L}{t}\exp\left[-\frac{t}{\tau_L}\right]\right)^{0.5}$
GTFC (Correlation Eqn. 3.42)	$D_{\text{eff}} = \frac{C_\mu}{\text{Sc}_t/\text{Le}}\frac{\widetilde{k}^2}{\widetilde{\varepsilon}}\left[1-e^{-t/\tau_L}\right]$	$\Xi = 1.613\left(\frac{R_f}{l_T}\right)^{0.333}\left(\frac{u'}{S_{L,0}}\right)^{0.526}(\text{Le})^{-0.140}$
GTFCp (Correlation Eqn. 3.45)	$D_{\text{eff}} = \frac{C_\mu}{\text{Sc}_t/\text{Le}}\frac{\widetilde{k}^2}{\widetilde{\varepsilon}}\left[1-e^{-t/\tau_L}\right]$	$\Xi = 1.696\left(\frac{R_f}{l_T}\right)^{0.393}\left(\frac{u'}{S_{L,0}}\right)^{0.530}\left(1+\frac{2\mathcal{L}}{R_f}\right)^{-1}$
GTFC-wb (Wall-bounded GTFC)	$D_{\text{eff}} = \frac{C_\mu}{\text{Sc}_t/\text{Le}}\frac{\widetilde{k}^2}{\widetilde{\varepsilon}}\left[1-e^{-t/\tau_L}\right]$	$\Xi = \Xi^{\text{GTFC}} + b\mathcal{F}\left(\Xi^{\text{TFC}}-\Xi^{\text{GTFC}}\right)$ where $b\mathcal{F} = \tanh\left(\left[\max\left(\frac{k^{3/2}}{\varepsilon y}, \frac{500\nu\beta^* k}{y^2\varepsilon}\right)\right]^4\right)$
TFC (Zimont's correlation)	$D_{\text{eff}} = \frac{C_\mu}{\text{Sc}_t/\text{Le}}\frac{\widetilde{k}^2}{\widetilde{\varepsilon}}$	$\Xi = \frac{Au'}{S_{L,0}}\left(\frac{\tau_t}{\tau_c}\right)^{0.25}$
XiFoamA (Algebraic correlation)	$D_{\text{eff}} = \frac{C_\mu}{\text{Sc}_t/\text{Le}}\frac{\widetilde{k}^2}{\widetilde{\varepsilon}}\left[1-e^{-t/\tau_L}\right]$	$\Xi = 1+\left[1+2\Xi_{sc}\left(0.5-b\right)\right]\Xi_{\text{c}}\left(\sqrt{\frac{u'}{S_L+0.01\mu_{S_L}}}\right)\text{Re}_\eta$
XiFoamT (Transport equation)	$D_{\text{eff}} = \frac{C_\mu}{\text{Sc}_t/\text{Le}}\frac{\widetilde{k}^2}{\widetilde{\varepsilon}}\left[1-e^{-t/\tau_L}\right]$	$\Xi \leftarrow \ldots$ $\ldots \leftarrow \frac{\partial}{\partial t}\left(\rho\Xi\right)+\frac{\partial}{\partial x_i}\left(\left(\rho u_i+\phi_\Xi\right)S_L\right)-\Xi\frac{\partial}{\partial x_i}\left(\phi_\Xi\right)=\rho\mathcal{R}-\Xi\rho\left(\mathcal{R}-\mathcal{G}'\right)-\Xi\rho\max\begin{pmatrix}\sigma_t-\sigma_s\\0\end{pmatrix}$

4

Results

In this chapter, the results and main findings of the thesis are presented. After having detailed the numerical methodology, different experimental test cases are used to verify and validate the implementation of the models, compare them under different scenarios, and state some guidelines and usage configurations. First, the theoretical case of a one-dimensional turbulent premixed flame propagating in statistically frozen turbulence is considered, as there is an analytical exact solution to which the numerical one can be compared. Then, the ICARE spherical combustion chamber is considered as it presents really advantageous characteristics to isolate the combustion effects and compare the behavior of different combustion models. Next, the Thermal-hydraulics, Hydrogen, Aerosol, and Iodine (THAI) containment is considered as it is a larger facility and other physical effects, such as buoyancy, play a relevant role. Finally, ENACCEF-2, a flame acceleration enclosure, is considered to sketch the ranges of validity of the models under the scenario of flame acceleration and supersonic flow conditions.

4.1. One-dimensional turbulent premixed flame in statistically frozen turbulence

To verify the implementation of the combustion models, the analytical case of a one-dimensional premixed flame propagating into a turbulent quiescent medium with statistically frozen turbulence is considered. This case presents an analytical solution (see [91] and [92]) that has been used in the literature as a theoretical framework to develop the ETFC combustion model. Nevertheless, all the combustion models presented in Chapter 3 can be used to simulate this scenario and assess their implementation.

4.1.1. Analytical solution of the problem

The one-dimensional problem is stated as a premixed flame that moves from left (burnt region) to right (unburnt region) into a turbulent medium with zero mean velocity. It can be sketched as:

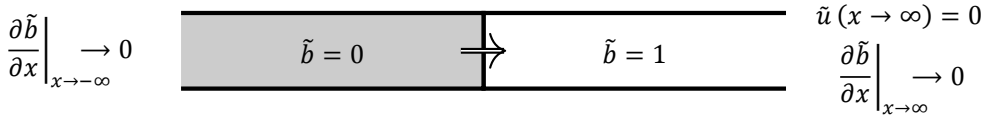

Figure 4.1: One dimensional premixed flame moving into statistically frozen turbulence.

To retrieve the analytical solution to this case, constant pressure is assumed, so the momentum equation doesn't need to be solved. As it is a one-dimensional case, only two variables ($\tilde{u}$ and $\tilde{b}$) require a transport equation, having mass conservation and regress-variable equation:

$$\frac{\partial}{\partial t}\left(\overline{\rho}\right) + \frac{\partial}{\partial x}\left(\overline{\rho}\widetilde{u}\right) = 0$$
$$\frac{\partial}{\partial t}\left(\overline{\rho}\tilde{b}\right) + \frac{\partial}{\partial x}\left(\overline{\rho}\widetilde{u}\tilde{b}\right) = \frac{\partial}{\partial x}\left(\overline{\rho}\left(D + D_t\right)\frac{\partial \tilde{b}}{\partial x}\right) + \rho_u S_t \left|\frac{\partial \tilde{b}}{\partial x_i}\right|$$

The boundary conditions at the infinite limits of the domain for each equation are given in Figure 4.1. To close the system, the density $\overline{\rho}$ has to be expressed in terms of the regress variable $\overline{\rho} = \overline{\rho}(\tilde{b})$. The state equation provided by the BML approach [16] can be used when rewritten in terms of the regress variable as:

$$\frac{1}{\overline{\rho}} = \frac{\tilde{b}}{\rho_u} + \frac{\left(1-\tilde{b}\right)}{\rho_b} \xrightarrow{\text{or alternatively as}} \overline{\rho} = \frac{\rho_u}{\tilde{b} + \frac{\rho_u}{\rho_b}\left(1-\tilde{b}\right)}$$

The full procedure and derivation with the corresponding function transformations and normalizations can be found in the original paper [91] and only the relevant results are going to be presented here for convenience. Due to self-similarity principles between premixed flames, a normalized distance variable can be defined as:

$$\xi = \frac{x - x_f(t)}{\Delta_f(t)} \tag{4.1}$$

where x is the horizontal coordinate, $x_f(t)$ is the flame position in time and $\Delta_f(t)$ is the flame thickness (also a function of time). If the flame is defined to be located at $\overline{b} = 0.5$, then the flame position in time is written as:

$$x_f(t) = x_f(t=0) + \int_0^t S_t(\tau)d\tau \tag{4.2}$$

where $x_f(t=0)$ is the location of the flame at the initial time and $S_t(t)$ is the known time-dependent turbulent flame speed used in the source term of the regress variable equation. Finally, the flame thickness can be analytically given as:

$$\Delta_f^2(t) = 4\pi \int_0^t D_t(\tau)d\tau \tag{4.3}$$

where $D_t(t)$ is the time-dependent diffusivity of the Laplacian term in the regress transport equation. With all these definitions, the traveling-wave solution can be expressed as:

$$\overline{b} = 1 - \frac{1}{2}\mathrm{erfc}\left(\xi\sqrt{\pi}\right) = \frac{1}{\sqrt{\pi}}\int_{\xi\sqrt{\pi}}^{\infty} e^{-\tau^2}d\tau \tag{4.4}$$

In order to verify the computational implementation, three variables will be computed from the numerical setup and compared with the analytical definitions presented before: $R_f(\overline{b}, t)$, $V_t(t)$, and $\delta_f(t)$. The first one represents the flame radius, or as this is a one-dimensional case, the distance of a given isosurface of $\overline{b}$ to the initial location of the flame front at a given time t. This can be compared to the analytical location of the flame, that can be expressed by rearranging Equations 4.1 and 4.2 as:

$$x(\overline{b},t) = \frac{\Delta_f(t)}{\sqrt{\pi}}\text{erfc}^{-1}\left(2\left(1-\overline{b}\right)\right) + x_f(t) \tag{4.5}$$

The second one, the turbulent flame velocity V_t, is defined as the temporal derivative of the flame front location (which is taken to be at $\overline{b} = 0.5$, consistent with [91]) as:

$$V_t = \frac{dR_f(\overline{b}=0.5,t)}{dt} \tag{4.6}$$

The turbulent flame velocity can be compared with the input turbulent flame speed $S_t(t)$ used for the source term. By doing so, it can be checked if the source term is properly applied over the regress variable and that the isosurface $\overline{b} = 0.5$ is a faithful reflection of the turbulent flame speed. Finally, the flame thickness $\delta_f(t)$ can also be computed based on the gradient of the profile of the regress variable, having:

$$\delta_f(t) = \frac{1}{\max\left(\left|\nabla\overline{b}\,(t)\right|\right)} \tag{4.7}$$

It can be noted that using Equation 4.7 to compute the flame thickness is equivalent to using the formulation based on the temperature gradient (see Equation 2.38). However, this is not the same as the calculation method based on the diffusivity and the laminar flame speed, which is the one used as input to the combustion model and it is widely used throughout the literature. Experimental studies (see Figure 73 of [46]), have shown that in real flames there is almost one order of magnitude of difference between the methods of computing the flame thickness. Since there are many definitions in the literature, the assessment of the flame thickness models is beyond the scope of this work.

It should also be pointed out that the analytical flame location depends on the turbulent flame speed used. Thus, there will be an analytical curve representing S_t from TFC (not time-dependent) and $S_t(t)$ from ETFC. To further validate the implementation of the GTFC and get an expression for the analytical flame location, some assumptions are required, given that the original correlation depends on the flame radius and not on the time from ignition (as is the case with the ETFC). Moreover, the flame radius for a one-dimensional flame tends to infinity, resulting in an infinite turbulent flame speed. Thus, to obtain an analytical solution for the GTFC, the radius $R_f(t)$ is replaced with the difference between the flame location and the flame initial location:

$$R_f(t) = x_f(t) - x_f(t=0) = \int_0^t S_t(\tau)d\tau \tag{4.8}$$

However, the turbulent flame speed for the GTFC presents a dependence on the flame radius instead of on the time directly so $S_t(t) = S_t(R_f(t))$. By including the original GTFC correlation into 4.8, the integral equation can be solved, obtaining an analytical expression for the flame radius that can be used to retrieve the analytical value of the turbulent flame speed:

$$R_f(t) = \left[\frac{2}{3}\cdot t\cdot 1.613\,S_L\left(\frac{1}{l_T}\right)^{0.333}\left(\frac{u'}{S_L}\right)^{0.526}\text{Le}^{-0.14}\right]^{3/2} \tag{4.9}$$

The flame front expression will be plugged into the GTFC turbulent flame speed correlation in the place of the flame radius. This provides a time-dependent analytical GTFC model as the exact solution that is compared with the numerical results where the flame radius is computed using the axial-based procedure described in Section 3.2.

4.1.2. Numerical solution

Once the analytical solution has been presented and the different equations have been described, the numerical setup is discussed before showing the results themselves. Two conditions of the Borghi diagram are presented, among the multiple ones that were tested, to stress out some model limitations and some adjustments made before moving onto experimental facilities. Both cases present the same chemical and mixture properties ($S_L = 0.1749$ m/s, $\rho_u = 1.0219$ kg/m^3, $\mu_u = 1.8455\times10^{-5}$ kg/(m s)) but not the same turbulence properties, locating the conditions in two different regions of the Borghi diagram (see Figure 4.2). The first one (red circle in Figure 4.2) presents high turbulence levels ($k = 1.5$ m^2/s^2 and $\varepsilon = 5$ m^2/s^3), locating the point within the corrugated flamelets region. The second configuration (green square) presents lower values of turbulence ($k = 0.015$ m^2/s^2 and $\varepsilon = 0.1$ m^2/s^3) so it lays in the wrinkled flamelets regime.

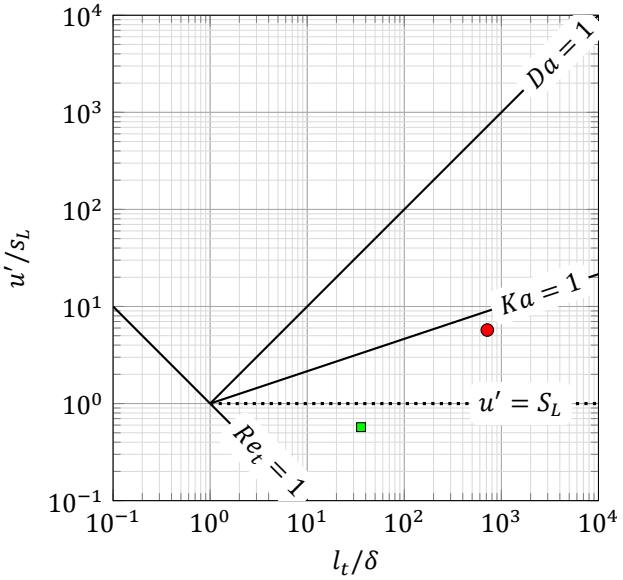

Figure 4.2: Borghi diagram with the two simulated scenarios: a high turbulence case in the corrugated flamelets region (denoted with ● , $k = 1.5$ m^2/s^2 and $\varepsilon = 5$ m^2/s^3) and a low turbulence case in the wrinkled flamelets regime (denoted with ■ , $k = 0.015$ m^2/s^2 and $\varepsilon = 0.1$ m^2/s^3).

This simple one-dimensional case was simulated over a cuboid mesh that spans 0.5 m $\times$ 0.0003 m $\times$ 0.0003 m for the first case and 0.1 m $\times$ 0.0003 m $\times$ 0.0003 m for the second case. Different grids where used due to different S_t values. Both had a resolution of $5000 \times 3 \times 3$ cells per direction. This makes that, even if the flame is one-dimensional, the solver is applied to a three-dimensional case. The simulation was initialized with a step in the regress variable $\tilde{b}$ and temperature $\widetilde{T}$ fields imposed at half the simulation domain. Thus, no ignition source term was required, neither the temperature and diffusion term corrections were used. The directions with 3 cells (y and z-axis) have been treated as symmetry planes. The boundary conditions for the remaining x axis are presented in Table 4.1, having `zeroGradient` for a Neumann-type boundary condition with value 0 and `fixedValue` for a Dirichlet-type boundary condition.

No transport equation is solved for S_L and both ends have `fixedValue` as boundary condition. The fields for k and ε are required for the combustion model even if turbulence is frozen. These fields are stored in a turbulence object within the code, so creating it is a necessary step, but no transport equations were solved for k nor ε (as `turbulence off` in the `turbulenceProperties` dictionary). The simulation times varied for each case and the timestep was automatically adjusted in both to keep a Courant number under 0.20. All variables were discretized using the `Gauss limitedLinear` (which is based on the Sweby limiter modified to accommodate central differences [128]) or either the vector version `limitedLinearV` or the strictly bounded version `limitedLinear01` for `U` and `b`, respectively. Timestepping was performed with the first-order `Euler` scheme.

Table 4.1: Boundary conditions for the one-dimensional flame. The subscript zero represents the value used for the field initial conditions.

Field	**Left** (burned)	**Right** (unburnt)
alphat	zeroGradient	fixedValue 0
b	zeroGradient	fixedValue 1
epsilon	zeroGradient	fixedValue ε_0
k	zeroGradient	fixedValue k_0
nut	zeroGradient	fixedValue 0
p	fixedValue 101325.00	zeroGradient
Su	fixedValue 0.1749	fixedValue 0.1749
T	zeroGradient	fixedValue 298.00
U	zeroGradient	fixedValue (0 0 0)
Xi	zeroGradient	fixedValue 1

1D turbulent premixed flame in the corrugated flamelets regime

The results of the high-turbulent corrugated flamelet are presented first as they are used to verify the solver implementation. This is the reason why GTFC-p has not been included in the study (as it follows the same implementation as the GTFC and it will be validated with the spherical combustion chamber). GTFC-wb has also not been included, because there are no walls and the solution will tend to GTFC. As previously described, the turbulent flame speed S_t used for the source term is compared with the turbulent flame velocity V_t obtained from the time-derivative of the flame radius in Figure 4.3a. It can be seen that only three models out of five present an analytical solution: TFC, ETFC, and GTFC have a known S_t which is spatially constant. However, the XiFoamA model has a turbulent flame speed that not only depends (indirectly) on time but also on the regress variable itself, so obtaining the analytical solution for it would be unwieldy. The situation for the XiFoamT is even worse, as Ξ doesn't present a fixed correlation but a transport equation. Thus, only a numerical solution is presented for the XiFoamA and XiFoamT models in Figure 4.3.

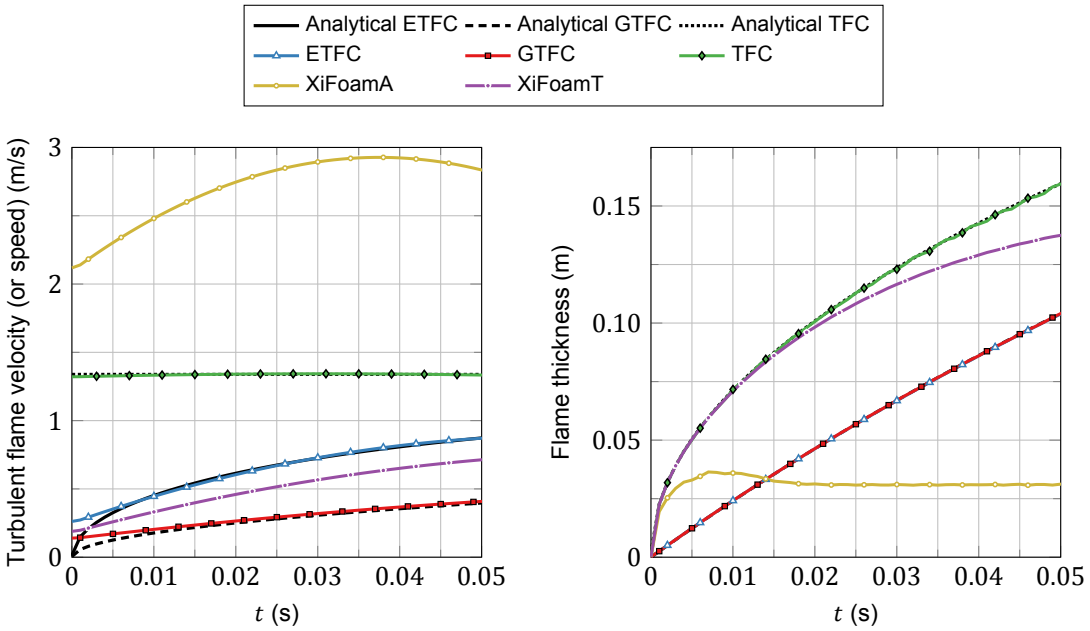

(a) Turbulent flame velocity.

(b) Flame brush thickness.

Figure 4.3: Results for the first considered set of parameters ($k = 1.5$ m^2/s^2 and $\varepsilon = 5$ m^2/s^3). The analytical curves show S_t and Δ_f while the numerical ones show V_t and δ_f.

The results show a substantial agreement between numerical and analytical results for those models where both are available. The largest discrepancy can be seen at the beginning but it is due to the flow adapting to the step in the fields. The turbulent flame speed predicted by the ETFC model tends asymptotically from zero (at ignition) to the turbulent flame speed value of the TFC, which can be seen numerically. The XiFoamT correlation is close to ETFC and presents the same growing trend. Finally, the XiFoamA significantly overpredicts the value of the turbulent flame velocity compared to the other models. Although it may seem that the trend is also different, the explanation for the downwards going part is that the extremes of the flame brush (i.e. $0.01 < \tilde{b} < 0.99$) is too close to the end of the domain, so solutions after the maximum shouldn't be considered as representative of the model, because they are influenced by the boundary conditions.

Similarly, the analytical flame thickness Δ_f (see Equation 4.3) is compared against the numerical one δ_f (see Equation 4.7), in Figure 4.3b. In this case, only two analytical solutions are available: the Δ_f from the time-constant diffusivity of the TFC model and the Δ_f from the time-dependent diffusivity of the ETFC model. The GTFC is overlapped with the results of the ETFC as both are the same: experimentally no information is provided on flame thickness so the time-dependent term of the ETFC has also been used to build the GTFC models. The difference between the flame thickness predicted by ETFC and TFC is widely reported in the literature (see the normalized flame thickness of Figure 6.11 in [31]). For the XiFoam-based models, it should be stressed that the diffusivity term is the same as for the ETFC. However, not having a spatially-constant value of S_t influences the results of the flame thickness obtained from the gradient method: as $S_t = S_t(\tilde{b})$, extra effects appear on the isosurfaces evolution in time that cannot be exclusively attributed only to the diffusive term. The XiFoamA starts with the same trend as the TFC but then it remains flat and it predicts smaller values of the flame thickness at all times. The smaller flame thickness is a consequence of all the isosurfaces of $\tilde{b}$ moving at similar rates: the turbulent flame speed exceeds the effects of the diffusivity. Finally, the XiFoamT follows the same initial trend as TFC but it also flattens out later in time.

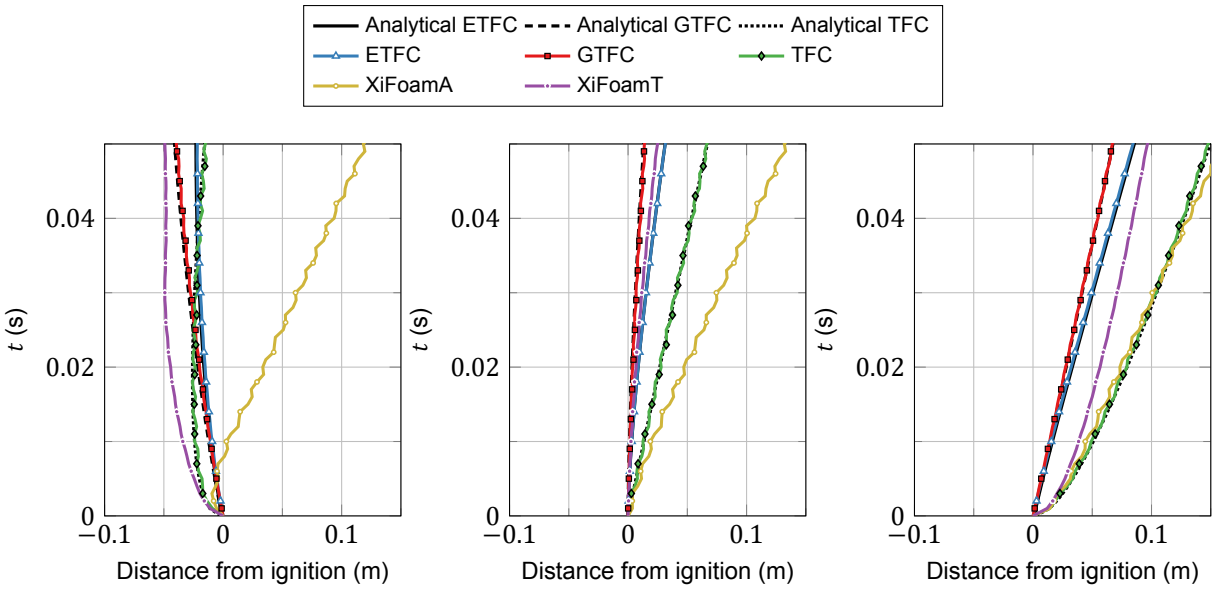

(a) Isosurface $\overline{b} = 0.10$. **(b)** Isosurface $\overline{b} = 0.50$. **(c)** Isosurface $\overline{b} = 0.90$.

Figure 4.4: Evolution in time of different $\tilde{b}$ isosurfaces for the different combustion models.

To better discuss the previous results, the location in time of different isosurfaces of $\overline{b}$ is presented in Figure 4.4. The horizontal axis represents the distance to the ignition location and the vertical axis the evolution in time. This unconventional representation has been chosen to mimic an $x - t$ diagram of pressure/shock wave reflection from gas dynamics. Three isosurfaces are represented: $\overline{b} = 0.1$, $\overline{b} = 0.5$ and $\overline{b} = 0.9$. The second one is usually taken to be the flame front location and its derivative provides the turbulent flame velocity, which was shown 4.3a. The S_t value used by the TFC model is

larger than that of ETFC, making that the flame location is more advanced in time. Then, by seeing all three $\overline{b}$ at the same time, conclusions can be extracted to further support the flame thickness results. On the one hand, the TFC has the largest flame thickness so indeed it presents the broadest difference between the extreme isosurfaces (having the less step gradient in between and thus the largest flame thickness). On the other hand, the XiFoamA has all three isosurfaces following similar trends, having little to no diffusion of the isosurface $\overline{b} = 0.1$ into the initially burned region, as it happens with all the other models. The fact that the interface is being compressed because the turbulent flame speed is dependent on $\overline{b}$ can be beneficial in some cases where too much spreading of the flame front can quench combustion and extinguish the flame. Thus, the combination of high S_t values together with small flame spreading effects results in a robust model that should provide flame growth and expansion in almost all scenarios, at the expense of some overprediction of the flame speed and front location.

There is one final remark that should be done between the analytical case and the numerical results. When computationally solving the momentum equation, pressure is not going to be exactly constant. One of the assumptions of the model is that pressure is constant throughout the flame, but advancing the solution in time with constant pressure is something that the segregated PISO algorithm can't handle. Thus, pressure fluctuations occur in the simulated domain and pressure is not constant, having pressure waves traveling from one side to the other of the domain. The range of pressures that occurs in the domain can be seen in Figure 4.5, having that the amplitude values of the fluctuations is less than 0.5%. Although it can be thought that it is due to incorrect boundary conditions or initialization, the phenomena is reported in the literature [60]. These pressure fluctuations have indeed their effect in the other fields, including $\overline{b}$. Therefore, the postprocessing done in the aforementioned paper was replicated (by using the `scipy.UnivariateSpline` [1] function with default parameters) to remove the oscillations of the flame front caused by the pressure fluctuations.

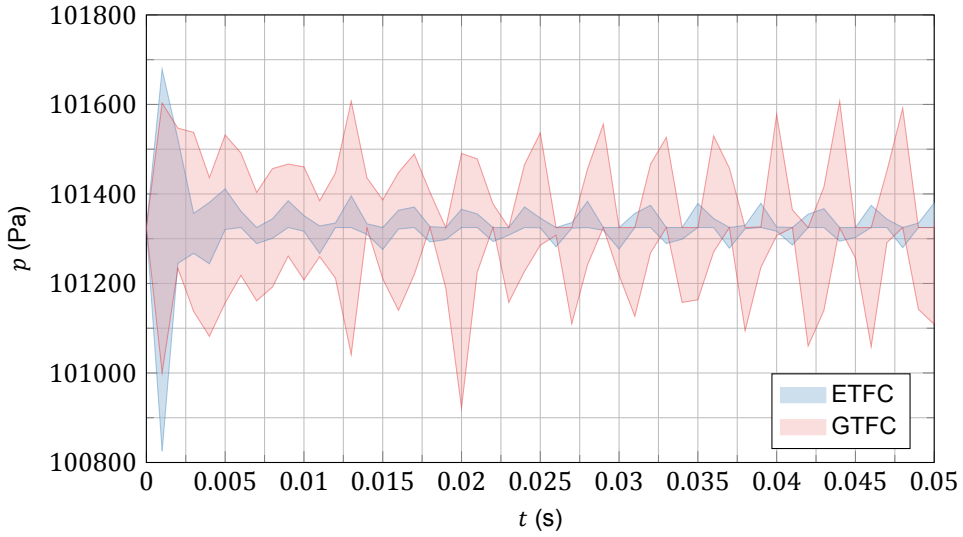

Figure 4.5: Pressure oscillations in time for the ETFC and the GTFC combustion models.

1D turbulent premixed flame in the wrinkled flamelets regime

In order to assess the capabilities of the different combustion models to deal with other combustion regimes, numerical simulations corresponding to the wrinkled flamelet regime are presented here. The results are presented as before: first the turbulent flame velocity V_t with the analytical turbulent flame speed S_t is shown in Figure 4.6a (with the only difference being that also the laminar flame speed S_L has been included in the plot) and secondly the analytical and numerical flame thickness, Δ_f and δ_f respectively, are presented in Figure 4.6b.

[1] Function that performs a 1D spline fit of a given degree (cubic spline by default) to a given set of data points. The number of knots for the smoothing conditions is by default the length of the weights vector

In Figure 4.6a the first thing that can be seen, as opposed to the previous corrugated flamelet, is that both XiFoam models have a turbulent flame velocity considerably larger than that of the other models. More importantly, this velocity is over the value of S_L. As both XiFoamA and XiFoamT are lower-bounded with $\Xi > 1.0$, both models predict larger velocities. However, neither the TFC nor ETFC will predict any velocity larger than S_L within the simulated time. But more relevant is the fact that they will not predict it even when time tends to infinity: ETFC will tend to the TFC value and the TFC model is constant in time, so it will keep predicting the same value, having $S_t(t = 0) = S_t(t \to \infty) < S_L$. It is widely recognized that the TFC gives more accurate values at higher levels of turbulence (especially with $u'/S_L > 4.0$ as depicted in [88]). The GTFC keeps growing and it eventually predicts $S_t > S_L$. However, the values $S_t < S_L$ are unphysical and should be avoided (the same way the XiFoam models do). Another interesting result is that the V_t from the ETFC start with an offset but it levels as time advances, approaching S_t. It is the same behavior as with the previous scenario. The slow adaptation to the analytical solution is due to the lack of the quasi-laminar source term in the ETFC, since the truncated-ETFC version is adopted here.

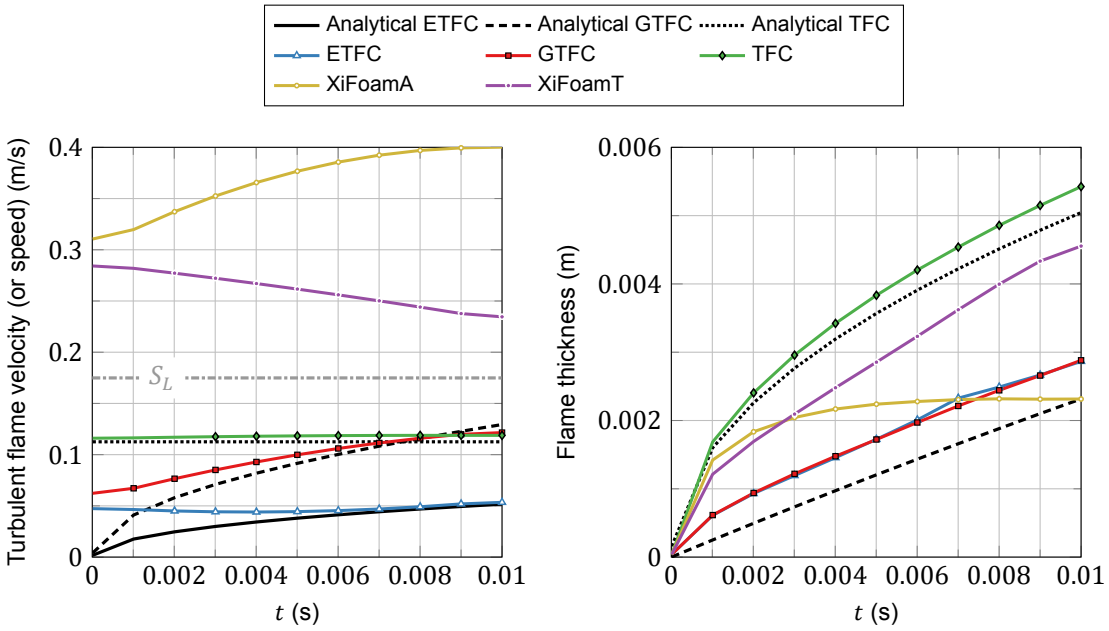

(a) Turbulent flame velocity.

(b) Flame brush thickness.

Figure 4.6: Results for the second considered set of parameters ($k = 0.015$ m^2/s^2 and $\varepsilon = 0.1$ m^2/s^3). The analytical curves show S_t and Δ_f while the numerical ones show V_t and δ_f.

The flame thickness results of Figure 4.6b show good agreement with the results of the previous scenario. There is a small offset between the numerical δ_f and the analytical Δ_f for both TFC and ETFC. As expected, the flame thickness of ETFC and GTFC also match. The XiFoamA ends up plateauing as before, while the XiFoamT follows the same trend as TFC, although with an offset from it.

4.1.3. Conclusions, model limitations, and improvements

From the results of this section, two conclusions can be drawn. The first one is that the implemented models are verified with the use of the analytical solution for a one-dimensional premixed flame moving into a frozen turbulent quiescent medium. Even when considering all the assumptions required to obtain the analytical solution, the agreement with the numerical results shows that the models are working as expected and they are consistent with the limitations described in the literature. The implementations agree well with the analytical model.

The second conclusion is that the different assumptions taken during the implementation phase have been made based on either physical considerations or numerical results. Limiting $\Xi > 1.0$ lays on the

first group: as done in the XiFoam-based models, the turbulent speed of a flame front cannot be smaller than the laminar flame speed. Turbulence should increase the velocity of the flame, especially in these simplified models where phenomena as local quenching that may reduce the turbulent flame speed are not considered. Thus, for the following results, the condition $\Xi > 1.0$ is applied to all models. Secondly, it was seen that large diffusivities for the Laplacian term of the regress variable equation may cause an extremely quick spreading of the flame, leading to extinction. Therefore, based on the compressed behavior of the XiFoamA and to promote the earlier stages of ignition, the value of D is kept to zero during $t < 0.00005$ s. By doing so, the homogeneous expansion of the flame front is promoted, instead of causing an unphysical thickening of the flame when the turbulence values are too high. The next section will further support and justify this ignition modeling assumption.

4.2. ICARE spherical combustion chamber

Once the combustion models were verified, real scenarios with experimental facilities are analyzed. The first one considered was the spherical combustion chamber developed by the ICARE (which stands for *Institut de Combustion, Aerothermique, Reactivite et Environnement*, or Combustion, aerothermodynamics, reactivity and environment institute in English) in Orléans, France. This spherical combustion chamber is focused in slow deflagrations in controlled turbulence, having as research objectives flame instabilities, turbulent flames within an initial homogeneous isotropic turbulence field, and the effect of spray on combustion. The relevant part for this thesis is the development of turbulent flames in an initial homogeneous and isotropic turbulence field. Homogeneous isotropic turbulence at the beginning of the experimental run is helpful when trying to isolate the combustion effects to those occurring from the turbulence itself.

Moreover, the facility presents some advantages over other spherical or cylindrical vessels that have been used in the literature to develop correlations for the turbulent flame speed. The first one is that the operations of the facility started in 2008 so the techniques and capture devices used can still be considered recent nowadays. Secondly, the experiments have been carried out with hydrogen mixtures. During a severe accident in a nuclear power plant, even if small traces of other species as carbon monoxide or steam exist, the main released gas is hydrogen. The fact that this vessel has been entirely operated with hydrogen mixture provides useful information and ensures that the correlation remains valid for a broad range of conditions. Moreover, the mixtures studied had a very lean hydrogen composition: the flammability went from no flame to complete spherical combustion, going through partial and complete combustion with ascending flames. The experiments with lean conditions are rather unique, since most (if not all) previous experiments considered richer mixtures which are easier to obtain. Thus, the study presented in [46] and [47] shows new insights into the turbulent flame speeds for lean mixtures of hydrogen.

4.2.1. Facility and experimental data description

The facility set up consists of an inner stainless steel sphere of 0.563 m of diameter and 42 mm of thickness concentrically located with an outer sphere, also of stainless-steel, of 0.640 m and 4 mm thickness. Between the two spheres, a thermal fluid is used to raise the temperature of the chamber to 573 K and keep a homogeneous and constant temperature at the walls. A total internal volume of 95 liters allows a maximum overpressure of 20×10^6 Pa, taking into account safety factors.

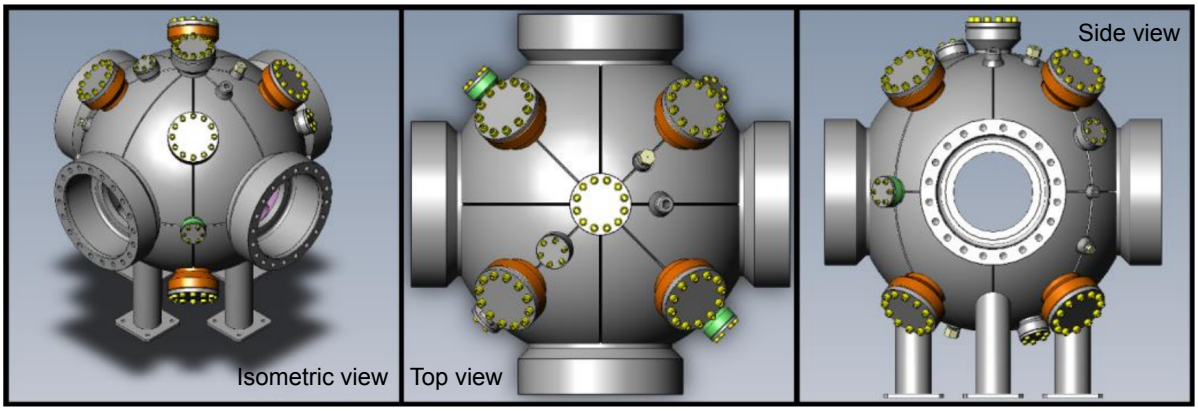

Figure 4.7: CAD design of the ICARE spherical combustion chamber. The larges holes represent the visual acquisition windows. The orange cylinders are the turbulence generation devices. The green cylinders represent the ignition system.

To perform optical measurements the sphere is equipped with four openings over the equatorial plane that allow the insertion of windows with different porthole sizes that further restrict the maximum allow-

able pressure. The one used for the study has an optic diameter of 200 mm and restricts the maximum pressure to 5×10^6 Pa. This window allows seeing a spherical flame with a maximum radius of 80 mm.

Ignition was performed with a tungsten electrode installed in the equatorial plane of the vessel and with the help of a high voltage generator. The discharge was synchronized with the capturing devices to start recording when the mixture was being ignited. Prior to ignition, eight fans were installed at the vertex of an inscribed cube to the inner sphere. These fans can turn at a maximum speed of 10000 rpm. To avoid leakages, the engine of the fan is located outside of the vessel and uses magnetic coupling with permanent magnets to transfer the torque to the fans installed inside the chamber without axis crossing the walls. The four-bladed propellers have a diameter of 130 mm and were carefully designed to obtain homogeneous and isotropic turbulence by sucking air through the propeller.

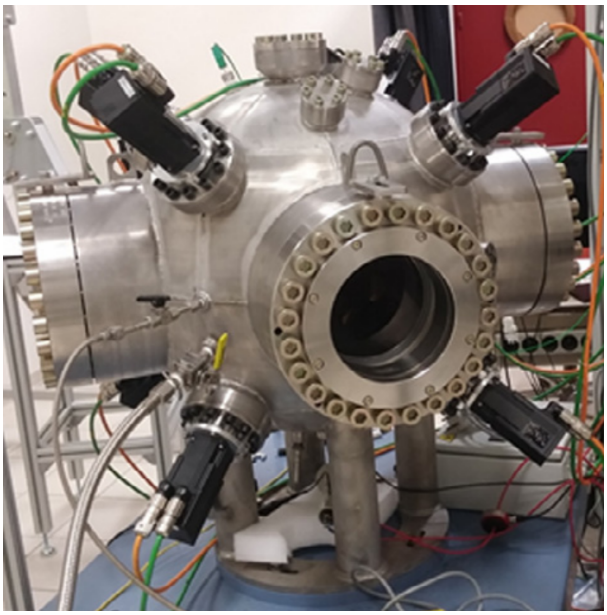

(a) Real picture of the facility.

(b) Propeller used in the spherical combustion chamber used to generate a homogeneous isotropic initial turbulence field.

Figure 4.8: Pictures from the ICARE spherical combustion chamber, obtained from [47].

A Particle Image Velocimetry (PIV) setup was used to measure the initial turbulence fields and to ensure a homogeneous and isotropic turbulence field. Moreover, Schlieren imaging with an ultrafast camera was used to capture the density gradients present in the interface between burnt and unburnt domains. The images captured with this device were used to determine the contour of the flame with high accuracy and even see the surface cellular structures of the flame. The main drawback of this technique is that the volumetric sphere is projected and not sliced into the capturing device, so the depth of the wrinkling cannot be perceived. Thus, multiple runs of the same setup were performed so the contours could be combined. Four holes at 40 degrees over the horizontal plane at each side of the sphere have a piezoelectric pressure transducer to capture pressure and thermocouples to measure the temperature of the mixture prior to ignition. The remaining holes are used to introduce the gas and create a vacuum in the vessel.

The postprocessing performed for the PIV is not directly relevant for this report, more information can be found in [46]. However, the treatment of the Schlieren images to get the radius will be briefly described. For each image, the intensity was corrected, the ignitor contours were removed and then a Canny filter was used to perform the edge detection. Problems were reported due to different luminosities so two thresholds are required for the upper and lower flame fronts of an expanding flame. Statistics can then be performed over the multiple runs performed for each configuration. Finally, the conditions that were experimentally tested with the different involved parameters are described in Table 4.2:

These conditions cover a broad range of mixture composition, from very lean (16 % of hydrogen) to almost stoichiometric (28 % of hydrogen), and a broad range of turbulence conditions (varying the

Table 4.2: Mixture and turbulence information for the experiments of the spherical combustion chamber, extracted from [47].

xH_2	u' (m/s)	l_T (mm)	S_L (m/s)	δ_f (mm)	Le_{eff}	u'/S_L	Ka	Da	Re_T
0.16	0.56 ± 0.01	43.9 ± 3.1	0.46 ± 0.02	0.523	0.458	1.22	0.22	30.6	45.1
	1.26 ± 0.03	49.0 ± 3.5				2.76	0.70	15.1	113.5
	2.08 ± 0.04	53.0 ± 2.7				4.50	1.42	10.0	201.6
	2.81 ± 0.03	52.4 ± 1.4				6.15	2.27	7.3	270.9
0.20	0.56 ± 0.01	43.9 ± 3.1	0.92 ± 0.03	0.382	0.561	0.61	0.06	105.0	38.9
	1.26 ± 0.03	49.0 ± 3.5				1.38	0.19	51.8	98.1
	2.08 ± 0.04	53.0 ± 2.7				2.25	0.39	34.2	174.1
	2.81 ± 0.03	52.4 ± 1.4				3.08	0.62	24.9	234.0
0.24	0.56 ± 0.01	43.9 ± 3.1	1.41 ± 0.05	0.351	0.712	0.40	0.03	211.8	33.4
	1.26 ± 0.03	49.0 ± 3.5				0.90	0.09	104.6	84.2
	2.08 ± 0.04	53.0 ± 2.7				1.47	0.18	69.0	149.5
	2.81 ± 0.03	52.4 ± 1.4				2.01	0.28	50.2	201.0
0.28	0.56 ± 0.01	43.9 ± 3.1	1.93 ± 0.03	0.350	0.956	0.29	0.02	331.9	28.1
	1.26 ± 0.03	49.0 ± 3.5				0.66	0.05	163.8	70.7
	2.08 ± 0.04	53.0 ± 2.7				1.07	0.10	108.2	125.6
	2.81 ± 0.03	52.4 ± 1.4				1.47	0.17	78.6	168.8

fan velocity from 1000 rpm to 4000 rpm). In Figure 4.9 a snapshot for each pair mixture-turbulence flame is shown. Some flame characteristics can be analyzed based on these images: the distributed reaction flames are heavily wrinkled as the combination of lean mixture with high turbulence returns a Karlovitz number well above unity. In general, turbulence drastically modifies the flame structure: an increase in the turbulence value wrinkles the flame surface. For very high turbulence values, the flame morphology is also affected by local extinctions. A more important effect can be seen due to thermo-diffusive instabilities caused by the hydrogen high molar diffusivity, having more wrinkled flames the leaner the concentration. The flame still presents a spherical shape even after the development time until $R_f = 60$ mm.

4.2.2. Numerical simulation setup

Once the experimental setup has been described, as well as the data that was retrieved from the different runs, it is time to present the numerical simulation model. The combustion models that were verified before are going to be used to simulate all the experiments carried out with the spherical combustion chamber, to test the capability limits of the different models. These simulations have a two-folded purpose. First of all, they serve as a verification for the GTFC-based models and the solver structure in general. As these combustion models are developed with the correlation provided by this facility [47], it is expected that the results of these models have a good agreement with the experiments. Secondly, by running the same simulation with different combustion models, their behavior under different mixture concentrations and turbulence levels can be assessed. The simulations will provide some guidelines for further experimental facilities that present more complex geometries and flow dynamics.

The spherical combustion chamber provided high quality homogeneous and isotropic turbulent initial conditions. This can be translated into the front flame seeing the same turbulence quantities as those existing initially. As the numerical simulations are RANS, all turbulence is modeled and the combustion-generated-turbulence cannot be predicted. It is expected that higher fidelity models as LES modeling provides correct properties ahead of the flame. However, the turbulence quantities were hold fixed from the initial values for the combustion model. This is not the same as keeping frozen turbulence, as the transport equations for k and ε are being solved and the source terms are included into the momentum and energy equations. However, these obtained values are not being updated into the

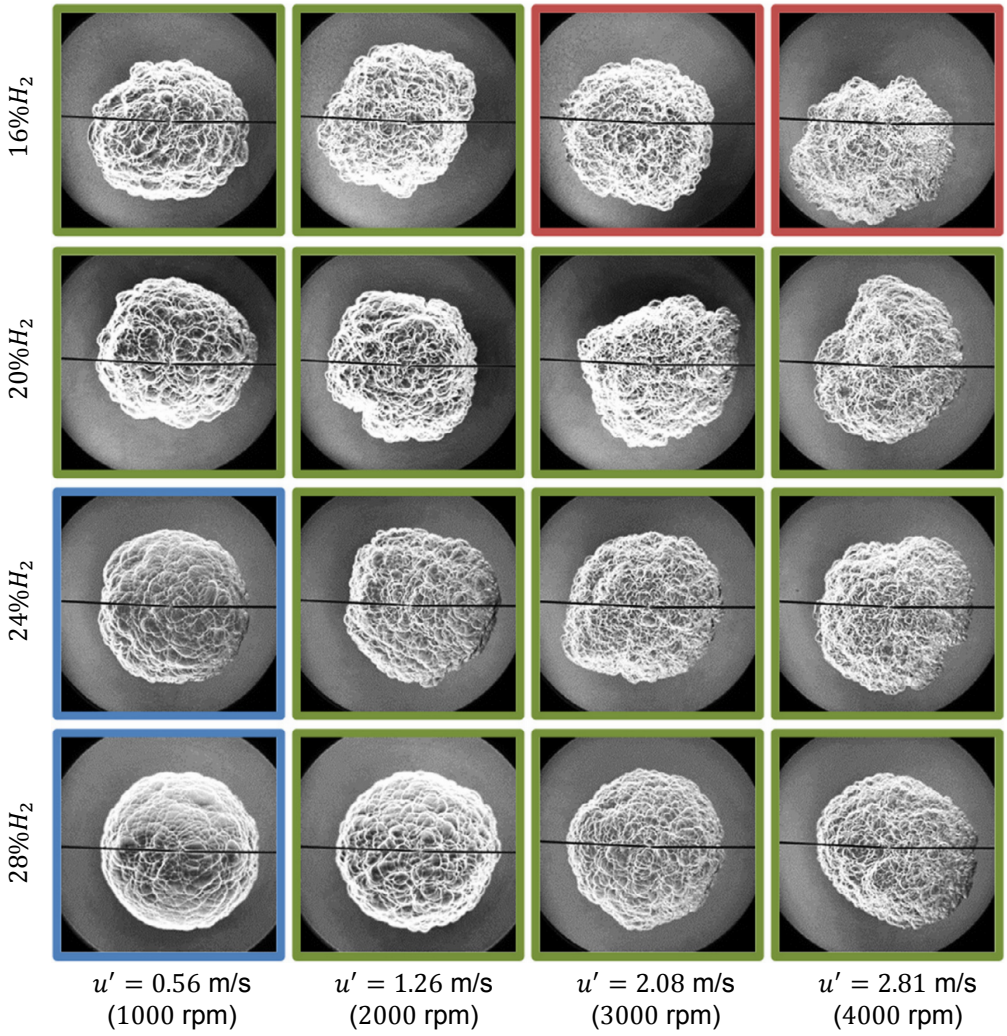

Figure 4.9: Tested configurations of hydrogen concentration and turbulence level. All the flames have a mean radius of 60 mm. Initial conditions were $p = 100$ kPa and $T = 293$ K. Image border-color corresponds to red (distributed reaction), green (corrugated flames), blue (wrinkled flames), adapted from [47].

combustion model, that uses k_0 and ε_0. Similar studies already presented this problematic [60] and required a large number of adjustments to include the turbulence model into a small vessel with an initial turbulent flow field. These changes included: the use of an ignition source term in the regress variable equation (increasing the uncertainty of the results due to the source strength), time delaying the activation of the turbulence model (to give the flow time to adapt to the sudden change in density and velocity that occurs in the ignition region and that produces large values of k and ε), and the use of extra source terms for each equation of the turbulence model (based on the initial values to correct the values ahead of the flame front, and get values close to the k_0 and ε_0). To avoid these problems, the initial turbulent field values were used for the combustion model at all times. The model $k-\varepsilon$ was used to model the turbulence for all the runs, although it is expected that the performance of the $k-\omega-$SST was similar (as no walls were simulated).

Thanks to the symmetry of the experimental facility, the mesh was an axisymmetric wedge inscribed in the sphere. The setup can be seen in Figure 4.10a: the triangular prism represents the actual mesh inscribed in the grey sphere, which is the full combustion chamber. The red circle is the maximum radius that was considered in the experiments. The distance between the maximum radius and the outer limits of the grid ensures that the boundary conditions don't affect the results. The main reason

to a mesh with a rectangular outer face instead of an axisymmetric grid with half a circle was the ease with which this mesh is generated: no edge curves means that the mesh is completely hexahedral (with the exception of the prisms of the axis of rotation), conformal and structured, without incurring into high skewed cells at the wall. The number of cells close to the ignition region can also be maximized by stretching the cells at the outer edges of the grid where the flame never reaches. The main downside of this approach is that no pressure rise can be computed, although the main interest here is the flame front development. If walls were included, the effects of different turbulence models had to be compared and the walls would require a finer mesh.

As the mesh is axisymmetric just one boundary condition is required per field(see Figure 4.10a), as the `axis` patch in OpenFOAM doesn't has an associated boundary condition (`empty` type), and both the `front` and `back` patches use an azimuthal symmetry boundary condition (denoted as `wedge` in the CFD solver) for all the fields. Thus, the only required boundary condition is on the three outer faces, all three having the same boundary condition for each field. The summary of them can be found in Table 4.3. No buoyancy effects were considered. As the number of cells increased compared to the one-dimensional laminar flame, the solver was running in parallel: four processors were used with the mesh split with the simple decomposition method, as the mesh has clear symmetries. Constant heat capacity at constant pressure c_p and fusion energy were assumed through the `hConst` thermodynamics model. The transport model used a constant μ and Pr not dependent on temperature (although dependent on the regress variable, as two pairs (μ, Pr) are provided, one for reactants and the other for products). As for the one-dimensional laminar flame, the `limitedLinear` schemes either in the default, vectorial, or strictly bounded version are used. The `Euler` scheme was used to advance in time and the timestep was chosen so that the maximum Courant number was 0.1.

Table 4.3: Boundary conditions for the spherical combustion chamber. Subscript zero represents the used value as initial condition and that depends on the mixture and turbulence properties.

Field	Outer faces	
alphat	fixedValue	0
b	fixedValue	1
epsilon	fixedValue	ε_0
k	fixedValue	k_0
nut	fixedValue	0
p	fixedValue	p_0
Su	fixedValue	$(S_L)_0$
T	fixedValue	T_0
U	zeroGradient	
Xi	zeroGradient	

Turbulence initial values were chosen to mimic the experimental u' and l_T values provided in Table 4.2. The actual values of turbulent kinetic energy used for each experimental turbulence level can be seen in Table 4.4, and were obtained with:

$$k_0 = \frac{3}{2}u'^2 \qquad \varepsilon_0 = \frac{0.2014\, k_0^{3/2}}{l_T}$$

Finally, the initialization of the combustion was done without the use of any source term in the regress variable transport equation. A region of the domain was patched with the adiabatic flame temperature and the burnt value of the regress variable $\tilde{b} = 0$, having that the flame propagated from there. Different H_2 concentrations required different patching ignition radius to achieve flame expansion. A larger ignition radius ensures that the flame will not get extinct, but as the experimental values of the radius R_f are restricted to $R_f < 80$ mm, the smallest possible radius that ignited most of the models was chosen. However, as it will be shown later, there are combustion models that would have required an even larger radius. To make a fair comparison between models, the same ignition radius was used for all the combustion models and turbulence levels of the same hydrogen concentration, even if that

Table 4.4: Initial turbulence values for the spherical combustion chamber.

Fan rotational speed (rpm)	Turbulent kinetic energy (m^2/s^2)	Turbulent kinetic energy dissipation rate (m^2/s^3)
1000	0.4704	1.4801
2000	2.3814	15.1047
3000	6.4896	62.8218
4000	11.8442	156.6693

meant some models not expanding. The patching radius were 10 mm, 8 mm, 6 mm, and 4 mm for $H_2 = 16\%$, $H_2 = 20\%$, $H_2 = 24\%$ and $H_2 = 28\%$ respectively. It can be seen that the leanest the mixture, the larger the patching radius is required to achieve flame expansion. The size ratio between these ignition patching and the maximum flame radius can be seen in Figure 4.10b.

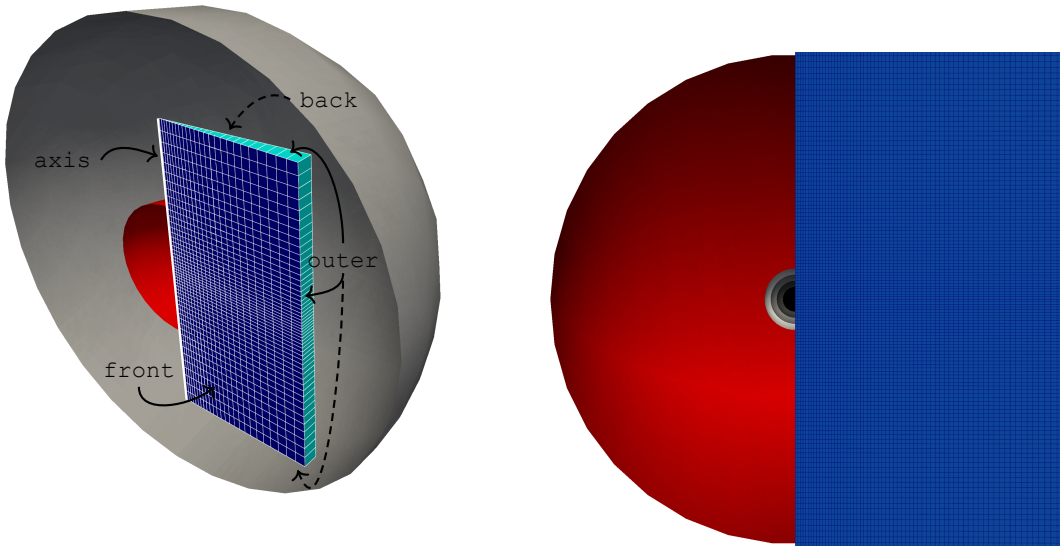

(a) Spherical combustion domain with its boundaries enclosed in the real vessel (grey) and with a sphere of the maximum equivalent radius for reference (red).

(b) Detail of the simulated region with the different ignition radius (concentric gray) with the maximum radius from experiments (red, same as Figure 4.10a).

Figure 4.10: Mesh dimensions of the domain for the numerical simulation of the spherical combustion chamber.

4.2.3. Mesh sensitivity study

Before presenting the results of the different combustion models, a mesh sensitivity study was carried out to pick the resolution that provides grid-independent results without incurring into too expensive simulations. Obtaining the resolution that achieves a trade-off between accuracy and computation expenses is the objective of this subsection. The chosen experimental conditions were $xH_2 = 0.28$ and $u' = 2.81$ m/s, as the combination of rich mixture with high turbulence promotes the flame expansion, being the less troublesome condition that reduces the possible influence of the size of the ignition domain. The combustion model used for the mesh sensitivity study is the GTFC. The mesh is generated by extruding a rectangle of sides 0.18 m$\times 0.36$ m at an angle of 0.0111 rad (or 0.6366 degrees), obtaining a triangular prism. The angle value was obtained as the outer edge has a length of 0.002 m and it is located at 0.18 m of the axis of rotation. An expansion ratio of 4 was used in all the grids to achieve a higher resolution close to the ignition region. However, as the number of cells was changed between different levels of refinement, also the ignition region has a different number of cells. Five levels of refinement were tested, going from M0 to M4. The details of each mesh are presented in Table 4.5. As the radial length of the mesh is half of the height, choosing the ratio of the number of cells was

straightforward. Only one cell is used in the azimuthal direction. The total cell count ratio between different meshes was always above 1.77 and below 4, being the ratios between the runtimes ranging between 1.92 and 7.21. The time it took M4 is disproportionate when compared with the number of cells it has: M4 has four times the amount of cells of M3 but it took more than seven times to simulate. This is likely due to the non-linear behavior of the parallel scalability and the fact that the same number of cores was used for all simulations, being outside of the optimal performance range.

Table 4.5: Mesh sensitivity study of the spherical combustion chamber.

Mesh	Number of cells per direction	Cell count	Run time (s)
M0	25 × 50	1250	16
M1	50 × 100	5000	47
M2	75 × 150	11250	108
M3	100 × 200	20000	207
M4	200 × 400	80000	1492

A detail of how these different grids look like can be seen in Figure 4.11. The relevant region of the domain is zoomed in for $t = 0.003$ s in all the grids. It can be seen that the refinement increases the number of cells that is contained in the flame front but also in the uniform burnt and unburnt regions, which is something Adaptive Mesh Refinement tries to address. It was not considered for this case as the number of cells and the simulation time were quite reduced even for the most refined mesh.

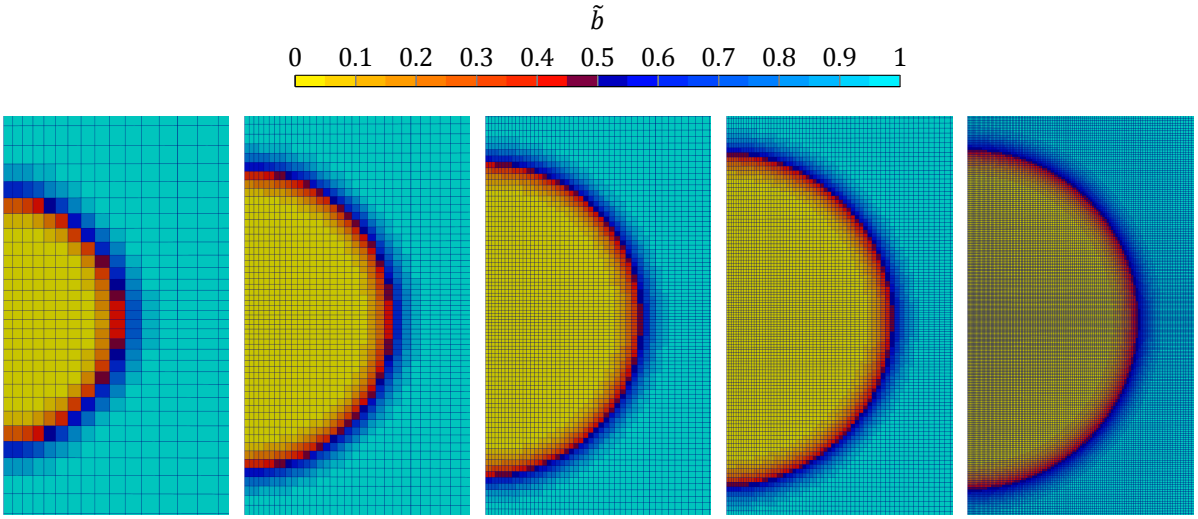

(a) Mesh M0. **(b)** Mesh M1. **(c)** Mesh M2. **(d)** Mesh M3. **(e)** Mesh M4.

Figure 4.11: Different grid resolutions used for the mesh sensitivity study of the spherical combustion chamber. Images are shown at $t = 0.003$ s.

To better compare the different grids, the evolution of three variables is presented. Firstly, the wrinkling factor Ξ, which is the ratio between the turbulent flame speed and the laminar flame speed, is plotted. From the experiments, only one curve is provided for the mean value of Ξ. Even if it is possible to convert the turbulent flame velocity ranges (with the density ratio and the laminar flame speed) into the wrinkling factor, no ranges are included in the third graph for the sake of clarity. This is the value used in the source term of the regress variable equation. The second one is the flame radius R_f, which is plotted together with the average experimental radius as well as the range covered by the different runs. The results from the numerical simulations have been shifted in time so that the patching radius r used for ignition matches the flame radius. This makes that $t_{\text{sim}} = 0$ s is not $t_{\text{exp}} = 0$ s but rather $t_{\text{exp}} = t(R_f = r)$. The last value is the time derivative of the flame radius, which is the turbulent flame velocity V_T. These values are also obtained from experiments, so both the mean and the range of the different runs are plotted.

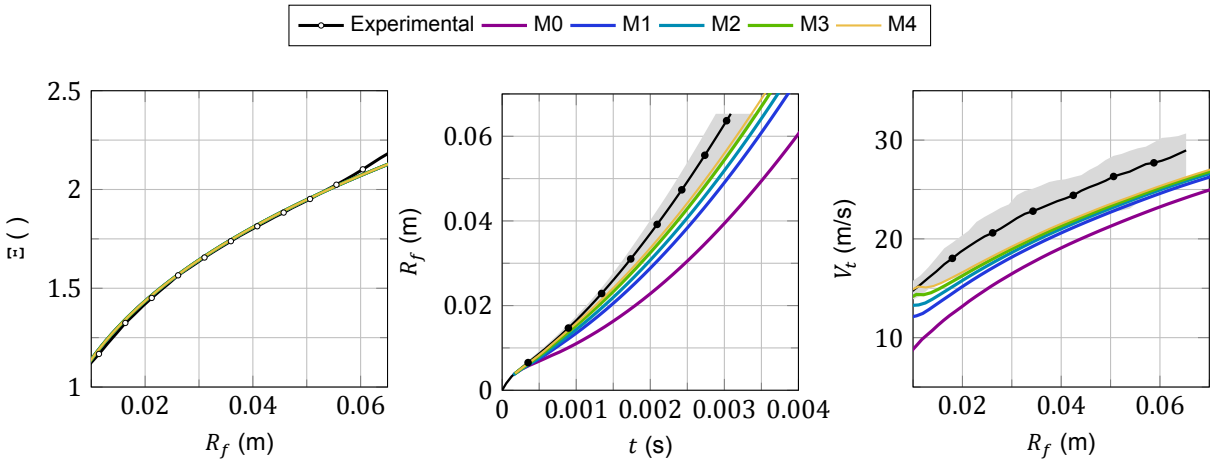

(a) Wrinkling factor. **(b)** Flame radius. **(c)** Turbulent flame velocity.

Figure 4.12: Spherical combustion chamber: mesh sensitivity results from OpenFOAM.

The postprocessing was first carried out with the solver directly in OpenFOAM. The value of Ξ plotted was obtained by averaging the variable over the whole domain. Using GTFC for the mesh sensitivity study allows doing so, as Ξ is spatially (not time) constant, given that the turbulence values used for the combustion models are fixed according to Table 4.4. The flame radius was computed with the integral method. The turbulent flame velocity was computed by first interpolating the flame radius with the function described before (`scipy.UnivariateSpline`) and then performing the time derivative, eliminating flame front fluctuations. As expected, the wrinkling factor (see Figure 4.12a) is consistent in all the meshes, as it only depends on the flame radius but not on any other flow variables. It can be seen that the predicted flame radius (see Figure 4.12b) converges towards the experimental values for the grids more refined than M2. Similar results are observed in the turbulent flame velocity (see Figure 4.12c), where even M1 and M2 provide results close to M4. The accuracy discrepancy between the different grids when plotting the flame radius versus time disappears when plotting the turbulent flame velocity versus the flame radius: little offsets in time appear for different mesh resolutions, but the turbulent flame velocity predicted at a given flame radius is consistent. None of the grid resolutions has a cell small enough to capture the flame front thickness obtained experimentally.

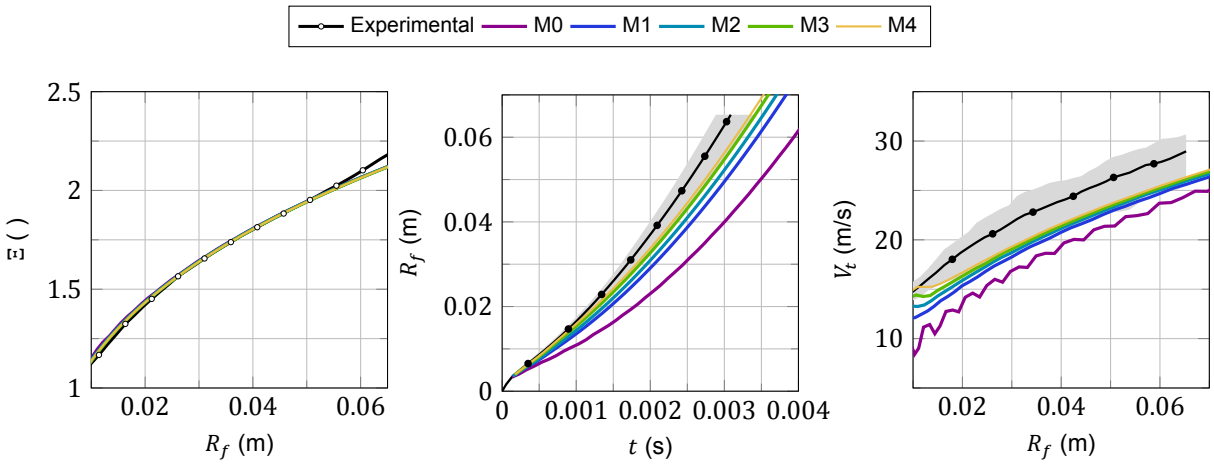

(a) Wrinkling factor. **(b)** Flame radius. **(c)** Turbulent flame velocity.

Figure 4.13: Spherical combustion chamber: mesh sensitivity results from ParaView.

For further validation, the postprocessing was also implemented independently into the data analysis and visualization application tool Paraview [3]. Thanks to the Python scripting interface, it is possible to

automate the functions to return just the desired quantities (Ξ, R_f, V_t) in time by reading the time folders of OpenFOAM. Paraview presents a relevant advantage against the postprocessing of OpenFOAM as it can compute isosurfaces straightforwardly. However, it presents two main disadvantages. Firstly, Paraview can only compute the variables for those times that have been saved (which requires more space on the disk in order to obtain good trend prediction), while OpenFOAM returns the variable every timestep, without having to write all fields. Performing the post-processing on the fly is the only option in some applications, such as for the ENACCEF2 case presented in Section 4.4, since the required sampling frequency is so high that would result in an enormous amount of data if the post-processing is performed a-posteriori. Secondly, it is faster to perform the postprocessing on the fly, especially for larger cases for which parallelization is used.

Sampling Ξ only at the isosurface $\overline{b} = 0.5$ (as done in Paraview, see Figure 4.13a) and doing so in the whole domain (as done with OpenFOAM) return the same consistent results. The flame radius was computed in Paraview with the average distance of the isosurface located at $\overline{b} = 0.5$ to the ignition location. However, it can be seen in Figure 4.13b that the flame radius trends, as well as the values themselves, are the same as those obtained with the integration method directly in OpenFOAM. As in this case there are fewer sampling points, the turbulent flame velocity (see Figure 4.13c) has been computed without interpolating the flame radius or any other special postprocessing. M0 presents larger oscillations than any other mesh resolution as the flame front location varies less smoothly than in the other grids. However, the average of those fluctuations would be equivalent to the results obtained with OpenFOAM in Figure 4.12c. The comparison between the results of OpenFOAM and of Paraview was done for other hydrogen concentrations and turbulence values, getting consistent results. Thus, the postprocessing performed in OpenFOAM can be trusted and hence used for the rest of the work.

The mesh selected for the rest of the simulations of the spherical bomb is M3. Even if M2 was already providing acceptable results in terms of the turbulent flame velocity, the flame radius development was more converged with M3. Moreover, the difference in time between these two is not that large (just twice) while the accuracy of the results of M3 is comparable to that of M4 with just a fraction of the computational expenses.

4.2.4. Combustion model analysis

The results of the different combustion models for simulating the spherical bomb are analyzed in this subsection. The same variables that were used for the mesh sensitivity study are shown here: Ξ, R_f, and V_T. For practical reasons, instead of showing the numerical results for the 16 experimental configuration, just four cases are detailed. These four cases are not the most representative of a nuclear accident but they correspond to the extreme configurations for hydrogen mixture concentration and turbulence levels, so they cover many different combustion regimes. Six combustion models are considered for the analysis: ETFC, GTFC, GTFCp, TFC, XiFoamA and XiFoamT. The GTFC-wb is not included as there are no walls as the solution is equivalent to that of GTFC.

As detailed in the previous subsection, mesh M3 will be used for these simulations. The postprocessing has been performed with OpenFOAM. The calculation of Ξ is straightforward for the TFC, ETFC, GTFC, and GTFCp, as Ξ is constant throughout the field, so taking a field average is equivalent to the value of Ξ at $\overline{b} = 0.5$. However, both XiFoamA and XiFoamT have spatially dependent Ξ fields. The approach used to compute Ξ at $\overline{b} = 0.5$ for the former is to get the maximum value of $4\overline{b}(1-\overline{b})\Xi$, which is taken in the flame front at $\overline{b} = 0.5$. The function $4\overline{b}(1-\overline{b})$ has a maximum of 1 located at $\overline{b} = 0.5$. This approach has been validated, as Paraview returns the same Ξ value for the XiFoamA obtained by computing the average value of Ξ of the isosurface $\overline{b} = 0.5$. The procedure followed for the latter is more involved and computationally slow, that's why it is only used for that combustion model. It is similar to the surface-averaged flame radius calculation procedure: the solver loops through all cells, checks if $0.475 < \overline{b} < 0.525$ for each cell, and if it does, the value is added to a list of which the average is then computed. Again, the results obtained with this approach were validated with Paraview. Finally, the flame radius has been computed used the volume integral method and the turbulent flame velocity is computed with the temporal derivative of the interpolated values of the flame radius.

The first condition that has been analyzed is characterized by a mixture with $xH_2 = 0.28$ and a turbulence value of $u' = 0.56$ m/s. As depicted by their properties in Table 4.2 and the blue color in Figure 4.9, it lays within the wrinkled flamelet regime. The results for the combustion models are presented in Figure 4.14. The configuration is characterized by very low turbulence values and high laminar flame speeds, as the mixture is close to the stoichiometric value. Some models, namely ETFC, GTFC, and GTFCp, predict values of $S_t < S_L$ (see the dashed and dotted-dashed black lines in Figure 4.14a, that show the value of the correlation used for GTFC and GTFCp respectively). However, as it was discussed previously, the bound $\Xi > 1.0$ was imposed in all models. The XiFoamT and the TFC predict slightly larger S_t than S_L, while the XiFoamA largely overestimates the value of Ξ. In the same figure can be seen that the provided correlations underestimate the experimental values: the correlation equation was obtained by performing regression of many different experimental runs, having that not all experimental runs have been adjusted equally. Nevertheless, it can be seen that physically, the experimental values are always $\Xi > 1$, so, by including this lower bound in all the models, an extra physical consideration is being included. Having (almost) all models predicting $\Xi \simeq 1$ makes that the flame radius development and the turbulent flame velocity is similar in all of them, except in the overpredicted the XiFoamA. The TFC is the only one that with similar Ξ predicts different flame radius. The difference is on the non-time dependent diffusivity term. In the flame radius curve can be seen that during the first 0.0005 s of the simulation, the behavior of all models (except the XiFoamA) is exactly the same: the predicted Ξ by all models is extremely close and the diffusivity value is being artificially restricted to be small so flame expansion is promoted during ignition. However, as soon as the actual D value is used, the flame front starts following another different trend: the flame starts to be more spread in space due to the higher diffusivity in the TFC, meanwhile having a smaller diffusivity term in models such as the ETFC that therefore predict a slower flame front evolution. The performance of the GTFC, GTFCp, and ETFC is the same as all models are being bounded with $\Xi > 1$ and the diffusivity term is equal as well. It should be noticed the great accuracy of the XiFoamT, being the only one that matches the trend of the turbulent flame velocity (and thus, that of the flame radius) for $R_f > 0.06$ m.

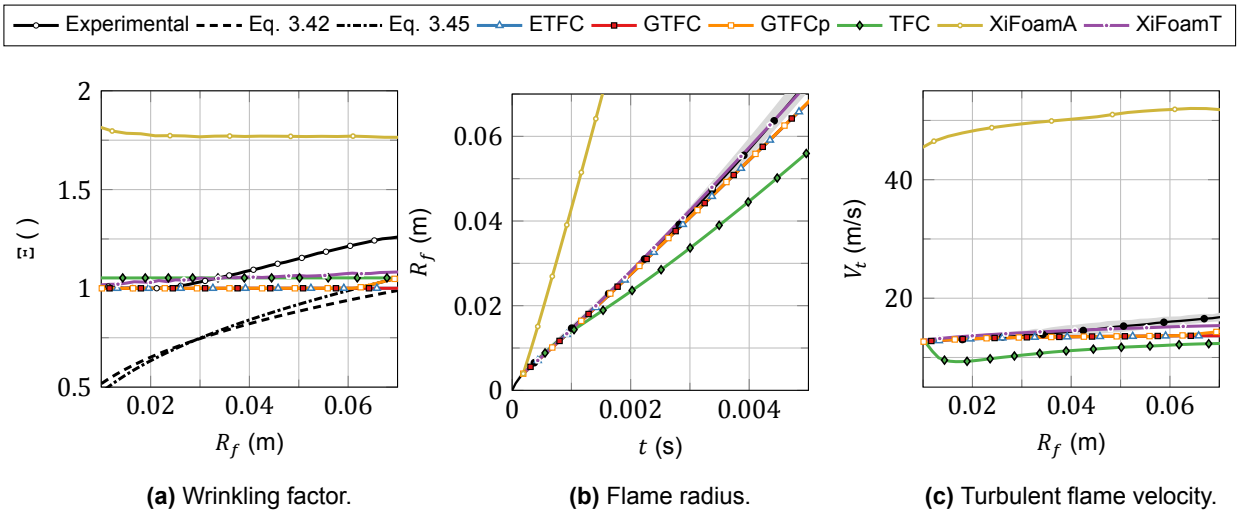

(a) Wrinkling factor. **(b)** Flame radius. **(c)** Turbulent flame velocity.

Figure 4.14: Numerical results of the spherical combustion chamber: $xH_2 = 0.28$, $u' = 0.56$ m/s.

The second considered flame is characterized by a leaner mixture ($xH_2 = 0.16$) but the same level of turbulence ($u' = 0.56$ m/s). These conditions make that the flame belongs to the corrugated flamelet regime, as now the laminar flame speed is lower than before, and therefore the ratio u'/S_L is higher. The ratio l_t/δ_f is quite similar for all flames, around ~ 100. The first thing that can be seen in Figure 4.15 is that now the models are more spread. By checking Ξ, it can be seen that the XiFoamA keeps largely overpredicting the values of Ξ while the TFC overpredicts it at the beginning, but as the flame develops, the experimental values are closer to those of the TFC. However, as the Ξ of the TFC is constant in time, the numerical value will not increase while the experimental value grows as the flame keeps developing. The XiFoamA also overpredicts both flame front development and the turbulent flame velocity, while the TFC has an accurate match of both. The explanation is again the larger not-time dependent diffusivity term that spreads the flame front. However, and as it will be presented later,

this is more a coincidence than an expected result: overpredicting Ξ and having a large diffusivity term cancel each other out in this case, returning values close to the experimental findings. The ETFC is the only model where the bound of $\Xi > 1$ is applied, even if it is only at the early stage of the flame development. The initial bounding of the ETFC happens for most cases, as the model predicts $\Xi = 0$ at $t = 0\ s$, having a transition time where $0 < \Xi < 1$ if the bound was not present. This model is usually coupled with a ignition and laminar source term that helps to sustain the flame, although enforcing $\Xi > 1$ promotes flame expansion without incurring into extra source terms. Smaller values of Ξ combined with the same diffusive term as models like the GTFC return a slower flame front in time and smaller turbulent flame velocity. The XiFoamT also predicts a smaller value of Ξ than the experiments, which gets translated into the same behavior of the ETFC. The GTFC and GTFCp both follow the correlations for Ξ, having that in this case they perfectly follow the flame front development as well as the turbulent flame velocity.

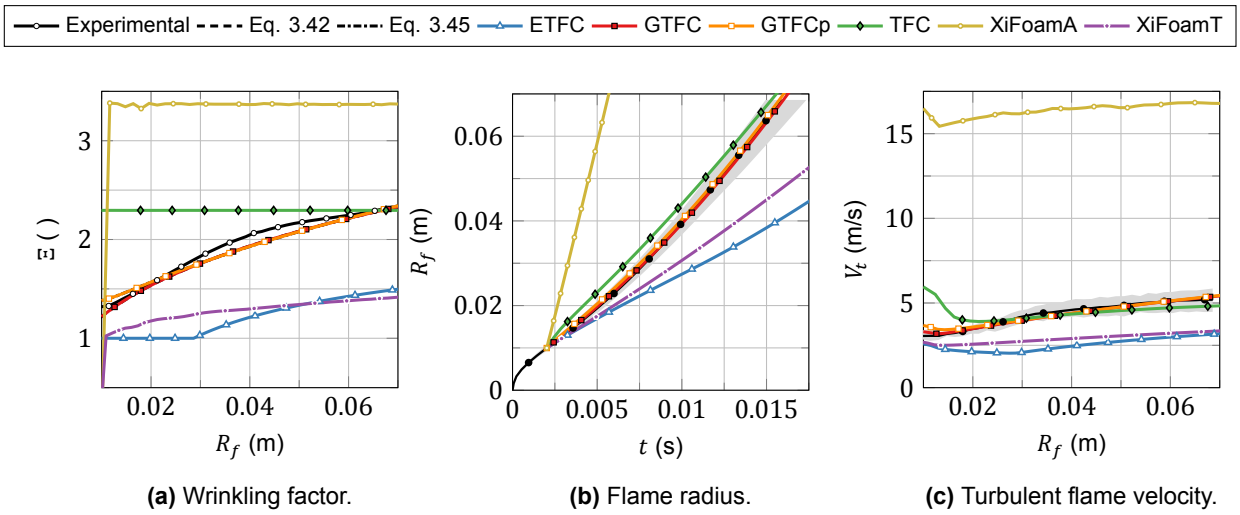

(a) Wrinkling factor. **(b)** Flame radius. **(c)** Turbulent flame velocity.

Figure 4.15: Numerical results of the spherical combustion chamber: $xH_2 = 0.16$, $u' = 0.56$ m/s.

The results of the third flame can be seen in Figure 4.16. It is the following one in order of u'/S_L values: it has a mixture of $xH_2 = 0.28$ and a turbulence value of $u' = 2.81$ m/s. This higher level of turbulence combined with near-stoichiometric conditions locates the flame also within the corrugated flamelet regime. Both the TFC and the XiFoamA overpredict Ξ and therefore also the flame front radius and the turbulent flame velocity. The point that was stated before about the TFC accurately predicting the second flame due to mere coincidence is confirmed here: the compensation between the overprediction of Ξ and the diffusivities is not a phenomenon that can be generalized. The bounding of the diffusivity term can be appreciated in the subtle change in the R_f trend of the TFC around $t = 0.005$ s, as it immediately goes from an almost zero value to the predicted value. The XiFoamT model underpredicts Ξ but it returns almost accurate flame development and close values of the turbulent flame velocity. The ETFC underpredicts Ξ with even lower values than those of the XiFoamT at a smaller flame radius, largely underestimating the flame radius development in time. Again, the GTFC and GTFCp models follow the correlations used as input and present accurate values for flame front development and turbulent flame velocity (as the correlations accurately fit the experimental results for this mixture and turbulence level).

Finally, the fourth flame (see Figure 4.17 is the one with higher u'/S_L, as the leanest mixture ($xH_2 = 0.16$) is combined with the highest level of turbulence ($u' = 2.81$ m/s), putting the flame into the low distributed flamelet regime (as the Karlovitz number goes slightly over 1). Thus, the flame can be used to test the robustness of the different combustion models when they are taken outside of their domain of best applicability. In fact, the TFC (and thus the ETFC) have their applicability limited to flames with Ka < 1 [88], while no information has been found for the limits of any of the XiFoam based solvers. The GTFC and GTFCp should be valid for this regime because the Ξ correlation is derived from the experimental results. Matching Ξ doesn't directly translates into accurate predictions of the flame radius or the turbulent flame velocity (even if it is the GTFC-based models the ones that better perform). The

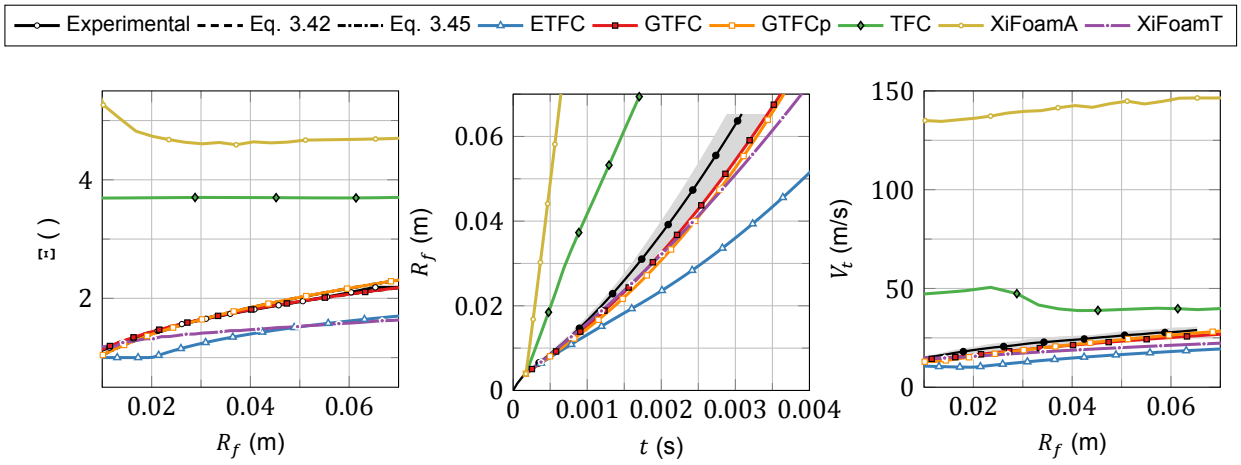

(a) Wrinkling factor. **(b)** Flame radius. **(c)** Turbulent flame velocity.

Figure 4.16: Numerical results of the spherical combustion chamber: $xH_2 = 0.28$, $u' = 2.81$ m/s.

most simple explanation that concerns all the models is the fact that the regress variable equation assumes a separation between burnt and unburnt species, which is a concept that starts to fade away within the distributed flamelet regime as the chemistry starts playing a more relevant role. Another explanation could be that the diffusive term is large: the behavior that was before only observable in the TFC can now be seen also in the GTFC and GTFCp: the flame radius development in time changes after 0.005 s of simulation time, moving the slope downwards and underpredicting the flame radius. However, the overall trends presented before (both XiFoamA and TFC overpredicting, good performance of GTFC and GTFCp, and variable behavior of ETFC and XiFoamT) are still applicable here. The quenching observed for XiFoamT is due to a small ignition, but the required ignition to achieve flame expansion with the model was too large compared with the maximum R_f from the experiments, so it was decided to keep these results for consistent ignition radius with other models. However, it cannot be generally stated that the XiFoamT model doesn't work in the distributed flamelet regime (or at least, that it performs worse than the others), only that the required initial radius for ignition is larger. It was indeed seen that a ignition patching radius of 0.15 m avoids quenching, at the expense of not being able to compare to one fourth of the flame development.

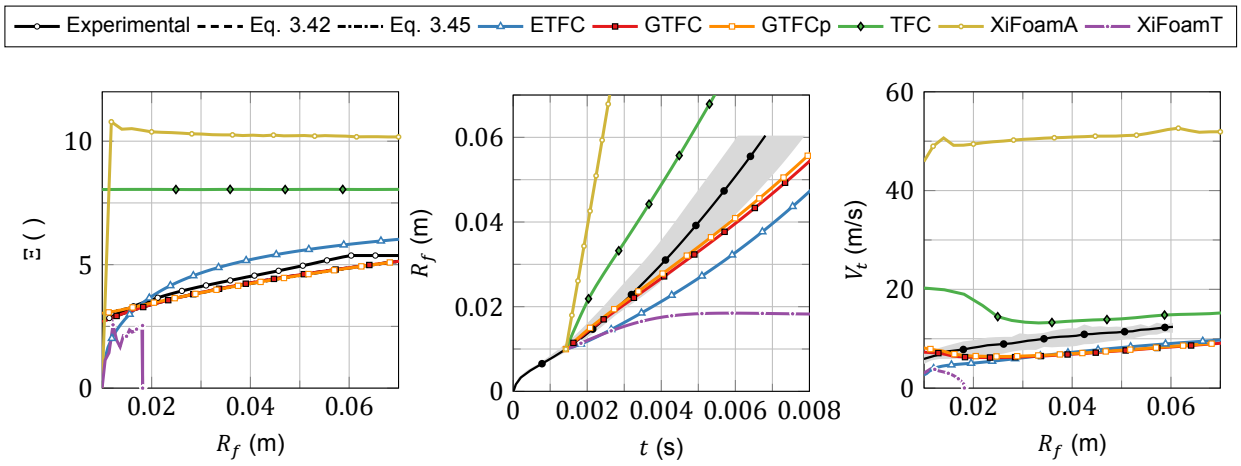

(a) Wrinkling factor. **(b)** Flame radius. **(c)** Turbulent flame velocity.

Figure 4.17: Numerical results of the spherical combustion chamber: $xH_2 = 0.16$, $u' = 2.81$ m/s.

To conclude the results, the flame radius of all 16 experimentally tested combinations of hydrogen and turbulence levels is plotted in Figure 4.18. Based on the previous detailed discussion of the four

extreme cases of the case matrix, the trends can be explained based only on the flame radius. Although not explicitly represented, the regimes of the flames can be inferred from the experimental values of the flames and the overall agreement of the numerical solutions: $xH_2 = 0.24$ and $xH_2 = 0.28$ both at $u' = 0.56$ m/s present a good agreement between most of the models having little to almost no discrepancy between the models. Moreover, the cases of $xH_2 = 0.16$ with $u' = 2.08$ m/s and $u' = 2.81$ m/s have not only large discrepancies between the numerical models but also show a broader range in the experimental results. This is due to the mixture composition, as the lean mixture at high turbulence is more unstable, and different runs return substantially different results. It can also be seen that as u' increases, the faster the flame moves in space. Nevertheless, the most relevant trends are that the XiFoamA mode always overestimates the flame front position in time. In general, the TFC also tends to over-predict the results, especially at large turbulence levels. This is expected, given that the TFC is a correlation based of fully-developed flames and the flames here analyzed are still expanding. GTFC and GTFCp provide accurate results for all the cases except those that lay within the distributed flamelet regime, where the diffusivity affects the flame development. The behavior of the ETFC and the XiFoamT is comparable in many cases and extracting guidelines is not meaningful, as no generalized trend can be observed. The only remarkable fact is that within the distributed flamelet regime, the XiFoamT requires a larger ignition radius to allow for flame expansion.

Wrapping up, the conclusions that can be extracted from the numerical simulations performed for the spherical combustion chamber are multiple. First, it can be stated that the GTFC and GTFCp are verified, given that they actually produce the values of the correlations for Ξ that fit the experimental information (always taken into account that the correlation doesn't accurately fit all experimental results). Secondly, the behavior of the different combustion models has been assessed under controlled turbulence conditions to isolate the effects of the combustion and validate the different models and reassure the assumptions done when performing simplifications. The results obtained are in line with the models that had been previously presented in the literature (mainly TFC and ETFC) while the explanations for the other models (the XiFoam and GTFC based ones) have been provided, with some extrapolations and hypothesis for further analysis. Even if the behavior of these combustion models is explained for this simple experimental facility, generalizing them to larger and more complex geometries is not trivial. Thirdly, some limitations to all the models have been presented and should be taken into account when performing simulations of real scenarios cases.

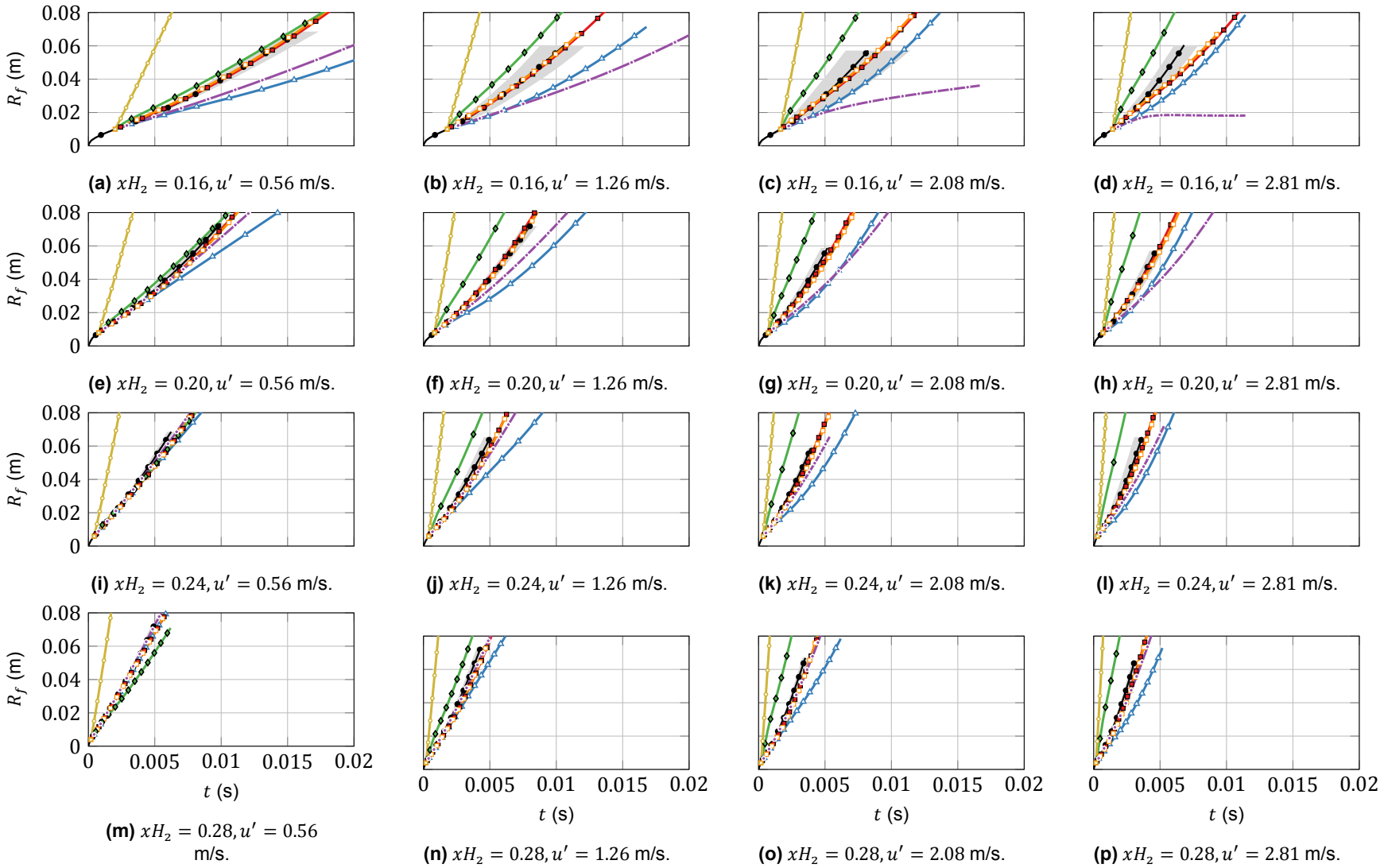

(a) $xH_2 = 0.16, u' = 0.56$ m/s. **(b)** $xH_2 = 0.16, u' = 1.26$ m/s. **(c)** $xH_2 = 0.16, u' = 2.08$ m/s. **(d)** $xH_2 = 0.16, u' = 2.81$ m/s.

(e) $xH_2 = 0.20, u' = 0.56$ m/s. **(f)** $xH_2 = 0.20, u' = 1.26$ m/s. **(g)** $xH_2 = 0.20, u' = 2.08$ m/s. **(h)** $xH_2 = 0.20, u' = 2.81$ m/s.

(i) $xH_2 = 0.24, u' = 0.56$ m/s. **(j)** $xH_2 = 0.24, u' = 1.26$ m/s. **(k)** $xH_2 = 0.24, u' = 2.08$ m/s. **(l)** $xH_2 = 0.24, u' = 2.81$ m/s.

(m) $xH_2 = 0.28, u' = 0.56$ m/s. **(n)** $xH_2 = 0.28, u' = 1.26$ m/s. **(o)** $xH_2 = 0.28, u' = 2.08$ m/s. **(p)** $xH_2 = 0.28, u' = 2.81$ m/s.

Figure 4.18: Numerical results for all the experimentally tested configurations of the spherical bomb, having increasing turbulence the most right the plot and increasing hydrogen concentration the more low the plot is, cf Figure 4.9. —●— represents the experimental results, —△— is the ETFC model, —■— is the GTFC model, —□— is the GTFCp model, —◇— is the GTFC model, —○— is the XiFoam algebraic model, and —·— is the XiFoam transport model.

4.3. Thermal-hydraulics, Hydrogen, Aerosol, and Iodine (THAI) containment

After having verified the combustion models with the one-dimensional turbulent flame and the spherical combustion chamber, together with some preliminary comparison between the different combustion models, the next facility poses a new set of challenges on its own. The Thermal-hydraulics, hydrogen, aerosol and iodine (THAI) containment (described in [70] and in [71]) is a larger facility than the spherical bomb (see the design of the vessel within the building in Figure 4.19, where a person for scale shows the size of the vessel), where other physical and flow phenomena become relevant. It is a project developed from 2007 by the OECD-NEA with the aim of obtaining experimental information for many fluid dynamic problems occurring in NPP: hydrogen distribution, hydrogen removal with PARs, and iodine and aerosol interactions with PARs. One of these objectives was the development of an experimental database to fill the gap in knowledge of hydrogen deflagration (hence the acronym HD to denote the relevant experiments) into vertically-oriented containments. The facility was developed by Becker Technologies GmbH with support from the German Ministry of Economics and Technology.

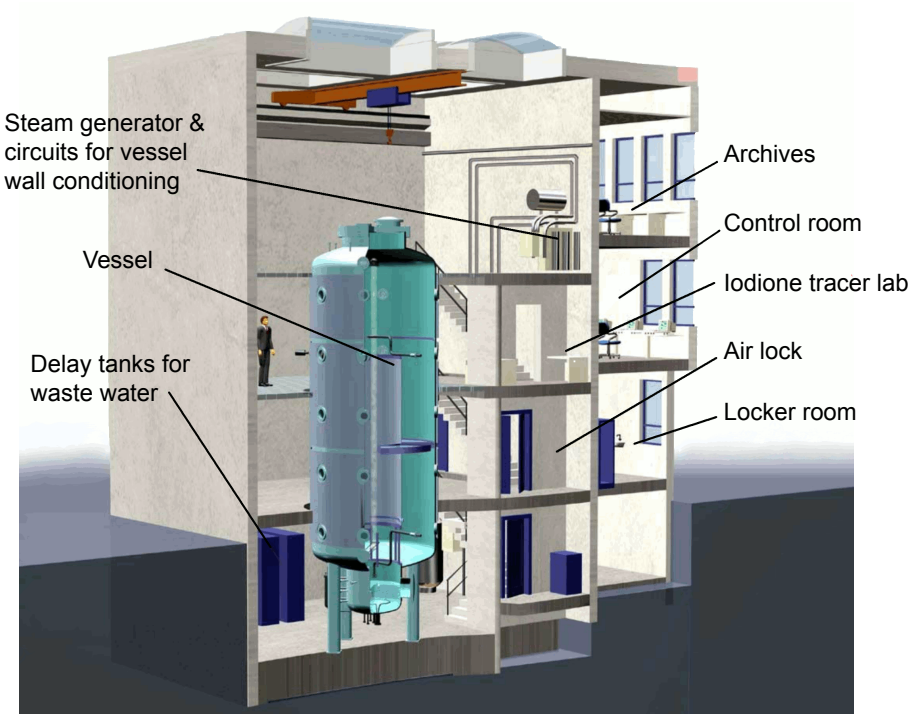

Figure 4.19: THAI physical description and building enclosure, modified from [53].

4.3.1. Facility description and experimental data description

The THAI containment has a main vessel with 9.2 m of height and 3.2 m of inner diameter made out of stainless steel, having a total volume of 60 m^3. It can withstand 14 bar of maximum pressure at 450 K. The containment is surrounded in its entirety with a 120 mm Rockwool thermal insulation. Moreover, the cylindrical part is double-walled (see red wall coloring in Figure 4.20a): first an inner wall of 22 mm thickness, then a gap of 16.5 mm filled with thermal oil to control the wall heating and cooling and finally an outer wall of 6 mm, which is coated with the Rockwool layer. Five block flanges (see white rectangles in Figure 4.20a) are installed in the vertical direction at heights of 2.1 m, 3.5 m, 4.9 m, 6.3 m, and 7.7 m, with two additional ones connecting to the non-cylindrical part of the vessel at 1.4 m and 8.4 m. Internal obstacles and condensate trays can be installed (see the cutaway of Figure 4.19), but for the deflagration experiments, no obstacles were considered. The selected test for the validation of the combustion models is the HD-15, as it consists of an ascending flame of a uniform mixture of hydrogen and air. Other tests were conducted including steam as a diluent and igniting at the top of

the vessel (the ignition locations can be seen as the red stars in Figure 4.20a). When igniting at the bottom (0.5 m above from the vessel's lower wall), buoyancy effects play a role in the experiment, as the initial conditions assume low values of turbulence. The experiment starts with the injection of the right proportion of hydrogen and air, gases that are mixed with the recirculation fans internally installed in the vessel. Between 10 and 15 minutes before igniting, the fans are disconnected, reducing turbulence in the containment. It can already be stated that the turbulent initial conditions prior to ignition were not measured, so the values used for the CFD calculations are taken from previous studies in the literature [117]. The other initial conditions of the HD-15 are a pressure of 1.504 bar, 366 K and 9.9 % in volume of hydrogen.

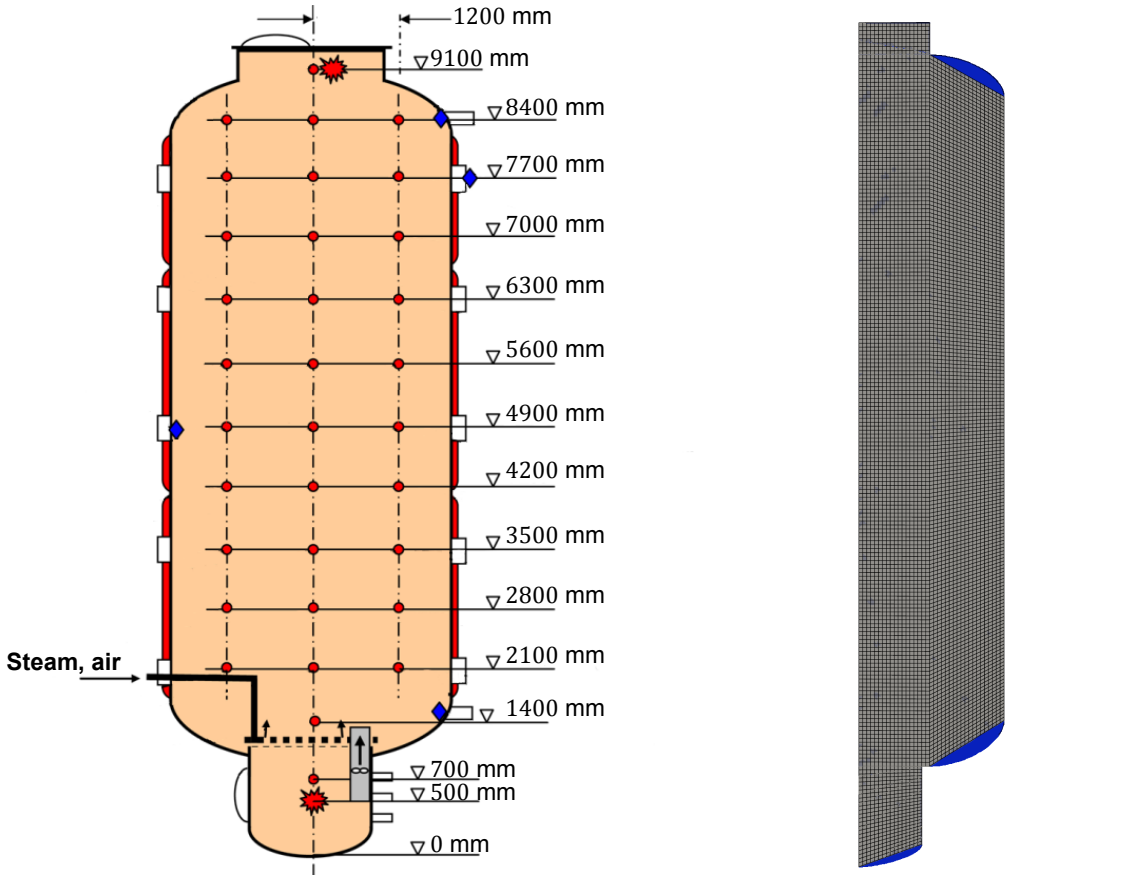

(a) THAI cutaway diagram with instrumentation, modified from [142].

(b) THAI real outline (blue) and grid simplifications.

Figure 4.20: THAI instrumentation and grid simplifications.

The instrumentation used to extract the data from the experiments consists of four systems. First, a 15-channel gas concentration measurement system is used to determine the amount of hydrogen present in the mixture before ignition. Second, an advanced flame front detection system is used: it consists of a grid of 43 fast thermocouples installed at different radial and axial locations (see the red dots of Figure 4.20a), that measures the flame arrival time as the appearance of the first steep change in temperature recorded. Third, a pressure measurement system comprised of four strain-gauge pressure transducers are installed at different locations of the wall (see the blue diamonds of Figure 4.20a). As it is a slow deflagration case, there is not a considerable pressure difference between probes, taking the results of the upper one for comparison with numerical results. Finally, 13 thermocouples are installed in the vertical direction of the vessel and others are installed in the walls to keep track of the temperature during the experiments. The repeatability of the test has been ensured by repeating the experiments multiple times and comparing the results in terms of pressure and temperature. Asymmetries have been found in the different runs, but they are caused by stochastic processes as turbulence or hydrodynamic instabilities rather than by fixed obstacles (as the fan, ignition system or injection pipe) [70].

4.3.2. Numerical simulation setup

After describing the experimental facility, the numerical simulation setup is introduced. Due to the different number of computational runs performed with the vessel, this section shows the parameters or configuration that are shared between all of them. Thus, and unless other clearly stated elsewhere, the configuration shown here applies to all the results of the section. The experimental facility presents an azimuthal symmetry that is again employed by using an axisymmetric geometry. This reduces the choice of boundary conditions only to the outer wall, as the axis of symmetry (with an `empty` boundary condition) and the axisymmetric planes (with a `wedge` boundary condition) are determined by the symmetry simplification. The boundary conditions used for the walls are presented in Table 4.6, where both ε and ω are included because turbulence models based on both are used. The initial turbulence values are the same as used in previous studies [117]. The ignition was performed by patching a region of 0.05 m with $\tilde{b} = 0$ and the adiabatic flame temperature. The laminar flame speed used is $S_L = 0.0897$ m/s. Since the turbulence is not controlled, as it was in the spherical combustion chamber, the combustion model uses the updated quantities from the turbulence model. Some meshing strategies have been used for the sake of higher quality metrics. If a structured, completely hexahedral mesh is desired, the curved transitions between the different-sized cylinders cause high skewed cells with large aspect ratios. Thus, the curves have been simplified to straight lines as can be seen in Figure 4.20b, where the blue contour represents the physical outline of the vessel and the computational mesh domain is represented in gray. Even if it can be argued that this can affect the results, previous studies [129] have used even more simplified geometries with only three concentric cylinders, in order to achieve higher grid quality. Numerical calculations were performed in parallel by using 16 processors.

Table 4.6: Boundary conditions for the THAI containment.

Field	Wall patches	
alphat	fixedValue	0
b	zeroGradient	
epsilon	epsilonWallFunction	4.8×10^{-5}
G	MarshakRadiationFixedTemperature	0
k	kqRWallFunction	1.5×10^{-4}
nut	nutkWallFunction	0
omega	omegaWallFunction	$\varepsilon/(\beta^* k) = 3.55$
p	zeroGradient	
Su	zeroGradient	
T	fixedValue	366.0
U	fixedValue	(0 0 0)
Xi	zeroGradient	

Buoyancy effects are relevant for the facility, so the buoyancy terms were included in the momentum and energy equations. The inclusion into the turbulence model is discussed in Section 4.3.5. The radiation was modeled with the P1 model, described in detail in Section 2.2.3, solving the radiation equations every 5 flow iteration timesteps. The custom implemented grey-mean absorption emission model, named `bGrayMeanAbsorptionEmission`, is used to compute the mixture properties while the wall properties are specified (having 0.001 m^{-1} for the emissivity and 0.8 m^{-1} for the absorptivity). The thermodynamic properties have been computed with the JANAF model (as the accuracy improvement compared to having a constant c_P is required to achieve a good peak pressure prediction) and the mixture coefficients were obtained from the `adiabaticFlameT` utility provided by OpenFOAM, as described in Section 3.6. The transport model assumed constant dynamic viscosity values (also described in Section 3.6), which is the same one used before for the spherical combustion chamber. All coefficients can be found in Appendix B.

4.3.3. Mesh sensitivity study

As done in Section 4.2.3 for the spherical combustion chamber, prior to assessing combustion and turbulence models, the independence of the results of the mesh resolution should be ensured. The numerical results are compared with the experimental results for three variables, namely vertical axial distance Y_f, flame front speed and vessel pressure (see for example Figure 4.21). The maximum distance over the y axis of the flame front was experimentally obtained with the flame front detection system. Numerically, the axial distance from the ignition point to the maximum vertical component of the isosurface $\overline{b} = 0.5$ is used. The derivative of this distance evolution in time provides the turbulent flame velocity, which is plotted versus the flame radius to avoid temporal shifts that may occur in the first plot. The high sampling throughput obtained with the solver postprocessing caused many fluctuations when computing the derivative, as it is an operation that exacerbates the subtle oscillations. Thus, the flame radius in time was interpolated with 50 equally spaced flame radii, $t = t(Y_f)$, taking the discrete derivative of each pair of points. Thirdly, the experimental pressure is compared with a probe located in the top wall of the computational domain. The pressure in the computational domain rises equally in all the cells belonging to the same horizontal plane, so probing any other location would provide similar trends. Metrics based on pressure, as the maximum pressure, maximum pressure rise or mean pressure rise were computed by taking the maximum or mean of the temporal evolution of the pressure or the pressure-time derivative, respectively.

The experimental results are briefly described, although the relevant phenomena are explained in more detail in the subsequent sections. The flame acceleration is caused in large part by the lower density of the ignited flame kernel: the buoyancy of the flame moves it upwards, causing turbulence and therefore flame expansion. The flame front velocity can be seen as almost linear during the first part of the vessel (up to $h = 5$ m). Then, there is an acceleration in the second part of the vessel which can be caused by many effects: the distortion of the flame moving towards the wall could promote an acceleration close to the wall, the higher temperature of the reaction due to the compression of the fresh gases can also increase the flame front velocity or the compression due to reflected acoustic waves bouncing from the top of the vessel that slows down the central part and increases mixing in the walls. Some of these effects can not be computed with the modeling assumptions that are considered.

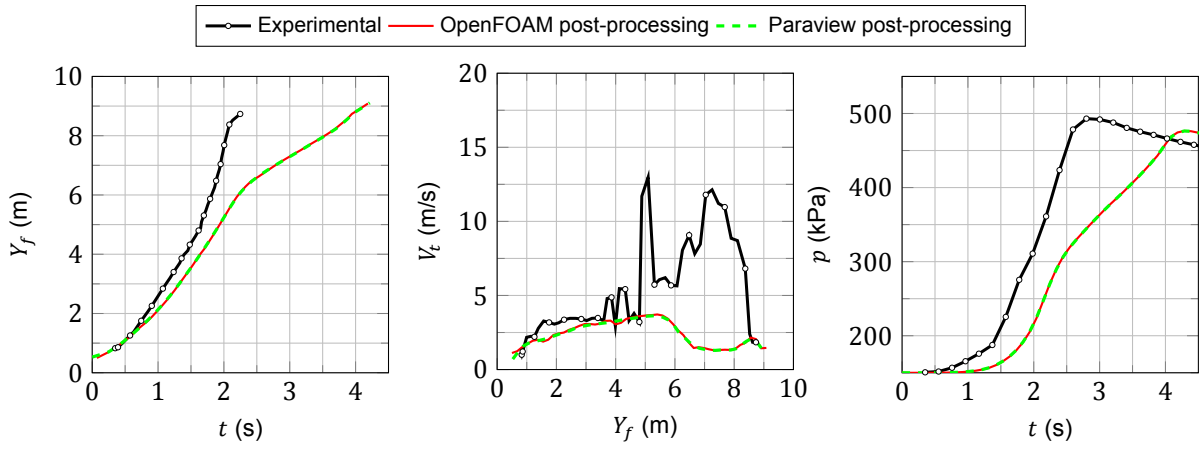

(a) Flame front location. **(b)** Flame front velocity. **(c)** Pressure.

Figure 4.21: Comparison of the postprocessing routines of Paraview and OpenFOAM with the experimental results.

Before showing the results of the mesh sensitivity study, the same procedure as for the spherical combustion chamber was followed for the THAI containment: the comparison of the postprocessing results obtained from OpenFOAM and Paraview. The results are shown in Figure 4.21. The procedure to compute the vertical location of the flame front is similar between OpenFOAM and Paraview, as both use the distance to either a group of cells between certain bounds or an actual isosurface (respectively). It is interesting to see how the results for the turbulent flame velocity are almost identical, even if the

OpenFOAM values have been interpolated to reduce the high amount of sampling points. The pressure sampling in both tools was performed the same way, with exception of the sampling frequency, having equal results in both. A temporal shift has been performed over the experimental data to match the first data point of the flame front vertical location with the average of the numerical simulations presented in each figure. The pressure was also corrected with the same temporal shift. All the results in the mesh sensitivity study have been obtained with the $k-\omega$−SST and the GTFC model.

As the geometry is considerably more complex than the spherical combustion chamber, the mesh sensitivity study required an approach of two parts, what explains the nomenclature used to describe the different meshes: Mp_qiqw. The first index p shows the resolution of the background mesh. It goes from zero to three, and each level has four times the amount of cells than the previous level (as each individual cell was divided in four instead of eight for a 3D problem, because the azimuthal direction still keeps one cell). How the different background meshes look can be seen from 4.22a to Figure 4.22d. From these, a refinement of the wall and ignition region was performed in order to systematically approach the refinement level of M3_0i0w. The wall refinement region was taken to be 0.1 m and the ignition was centered in the symmetry line at a height of 0.6 m with a radius of 0.2 m. The ignition refinement wasn't centered in the ignition location (which was located at 0.5 m) given that the buoyancy effects move the kernel upwards, requiring more refinement above than below the ignition location. The second index describes the local resolution of the ignition and the walls going from 0 (which means no refinement over the baseline grid) to 3 (with three levels of refinement together with transition cells between levels), as it can be seen throughout Figure 4.22. There are no cells smaller than those of the most refined baseline grid (i.e. M3_0i0w).

Adaptive Mesh Refinement (AMR) was also used. The main drawback of the current implementation is that the initial cell refinement level is not transferred to the AMR algorithm: any cell is refined if the selected variable lies between bounds, regardless if it was initially refined. In order to avoid a refinement on regions that were already refined (i.e. walls and ignition region), the AMR use has been restricted to the uniform baseline meshes (from Figure 4.22a to Figure 4.22d). The activation of AMR was delayed until $t = 0.5$ s to allow some flow development. The exact number of cells, along with the corresponding computational time, is presented in Table 4.7.

Table 4.7: Computational time in hours and number of cells (in parentheses) of the mesh sensitivity study of the THAI vessel. The adaptive mesh refinement cases show the initial number of cells.

	M0	M1	M2	M3
0i0w	0.0505 (7204)	0.2964 (28816)	2.4089 (115264)	43.7994 (461056)
1i1w	0.1352 (9142)	0.8255 (37882)	7.8686 (147019)	
2i2w	0.4377 (19033)	3.6705 (71614)		
3i3w	6.6172 (52837)			
AMR1	0.1200 (7204)	0.4867 (28816)	3.8258 (115264)	
AMR2	0.1769 (7204)	1.2647 (28816)		
AMR3	0.7275 (7204)			

To compare the performance of all the grids, Figure 4.23 presents the results for the background grids, i.e. Mp_0i0w. From these figures, two things can be extracted. Firstly, the most refined mesh (M3_0i0w) captures the acceleration at $h = 5$ m while none of the other models does. The pressure curve for this mesh shows an excellent agreement with the experimental results. Secondly, the first part of the vessel, $h < 5$ m, shows a convergence the more refined the grid is, attaining mesh independence for M2_0i0w.

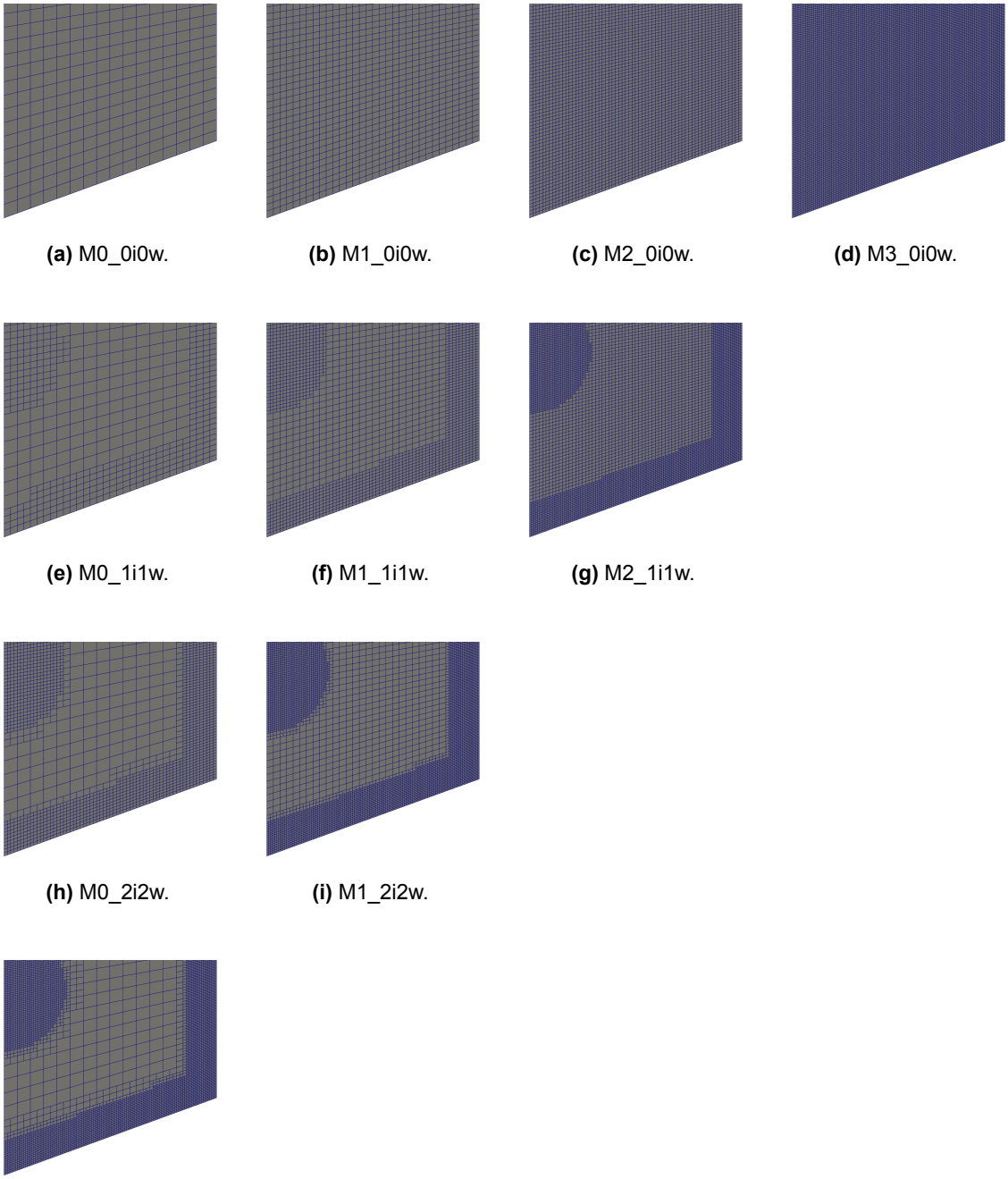

(a) M0_0i0w. **(b)** M1_0i0w. **(c)** M2_0i0w. **(d)** M3_0i0w.

(e) M0_1i1w. **(f)** M1_1i1w. **(g)** M2_1i1w.

(h) M0_2i2w. **(i)** M1_2i2w.

(j) M0_3i3w.

Figure 4.22: Detail of the mesh sensitivity strategy followed.

The results of applying the AMR over the background mesh can be seen in Figure 4.24. The three background grids that allow for wall refinement were simulated with AMR, having as reference the cell size of M3_0i0w. Thus M0 allowed for AMR with one, two, or three levels of refinement. However, no combination was able to capture the second acceleration of the flame. The adaptive mesh refinement provides a more detailed flame front resolution, but this doesn't necessarily translate into an improvement of the flame front dynamics.

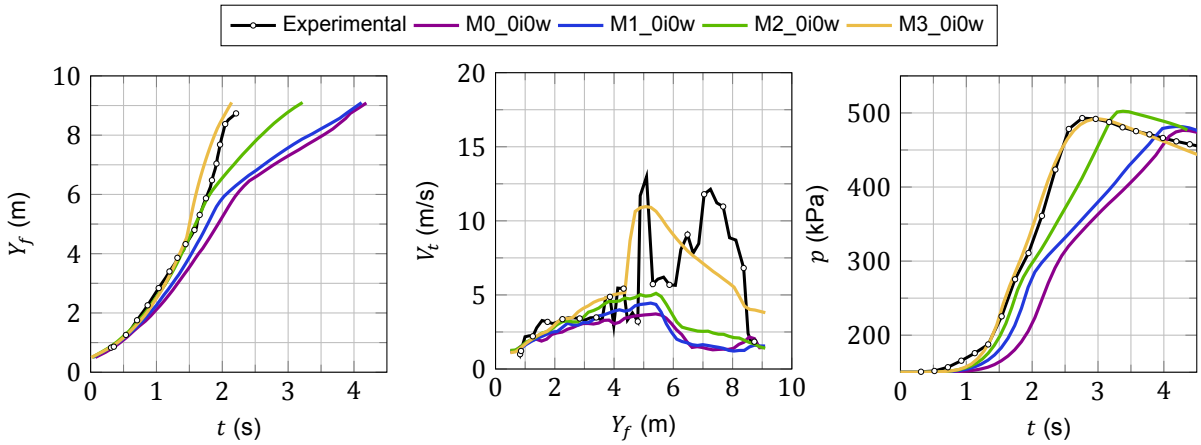

(a) Flame front location. **(b)** Flame front velocity. **(c)** Pressure.

Figure 4.23: Mesh sensitivity THAI vessel: background meshes without further refinements at the wall nor the ignition region.

One interesting result is that, with the exception of M1_AMR1, all the other grids with AMR predict an earlier flame front arrival time of around 1 s than the same grid without mesh refinement. The case of M1_AMR1 is particular: the arrival time for M1_0i0w is a little above 4 s and the time of arrival for M1_AMR1 is slightly below 4 s. It was expected that AMR will only refine locally, not triggering turbulence generation in the flame front near the wall. However, changing the flame front can produce significant differences. Four grids are plotted in Figure 4.25: mesh M0_0i0w in Figure 4.25a, mesh M1_0i0w in Figure 4.25b, mesh M1_AMR1 in Figure 4.25c and mesh M0_AMR1 in Figure 4.25d. It can be seen that the effects of AMR are more pronounced in M0 than in M1, having a different shape of the flame front, creating a more symmetric flame (with respect to the axisymmetric axis) in the case of M0_AMR1. The reason why AMR doesn't trigger this effect on M1 with just one level of refinement (although it does for two) is not clear. The consequences are two. Firstly, M0_0i0w, M1_0i0w, and M0_AMR1 have the most upper flame front location not exactly in the centerline but with an offset from it (not having a symmetric flame). This denotes different dynamics in the flow field within the flame, having that these dynamics are even more accentuated when the flame reaches the end of the vessel. Secondly, M0_AMR1 doesn't have the centerline flame front gradient aligned with the vertical direction, so (assuming the same values for all the other variables) the source term causes the flame in M1_AMR1 to expand slower vertically than in M0_AMR1.

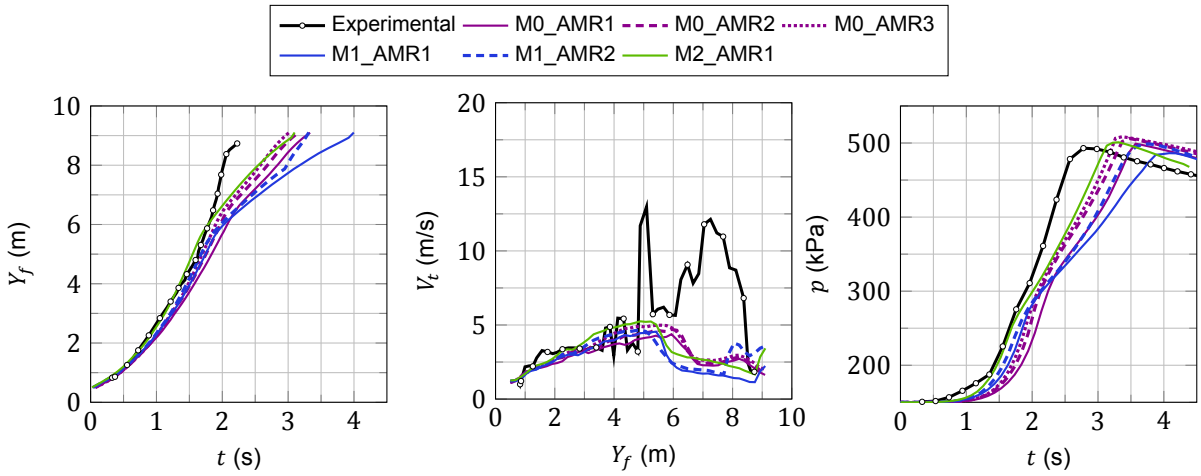

(a) Flame front location. **(b)** Flame front velocity. **(c)** Pressure.

Figure 4.24: Mesh sensitivity THAI vessel: results with adaptive mesh refinement.

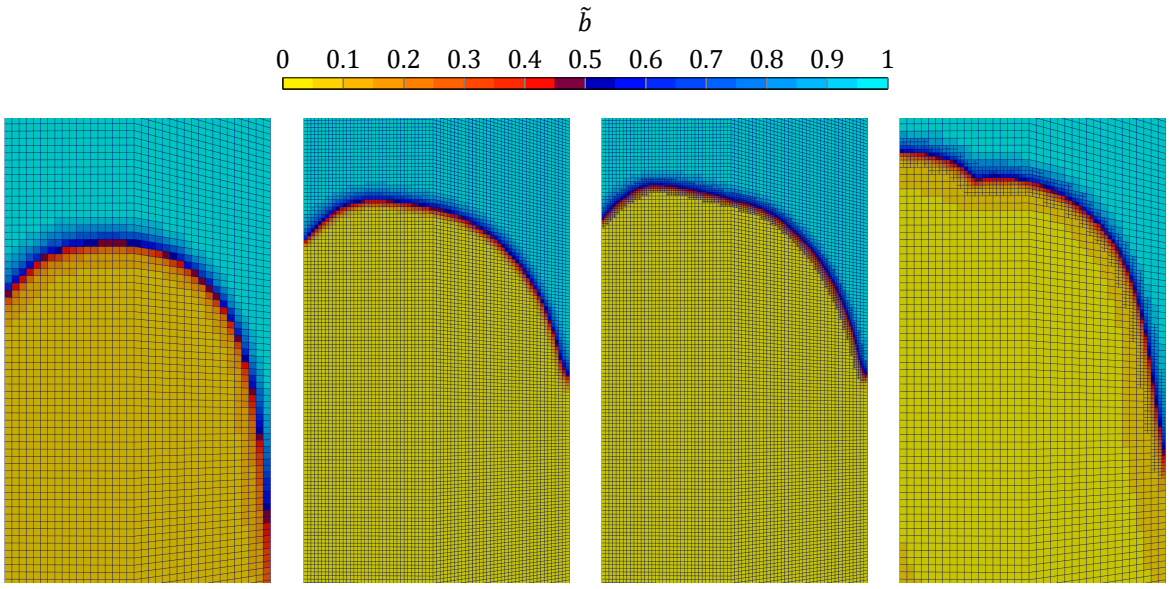

(a) M0_0i0w. **(b)** M1_0i0w. **(c)** M1_AMR1. **(d)** M0_AMR1.

Figure 4.25: Detail of the flame front evolution at the centerline at $t = 2.3$ s for selected grids.

Finally, in Figure 4.26 the results for the grids with the same level of refinement in the wall and ignition regions but with different background grid resolutions can be observed. Except M0_3i3w, which suffers from a delayed flame expansion due to excessive turbulence generation near the flame in the transition between refinement levels and also overpredict the peak pressure, all the other grids show good agreement in terms of the vertical flame front coordinate and the pressure. Regarding the flame front velocity, both M1_2i2w and M2_1i1w can capture the acceleration at the half vessel, even if the magnitude of M1_2i2w is smaller.

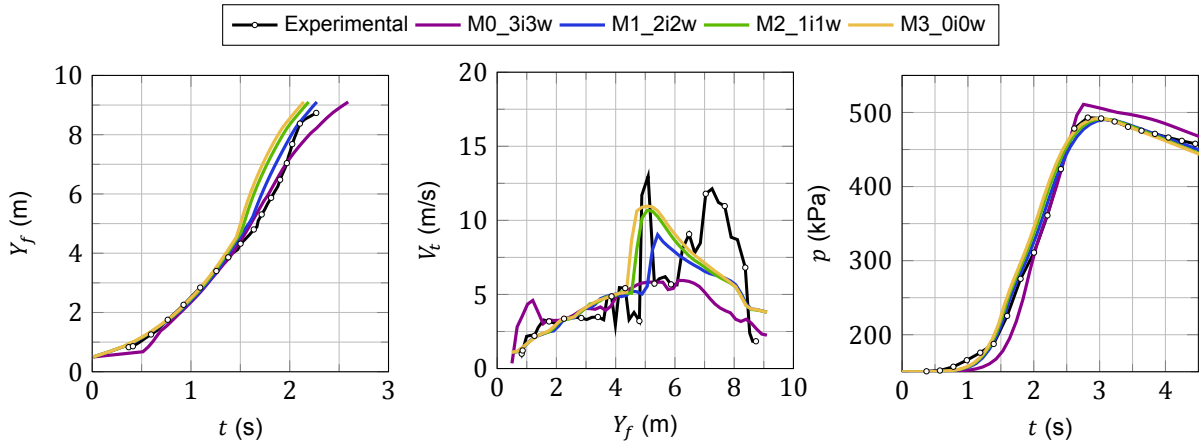

(a) Flame front location. **(b)** Flame front velocity. **(c)** Pressure.

Figure 4.26: Mesh sensitivity THAI vessel: same ignition and wall refinement, different background mesh resolutions.

To further support the choice of one grid over the other, some metrics are shown in Table 4.8. Only the results of some selected grids have been included for brevity. The relative error is computed with respect to the experimental results but it can be seen that the sign of the relative error has been left. When dealing with nuclear safety it is no the same as overpredicting the maximum allowable pressure of a containment or underpredicting it. Even if the relative errors seem large, specially those of the pressure rise, the order of magnitude is similar to previous studies with other solvers [117], attaining if not the same even better relative errors. It can be seen that, even if the peak pressure error is the

same for both M0_0i0w and M0_3i3w grids, the remaining metrics present considerably better results for the M0_3i3w mesh than for the M0_0i0w mesh. The last three rows show M1_2i2w, M2_1i1w, and M3_0i0w, which are considered to be the best grids based on the previous images. All three have the maximum pressure rise as the worse metric, but the other two perform similarly in all of them.

Table 4.8: THAI vessel pressure metrics for the selected relevant meshes.

Combustion model	Peak pressure [Pa] (Relative error [%])	Max. pressure rise [Pa/s] (Relative error [%])	Mean pressure rise [Pa/s] (Relative error [%])
M0_0i0w	476610.44 (-3.48)	238096.49 (-30.52)	154677.85 (-35.30)
M0_3i3w	510976.54 (3.48)	373831.10 (9.08)	274767.21 (14.93)
M1_2i2w	490488.08 (-0.67)	273276.90 (-20.25)	206248.98 (-13.73)
M2_1i1w	491391.17 (-0.48)	288432.11 (-15.83)	212485.53 (-11.12)
M3_0i0w	492006.22 (-0.36)	292543.87 (-14.63)	211709.98 (-11.44)
Exp	493783.59 (0.0)	342686.89 (0.0)	239070.48 (0.0)

With the current approach and the previous results, the mesh that has been selected to perform the rest of the simulations of THAI is M1_2i2w. It shows mesh independent results, comparable to those of M3_0i0w (see Figure 4.26 as well as Table 4.8) without incurring into the large computational costs of M2_1i1w or M3_0i0w. Thus, it is the mesh represents the most desirable tradeoff between accuracy of the results and computational expenses. However, the best strategy would also include local refinement in the flame front with AMR. Since this is not possible with the current implementation, it is suggested to be investigated in the future: preserving the cell level from the baseline grid when refined with the local refinement can be used as an ulterior variable to perform AMR.

4.3.4. Courant–Friedrichs–Lewy number investigation

As described in the methodology (see Section 3.1), two Courant-Fredrichs-Lewy numbers, are used during the simulation: one based on the flow velocity ($\mathrm{Co}_{\mathrm{CFL}}$) and the other one based on the turbulent flame speed (Co_{S_t}, which thanks to the bound $\Xi > 1$ makes S_t equal or larger than S_L at any time). It was expected that by using $\mathrm{Co} < 1$, the condition to achieve convergence was fulfilled, not requiring further analysis. If only the flow-based CFL number is used, experimental cases as THAI where the initial flow field is zero will make that the CFL tends to zero, so the timestep increases without considering the combustion flame speed. Nevertheless, with the inclusion of the S_t based CFL number, it was expected to achieve convergence if the flow did fulfill $\mathrm{Co} < 1.0$. However, after performing different simulations it was clear that some models largely depend on the value chosen to limit the timestep determination.

First, the GTFC model with the $k-\omega-$SST was tested. This model was used for the mesh sensitivity study, where a value of $\mathrm{Co} < 0.40$ was employed to determine the timestep to advance the simulation in time. This value was chosen to keep a safe distance to the $\mathrm{Co} < 1$ convergence condition, as during a single timestep the velocity could suddenly increase in some cells causing the Co to locally go above one. This combination of combustion and turbulence model is just slightly sensitive to the $\mathrm{Co}_{\mathrm{max}}$ used, as it can be seen in Figure 4.27, having $\mathrm{Co}_{\mathrm{max}} = 0.05$, $\mathrm{Co}_{\mathrm{max}} = 0.10$, $\mathrm{Co}_{\mathrm{max}} = 0.40$ and $\mathrm{Co}_{\mathrm{max}} = 0.80$. The results for all the cases where $\mathrm{Co}_{\mathrm{max}} > 0.10$ are almost the same, having the largest differences in the flame front velocity. The only case where results are significantly different is with $\mathrm{Co}_{\mathrm{max}} = 0.05$, where the small timesteps obtained from the small maximum Co number make the solver too dissipative so that the flame doesn't expand from the initial conditions. The temporal derivative term of the regress variable transport equation is negligible when compared with the other terms of the equation, so there is no change in time. Even if the simulation time of the case with $\mathrm{Co}_{\mathrm{max}} = 0.10$ was around four times

higher than that of $Co_{max} = 0.40$, in order to provide fully consistent results, the following simulations all have been carried out with $Co_{max} = 0.10$.

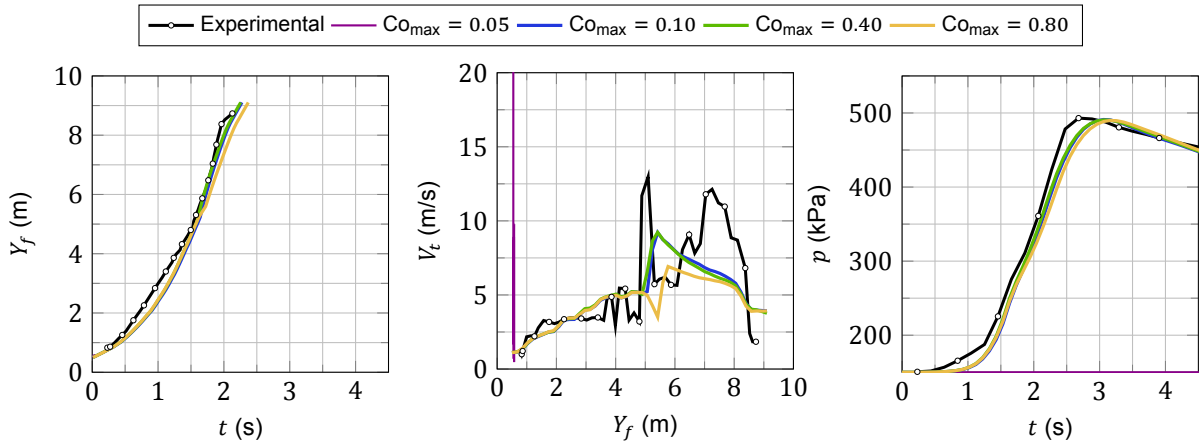

(a) Flame front location. **(b)** Flame front velocity. **(c)** Pressure.

Figure 4.27: Effect of the maximum Courant number in THAI vessel for the GTFC with the $k-\omega$−SST.

However, this behavior was not seen with all models. For example, the TFC model combined with the buoyant-$k-\varepsilon$ model is strongly dependent on the Co_{max} chosen. In Figure 4.28 the same four Co_{max} tested before for the GTFC are shown for the combination of TFC with buoyant-$k-\varepsilon$. In fact, only one of the four ones doesn't prematurely end. $Co_{max} = 0.05$ produces the same results as the GTFC with $k-\omega$−SST without promoting the flame expansion. $Co_{max} = 0.40$ and $Co_{max} = 0.80$ crash because the timestep is too large for a sudden change in the velocity flow field. This happens in both cases when the flame front first contacts with the right wall, creating unphysical values of turbulence and leading the solver to a halt. Moreover, it can be seen that the development of the flame is slower in $Co_{max} = 0.40$ and in $Co_{max} = 0.80$ (before crashing) than in $Co_{max} = 0.10$. The reasons under this behavior are unclear: it is believed that smaller timesteps make up for a more stable simulation and promote turbulence generation which induces larger S_t, as long as the timestep is not too small to make the flame not expand (which is what occurs with $Co_{max} = 0.05$).

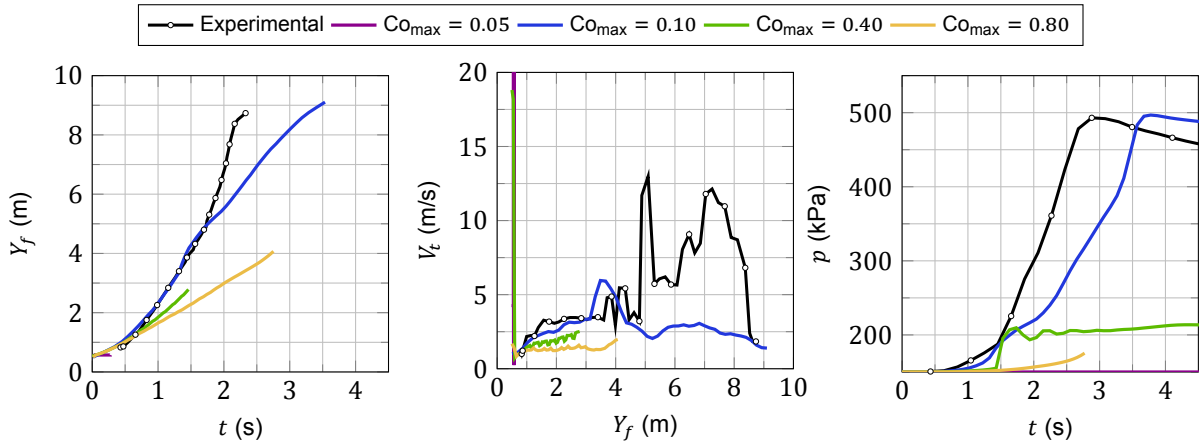

(a) Flame front location. **(b)** Flame front velocity. **(c)** Pressure.

Figure 4.28: Effect of the maximum Courant number in THAI vessel for the TFC combined with the buoyant $k-\varepsilon$.

To further support the previous discussion, it can be seen in Figure 4.29 the regress variable field at the same timestep for three different Co_{max} values (the smallest one not being included as the flame doesn't expand from the initial conditions). For large CFL values, the ignited flame kernel expands too slowly compared to the force caused by buoyancy effects. This makes that the burnt, low-density products rise as if a bubble within a flow column. This motion causes the burnt region to be within a vortex flow field that imparts a rotational velocity on the flame, creating the shape shown in Figure 4.29c. If the maximum allowable Courant number is reduced more, the flame kernel from ignition expands slightly before ascending, creating a vortex and crashing when the flame front touches the wall. Neither of these behaviors appears in the $Co_{max} = 0.10$, so it is the maximum Co number that has been used to determine the timestep of the simulations presented from now on.

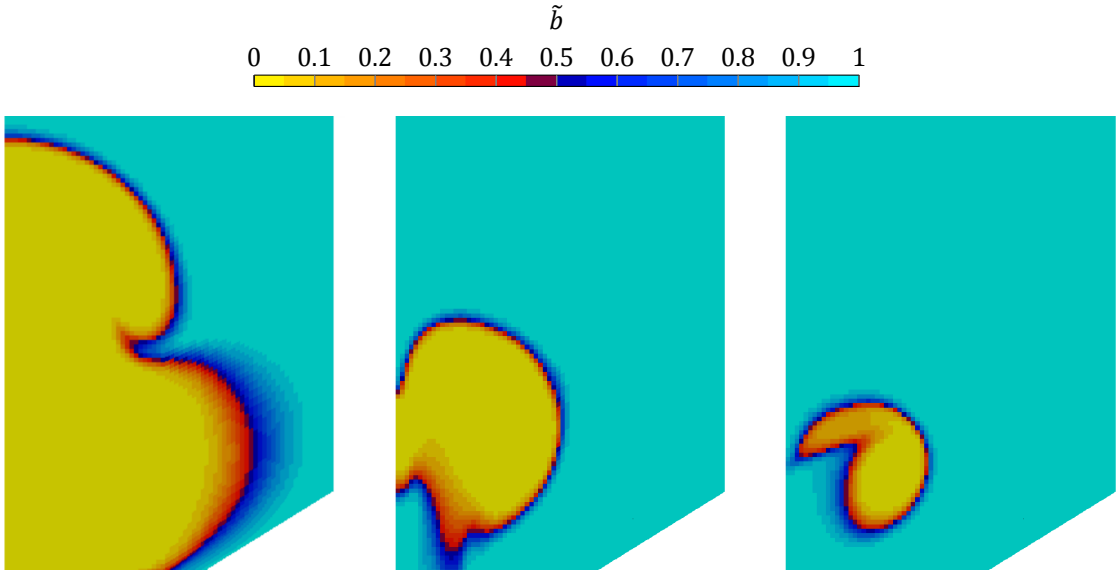

(a) $Co_{max} = 0.10$. **(b)** $Co_{max} = 0.40$. **(c)** $Co_{max} = 0.80$.

Figure 4.29: Detail of the flame front with the TFC model at different Courant number, time = 1.3 s.

4.3.5. Turbulence model effects

This subsection attempts to show some preliminary results of the use of different turbulence models with selected combustion models. As explained in the methodology, OpenFOAM has already included many models from which the $k-\varepsilon$, buoyant-$k-\varepsilon$, $k-\omega$ and $k-\omega$−SST have been selected for this study. It is expected that more recent models as the $\overline{v^2}-f$ or Reynolds Stress Models could provide better results, not to mention that simulating the case with LES would yield even more accurate results. Even if the formulation of the models is similar, including or replacing just a few terms between them, they influence the combustion model making it perform completely differently in some cases.

The four turbulence models with the TFC combustion model are presented in Figure 4.30. For this combustion model, it can be seen that the only model that predicts a flame development close to the experimental results is the buoyant-$k-\varepsilon$. All the other models don't include a term related to buoyancy generation in the turbulence transport equations, predicting a flame rising without largely expanding, entering a vortex flow similar to the one described in the previous subsection for large values of Co_{max}. Thus, the flame rises slower (as it is mainly driven by buoyancy) and the pressure rise doesn't even approach the experimental maximum value (because the flame front doesn't expand). Buoyancy terms in the turbulence model promote flame expansion: even if there is an increase in the dissipation as well, the flame-rising motion creates turbulence that is required in the combustion model. The bound $\Xi > 1$ is physically correct, but large values of turbulence may be required until the actual value of $S_t > S_L$, so the flame can expand faster. Similar behavior was obtained with other models (namely the ETFC, the XiFoamA, and the XiFoamT).

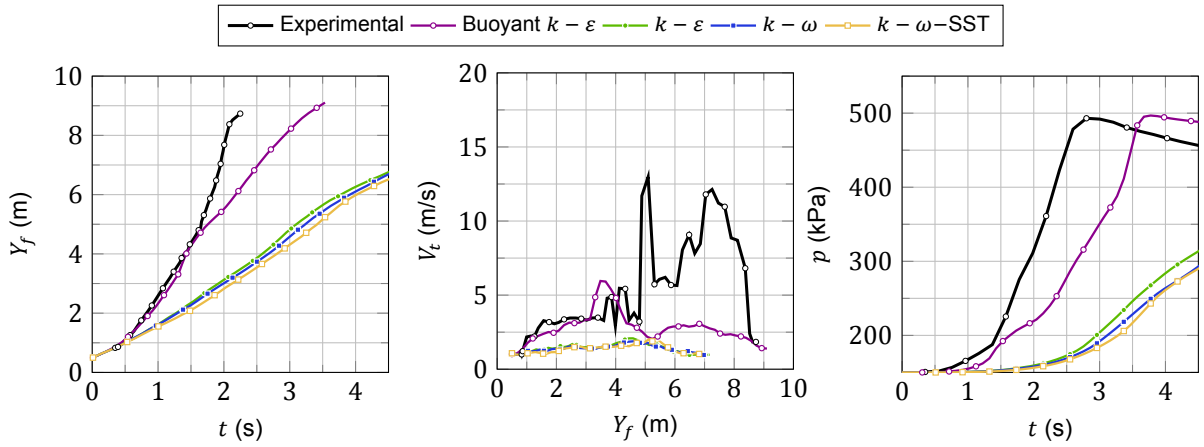

(a) Flame front location. **(b)** Flame front velocity. **(c)** Pressure.

Figure 4.30: Comparison of the TFC with different turbulence models.

The GTFC-based models are not affected as the flame radius and Lewis number dependence makes the unbounded S_t value to be closer to S_L (even if at earlier stages the bound $\Xi > 1$ is being used). However, the GTFC-based models require a smaller turbulence generation, which combined with the flame expansion quickly makes $S_t > S_L$ without requiring bounds. Thus, the flame expands while rising, being less sensitive to the turbulence models compared to the other combustion approaches. The results for the GTFC can be seen in Figure 4.31. The buoyant-$k-\varepsilon$ and $k-\omega$ turbulence models give similar performance. The $k-\omega$−SST model, due to its blending functions, achieves a more controlled turbulence values and therefore flame ascent.

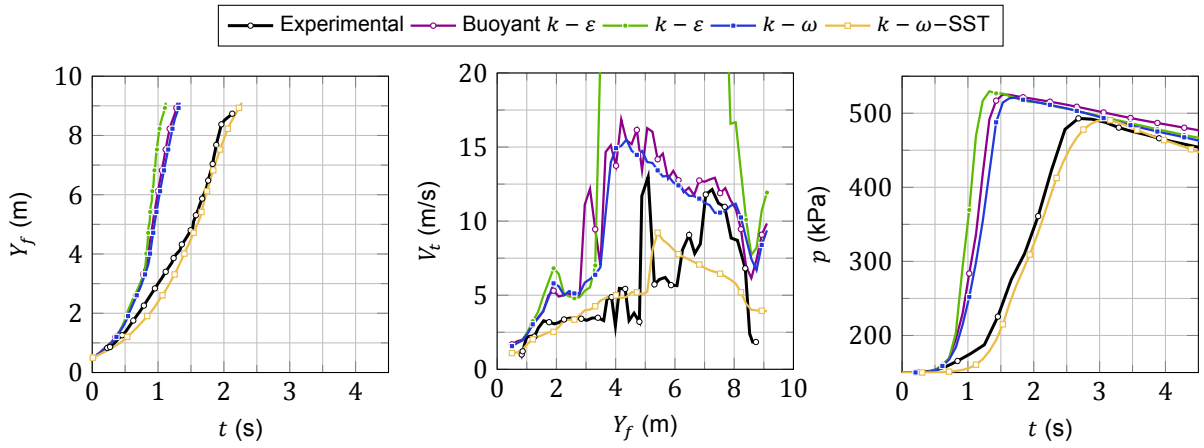

(a) Flame front location. **(b)** Flame front velocity. **(c)** Pressure.

Figure 4.31: Comparison of the GTFC with different turbulence models.

It is somehow counterintuitive that adding the buoyancy term in the turbulence transport equations of the $k-\varepsilon$ gives slower flame front velocities than not adding it (see Figure 4.31a). To further understand the effects of the turbulence models, the regress variable field when the flame front is around 7.0 m for the different considered models can be seen in Figure 4.32. All the models have a flame front propagating close to the wall, as the combustion model is the GTFC, which doesn't limit S_t values at the wall. It can be seen that the wall development is larger in the $k-\varepsilon$ than in the buoyant-$k-\varepsilon$, having also a more developed central flame. The limitations of the $k-\varepsilon$ model (with and without buoyancy term) for internal flows are known. Moreover, the buoyant-$k-\varepsilon$ also includes a dissipation term in the turbulence model due to the buoyancy effects, which can explain the faster flame expansion in the $k-\varepsilon$.

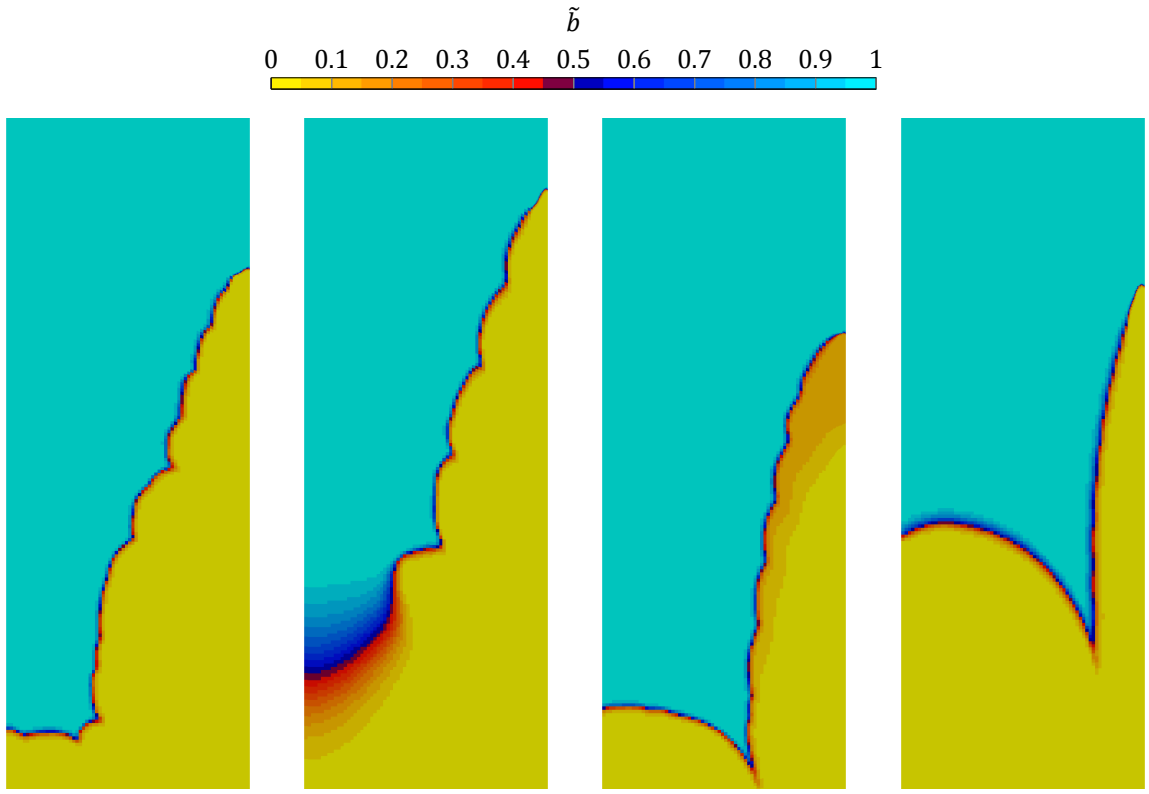

(a) Buoyant-$k-\varepsilon$, $Y_f = 7.35$ m at $t = 1.1$ s ($t = 1.0715$ s).

(b) $k-\varepsilon$, $Y_f = 7.86$ m at $t = 1.0$ s ($t = 0.9587$ s).

(c) $k-\omega$, $Y_f = 6.93$ m at $t = 1.1$ s ($t = 1.1062$ s).

(d) $k-\omega$−SST, $Y_f = 7.24$ m at $t = 1.9$ s ($t = 1.8640$ s).

Figure 4.32: Regress variable field snapshots when $Y_f \simeq 7.0$ m for different combustion models with the GTFC combustion model. The exact time at which $Y_f = 7.0$ m is presented between brackets.

Finally, and given the expected accuracy improvement of the GTFC-wb combustion model, it was also assessed under different turbulence models (see Figure 4.33 for the results). The $k-\omega$−SST is, as with the GTFC, the model that predicts a slower flame front development. However, when combined with the wall bounding approach in the combustion model (which reduces the flame front expansion at the wall, due to constrained S_t values) an underprediction of the flame velocity is observed. The slow flame velocity causes a slower rise in the pressure in the second half of the domain, producing a smaller pressure peak in the domain. The smaller peak pressure due to slower pressure rise is a behavior seen in mixtures with diluent [117] but it shouldn't be predicted in this case. The behavior of the other turbulence models is similar. The only feature that requires further explanation is the strange pressure profile around $t = 2$ s of the buoyant-$k-\varepsilon$, as shown in Figure 4.33c. This is caused by a sudden generation of turbulence near the wall due to the buoyancy term in the turbulence transport equations. Higher turbulence makes S_t values and diffusion coefficients higher, causing a flame front spreading. However, with the GTFC-wb, it also affects the blending function. The boundary layer has been thickened, so the GTFC model has switched to the TFC in a larger area, creating a sudden change in the flow dynamics leading to the rapid increase in the pressure. The $k-\omega$ is the model that best performs in the flame front development and velocity, although it overpredicts the time at which the maximum pressure is attained.

This section cannot be concluded without stating that the only model that should be applicable in THAI is the buoyant-$k-\varepsilon$. All the other models lack the buoyancy terms in the turbulence transport equations, which in a scenario where buoyancy effects are characteristic shouldn't be neglected. As it was outside the scope of this thesis, the buoyancy source terms weren't included in the $k-\omega$ nor the $k-\omega$−SST models, but a fair comparison would require the inclusion of these terms in the corresponding equations, so all models create turbulence due to buoyancy flow motion.

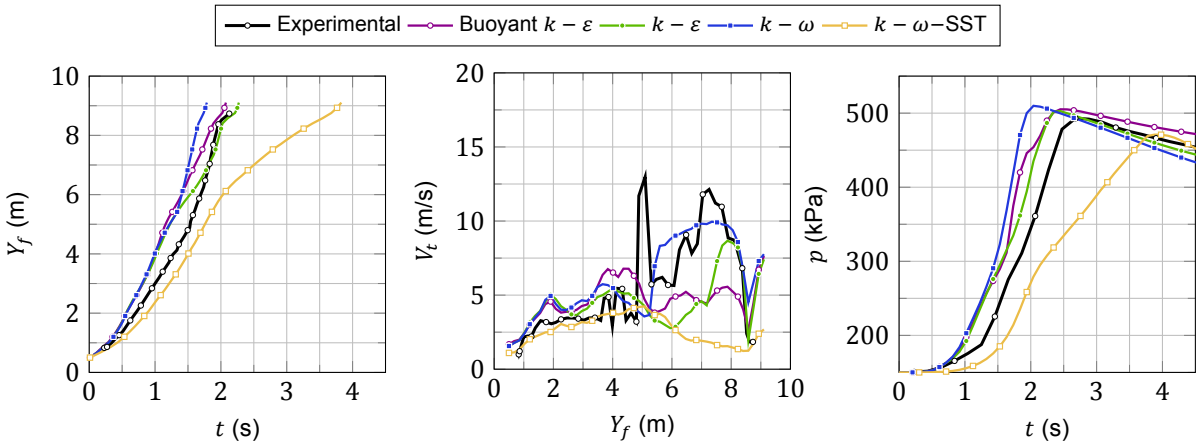

(a) Flame front location. **(b)** Flame front velocity. **(c)** Pressure.

Figure 4.33: Comparison of the GTFC-wb with different turbulence models.

4.3.6. Combustion model analysis

To conclude the results of the THAI containment, the comparison of the different combustion models is shown here. As previously discussed, the behavior of the regress variable equation is largely conditioned by the turbulence model: not only does it affect the flow field in which $\tilde{b}$ is being transported but also dictates the rate at which $\tilde{b}$ moves and spreads (through S_t and D_t). Thus, all the models have been evaluated with the buoyant-$k-\varepsilon$ and the $k-\omega$−SST.

In Figure 4.34, the results for the seven combustion models with the $k-\omega$−SST combustion model are presented. As discussed before, the TFC, the ETFC, and the XiFoam-based solvers require the buoyancy term in the turbulence equations to achieve flame expansion and not only the flame rising due to buoyancy. The slower combustion makes that the peak pressure is not attained within the 5 s of simulation and, as described before, is lower than that of the other models. Among the GTFC-based models there are also some discrepancies. The GTFCp overpredicts the flame front location evolution in time (having, therefore, a larger flame velocity which is also larger than the experimental) and also the pressure peak. The flame radius appears twice on the wrinkling factor correlation of the GTFCp (see Equation 3.45). The GTFCp model yielded good results in the case of the spherical bomb, but THAI presents considerably larger dimensions, so interactions with the extra R_f in the correlation are observed. The GTFC shows a good agreement in terms of the flame front location, the flame velocity, and the pressure profile. Finally, the GTFC-wb follows the GTFC during the first half of the vessel and it flattens of during the second half, leaning more towards the TFC trend.

The second tested turbulence model is the buoyant $k-\varepsilon$, given that it is the only one that accounts for buoyancy-generated turbulence. The results for the combustion models can be seen in Figure 4.35. The behavior of the GTFCp follows that of the GTFC: the turbulence generated by the buoyancy motion of the burnt products generates higher turbulence, causing higher S_t values that can also be seen in the flame velocity plot (see Figure 4.35b. The GTFC-wb, previously discussed, has more restricted effects from the buoyancy-generated turbulence, as it switches to the TFC model close to the wall. The results of the ETFC are close to those of the GTFC-wb in terms of the Y_f and also of the flame velocity, but not in the pressure, overpredicting the peak and the arrival time. The ETFC required extra bounding in the turbulence model to avoid unrealistic generation of turbulence during the simulation. The other models (the TFC, the XiFoamA, and the XiFoamT) present similar results in terms of the flame front location and velocity. All these three models underpredict the time at which the maximum pressure occurs. Both the ETFC and the XiFoamA were halted before reaching the specified simulation end time. This was caused in the two cases by high turbulence values in the upper-right corner of the main cylindrical part that triggered high-velocity values that couldn't be accommodated by the automatic timestep algorithm. However, this happens after reaching the maximum pressure, so the statistics of the results can be computed.

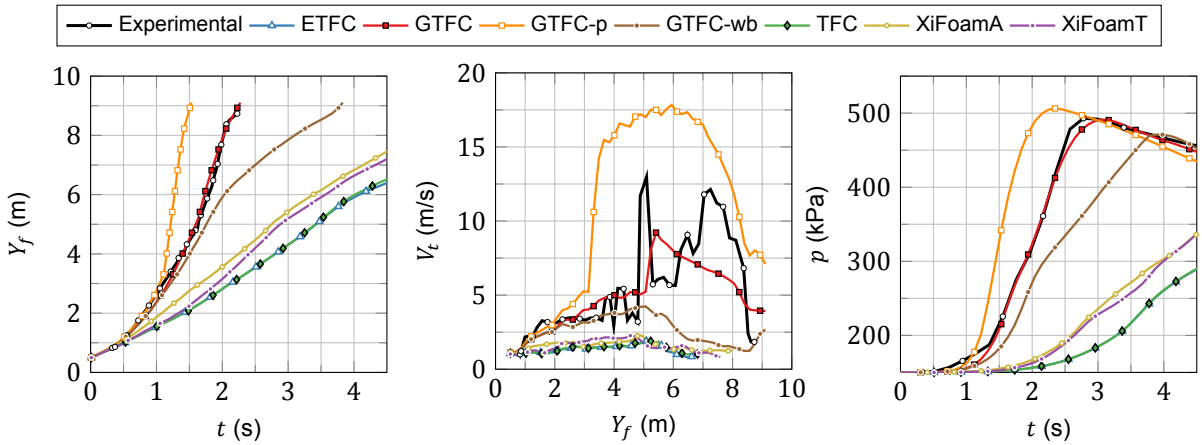

(a) Flame front location. **(b)** Flame front velocity. **(c)** Pressure.

Figure 4.34: Comparison of the combustion models with the $k-\omega$−SST.

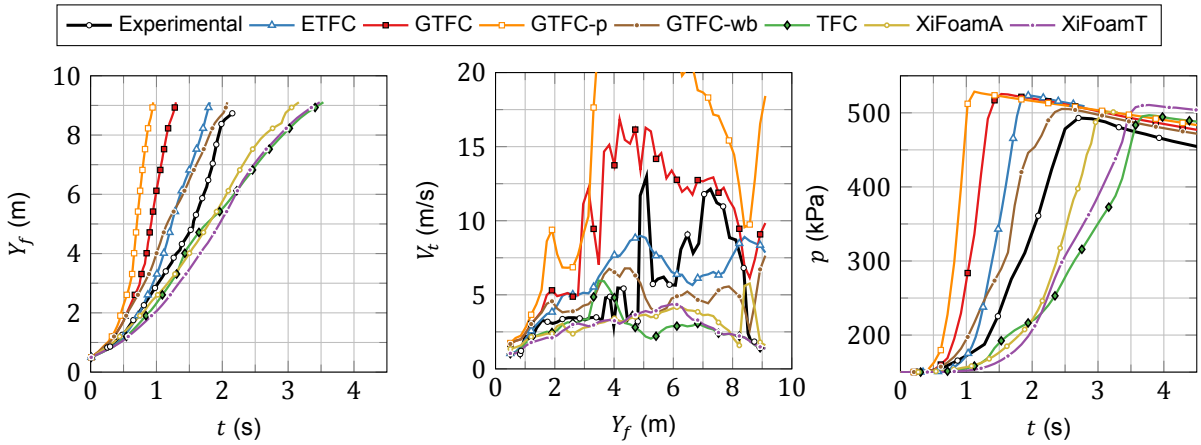

(a) Flame front location. **(b)** Flame front velocity. **(c)** Pressure.

Figure 4.35: Comparison of the combustion models with the buoyant $k-\varepsilon$.

To further support the discussion, the regress variable field is compared to the experimental data obtained from the flame front detectors. These contours are shown in Figure 4.36a, having considered two combustion models for the numerical results with the $k-\omega$−SST turbulence model, namely the GTFC (see Figures 4.36b, 4.36c, and 4.36d) and the GTFC-wb (see Figures 4.36e, 4.36f, and 4.36g). The experimental results show the flame front at different times: the flame kernel starts with a bubble-like shape which ascends in the middle of the vessel until half the height. At this point, when the flow dynamics start to become more complex, the bouncing acoustic pressure oscillations from the top of the containment, combined with the turbulence generated at the walls and with the higher reactivity of the compressed unburnt gases creates a flame front that moves closer to the wall. The numerical results are plotted for flames with similar flame front heights, even if that means different timesteps. The flame at $Y_f \simeq 2.0$ m presents almost the same shape for both models: this is expected as during the first stage of the combustion the flame has no interaction with the walls so the blending function is switched completely to GTFC in the flame front. However, the behavior at the second Y_f is already different. The GTFC presents a considerable flame development at the wall, whereas the shape of the flame front in the GTFC-wb case is more spherical. Comparing these two figures with the experimental results it can be seen that the GTFC flame front at $Y_f \simeq 8.0$ m resembles the experimental profiles way more than the GTFC-wb does. However, it cannot be ensured that it is nothing else that a coincidence: only some experimental phenomena can be numerically accounted for with these low-fidelity models. The trend continues for the last Y_f value.

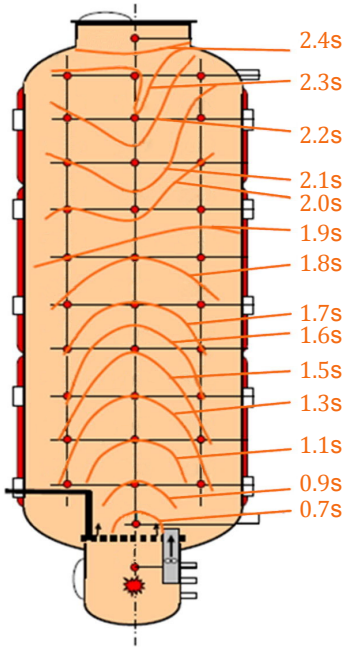

(a) Flame front location from the experimental detectors, modified from [70] to match numerical times.

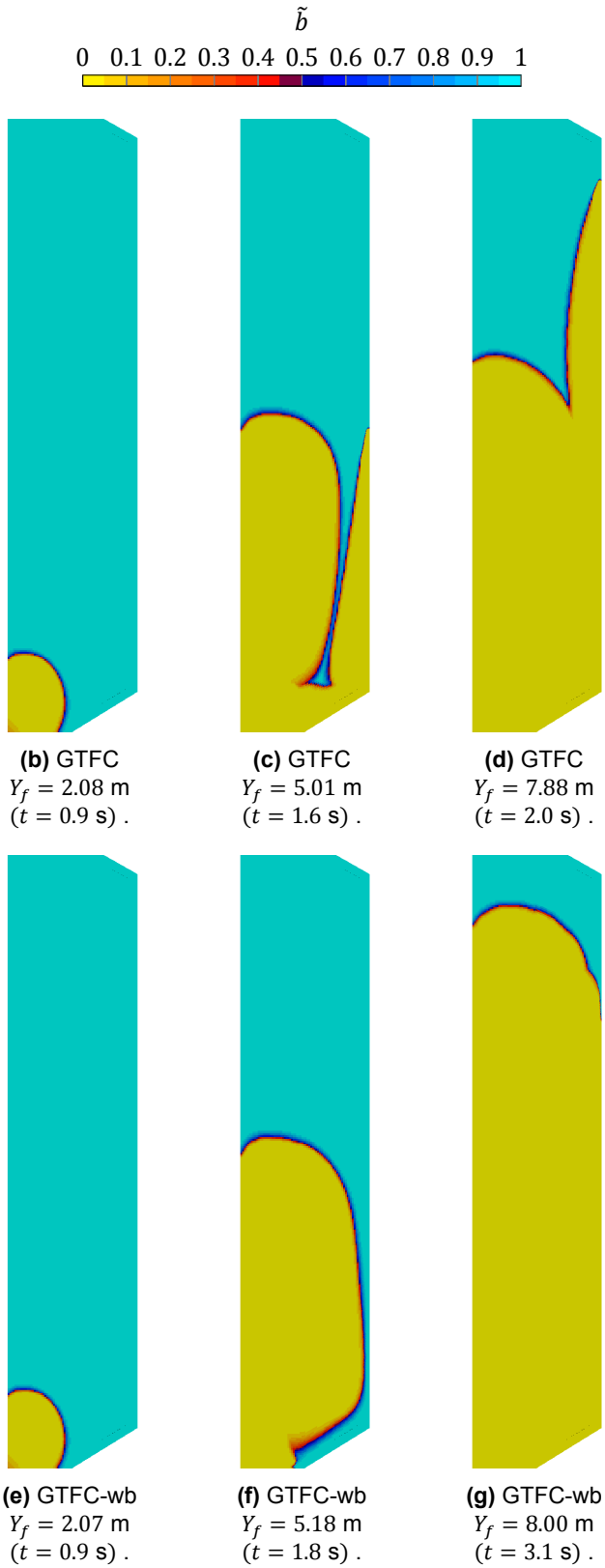

(b) GTFC $Y_f = 2.08$ m $(t = 0.9$ s$)$.

(c) GTFC $Y_f = 5.01$ m $(t = 1.6$ s$)$.

(d) GTFC $Y_f = 7.88$ m $(t = 2.0$ s$)$.

(e) GTFC-wb $Y_f = 2.07$ m $(t = 0.9$ s$)$.

(f) GTFC-wb $Y_f = 5.18$ m $(t = 1.8$ s$)$.

(g) GTFC-wb $Y_f = 8.00$ m $(t = 3.1$ s$)$.

Figure 4.36: Comparison of the flame front for different combustion models with the $k - \omega$−SST turbulence model and the experimental results.

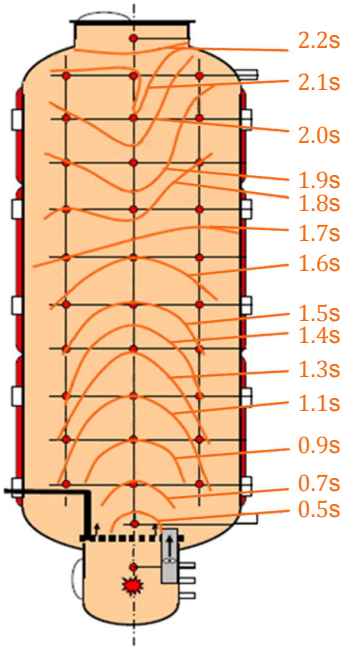

(a) Flame front location from the experimental detectors, modified from [70] to match numerical times.

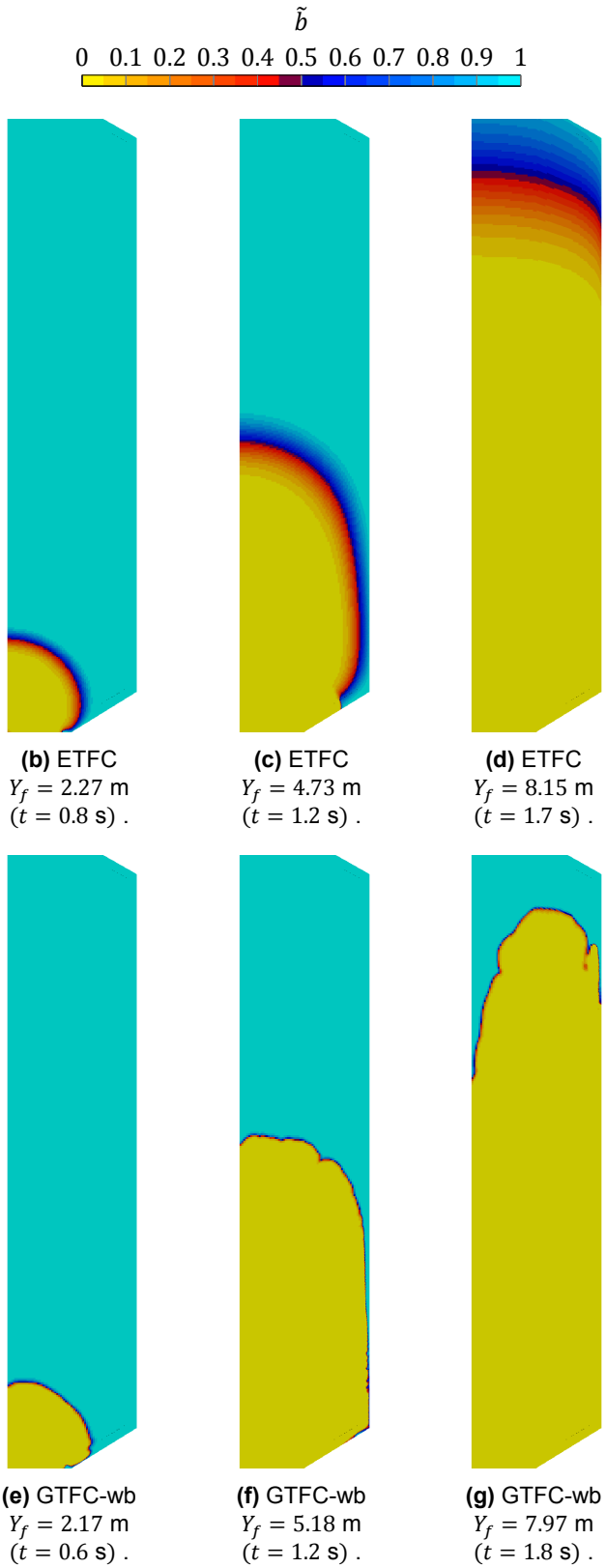

(b) ETFC $Y_f = 2.27$ m $(t = 0.8$ s$)$.

(c) ETFC $Y_f = 4.73$ m $(t = 1.2$ s$)$.

(d) ETFC $Y_f = 8.15$ m $(t = 1.7$ s$)$.

(e) GTFC-wb $Y_f = 2.17$ m $(t = 0.6$ s$)$.

(f) GTFC-wb $Y_f = 5.18$ m $(t = 1.2$ s$)$.

(g) GTFC-wb $Y_f = 7.97$ m $(t = 1.8$ s$)$.

Figure 4.37: Comparison of the flame front for different combustion models with the buoyant-$k - \varepsilon$ turbulence model and the experimental results.

Similarly to before, some snapshots of the regress variable field at different radii for the buoyant-$k - \varepsilon$ turbulence model coupled with two combustion models are shown: the ETFC (whose results can be

seen in Figures 4.37e, 4.37f, and 4.37g) and the GTFC-wb (whose results can be seen in Figures 4.37e, 4.37f, and 4.37g). The first thing that can be seen is that the shape of both combustion models at $Y_f \simeq 2.0$ m is very similar between them, but it is different from the results of the $k-\omega-$SST (compare just Figures 4.37e and 4.36e for the same combustion model): in this case, the flame expands more in the vicinity of the wall, probably due to the inherent limitations of the $k-\varepsilon$ turbulence model near walls. The shape of the flame front at $Y_f \simeq 8.0$ m for the ETFC is almost flat whereas the GTFC-wb presents an advanced flame front closer to the wall (but not exactly right on it, where it is very limited the flame front advancement). Finally, the ETFC presents larger diffusivities that spread the flame brush. This is caused by higher turbulence levels in the ETFC than in the GTFC-wb.

4.3.7. Conclusions

The Thermal-hydraulics, Hydrogen, Aerosol and Iodine containment, shortened as THAI, is a vessel whose experimental data has been used to validate the implemented solver in a more realistic scenario, as its larger dimensions together with the relevance of buoyancy increase the complexity of the physical effects. The case has been thoroughly studied and the results were presented, sketching the problems and solutions taken to overcame them.

Different combustion and turbulence models have been combined in the quest for recommendations and some standards for simulating nuclear facilities. To do so, and supported also with the discussion of the previous subsections, Table 4.9 is included. Three metrics are used: the maximum pressure during the numerical simulation, the maximum pressure rise (i.e. the temporal derivative of the pressure evolution in time), and the mean pressure rise (taking only those values over 0.1 MPa/s to perform the average, as done in previous studies [117]).

From the GTFC-based models, three conclusions can be extracted. First, the GTFCp predicts accurate results with neither of the two tested turbulence models, hence its metrics have not been included. This is most probably due to the presence of the flame radius twice in the correlation, which worked for reduced values but it hasn't for this large vessel. Second, when using the $k-\omega-$SST, bounding the combustion model at the wall (GTFC-wb) is detrimental against not bounding it (GTFC): the pressure metrics clearly improve and the flame front shape is closer to the experimental profiles (see Figure 4.36). Third, if other turbulence models are tested with the GTFC-wb, accurate results are obtained: the results of the GTFC-wb with $k-\varepsilon$ are relatively accurate, apart from having an overestimation error. The buoyancy-$k-\varepsilon$ produces a sudden increase of the pressure during the flame ascent (see Figure 4.33c), causing more inaccurate results than the $k-\omega-$SST. The flame front development was more consistent was with the $k-\omega$ (even if a larger peak pressure and earlier time where pressure was maximum are predicted, having a larger maximum pressure rise). Finally, including the buoyancy-generated turbulence produces an excess of turbulence, greatly overestimating the time of maximum pressure and therefore having the largest pressure rise.

Only the results of the buoyant-$k-\varepsilon$ for the ETFC, the XiFoamA, the XiFoamT, and the TFC are included, given that those models with other turbulence models don't produce enough turbulence to promote flame expansion, having only a region of light, burnt products that rise due to buoyancy within a large unburnt domain. There is no single model that provides consistently better results for all the metrics at the same time. The exceptional accuracy of the maximum pressure rise of the XiFoamT can't be attributed to any special characteristic of the model that would make it predict better pressure characteristics. Also, the peak pressure prediction of the TFC model shows a remarkable precision, which again contrasts with the lack of accuracy with the other metrics.

In general, it can be stated that using the GTFC-based models is a more robust approach: no special requirements on the maximum Courant number or turbulence model are needed, achieving flame propagation in all cases. This contrasts with a usual overprediction in all cases and metrics. The GTFC combined with the $k-\omega-$SST and the GTFC-wb with either the $k-\varepsilon$ or the $k-\omega$ produce accurate results. The addition of the buoyancy term in the transport equations for turbulence worsens the overprediction, causing even larger mismatches for the GTFC and GTFC-wb. The sensitivity of the non-GTFC-based models to the initial conditions can be attributed to the complexity of the physical

simulated phenomena, low turbulence values and lean mixtures. In terms of the pressure metrics, one of the best non-GTFC models could be the XiFoamT, while the flame front is clearly better captured with the ETFC (as it captures the acceleration at the second half of the vessel).

Table 4.9: Pressure-related metrics for selected turbulence and combustion models used in the THAI containment.

	Peak pressure [Pa] (Relative error [%])	Max. pressure rise [Pa/s] (Relative error [%])	Mean pressure rise [Pa/s] (Relative error [%])
GTFC $k-\omega$−SST	491238.18 (-0.51)	279029.16 (-18.57)	211045.31 (-11.72)
GTFC-wb buoyant $k-\varepsilon$	505291.31 (2.33)	765979.76 (123.52)	227628.32 (-4.79)
GTFC-wb $k-\varepsilon$	503598.15 (1.98)	393962.80 (14.96)	223267.51 (-6.61)
GTFC-wb $k-\omega$	510332.27 (3.35)	524955.70 (53.19)	287219.77 (20.14)
GTFC-wb $k-\omega$−SST	471129.18 (-4.59)	229558.26 (-33.01)	128206.02 (-46.37)
ETFC buoyant-$k-\varepsilon$	523315.28 (5.98)	581055.39 (69.56)	389960.08 (63.11)
XiFoamA buoyant-$k-\varepsilon$	503032.21 (1.87)	459360.09 (34.04)	257583.18 (7.74)
XiFoamT buoyant-$k-\varepsilon$	510704.79 (3.42)	339830.03 (-0.83)	189338.19 (-20.80)
TFC buoyant-$k-\varepsilon$	496850.09 (0.62)	392253.52 (14.46)	172327.18 (-27.92)
Experimental	493783.59 (0.0)	342686.89 (0.0)	239070.48 (0.0)

4.4. ENACCEF-2: flame acceleration enclosure

The third and final experimental facility that has been used to validate the combustion model implementation is ENACCEF-2 [14], which stands for *Enceinte d'accélération de flamme* (or flame acceleration enclosure in English). The vessel has been recently constructed and the experiments are still under development, so not all the results are known yet. Of course, the repeatability of the results has not been assessed as far as known. It has been the continuation of a previous containment, ENACCEF-1, whose objective was also the generation of data for the validation of combustion models. For the ENACCEF-2 enclosure, not only air and hydrogen will be considered but also diluents and stratified mixtures, which entails new requirements in the combustion code. However, the denoted Step0 is considered, as the mixture of pure hydrogen with air is an excellent way to further validate the implementation of the different combustion models.

The enclosure, as its name entails, has been designed to promote flame acceleration thanks to different annular obstacles, or baffles, located along the flow direction. These obstacles present a constrain in the available area, causing the flame to accelerate. As the vessel has been developed as a joint project between the IRSN and ICARE due to the interest for the NPP safety community, relevant features as lean hydrogen mixtures are part of the experimental setup.

4.4.1. Facility description and experimental data description

ENACCEF-2 is an enclosure that consists of a vertical tube with a height of 7.65 m and an internal diameter of 0.23 m. To achieve flame acceleration nine annular obstacles (see Figure 4.38) have been installed. They have a thickness of 4 mm and a blockage ratio, defined as:

$$BR = 1 - \left(\frac{d}{D}\right)^2 = 1 - \left(\frac{r}{R}\right)^2$$

where d represents the obstacle diameter and D the inner diameter of the pipe (or r obstacle radius and R inner radius). The used obstacles have a $BR = 0.63$, which represent an inner obstacle diameter of 0.14 m.

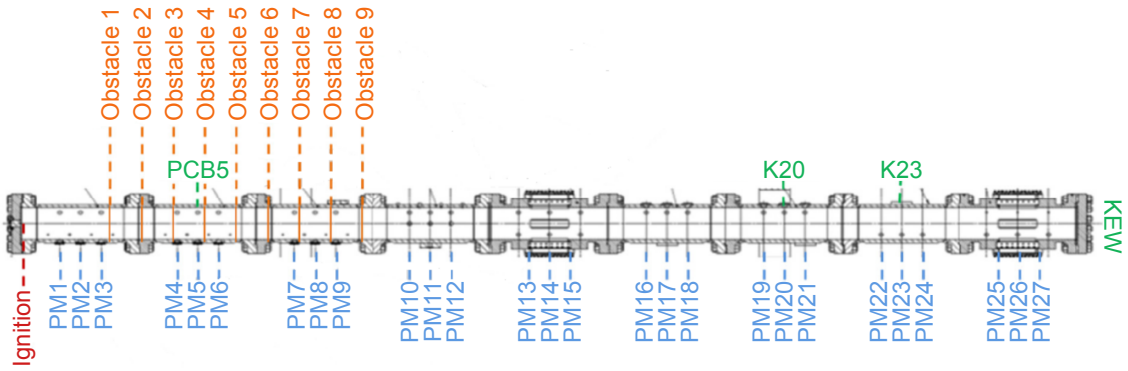

Figure 4.38: Diagram of the ENACCEF-2 facility [14], the real orientation of the vessel is vertical.

The facility is made out of 9 submodules (see Figure 4.38), assembled in the vertical direction, although there are only three different kinds of submodules. Submodule T1 is perforated with ten ports: one port for gas sampling at half-submodule height, three equally-spaced ports have sapphire windows to detect the flame passage along the tube with the use of photomultipliers (PM in Figure 4.38), three equally-spaced ports (thus located at the same height as the sapphire windows but at different azimuth) are connected to pressure transducers to measure the pressure as combustion occurs, and three ports can be used to fill and vacuum the facility. Submodule T2 has the same number and port-disposition for the photomultipliers and pressure transducers, combined with another port to sample the gas mixture and only two ports to fill and vacuum the facility. The relevant asset of submodule T2 is the possibility of

performing visual flow inspection: four rectangular ports diametrically opposed at two different perpendicular planes are equipped with windows (with a size of 282 mm $\times$ 50 mm), through which high speed PIV system can be used to measure the velocity field ahead of the flame. Submodule T3 is the ignition module with only two ports: one to install the spark plug and the other as a draining port to evacuate the liquid phase. In total, one submodule T3, seven submodules T1 and two submodules T2 compose the whole containment.

With the instrumentation of the vessel, the flame arrival time can be computed as the time where the voltage drop from the photomultipliers occurs (see upper right plot of Figure 4.39). From the flame trajectory, the velocity of the flame front can also be computed. Some information from the pressure transducers has already been retrieved as well. In the lower right subfigure of Figure 4.39 it can be seen the pressure profiles at different heights. The pressure is relatively constant before the first incident shock arrives, which is caused by the flame acceleration in the baffles that create supersonic flow conditions. Moreover, it can be seen how the transducers also capture the reflected shockwave resulting from the pressure wave bouncing at the end of the vessel. Interesting flame dynamics are expected to occur with the expanding, upwards rising flame front and the reflected, downwards moving shockwave.

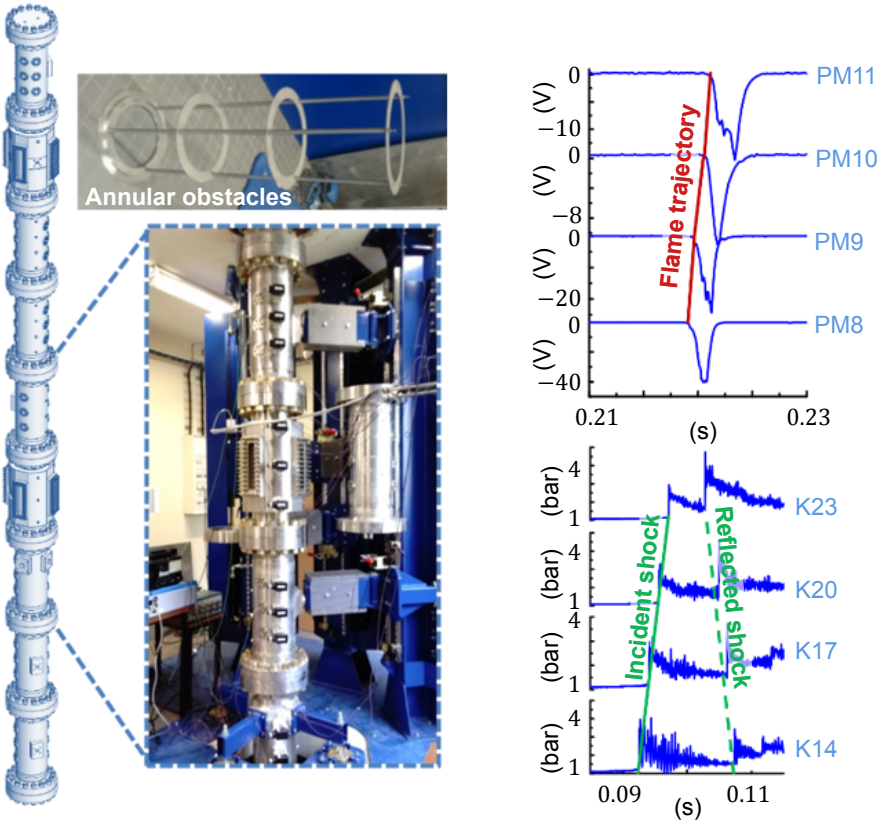

Figure 4.39: Physical appearance of ENACCEF-2 and main relevant phenomena, modified from [24].

The experimental initial conditions for Step0 are a temperature of 363 K, a pressure of 1 bar, and a mixture composed of 13% of hydrogen and 87% of air. The experimental procedure was to first vacuum the whole facility to just 80 Pa to ensure the removal of any mixture left in the facility from previous runs. Then, the mixture is obtained by mixing gaseous hydrogen (purity of 99.95%) with dried air from the surroundings and injected into the containment at 1 bar. Finally, the mixture is ignited at the bottom of the facility with a spark plug. Further experiments have been planned to study problems relevant to nuclear safety accident scenarios: mixtures with diluents, different ignition locations to see the effect of different flame propagation directions, temperature and species gradient, and spray configurations to analyze the effect of water spray on combustion dynamics.

4.4.2. Numerical simulation setup

The following numerical setup that has been used to model the experimental results. The same combustion models as for the THAI vessel have been used, although the reduced number of cells allowed for just 8 processors for the computations in parallel. Even if it is expected that the buoyancy effects are not as relevant as previously, the buoyancy term has been included in the momentum and energy transport equations because the enclosure is located perpendicular to the ground, having the flame expanding against gravity. Radiation effects were not included, as preliminary tests returned exactly the same behavior for the case with and without radiation modeling (see the overlapping curves in Figure 4.40), with the increased computational expenses that modeling radiation entails.

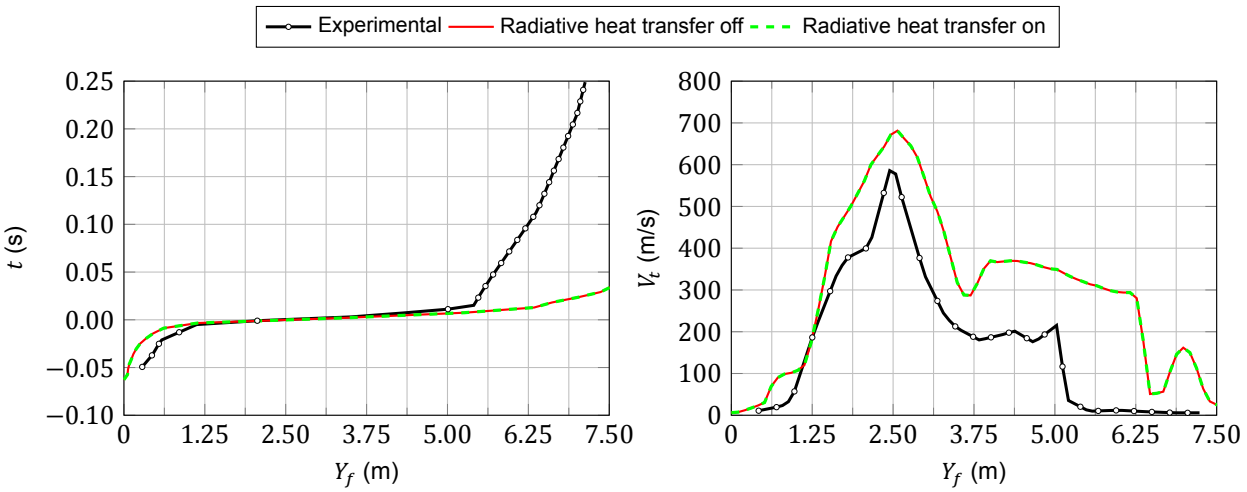

(a) Flame front location.

(b) Flame front velocity.

Figure 4.40: Comparison of results with and without radiation modeling.

As with all the previous experimental facilities, the cylindrical shape of the vessel is going to be exploited to generate an axisymmetric wedge mesh. Thus, the axis and the faces of the axisymmetrical direction are defined by the simplification of azimuthal symmetry (having an `empty` and a `wedge` boundary condition, respectively). The boundary conditions used for the walls are presented in Table 4.10. The initial turbulence levels are not measured from the experimental vessels, so a study on the effect of different results is presented in Subsection 4.4.3. A no-slip boundary condition used for the velocity field is used (being equivalent to a fixed value of 0 m/s). The schemes used are based on the `limitedLinear` schemes, either in the default, vectorial, or strictly bounded version. Time evolution is analyzed with the `Euler` scheme. Finally, a transonic correction has been used for the PIMPLE algorithm, which is described in the OpenFOAM code to improve convergence and stability. The laminar flame speed was $S_L = 0.27487$ m/s.

The postprocessing has been directly performed with OpenFOAM, following the discussion presented in Subsection 4.2.3. In this case, the strategy is even more imperative: the flame front position has been computed with the axial-based distance method. Pressure probing is also performed at the wall at some selected locations (namely, 0.427 m, 1.277 m, 2.227 m, 2.977 m, 3.827 m, 4.677 m, 5.527 m, 6.527 m, 7.227 m, and 7.650 m) that match the location of the pressure transducers for which experimental data is available. The numerical flame front location data has been shifted, as stated in the experimental proposal, to match the experimental flame front location at the photomultiplier at 2.277 m. Thus, each model has undergone a different temporal shift, used for both the flame front location and pressure. The flame front velocity has been computed with the temporal derivative of the flame front position. However, in this case, as the flame front recedes after the interaction with the reflected pressure wave, Y_f doesn't monotonically increase. Thus, and to avoid multiple V_t values for a given Y_f, the values of Y_f have been bounded with an accumulative maximum function `np.maximum.accumulate` [2]. Then

[2] Accumulate the input vector, so that every $i + 1$ element is equal or larger than the element i, having that when a flame position is seen, not lower heights are allowed

the curve $t = t(Y_f)$ is interpolated at equally-spaced flame front locations and the temporal derivative is computed.

Table 4.10: Boundary conditions for the ENACCEF-2 enclosure. Subscript zero represents the conditions used to initialize the fields.

Field	Wall patches	
alphat	fixedValue	0
b	zeroGradient	
epsilon	epsilonWallFunction	ε_0
k	kqRWallFunction	k_0
nut	nutkWallFunction	0
omega	omegaWallFunction	ω_0
p	zeroGradient	
Su	zeroGradient	
T	fixedValue	363.0
U	noSlip	
Xi	zeroGradient	

4.4.3. Initial conditions for the numerical simulation

In this case, the initial turbulence is not specified from the experiments. This also happened in the THAI vessel, although, due to the number of studies that have been developed since then, the community has somehow agreed on what low-turbulence values are taken for the numerical simulations. However, the recentness of this vessel has made that no guess on the initial turbulence values (k_0, ε_0, and ω_0) is available. The runs in this subsection were executed with the mesh obtained from the sensitivity analysis (see Subsection 4.4.4), although are presented before because the results further support the choices made for the sensitivity analysis.

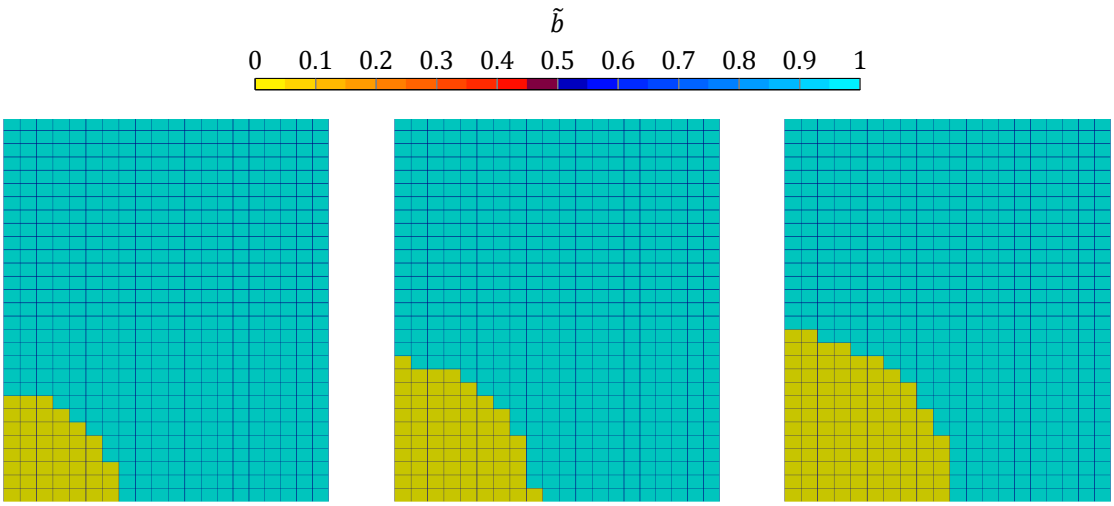

(a) Smallest ignition patching size.

(b) Intermediate ignition patching size.

(c) Largest ignition patching size.

Figure 4.41: Different ignition radii for the sphere initial condition patching in ENACCEF-2.

Before showing the results of different turbulent initial conditions, the size of the ignition region was also tested. The center of the sphere used to patch the regress variable and temperature fields (with a value of $\tilde{b} = 0$ and the adiabatic flame temperature) is located in the coordinate $(0, 0, 0)$. Three different radii for the patching sphere have been tested: 40 mm (see Figure 4.41a to compare the ignition sphere size with the local cell size), 50 mm (Figure 4.41b), and 60 mm (Figure 4.41c).

When simulating the case with the three ignition spheres, results (see Figure 4.42) are consistent and similar between them. These tests were carried out with the GTFC combustion model and the $k-\omega$−SST turbulence model. In the literature [122], it is widely acknowledged that different ignition radii only cause a temporal shift in the results, hence the sphere of 50 mm of radius has been chosen. This is the one used for the mesh sensitivity study.

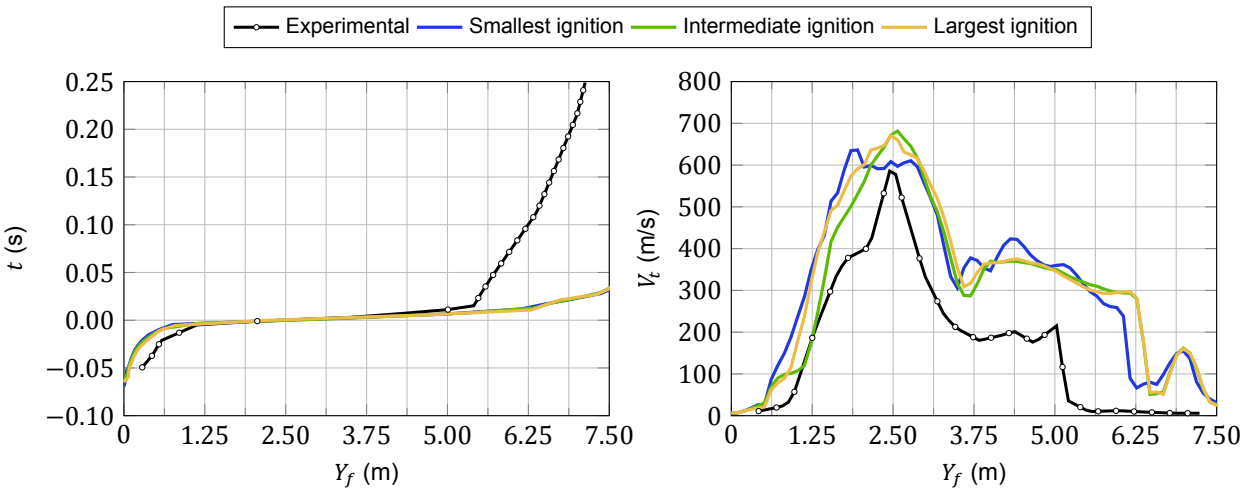

(a) Flame front location.

(b) Flame front velocity.

Figure 4.42: Results for different ignition radii.

Regarding the turbulence initial conditions, four pairs have been tested. The results are shown for the GTFC-wb combined with the $k-\omega$−SST, although no much difference is expected for other combinations of combustion and turbulence models (as all the possible values are associated with small turbulence). The first pair that was used is the initial conditions of the THAI vessel, given that it was also a quiescent initial flow field and the conditions have been extensively used in the literature. The other three pairs have been obtained using the procedure described for pipe flow as:

$$k_0 = \frac{3}{2}\left(U_\infty I\right)^2 , \qquad l_{t,0} = 0.07D , \qquad \varepsilon_0 = \beta^* \frac{k_0^{3/2}}{l_{t,0}} , \qquad \omega_0 = k_0 \varepsilon_0 \beta^* ,$$

where U_∞ is the freestream inflow velocity that has been substituted with the laminar flame speed ($S_L = 0.27487$ m/s), I is the turbulence intensity level (having tried three values: 0.05, 0.10, 0.15), D is the inner diameter of the main tube and $\beta^* = 0.09$ is a turbulence model constant. The actual values can be seen in Table 4.11. Even if the tests were performed with the $k-\omega$−SST, the values of ε_0 have been included as further simulations use turbulence models based on the turbulent dissipation rate.

Table 4.11: Considered initial conditions for the ENACCEF-2 enclosure.

	k_0 (m^2/s^2)	I (%)	$l_{t,0}$ (m)	ε_0 (m^2/s^3)	ω_0 (s^{-1})
THAI_IC	1.5×10^{-4}	3.64	0.00345	4.80×10^{-5}	3.555
$I = 5\%$	2.8×10^{-4}	5.00	0.01608	2.63×10^{-5}	1.045
$I = 10\%$	11.3×10^{-4}	10.00	0.01608	21.25×10^{-5}	2.090
$I = 15\%$	25.4×10^{-4}	15.00	0.01608	71.68×10^{-5}	3.136

The results for these four initial conditions of the turbulence flow field are presented in Figure 4.43. It can be seen that there are no big differences between the different cases, being the most remarkable feature the longer second velocity peak in the case of $I = 15\%$.

This test was carried out as a fail-safe after the following simulations: the mesh sensitivity, the turbulence model, and the combustion model analysis. The initial conditions that were used are the same

ones as for the THAI vessel. Even if the initial turbulent length scale is not the one from the pipe flow correlation, this doesn't influence the results.

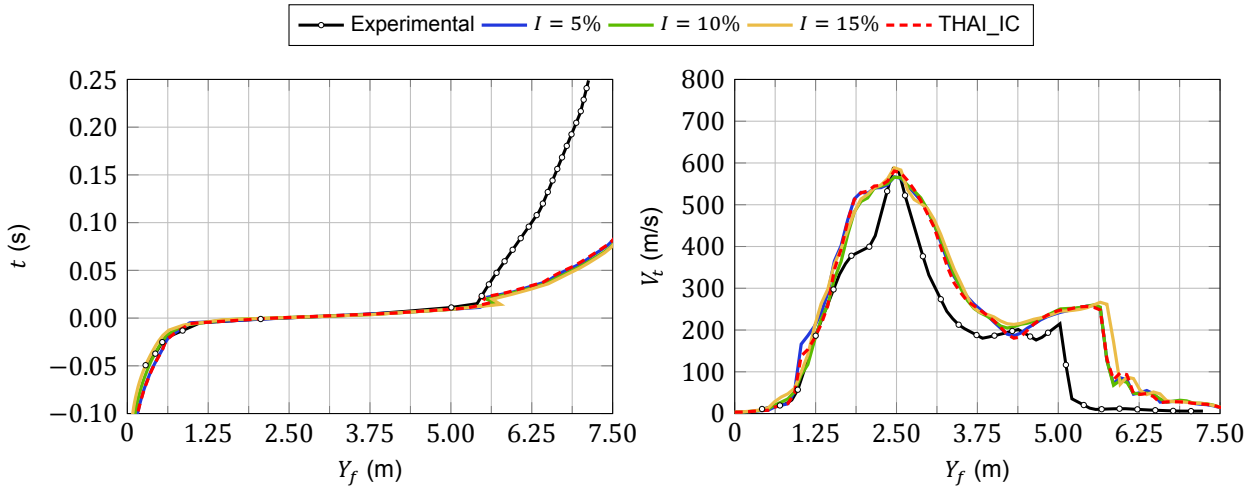

(a) Flame front location.

(b) Flame front velocity.

Figure 4.43: Different initial conditions for the turbulence model.

4.4.4. Mesh sensitivity study

As opposed to what happened with the THAI vessel, no meshing strategies regarding curved geometry were necessary. The mesh is simply a rectangle with the radius as the base and the length as height. However, the annular obstacles presented a challenge in this case. There were two alternatives to numerically simulate the annular obstacles located along the flow direction. One assumes infinitely thin baffles while the other uses a row of cells (having baffles with, at least, one cell thickness). Both approaches present some disadvantages: the first one has a singularity point that causes troubles with Adaptive Mesh Refinement when used with more than two levels of refinement (as hanging nodes appear) while the second one has faces in the main flow direction (that may not be properly resolved with RANS turbulence models). The first one was chosen, so all the following cases have been simulated with infinitely thin baffles (thus restricting the AMR maximum refinement level to one).

For ENACCEF-2, the same approach as for the mesh sensitivity study of the THAI vessel was followed: four different background meshes were created, applying incremental refinements to some regions to get locally higher refinement levels. The full matrix was generated as the one of Figure 4.22, although it is not included in its entirety because it was deemed not necessary. Only five representative grids are shown in Figure 4.44, where the baffle has also been included to denote the face that acts as a blocking annular obstacle. In Figure 4.44e, the most refined grid (M3_0i0w), which is used as a reference, is presented. Towards the left, less refined grids are shown: the M0_2i2w (see Figure 4.44a) with M0 as background and two levels of local mesh refinement, the M2_0i0w (see Figure 4.44b) which is only the background mesh, the M2_1i1 (see Figure 4.44c) which is the M2_0i0w mesh locally refined both on the ignition and walls region and the M2_AMR1 (see Figure 4.44d) where AMR has been applied to M2_0i0w and it can be seen how the face-thick baffle effectively obstructs the flame development.

The background mesh was generated, as well as that of the THAI vessel, with `blockMesh`. The additional local refinement next to the walls and in the ignition region was obtained with the use of the utility `snappyHexMesh`, making it straightforward the refinement between background mesh levels. The local refinement step with `snappyHexMesh` also causes cell refinement in the azimuthal direction, so the front face was extruded in the azimuthal direction with `extrudeMesh` to obtain the wedge axisymmetrical mesh. Two extra steps were required for ENACCEF-2 to use internal faces of the mesh as physical faces (to which boundary conditions could be applied). Each one of these two steps was followed for each baffle: first different topological sets were created with `topoSet` (a `pointSet`

was obtained from a box only including points of each baffle face, a `faceSet` was obtained for each `pointSet`; and a `faceZoneSet` was generated for each `faceSet`) and then the baffle was created with the utility `createBaffles` (which requires `faceZones` to generate each baffle). The local refinement in ENACCEF-2 was done using a sphere of radius 0.05 m centered at the origin for the ignition region and 0.015 m to refine close to the walls.

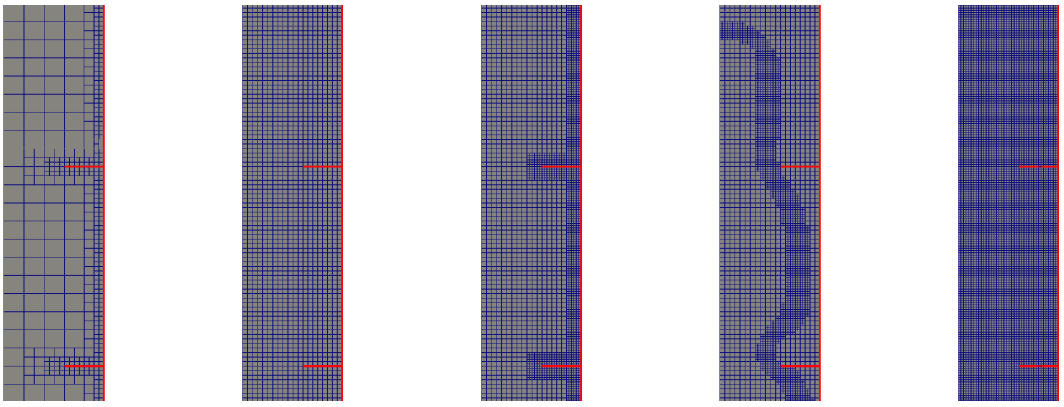

(a) M0_2i2w. **(b)** M2_0i0w. **(c)** M2_1i1w. **(d)** M2_AMR1. **(e)** M3_0i0w.

Figure 4.44: Detail of a baffle refinement in ENACCEF-2 for different grid resolutions, the black lines represent the cells and the red lines are the lines taken as walls.

All the 10 meshes were generated and simulated, using the GTFC with the $k-\omega$−SST model. The runtime in hours for each one of them is shown in Table 4.12, where also the number of cells is included. In the case of the AMR, the number of cells is the initial one. However, the number of cells after each refinement can be checked, having a maximum of 3349, 9142, and 36295 cells for M0_AMR1, M1_AMR1 and M2_AMR1, respectively. These peak cell count values can be compared to the cell counts of the mesh composed of the same background grid with one level of local refinement in the wall and ignition region, having a $+5.01\%$, -11.01%, and -20.79% of cells in the AMR case (having all of them located in the flame front instead than on the ignition region/walls).

Table 4.12: Computational time in hours and (number of cells) of the mesh sensitivity study of the ENACCEF-2 facility.

	M0	M1	M2	M3
0i0w	0.0519 (1900)	0.2519 (7600)	1.8839 (30400)	27.3033 (121600)
1i1w	0.1211 (3181)	0.5800 (10273)	6.3164 (45820)	
2i2w	0.3753 (5923)	3.5192 (28150)		
3i3w	3.1567 (24937)			
AMR1	0.5319 (1900)	0.5319 (7600)	3.6714 (30400)	

Similar to what was done in Subsection 4.3.3, Figure 4.45 shows the results for all the background meshes. However, in this case, there is not a big mismatch between the different grids in terms of the flame velocity. The acceleration along the main part of the tube is achieved due to flame acceleration and flow constriction and not due to buoyancy nor slow turbulence generation near the wall as it happened in Section 4.3.3. However, there are significant differences concerning the location of the pressure-flame front interaction and the flame front velocity after the interaction: the more refined the grid the more the flame travels before the pressure shockwave collapses with the flame front and also the smaller the effect of this interaction of the flame front speed. Both these effects could be re-

lated: the mesh with the more detailed resolution has higher values of turbulence, making the S_t values larger. Larger S_t values make that the flame travels more while the pressure wave reaches the end of the vessel and bounces back. Moreover, the flame front is expanding faster so the pressure wave encounters a faster flame front: being harder to stop it, to push it backward (as the M0_0i0w and the M1_0i0w do) and to reduce its speed once the flame front keeps expanding. However, and even if the experimental values are between M0_0i0w and M1_0i0w, the mesh sensitivity is achieved for the mesh whose results don't change anymore if further refined. Thus, it can be stated that the only background mesh whose performance is similar to the reference case (M3_0i0w) is the mesh M2_0i0w.

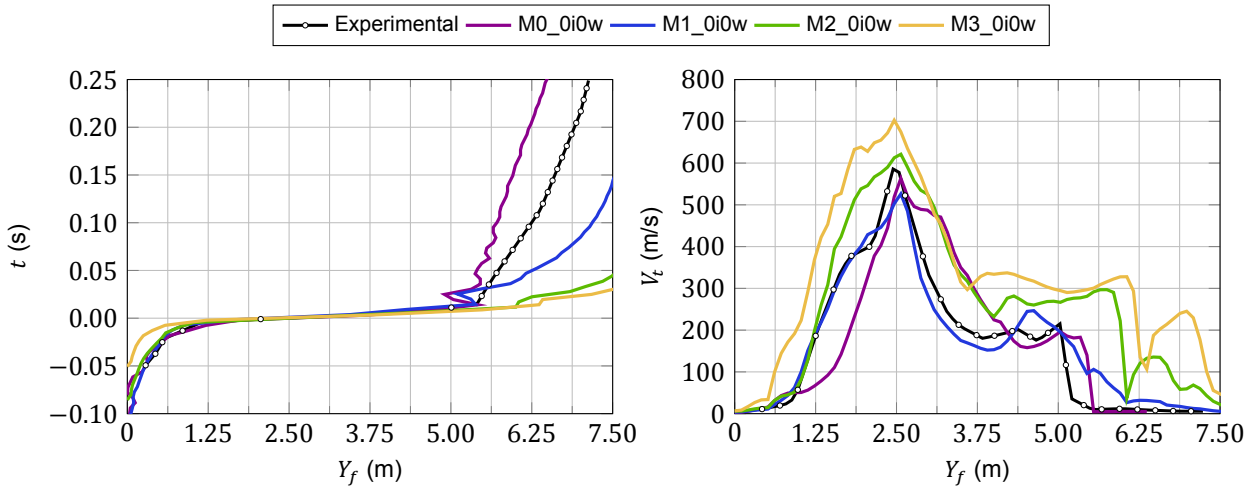

(a) Flame front location.

(b) Flame front velocity.

Figure 4.45: Mesh sensitivity ENACCEF-2 containment: background meshes without further refinements at the wall nor the ignition region.

In Figure 4.46, the results for the grids where the same smallest cell size is present in the walls (so also in the baffles) and in the ignition region are shown. It can be seen that there is a good level of agreement between all the grids with respect to M3_0i0w (not so much with the experimental results) both the flame vertical axial distance and the flame velocity. This supports the previous discussion: only the walls are being refined in these meshes, so having the same cell size near the wall makes that the same (or similar) turbulence levels are obtained in the vicinity of the wall. The turbulent flame speed, which is based on the turbulence model, plays a crucial role. Apart from M0_3i3w, whose flame velocity is slightly underpredicted all the other grids show equivalent results, with drastic differences in computational time.

Finally, the effects of AMR are considered (see Figure 4.47). It can be seen that even just one level of AMR can provide accurate results as long as the background mesh is fine enough: neither M0_AMR1 nor M1_AMR1 predict acceptable results. This can be explained as the turbulence in the walls should be generated ahead of the flame front: the pressure wave travels ahead of the flame front propagation, creating turbulence in the baffles from which higher or smaller S_t values are predicted by the combustion model. Similar behaviors to those of M0_0i0w and M1_0i0w are observed in M0_AMR1 and M1_AMR1 regarding the flame backing after the pressure-wave flame front interaction and the flame front position after this event. As stated, AMR can provide better results if combined with a fine enough background mesh. M2_AMR1 clearly shows that: M2_0i0w (whose results are already close to the reference grid) is improved with the addition of one level of refinement.

To conclude this section, a discussion of the best grids is presented, together with the arguments for the chosen one. From all the tested grids, the only ones that performed similarly to the reference grid are M0_3i3w, M1_2i2w, M2_AMR1, and M2_1i1w. The first three ones have a similar number of cells (because even if the background mesh has different baseline levels, ENACCEF-2 is a long facility and most of the domain are walls) and similar runtimes, discarding M2_1i1w. The final choice between the three has been made based on pragmatic reasoning: the pressure-wave flame front interaction

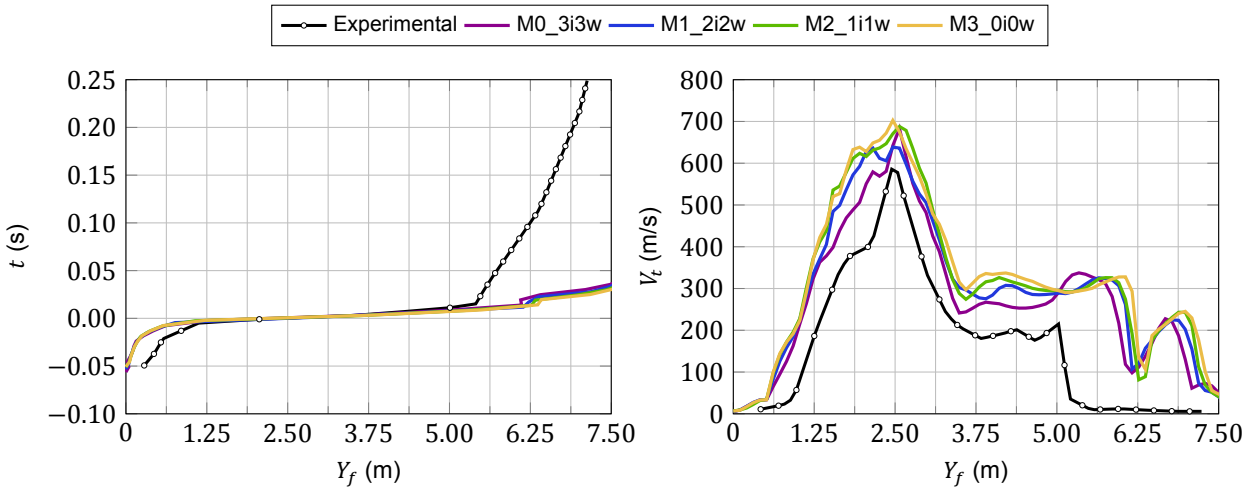

(a) Flame front location. **(b)** Flame front velocity.

Figure 4.46: Mesh sensitivity ENACCEF-2 containment: same ignition and wall refinement, different background mesh resolutions.

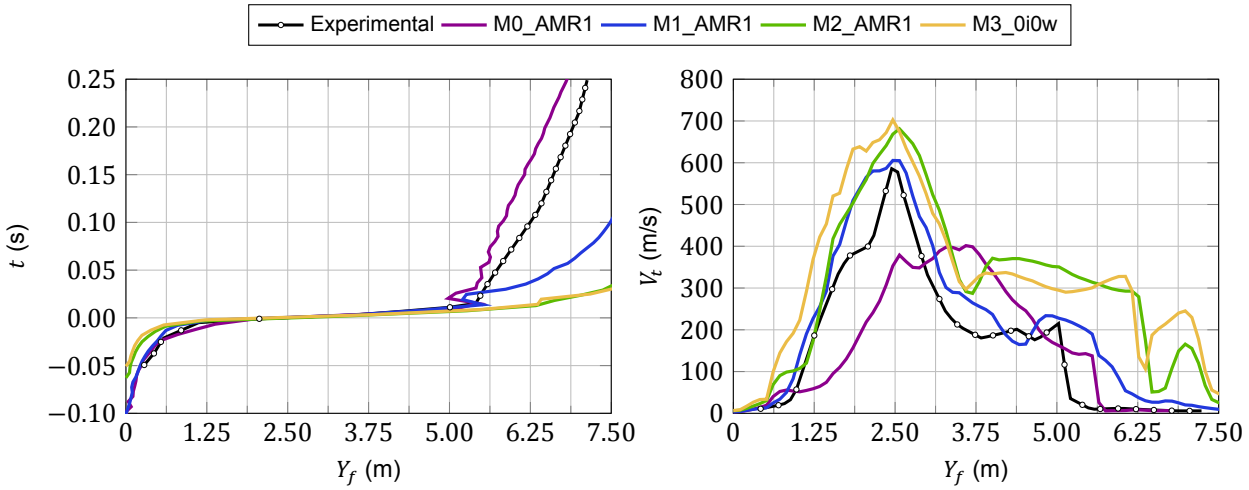

(a) Flame front location. **(b)** Flame front velocity.

Figure 4.47: Mesh sensitivity ENACCEF-2 containment: results with adaptive mesh refinement.

is a relevant phenomenon of the simulation and its accurate modeling will determine the accuracy of the calculations. Even if no pressure curves are shown here, the model that can best capture that is M2_AMR1: instead of having a large number of cells in the baffles and the ignition region, they are located right in the flame front, where this interaction occurs (while keeping the same level of resolution in the flame front close to the wall). Thus M2_AMR1 is the mesh that will be used for the rest of the simulations.

4.4.5. Turbulence model effects

Consistent with Section 4.3.5, three combustion models (namely the TFC, GTFC, and GTFC-wb) are tested for the ENACCEF-2 enclosure with the four different turbulence models: $k-\omega$, $k-\omega$, $k-\omega-$SST and buoyant-$k-\varepsilon$.

In Figure 4.48 the results are shown for the TFC with the four considered turbulence models. As opposed to the THAI vessel, all the turbulence models cause the flame to expand, with and without the buoyancy term included in the turbulence model. As the buoyancy effects in this vessel are less relevant and the flame is ignited right at the bottom of the enclosure, by having contact with the wall, the spread of the flame is promoted. This is due to the fact that turbulence is produces next to the wall, hence contributing to the flame speed. However, the model that provides best results is the buoyant-$k-\varepsilon$, especially when considering the flame velocity, where, even if underpredicted, the peak velocity is closely computed. It also provides a closer slope after the pressure-wave interaction with the expanding flame front. All the other models perform really similar, with the exception of the $k-\omega$−SST, which is the one that better captures the second flame front acceleration of $Y_f = 5$ m (although it locates it later in time). It is interesting also to see that the interaction between the pressure wave and the flame front occurs in all the models equally: even if the way the different models predict the trend at which the flame front enters the region of the baffles, both the region of the baffles and the subsequent tube development takes the same time in all models.

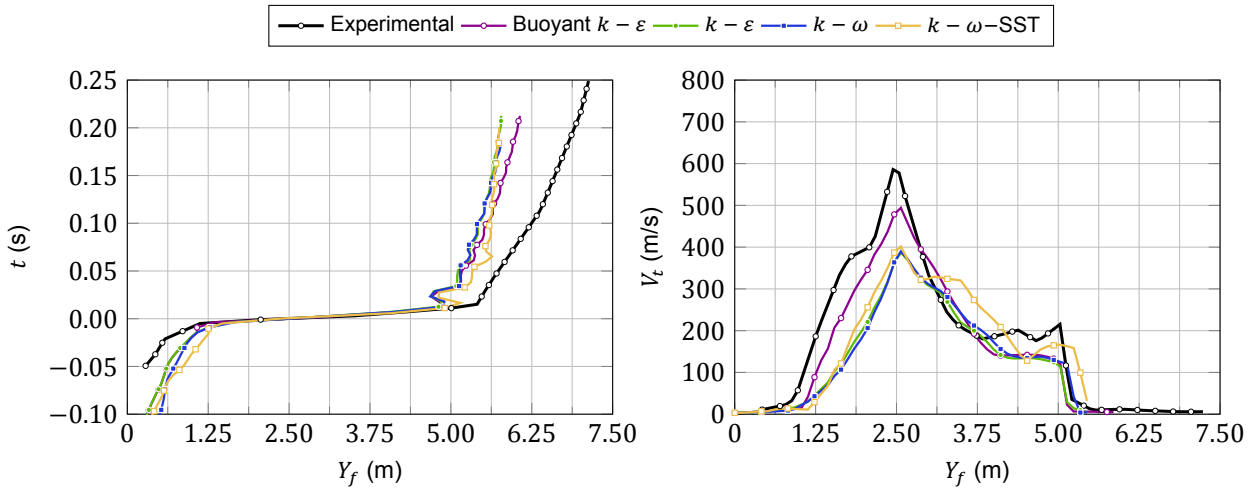

(a) Flame front location.

(b) Flame front velocity.

Figure 4.48: Comparison of the TFC with different turbulence models.

The results for the different turbulence models combined with the GTFC combustion model are shown in Figure 4.49. The main conclusion that can be drawn is that the model overpredicts both the flame front development and the flame front velocity regardless of the turbulence model. The differences between including the buoyancy term in the transport equations for turbulence are negligible (cf. the overlapping lines for $k-\varepsilon$ and buoyant-$k-\varepsilon$): the GTFC imposes large S_t values without being affected by the turbulence generated by buoyancy. The $k-\omega$ is the model that most overpredicts both variables, being the $k-\omega$−SST the closest one, even if the deceleration and interaction caused by the reflected pressure shockwave are almost none.

Finally, the results for the GTFC-wb combustion model are presented in Figure 4.50. As with the GTFC, the effects of the buoyancy term in the transport equations for turbulence is negligible - although in the GTFC-wb case, the two models perform slightly different (as it can be seen in the flame velocity at around $Y_f \simeq 6$ m). In this case, the $k-\omega$ is the model that performs best, which may seem surprising, given that it was the worst model with the GTFC. The $k-\omega$ model just slightly overpredicts the location at which the flame front interacts with the reflected pressure wave as well as the flame front development in time after the event. This comes at the expense of underpredicting the peak velocity (when compared with the other turbulence models). The performance of the $k-\omega$−SST is also better in the GTFC-wb than in the GTFC model, although it largely overpredicts the flame front velocity after its interaction with the reflected pressure shockwave.

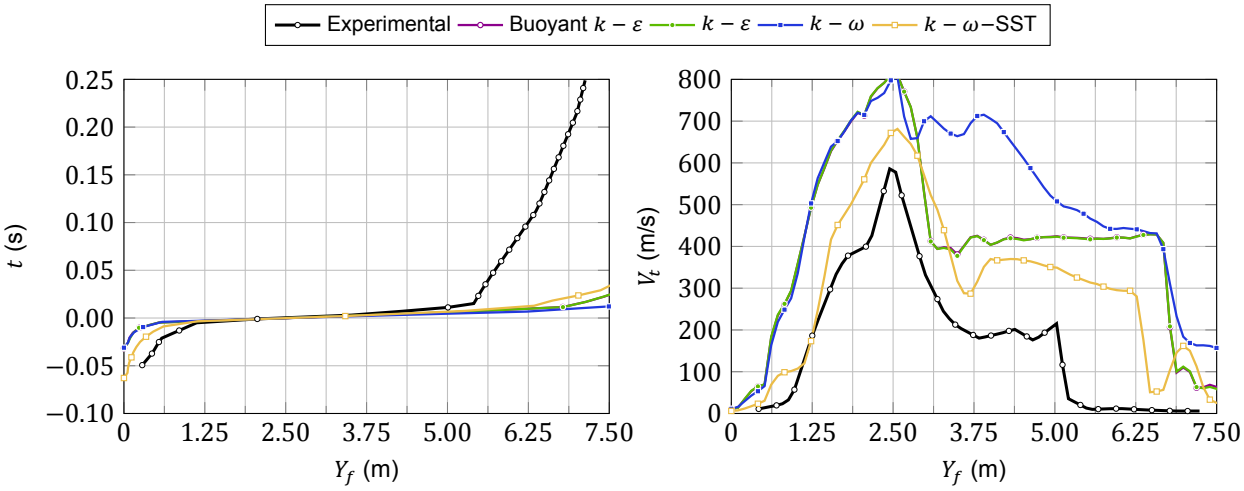

(a) Flame front location. **(b)** Flame front velocity.

Figure 4.49: Comparison of the GTFC with different turbulence models.

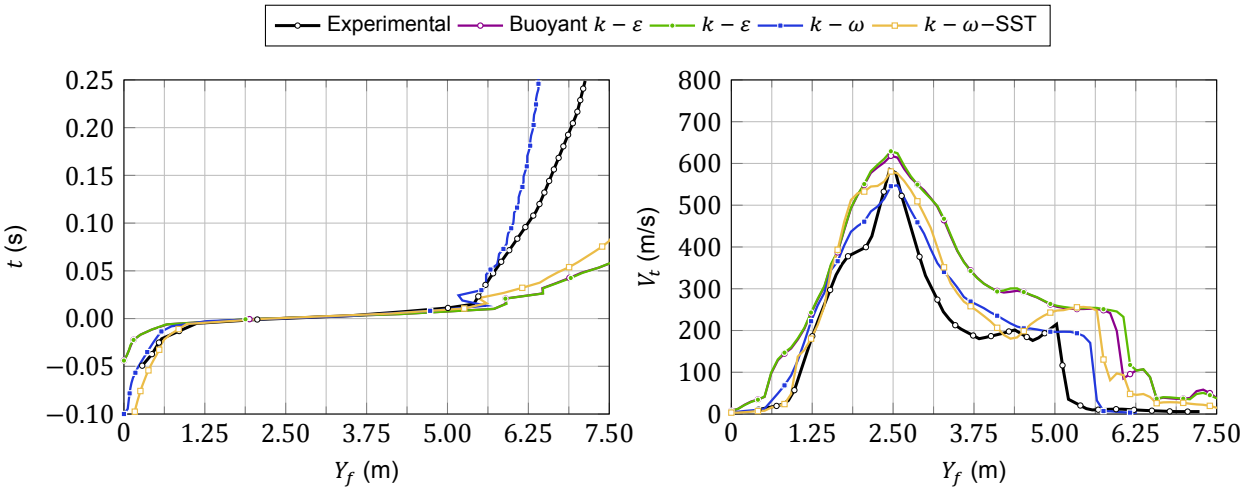

(a) Flame front location. **(b)** Flame front velocity.

Figure 4.50: Comparison of the GTFC-wb with different turbulence models.

From the previous discussion, two points require further explanation. First of all, the overprediction of the $k-\omega$ with the GTFC when compared to the TFC. It can be seen in Figure 4.51 the flame front after passing the baffle region and after the interaction with the reflected pressure wave. It is clear that the diffusivity of the GTFC is very large when compared to that of the TFC as revealed by the spread of the flame front brush. The turbulent diffusivity is mainly controlled by turbulence (although in the case of the GTFC, it has also a temporal component) so it can be stated that the GTFC has larger values of turbulence, which also explains the larger turbulent flame speed values and the smaller influence of the reflected pressure wave (which faces a faster flame front). This turbulence is also promoted by the faster flame propagation through the baffles, creating a positive feedback look: the larger turbulence values spread the flame (through the diffusivity term) and accelerate it (through the turbulent flame speed), creating even more turbulence.

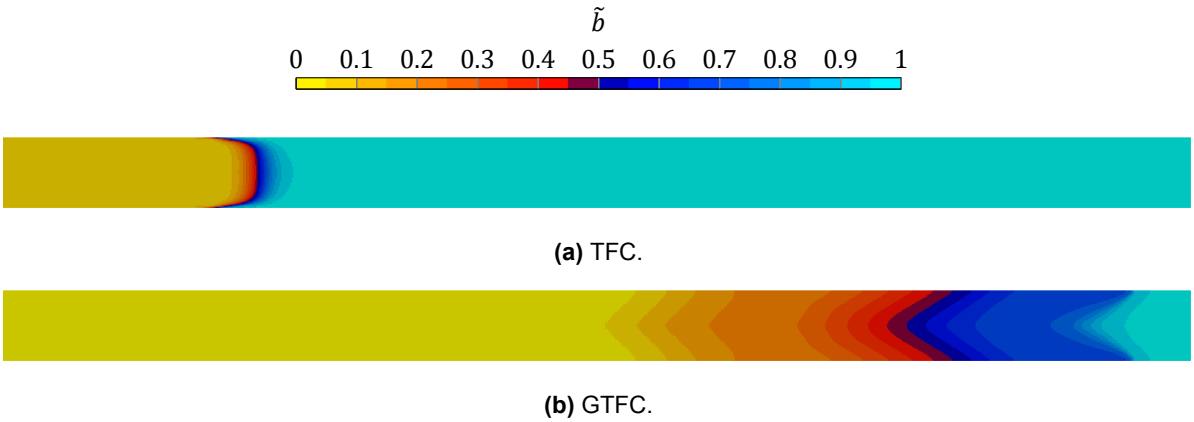

(a) TFC.

(b) GTFC.

Figure 4.51: Flame front after the baffles region in ENACCEF-2. Both combustion models were coupled with the $k-\omega$ turbulence model.

Finally, the accurate results of the GTFC-wb when coupled with the $k-\omega$ are promising when compared with the performance of the combustion model with other turbulence models as well as the turbulence model with the GTFC. However, and given that the blending function depends on the turbulence values, the influence of the turbulence models is even stronger in the GTFC-wb. To further analyze this, the value of the blending function within the flame brush was computed. The time at which flame development occurs is different for each turbulence model. The flame brush is considered to be those cells whose level of refinement is 1 in the AMR field. The statistics of this conditioned blending function as well as the statistics of the regress variable in the whole domain can be seen in Figure 4.52, presenting the range of the variable in the field, the quartiles 25 and 75, and the average for each of the two variables. It must be recalled that when the blending function value is 0, the model is GTFC, and when it is 1, the model is TFC.

The blending function in the $k-\varepsilon$ (see Figure 4.52a) quickly oscillates in time between 0 and 1, switching between both models until the whole unburnt mixture is consumed. It can be seen that the drop in $\tilde{b}$ that occurs at around $t = 0.05$ s (which is associated with the flame front crossing the domain), happens when the blending function is also towards the GTFC. Thus, the large velocity of the GTFC occurs during the flame development of the GTFC-wb coupled with the $k-\varepsilon$. The results of the $k-\omega$−SST (see Figure 4.52b) are similar. The first part (up to $t = 0.125$ s) shows that the GTFC-wb is acting as the TFC, although there is no flame expansion as denoted by the $\tilde{b}$ quartiles and mean. While the flame develops and burns the mixture (when the quartiles of $\tilde{b}$ decrease in time from $t = 0.15$ s on) the value of the model has completely switched to the GTFC. This is the reason why almost all the unburnt mixture is consumed, having only some cells at the end of the domain with low but not-zero values of $\tilde{b}$. The flame front has vanished as shown with the mean of $\tilde{b}$. Finally, Figure 4.52c shows the behavior for the $k-\omega$. After a brief period where both models are being applied and slightly promote the development of the flame (as depicted by the mean of $\tilde{b}$ until $t = 0.10$ s), when the flame expands ($t > 0.10$ s) the model completely switches to the TFC. This makes that the the flame position with time after the interaction with the pressure wave is underpredicted (leaning towards the results of the TFC) instead of largely overpredicted (as it happens in the GTFC). The switch occurs in the $k-\omega$ and not in the other models as the $k-\omega$ predicts a thickening of the boundary layer, covering almost all the vessel diameter (and hence of the flame front) and transitioning the model almost completely to TFC for the rest of the simulation.

Two main conclusions can be extracted from this subsection. First, the influence of the buoyancy in the turbulence transport equations is smaller than in the THAI vessel, although it improves the results in the TFC model. In reality, buoyancy is indeed present, but its effect is limited due to the fast flame propagation. Secondly, the GTFC and GTFC-wb overpredict the flame front position (and therefore velocity) with almost all turbulence models. The only remaining combination is the GTFC-wb with $k-\omega$ as an accurate candidate, due to the model transition to the TFC model after the reflected pressure shockwave interacts with the flame front.

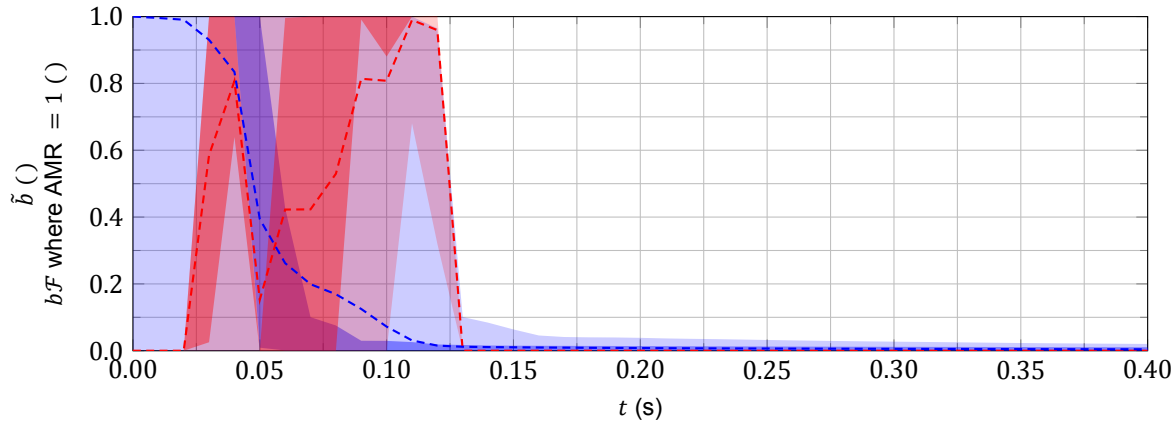

(a) $k-\varepsilon$.

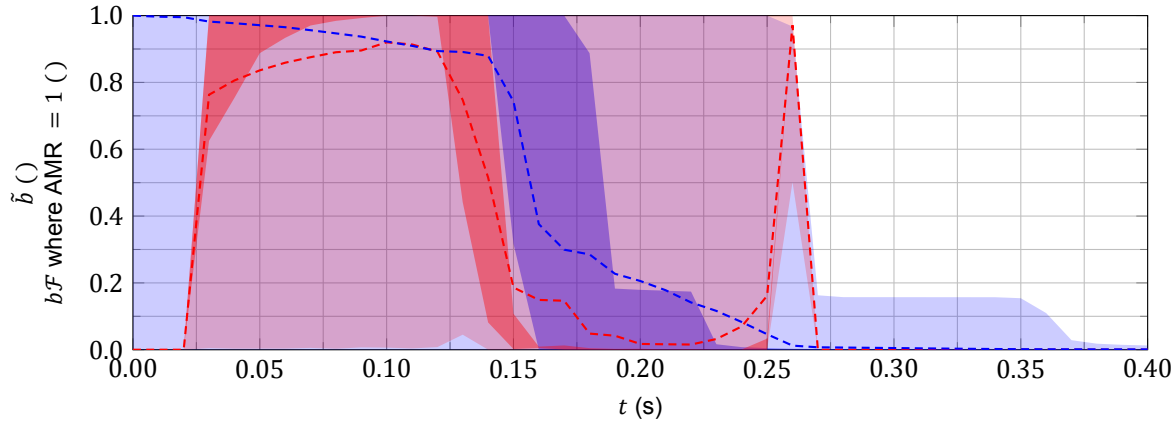

(b) $k-\omega$−SST.

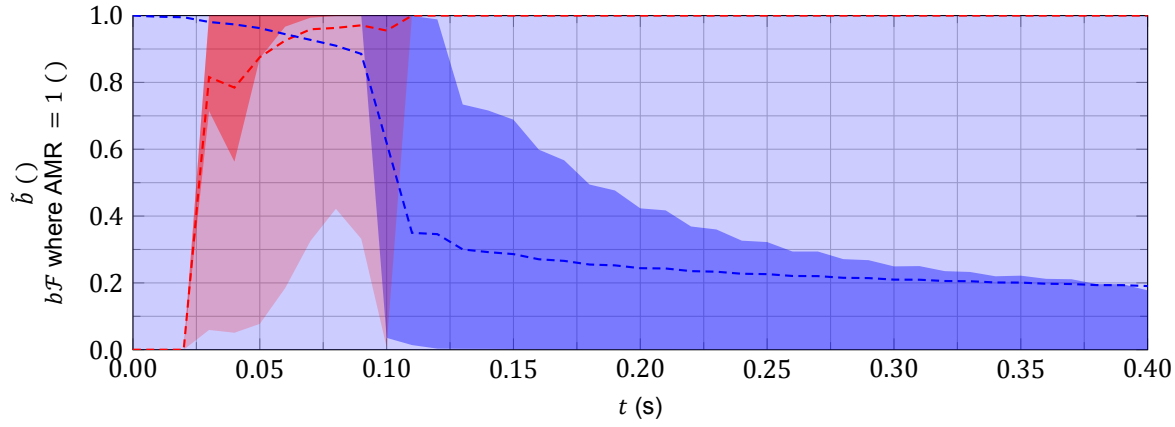

(c) $k-\omega$.

Figure 4.52: Blending function within the flame brush for different turbulence models combined with the GTFC-wb in ENACCEF-2. ▭ represents the range of the blending function within the flame front (where the level of refinement is 1), ▭ the quartiles $25 \sim 75$ of the blending function within the flame front and ---- the average value of the blending function within the flame front, while ▭ represents the range of the regress variable $\tilde{b}$ in the whole domain, ▭ the quartiles $25 \sim 75$ of the regress variable in the whole domain and ---- the average value of the regress variable in the whole domain.

4.4.6. Combustion model analysis

After testing the turbulence models, the comparison of the seven combustion models was performed with two turbulence models: the $k-\omega-$SST and the buoyant-$k-\varepsilon$. Even if the choice may look arbitrary, the reasons to do so were two. First of all, the performances of the $k-\omega$, $k-\varepsilon$ and $k-\omega-$SST are rather similar for the TFC. However, their behavior is different in the GTFC and GTFC-wb: the pair GTFC-wb with $k-\omega$ performs better due to the model transitioning to the TFC as explained, but there was nothing else indicating that the $k-\omega$ would perform consistently better. In the GTFC, the $k-\omega$ overpredicts while the $k-\omega-$SST is closer to the experimental values. Secondly, even if the buoyancy effects are small, they still occur in reality, so the only turbulence model that includes the source term due to buoyancy should be analyzed.

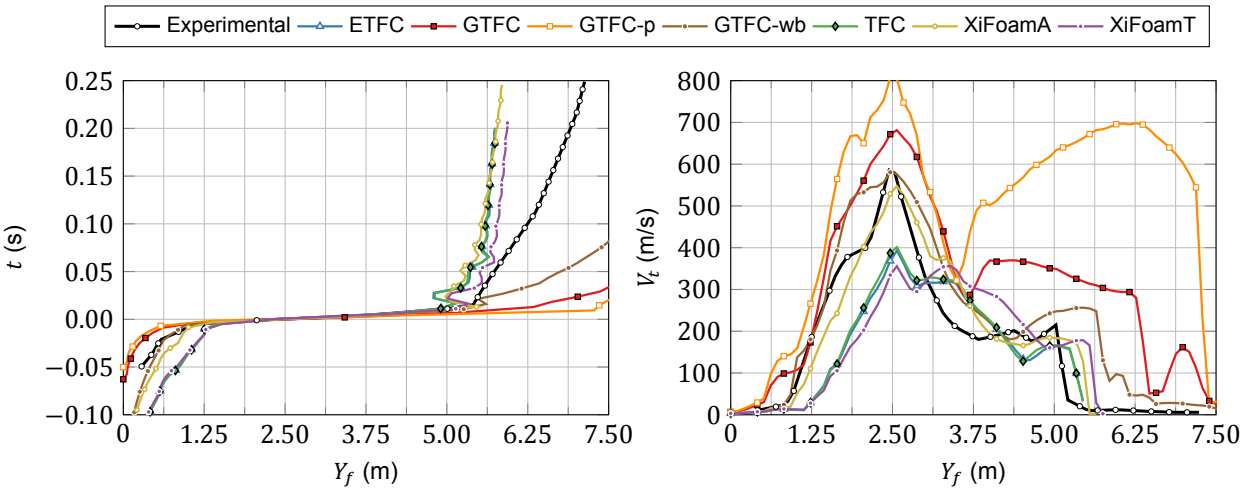

(a) Flame front location.

(b) Flame front velocity.

Figure 4.53: Comparison of the combustion models in ENACCEF-2 with the $k-\omega-$SST.

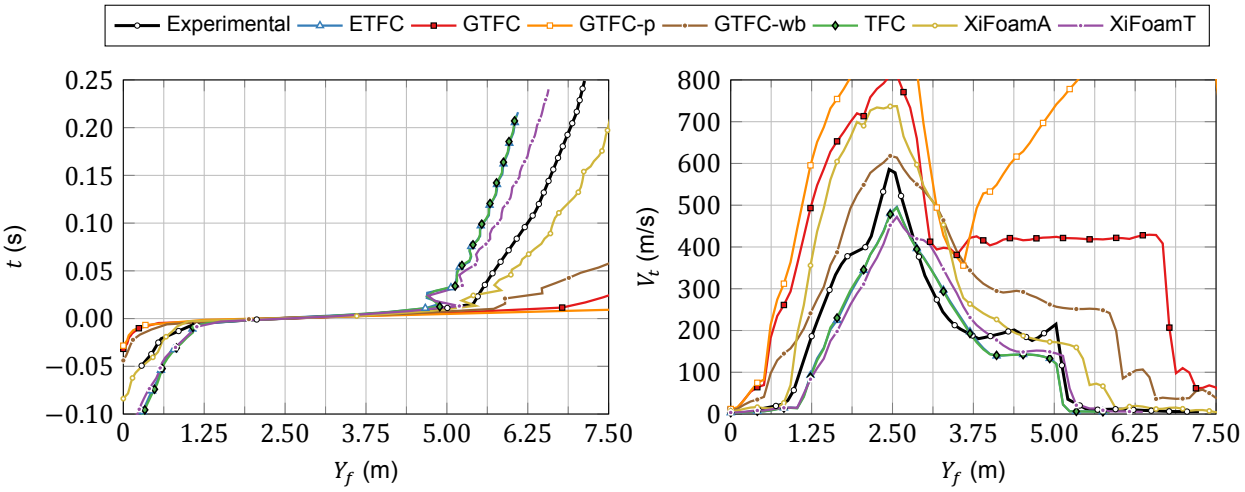

(a) Flame front location.

(b) Flame front velocity.

Figure 4.54: Comparison of the combustion models in ENACCEF-2 with the buoyant-$k-\varepsilon$.

In Figure 4.53 the results are shown for the $k-\omega-$SST. The first thing that can be seen is that the GTFCp largely overpredicts (the same way it did in the THAI vessel) due to the formulation with a double influence of the flame front location. However, all the GTFC-based models overpredict the flame velocity, the time at which the interaction of the flame front with the pressure wave occurs and the flame velocity after the interaction. The one that better models the flame velocity is the GTFC-wb, even if

the velocity after the interaction of the pressure wave with the flame front is largely overpredicted. The performance of the ETFC and the TFC is really similar, overlapping in most of the flame development and flame front velocity. The flame front velocity obtained from the XiFoamT is close to that of the TFC or ETFC. XiFoamA also accurately predicts the peak velocity, although it underpredicts the flame front development after the interaction of flame front with pressure wave.

The results of the combustion models with the buoyant-$k-\varepsilon$ are shown in Figure 4.54. It can be seen that the GTFCp still largely overpredicts the flame front velocity, so much in this case that no interaction occurs between the reflected pressure wave and the flame front. The GTFC also overpredicts the flame velocity (especially the second part) and the large turbulent flame speeds make that the reflected pressure wave almost doesn't affect the expanding flame. However, the GTFC-wb predicts some deceleration due to the reflected pressure shockwave and it accurately predicts the peak velocity. The XiFoamA is overpredicting the flame velocity and the development after the pressure wave-flame front interaction (even if the interaction is located at the correct height). The XiFoamT still performs similarly to the TFC for both variables. The behavior of the TFC and ETFC is also still the same. One possible explanation is the small values of the Lagrangian time due to the large turbulence values, making that the ETFC fully transitions to the TFC after passing through the baffles (the two lines don't overlap below $Y_f = 1$ m and there are some differences for the flame position around $Y_f = 5$ m).

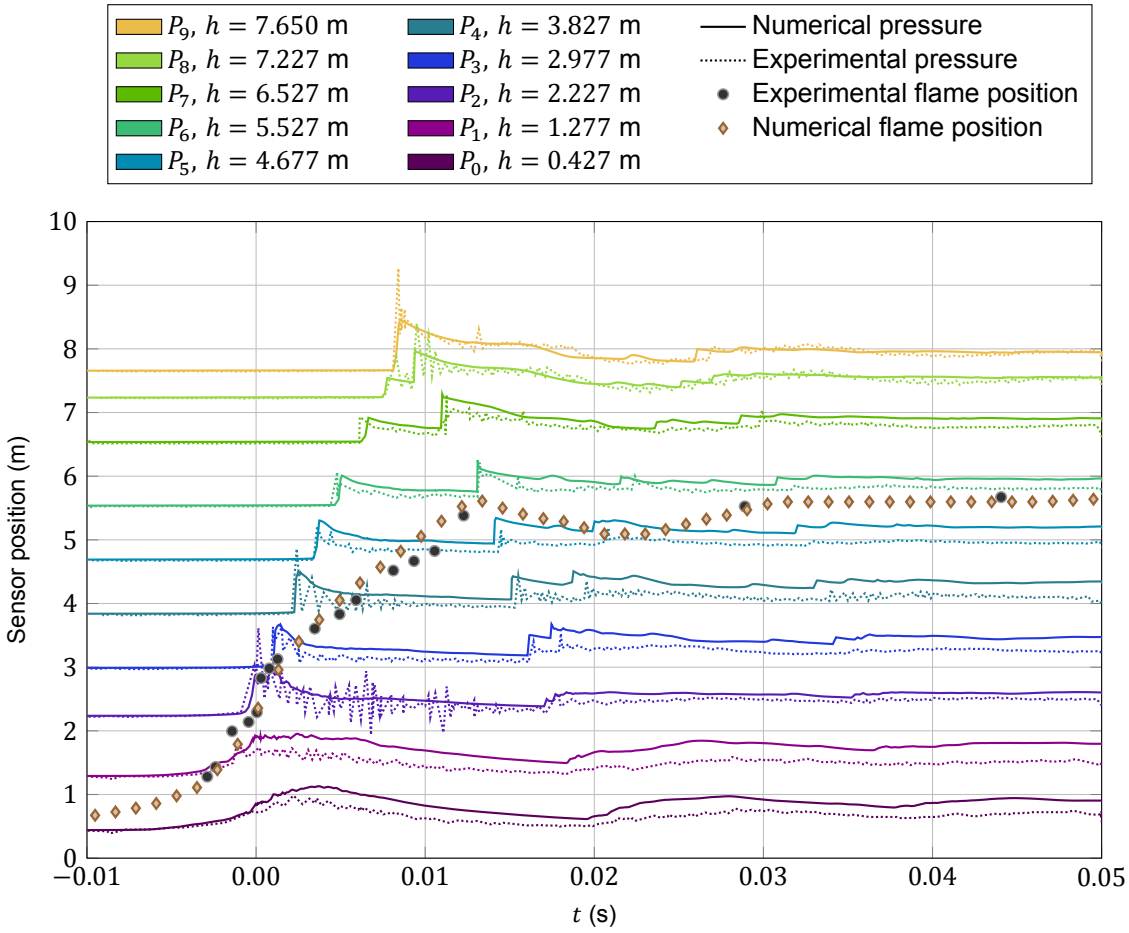

Figure 4.55: Pressure history of the GTFC-wb with the $k-\omega$ in ENACCEF 2.

An image of the pressure histories combined with the flame front position can be seen in Figure 4.55 for the GTFC-wb combustion model and the $k-\omega$ turbulence model. This pair was chosen as the combustion model is one of the main findings of the thesis and its coupling with the $k-\omega$ turbulence model shows promising results. However, the pressure profiles for most combinations of combustion and turbulence model are similar to these. No more pressure figures have been included as the exact

pressure values have not been yet experimentally provided and these are only preliminary results. The numerical pressures have been normalized with the initial value and the maximum value of each probe. It can be seen that the forward pressure wave is correctly captured both in time and amplitude, capturing also the times of the reflected pressure wave. The amplitude of everything that happens after the first wave is slightly off, although many multiple interactions are captured. Up to four pressure jumps (first forward pressure wave, reflected wave, second forward wave after pressure and flame front interaction, and second reflection at the end wall) can be seen. This detail also shows that no information is experimentally retrieved yet about the backward motion of the flame after the pressure wave interaction, so the distance that the flame recedes is unknown.

To further illustrate the interaction between the reflected pressure shock wave and the expanding flame front, in Figure 4.56 different snapshots of the flame front propagation can be seen. The left part of each timestep shows the pressure field, while the right part of the domain shows the regress variable field. The shockwave reflection at the end of the domain occurs between t_0 and t_1 while the flame expands between t_0 and t_6. It is at t_6 that the pressure shockwave and the flame front interact. Physically the interaction presents really complex phenomena that cannot be numerically computed with the present low-fidelity model. However, it can be seen how the flame front is slowed down and it recedes already at t_7, also modifying the flame front shape. Moreover, at t_8, a second pressure wave is generated from the interaction, which moves to the top wall of the enclosure, reaching it almost at t_9.

4.4.7. Conclusions

The preliminary experimental results obtained from the ENACCEF-2 enclosure have been shown, together with the facility and capturing devices. After presenting the numerical model and the effect of the initial conditions, a mesh sensitivity study was conducted, followed by a study of the effect of the turbulence and combustion models. From the mesh sensitivity study, it can be concluded that a refinement near the walls is interesting to properly achieve convergence on the results. This can be obtained through a fixed refinement local region or with Adaptive Mesh Refinement in the flame front location, being the latter the chosen approach as it is more computationally efficient and better captures the flame front interaction with the pressure wave. The effects of turbulence and the combustion model can be summarized as follows. On the one hand, the performance of the TFC is stable regardless of the turbulence model. The TFC shows almost the same results as the ETFC (which is consistent with previous studies) and close behavior to that of the XiFoamT. The behavior of the XiFoamA model depends on the turbulence model, although the results show good agreement with the experiments. On the other hand, it can be said that the GTFC-based models overpredict the flame front position and velocity regardless of the turbulence model, except for the GTFC-wb with the $k-\omega$. For this combination, accurate results were obtained in terms of both metrics, as the model transitions to the TFC after the interaction between pressure wave and flame front. It is evident that the overprediction of the S_t is crucial in the erroneous behavior of the GTFC model. Limiting its values through the use of blending functions, as done in the GTFC-wb, seems to be a reasonable solution, as it allows the model to first, retain the improved features of flame evolution prediction for slow deflagrations, and second, to be applied to fast deflagrations with reasonably accuracy. The interaction itself is accurately retrieved and shows good agreement with the experimental results.

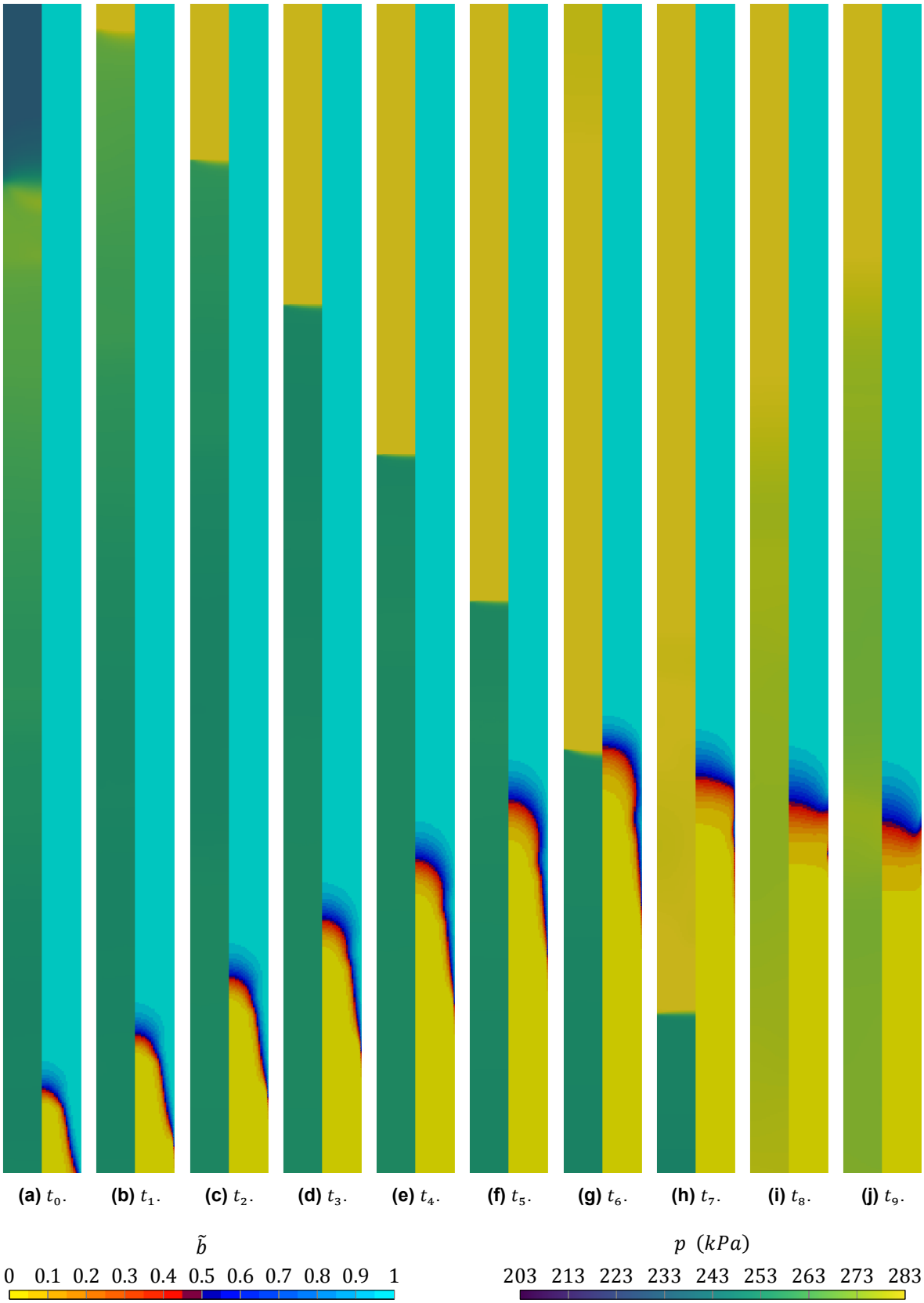

Figure 4.56: Snapshots showing the reflected pressure shockwave interaction with the expanding flame front. Results obtained for the GTFC-wb with the $k-\omega$. The left side of each timestep shows the pressure field and the right side the regress variable field. $t_0 = 0.125$ s and the increment between time steps is $\Delta t = 0.001$ s.

5

Conclusions and future work recommendations

This work has investigated the numerical modeling of turbulent hydrogen combustion for nuclear safety management. During a severe accident in a Pressurized Water Reactor (PWR), hydrogen can be generated in large quantities. Even if autocatalytic devices that convert the hydrogen to steam are present throughout the reactor containment, the hydrogen can mix with the air of either the enclosure (as in the Three Mile Island accident) or the environment (as in the Fukushima Daiichi power plant accident), leading to a slow deflagration process with a premixed flame. The initial conditions of turbulence are low, having a laminar flame that, due to the presence of obstacles in the containment and the flame dynamics, may evolve to a turbulent regime. The combustion process creates dynamic pressure loads that can damage the structural integrity of the reactor containment. The accurate prediction of the pressure loads in the event of a severe accident is, therefore, of utmost importance for nuclear safety.

This challenge has been analyzed from a numerical modeling point of view, presenting the different available approaches and the necessary simplifications to compute the complex phenomena of turbulent combustion. The phenomenological description and the mathematical analysis have been presented for the combustion and other phenomena that appear coupled to it (as radiative heat transfer). The approach used to model combustion is based on the flame speed models, defining a turbulent flame speed at which the flame front moves. Models as the Turbulent Flame-speed Closure (TFC) or the Extended Turbulent Flame-speed Closure (ETFC) belonging to the flame speed models have been described in the literature. The description of the Computational Fluid Dynamics (CFD) tool, OpenFOAM, was also presented with the different available models and the custom implementations of the thesis: adapting the solver to the specific requirements of the problem.

Four cases were considered to verify, validate, and assess the capabilities of the implemented solver. The first one was a one-dimensional premixed flame that moves into frozen turbulence. This case was chosen as it has an exact analytical solution that can be compared to the numerical solution obtained from the solver. The second facility was the ICARE (*Institut de Combustion, Aerothermique, Reactivite et Environnement*) spherical combustion chamber, which has been used to provide the correlations used to define the GTFC-based (Goulier Turbulent Flame-speed Closure) models. Thus, the behavior of the GTFC-based models has been compared to that of models available in the literature (mainly TFC and ETFC) to see how do they perform with experiments where turbulence was controlled and detailed data can be obtained. The third case was the Thermalhydraulics, Hydrogen, Aerosol, and Iodine (THAI) containment, where a larger facility is considered. The flow dynamics are different from the ICARE spherical combustion chamber as now the buoyancy effects present a relevant role in the development of the flame front. Different turbulence models were used to analyze the flame evolution in time as well as the accuracy of the pressure peak and rise predictions. The fourth and last facility was

the ENACCEF-2 (*ENceinte d'ACCélération de Flamme*), which, even if still under development, can provide some interesting preliminary results. The enclosure presents a series of baffles that accelerate the flame almost up to the detonation point, creating a series of shockwaves that bounce at the end of the vessel and interact with the flame front, producing complex flow patterns.

In order to link the results obtained with the research questions formulated at the beginning of the thesis, these questions are recalled, and an answer to them is provided:

1. How can the current combustion model formulation be implemented in an open-source platform as OpenFOAM? Can the simulations be less case-dependent, in terms of ignition or other model constants, in this new framework? How can these new combustion models be verified?

    - Both the premixed combustion models described in the literature as well as the ones devised in this thesis have been reformulated to comply with the implementation of premixed combustion models available in OpenFOAM and with all the non-combustion-related libraries (as thermodynamics, pressure-velocity coupling, numerical schemes and discretization). The verification of the models was performed with the one-dimensional premixed flame moving into frozen turbulence and the ICARE spherical bomb. The flame-gradient models depend on constants that were tuned in the literature based on many experimental scenarios and the correlations are the same for all the cases. The presented results conclude that the best ignition method is the patching performed with `setFields`, deeming the ignition based on source terms as disadvantageous, as it is defined with more parameters which considerably affect combustion. Thus, the ignition can be performed with just one case-dependent constant: the patching radius. The implemented models can be used for new cases without any user-tuned parameters apart from the ignition radius (and the adjustment of timestep and mesh discretization).

2. Can Adaptive Mesh Refinement be implemented for axisymmetric geometries in the open-source CFD code?

    - The standard version in OpenFOAM could not handle AMR in case of 2D axisymmetric geometries. For this reason, a new approach has been implemented, which is able to correctly perform AMR in 2D axisymmetrical grids. This methodology provides the advantage of locally refining certain features of the flow field (e.g. the flame front) without requiring a grid with a considerably fine resolution. The reduction of computing time can go down by almost half, while attaining similar results in the flame front development. AMR introduces new parameters in the simulation setup as the field on which the grid refinement is based on, but general guidelines have been provided to achieve consistent results. Nevertheless, there are cases where using AMR doesn't directly translate into more accurate results, requiring higher grid resolution near the wall (to partially account for the larger gradients in the boundary layer) and in the ignition location (to smoothly handle the change in value through the flame front) to predict the expected flow behavior.

3. How should the experimental correlation of Goulier be coupled with classical combustion models as the TFC (Turbulent Flame-speed Correlation) proposed by Zimont to better predict flame development?

    - By defining the TFC correlation in terms of the flame wrinkling ratio (which is the ratio between the turbulent flame speed and the laminar flame speed), the TFC model was implemented into OpenFOAM. This served as a baseline for the GTFC, which is based on the experimental correlation of Goulier [47]. The correlation already provides the ratio between the flame speeds, but not the diffusivity term for the regress variable transport equation, which has been obtained from the ETFC (Extended Turbulent Flame-speed Closure) described by Lipatnikov, as it has been described in the literature the increased accuracy when predicting the flame thickness. The GTFC model was further improved with the use of a wall-bounding function (called GTFC-wb), where the flame speeds obtained in the vicinity of the walls were restricted to the values of the TFC model. This was required as, since the correlations are

provided without accounting for wall effects as quenching, the turbulent flame speed at the wall is unrealistically high (promoting wall flame acceleration).

4. What is the effect of different turbulence models in the combustion models? Can some general guidelines be provided?

    - The combustion models presented in this thesis are highly dependent on the turbulence of the flow field, since they are constructed based on properties as the root mean square velocity fluctuation and the integral length scale. Thus, it is shown that the same combustion model used with different turbulence models can produce distinct results, specially in terms of the flame front development. Even so, some general guidelines can be stated based on the results of the thesis. Overall, the combination of the GTFC-wb and the $k-\omega$ turbulence model provides good results for the tested scenarios. The TFC and the ETFC models require the buoyancy-generated turbulence terms into the turbulence model equations in order to achieve accurate results.

5. How do the different combustion models perform under conditions such as flame acceleration or buoyancy flows?

    - The behavior of the models was assessed with two different facilities, one where buoyancy was the main mechanism behind the flame expansion and the other where flame acceleration played a relevant role. The buoyancy effects, considered with THAI, have shown that the source term of buoyancy in the turbulence model is essential to achieve accurate results (and even flame propagation) with models as TFC or ETFC. On the other hand, the proposed GTFC model performs equally good, obtaining similar (or even better results in some metrics) when compared with the literature [69, 117, 129] in terms of the peak pressure and pressure rise. The solver is also capable to deal with the flame acceleration and reflecting shockwaves, all present in the ENACCEF-2 facility. However, in this case the GTFC-based models overpredict the flame front evolution mainly due to the high levels of turbulence generated in the enclosure.

Some other lessons can also be extracted from the results of the thesis that were not anticipated in the research questions. One of them is the influence of the time discretization based on the Courant number. When the timestep is modified to keep the Courant number under a given threshold, two things had to be considered. Firstly, as the flame front is moving at the turbulent flame speed, this velocity should also be included to determine the Courant number. Secondly, the value of the Courant number used as threshold has a large impact for some combustion models (namely the TFC and ETFC) while the proposed GTFC gives more consistent results within a wider range of threshold values. Another lesson, which was already briefly discussed, is that the refinement aimed to resolve the gradients at the wall drastically changes the results. It is worth stressing it out as it is rarely done in the nuclear safety community, but it was shown with the results of THAI, that refining the wall can produce more accurate results.

Future work recommendations

Based on the results of this thesis some recommendations can be stated for future work aimed to improve the performance of the model implemented in this thesis for nuclear safety studies:

- As all the thesis was carried out with axisymmetric meshes, spending some time to implement the AMR on this kind of grids, it is strongly advised to evaluate the solver in cases where the geometry is required to be three-dimensional. It is true that performing axisymmetric analysis is a simplification assumption and the cases here presented could have been simulated with a three-dimensional mesh, although not many differences are expected as the turbulence modeling has been done with RANS. The point is to use a case where the flow is inherently three-dimensional and no geometrical simplifications can be used. Different facilities exist [62], although the RUT facility [76] seems like a good candidate to continue the work carried out for ENACCEF-2, as it also

deals with the detonation regime and presents shockwaves in the flowfield. Simulating any 3D case could help to further validated the solver. For example, the RUT facility is a curved pipe with a discharge chamber, so the flame radius definition used in this thesis should be complemented with new approaches, as the distance to the ignition point is no longer a meaningful metric for that case.

- The solver where the combustion model was implemented doesn't include some of the features available in other solvers of the literature. These features were outside the scope of this thesis, but they would allow the comparison of performance and results between different codes for the same experimental case. Some of the most noticeable differences that can be pointed out are a coupled density-based solved or implicit time marching schemes. However, there are also some minor implementations that would allow a more faithful comparisons between codes. The three main factors that have not been included and should be considered when compared with previous in-house studies [117, 122] are: the full ETFC combustion model (as the laminar source term is not included in the truncated-ETFC version here presented, even if the differences are not expected to be large), the preferential diffusion effects F (which are implicitly included in the GTFC-based models) and quenching effects G (which have been accounted near the wall with the GTFC-wb, but another model can be constructed based on the correlation from Goulier and the usual formulation of G [122] included on the turbulent flame speed source term). Regarding this last effect, a strained laminar flame speed can be used in OpenFOAM instead of the unstrained laminar flame speed which is currently used. Nevertheless, the limitations on the strain calculation with RANS models should be acknowledged.

- The source term in the regress variable transport equation is mainly based on turbulence effects and not on chemical parameters. It has been proved that these models can provide accurate results in many different types of scenarios. However, in the quest of better results, the main question that can be asked is whether more accuracy would be achieved with better turbulence models (as LES) or with better combustion models (that either take into account multiple chemical reactions or just include fluctuations of the regress variable in the calculations). Even if both approaches should provide better results, it is claimed that the use of LES can give more insights into the combustion model implemented, and given that LES models are included in OpenFOAM, a small number of changes is required in order to run the same simulation case with improved turbulence modeling. Multiple phenomena when dealing with the filter size and the flame front have been described and will surely require a dedicated analysis in such simulation [114].

- The reactants in the combustion process in real accident scenario have diluents, such as steam or carbon monoxide, apart from the fuel and oxidizer. The effects of these diluents shoul be accounted for: CO may react exotherminally and N_2 wouldn't remain inert at high temperatures. However, for the current low-fidelity models here presented, the most straightforward approach would be assuming that the diluents are part of the reactants mixture, without the need of a transport equation is to track them. This simplification of course, neglects some effects, e.g. stratification due to different densities within the reactants. The effect of the diluents in the combustion process would be accounted for through the thermodynamic properties, which are computed with a high-fidelity chemistry code. By having different thermophysical properties for the reactants and products mixtures, combined with updated combustion properties as the laminar flame speed, the effects of the diluents should be captured. To obtain these properties, accurate thermodynamic calculators as Cantera would have to be used, as the current approach of OpenFOAM (see Section 3.6 for the full procedure) cannot include diluents in the mixture. To update the laminar flame speed, different correlations have been proposed in the literature for mixtures with diluents [117] [122], so their performance should be assessed. To sum up, no implementation should be required in the solver to account for mixtures with diluents. However, more accurate methods as using transport equations for the diluent mixture fraction exist, so it is strongly advised to perform tests to evaluate whether they are required or the current implementation already provides accurate results.

- Current combustion models used in nuclear safety rely on the fully premixed regime. However, in reality, a more general partially-premixed combustion regime occurs due to, for example, stratification (due to the density difference of the reactants). In such cases, modifying the thermo-

dynamic properties and laminar flame speeds wouldn't suffice. The use of a mixture fraction, $\widetilde{Z}$, largely used in the case of non-premixed combustion modeling, that describes the fuel/oxidizer concentration (and potentially also its fluctuations) can model the local departure from perfectly mixed condictions without requiring advanced combustion models [93]. The same correlations could be used and modifying the laminar flame speed, depending on local mixture properties and the local equivalence ratio, would produce an effect on the results of the models.

In conclusion, this thesis has achieved two milestones that will pave future investigations on the topic. Firstly, the implemented combustion solver includes two models that were already available in the literature and proposes new models based on recent experimental data that has been obtained with the nuclear safety in mind. The results obtained look promising for the different vessels that have been analyzed. Secondly, the code implemented in the thesis provides the foundations to continue improving the available models for hydrogen combustion in nuclear safety within an open source framework. Having a tool where it is possible to completely access the code allows to manipulate and adapt the code to the necessities of the sector and of specific cases, achieving more accurate results.

A

OpenFOAM description

As described in the introduction, there are different codes to perform CFD simulations: including not only the equations, but also numerical schemes, linear system solution algorithms. The one that has been used for this thesis is OpenFOAM [68], which is a multipurpose toolbox written in C++ for the resolution of partial differential equations, especially those related to Computational Fluid Dynamics. Although it already includes many solvers, the open-source code is its true potential: every part of the code can be accessed, manipulated, and eventually reformulated to suit the specific requirements of a project. The source code is fully documented and the clear syntax presents a readable implementation of new models and equations. The C++ source code can be compiled afterward, obtaining an automatically parallelizable solver without the need for programming at low levels. Another big strength is that it is free and there are no license costs. However, OpenFOAM is a fragmented project with many parallel versions and forked projects (the version used for this thesis is `OpenFOAM v1812`), it doesn't have a Graphical User Interface (GUI) and, even if there is a large community, sometimes it is hard to implement new applications as not sufficient details of the underlying code structure are provided for high-level coding. Moreover, during the latest versions the entanglement between different libraries and applications has increased and the virtualization of functions and class inheritances is widespread, increasing the complexity of the code and, even if possible, making it harder to reach and modify.

As there is no GUI, the simulations initially have several plain text input files located in three basic directories, having the tree structure that is presented in Figure A.1. Additional files and folders can be required to performed certain pre and postprocessing tasks. New folders may include the `processorsX` folder (for parallel execution of the solver), time directories (with the data saved at the desired intervals) and the `postProcessing` folder (with data from OpenFOAM postprocessing modules).

The `0/` folder contains the fields with the initial conditions and boundary conditions used for the initialization of the application and the solution procedure. Some of the fields that commonly appear are `U` (velocity field) or `p` (pressure field). The `constant/` folder contains the mesh (under the subfolder `polyMesh/`), the properties of the flow (having a file for the combustion, another for the thermophysical and another for the turbulence properties) and the inclusion of additional options in the solver with `fvOptions` (as source terms). Other files usually contained in this folder are the `g` file (with the direction and magnitude of the gravitational force), the `dynamicMeshDict` file (with the configuration for the dynamic mesh library), and the `boundaryRadiationProperties` and the `radiationProperties` file (when radiation modeling is accounted for). Finally in the `system/` folder, the files regarding the simulation are included. The `blockMeshDict` file has the description of a hexahedral mesh defined with its vertex, faces, and blocks, the `controlDict` file dictates how the simulation is carried out (when to start, when to end, the timestep size, when to write data to disk...), the `decomposeParDict` file is used to decompose a given case into the processors folders for parallel execution, the `setFieldsDict` file contains the initialization for non-spatially-uniform fields, the `fvSchemes` file includes the numerical schemes used for discretization and the `fvSolution` file has the setup for the

linear system resolution and the pressure-velocity coupling. Other files that commonly appear in this folder are the `probes` file (to perform probing in the field to extract information of a given variable), the `extrudeMeshDict` file (e.g. to extrude a mesh in the axial direction), the `snappyHexMeshDict` file (used to perform more detailed grids or to perform mesh refinement) and the `fileUpdate` file (that can be used to change any given field at a specified time during the simulation).

The description above presents the setup for a given case. However, the compilation of applications (name given to the different solvers) and libraries is based on another folder structure. The default applications and libraries of OpenFOAM are located in `$FOAM_APP` and `$FOAM_SRC` respectively. Users can modify these libraries by copying the baseline application/library into their `/home` directory, modifying the code and compiling them (by calling `wmake`). Then, the libraries have to be linked to the application where they are required: depending on whether they are required for compilation (including the new library in the `Make/options` file of a given application) or just called in runtime (linking them directly in the `controlDict` of a given case). Both libraries and applications are described with the header files `.H` and the code files `.C`.

Apart from OpenFOAM, other tools were used during the course of the thesis. Paraview [3] was employed for field visualization and to validate the postprocessing approach. Thanks to its scripting interface and batch execution it is relatively easy to implement routines that can be then executed in parallel when many cases are being analyzed, without manually having to do filters, select surfaces and introduce values. Python was also used for postprocessing, data handling, and figure generation. Finally, Linux was used to automate the execution of the cases, launching the solver and then the postprocessing routines. It was also required to interact with the computer cluster that was used for the larger cases.

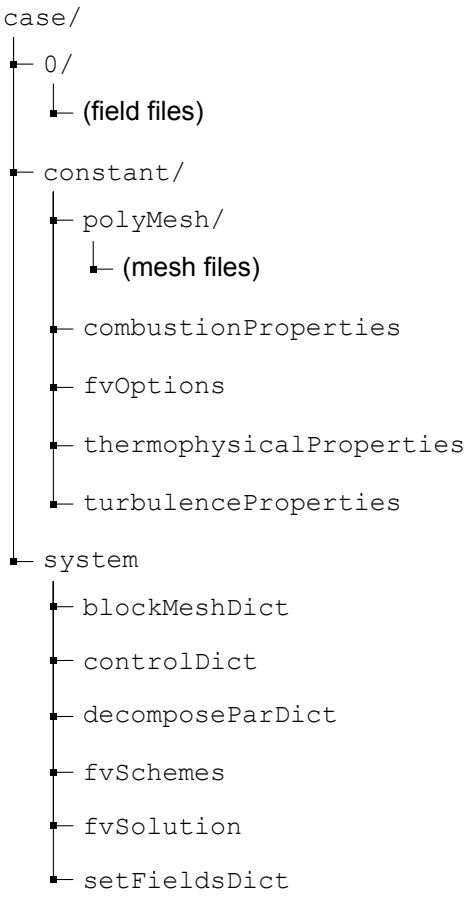

Figure A.1: Initial folder structure for a case in OpenFOAM

B

Thermophysical properties

This appendix includes the thermophysical properties for the spherical bomb (separated by hydrogen concentration, see Table B.1), the THAI vessel (see Table B.2) and ENACCEF-2 (see Table B.3).

Table B.1: Thermodynamic, transport and combustion properties for the different hydrogen concentrations

	Hydrogen volume	$H_2 = 16\%$	$H_2 = 20\%$	$H_2 = 24\%$	$H_2 = 28\%$
Reactants	W (kg/kmol)	24.5439	23.4765	22.4011	21.3285
	c_P (J/(kg K))	1184.3163	1237.6083	1296.4397	1361.0246
	Δh_f^0 (J/kg)	-353067.3429	-368956.7312	-386497.7314	-405754.1671
	μ ((N s)/m^2)	1.8205×10^{-5}	1.8163×10^{-5}	1.8113×10^{-5}	1.8052×10^{-5}
	Pr	0.5292	0.5053	0.4859	0.4706
Products	W (kg/kmol)	26.6759	26.0340	25.2650	24.3111
	c_P (J/(kg K))	1444.4552	1538.2642	1631.6721	1725.1860
	Δh_f^0 (J/kg)	-2224753.6752	-2765263.2580	-3276448.1622	-3701941.7142
	μ ((N s)/m^2)	6.3875×10^{-5}	7.0720×10^{-5}	7.6123×10^{-5}	7.9545×10^{-5}
	Pr	0.6992	0.6960	0.6878	0.6662
Combustion	$S_{L,0}$ (m/s)	0.46	0.92	1.41	1.93
	Le_{eff}	0.458	0.561	0.712	0.956
	L' (m)	-0.00119	-0.00042	-0.00021	0.00020
	Φ	0.455	0.596	0.753	0.927
	T_{ad} (K)	1871.02	2178.33	2426.76	2588.77

Table B.2: Thermodynamic, transport and combustion properties for the THAI HD-15 simulation

Reactants	W (kg/kmol)		26.1921			
	T_{low} (K)		200.00			
	T_{common} (K)		1000.00			
	T_{high} (K)		6000.00			
	a_i (for $T_{low} < T < T_{common}$)	{	3.08418	0.00119914	-3.91075×10^{-7}	
			6.12215×10^{-11}	-3.58442×10^{-15}	-967.736	
					4.70618	}
	a_i ($T_{common} < T < T_{high}$)	{	3.45757	0.000159858	-4.83442×10^{-7}	
			1.95496×10^{-9}	-1.13906×10^{-12}	-1037.04	
					2.86498	}
	μ ((N s)/m^2)		2.1535×10^{-5}			
	Pr		0.583165			
Products	W (kg/kmol)		27.5561			
	T_{low} (K)		200.00			
	T_{common} (K)		1000.00			
	T_{high} (K)		6000.00			
	a_i ($T_{low} < T < T_{common}$)	{	3.02578	0.00145863	-4.71811×10^{-7}	
			7.18827×10^{-11}	-4.09125×10^{-15}	-4074.37	
					5.62397	}
	a_i ($T_{common} < T < T_{high}$)	{	3.63914	-0.000745735	1.75227×10^{-6}	
			-1.72783×10^{-10}	-3.92500×10^{-13}	-4188.06	
					2.65804	}
	μ ((N s)/m^2)		4.62213×10^{-5}			
	Pr		0.705248			
Combustion	$S_{L,0}$ (m/s)		0.0897			
	Le$_{eff}$		0.334			
	L' (m)		-0.0002458			
	Φ		0.2628			
	T_{ad} (K)		1382.95			

Table B.3: Thermodynamic, transport and combustion properties for the ENACCEF-2 Step 0 simulation

Reactants	W (kg/kmol)		25.3603			
	T_{low} (K)		200.00			
	T_{common} (K)		1000.00			
	T_{high} (K)		6000.00			
	a_i (for $T_{low} < T < T_{common}$)	{	3.07921	0.00118691	-3.83041×10^{-7}	
			5.97173×10^{-11}	-3.48934×10^{-15}	-962.657	
					4.51802	}
	a_i ($T_{common} < T < T_{high}$)	{	3.42102	0.000416651	-1.10714×10^{-6}	
			2.55263×10^{-9}	-1.34386×10^{-12}	-1033.12	
					2.79333	}
	μ ((N s)/m^2)		2.1377×10^{-5}			
	Pr		0.555945			
Products	W (kg/kmol)		27.1231			
	T_{low} (K)		200.00			
	T_{common} (K)		1000.00			
	T_{high} (K)		6000.00			
	a_i ($T_{low} < T < T_{common}$)	{	3.00236	0.00152595	-4.88233×10^{-7}	
			7.35767×10^{-11}	-4.14656×10^{-15}	-5031.70	
					5.70701	}
	a_i ($T_{common} < T < T_{high}$)	{	3.65628	-0.000751540	1.77760×10^{-6}	
			-1.92494×10^{-10}	-3.80328×10^{-13}	-5160.39	
					2.51722	}
	μ ((N s)/m^2)		5.20313×10^{-5}			
	Pr		0.702876			
Combustion	$S_{L,0}$ (m/s)		0.27487			
	Le_{eff}		0.3348			
	L' (m)		-0.0002458			
	Φ		0.356692			
	T_{ad} (K)		1661.46			

Bibliography

[1] RG Abdel-Gayed, D Bradley, and AKC Lau. The straining of premixed turbulent flames. In *Symposium (International) on Combustion*, volume 22, pages 731–738. Elsevier, 1989.

[2] J. Ahn, C. Carson, M. Jensen, K. Juraku, S. Nagasaki, and S. Tanaka. *Reflections on the Fukushima Daiichi Nuclear Accident: Toward Social-Scientific Literacy and Engineering Resilience*. Springer International Publishing, 2014. ISBN 978-3-319-12090-4. Page 229.

[3] James Ahrens, Berk Geveci, and Charles Law. Paraview: An end-user tool for large data visualization. *The visualization handbook*, 717(8), 2005.

[4] AE Alajmi, Ibrahim E Abdalla, T Bengherbia, and Zhiyin Yang. Numerical simulation of spray combustion of conventional fuels and biofuels. *Advances in Fluid Mechanics*, 10:325, 2014.

[5] Ansys. Fluent version 12.0 user guide. *Ansys Inc*, 6, 2009.

[6] A Attavino, L Koloszar, P Planquart, M Adorni, and A Parente. Numerical investigacion of the effect of buoyancy forces on the deflagration of hydrogen in the THAI facility. In *18th International Topical Meeting on Nuclear Reactor Thermal Hydraulics, NURETH 2019*, page 12, 2019.

[7] E. Bachellerie, F. Arnould, M. Auglaire, B. de Boeck, O. Braillard, B. Eckardt, F. Ferroni, and R. Moffett. Generic approach for designing and implementing a passive autocatalytic recombiner PAR-system in nuclear power plant containments. *Nuclear Engineering and Design*, 221(1):151–165, 2003. doi: 10.1016/S0029-5493(02)00330-8.

[8] Ahmad Baniabedalruhman. *Dynamic meshing around fluid-fluid interfaces with applications to droplet tracking in contraction geometries*. PhD thesis, Michigan Technical University, 2015.

[9] D Baraldi, AG Venetsanos, E Papanikolaou, M Heitsch, and V Dallas. Numerical analysis of release, dispersion and combustion of liquid hydrogen in a mock-up hydrogen refuelling station. *Journal of Loss Prevention in the Process Industries*, 22(3):303–315, 2009.

[10] Daniele Baraldi, Herve Barthelemy, Luc Bauwens, Alain Bengaouer, Sile Brennan, Marco Carcassi, Espen Funnemark, Eduardo Gallego, and Andrey Gavrikov. Achievements of the EC network of excellence HySAFE. *HySAFE*, 2009.

[11] JK Bechtold and Moshe Matalon. The dependence of the Markstein length on stoichiometry. *Combustion and flame*, 127(1-2):1906–1913, 2001.

[12] Ali Cemal Benim and Khawar J. Syed. Chapter 2 - Concepts related to combustion and flow in premix burners. In *Flashback Mechanisms in Lean Premixed Gas Turbine Combustion*, pages 5 – 18. Academic Press, Boston, 2015.

[13] A Bentaib, A Bleyer, N Chaumeix, B Schramm, P Kostka, M Movahed, HS Kang, and M Povilaitis. Final results of the sarnet hydrogen deflagration benchmark. effect of turbulence on flame acceleration. In *5th European Review Meeting on Severe Accident Research. Cologne, Germany*, pages 21–23, 2012.

[14] A Bleyer, L Maas, N Chaumeix, and A Bentaib. Benchmark exercise on hydrogen flame propagation in stratified atmosphere. Step0: preliminary comparison report. Unpublished, 2018.

[15] Roland Borghi. Turbulent combustion modelling. *Progress in energy and combustion science*, 14(4):245–292, 1988.

[16] KNC Bray, Paul A Libby, and JB Moss. Unified modeling approach for premixed turbulent combustion—part I: General formulation. *Combustion and flame*, 61(1):87–102, 1985.

[17] W Breitung, C Chan, S Dorofeev, A Eder, B Gerland, M Heitsch, R Klein, A Malliakos, J Shepherd, E Studer, et al. Flame acceleration and deflagration-to-detonation transition in nuclear safety. *Organisation for Economic Co-operation and Development, Paris, France, Technical Report No. NEA/CSNI*, 2000.

[18] Nicholas Burali, Simon Lapointe, Brock Bobbitt, Guillaume Blanquart, and Yuan Xuan. Assessment of the constant non-unity Lewis number assumption in chemically-reacting flows. *Combustion Theory and Modelling*, 20(4):632–657, 2016.

[19] Alexander Burcat. Thermochemical data for combustion calculations. In *Combustion chemistry*, pages 455–473. Springer, 1984.

[20] Sebastien M Candel and Thierry J Poinsot. Flame stretch and the balance equation for the flame area. *Combustion Science and Technology*, 70(1-3):1–15, 1990.

[21] Jon Carmack, Frank Goldner, Shannon M Bragg-Sitton, and Lance L Snead. Overview of the US DOE accident tolerant fuel development program. Technical report, Idaho National Laboratory (INL), 2013.

[22] Siemens CD-Adapco. STAR CCM+ user guide version 12.04. *CD-Adapco*, 2017.

[23] Chong M Cha. Transported pdf modeling of turbulent premixed combustion. *AY Klimenko 53*, page 77, 2002.

[24] Nabiha Chaumeix. ENACCEF: Enceinte d'accélération de flamme. `https://icare.cnrs.fr/recherche/moyens-experimentaux/ct-enaccef/`, 2021. [Online; accessed 1-April-2021].

[25] Carlo Cintolesi, Håkan Nilsson, Andrea Petronio, and Vincenzo Armenio. Numerical simulation of conjugate heat transfer and surface radiative heat transfer using the p1 thermal radiation model: Parametric study in benchmark cases. *International Journal of Heat and Mass Transfer*, 107: 956–971, 2017.

[26] United States Nuclear Regulatory Commission. Power plant diagrams. `https://www.nrc.gov/reading-rm/basic-ref/students/for-educators.html`, 2020. [Online; accessed 1-April-2021].

[27] U.S. Nuclear Regulatory Commission. 2012-2013 information digest. Technical report, U.S. Nuclear Regulatory Commission, 08 2012.

[28] Alexis Coppalle and Pierre Vervisch. The total emissivities of high-temperature flames. *Combustion and Flame*, 49(1-3):101–108, 1983.

[29] Richard Courant, Kurt Friedrichs, and Hans Lewy. Über die partiellen differenzengleichungen der mathematischen physik. *Mathematische annalen*, 100(1):32–74, 1928.

[30] Rainer N Dahms, Michael C Drake, Todd D Fansler, T-W Kuo, and N Peters. Understanding ignition processes in spray-guided gasoline engines using high-speed imaging and the extended spark-ignition model sparkcimm. part a: Spark channel processes and the turbulent flame front propagation. *Combustion and flame*, 158(11):2229–2244, 2011.

[31] S. De, A.K. Agarwal, S. Chaudhuri, and S. Sen. *Modeling and Simulation of Turbulent Combustion*. Energy, Environment, and Sustainability. Springer Singapore, 2017. ISBN 9789811074103.

[32] Eugene P Dougherty and Herschel Rabitz. Computational kinetics and sensitivity analysis of hydrogen–oxygen combustion. *The Journal of Chemical Physics*, 72(12):6571–6586, 1980.

[33] M Düsing, A Sadiki, and J Janicka. Towards a classification of models for the numerical simulation of premixed combustion based on a generalized regime diagram. *Combustion Theory and Modelling*, 10(1):105–132, 2006.

[34] M el Abbassia, DJP Lahaye, and C Vuik. Modelling turbulent combustion coupled with conjugate heat transfer in OpenFOAM. In *10th Mediterranean Combustion Symposium*. Reports of the Delft Institute of Applied Mathematics Naples, Italy, 2017.

[35] Pontus Eriksson. The Zimont TFC model applied to premixed bluff body stabilized combustion using four different RANS turbulence models. In *Turbo Expo: Power for Land, Sea, and Air*, volume 47918, pages 353–361, 2007.

[36] Thomas Filburn and Stephan Bullard. Nuclear fuel, Cladding, and the "Discovery" of Zirconium. In Thomas Filburn and Stephan Bullard, editors, *Three Mile Island, Chernobyl and Fukushima: Curse of the Nuclear Genie*, pages 105–114. Springer International Publishing, 2016. ISBN 978-3-319-34055-5. doi: 10.1007/978-3-319-34055-5_10.

[37] Annette Fisher and Sarma Rani. Comparison of wide band, narrow band, and SLW models with HITRAN and HITEMP for predicting radiative heat transfer. In *47th AIAA Thermophysics Conference*, page 4537, 2017.

[38] C Fureby. Large Eddy Simulation of combustion instabilities in a jet engine afterburner model. *Combustion science and technology*, 161(1):213–243, 2000.

[39] Xinfeng Gao and Clinton Groth. Parallel adaptive mesh refinement scheme for three-dimensional turbulent non-premixed combustion. In *46th AIAA aerospace sciences Meeting and Exhibit*, page 1017, 2008.

[40] B. Gera, P. K. Sharma, R. K. Singh, and K. K. Vaze. CFD analysis of passive autocatalytic recombiner. *Science and Technology of Nuclear Installations*, 2011:1–9, 2011. doi: 10.1155/2011/862812. Publisher: Hindawi Publishing Corporation.

[41] R Gharari, H Kazeminejad, N Mataji Kojouri, and A Hedayat. A review on hydrogen generation, explosion, and mitigation during severe accidents in light water nuclear reactors. *International Journal of Hydrogen Energy*, 43(4):1939–1965, 2018.

[42] Sandip Ghosal and Luc Vervisch. Stability diagram for lift-off and blowout of a round jet laminar diffusion flame. *Combustion and Flame*, 124(4):646–655, March 2001. doi: 10.1016/S0010-2180(00)00224-8.

[43] G Gianetti, L Sforza, T Lucchini, G D'Errico, P Soltic, J Rojewski, and G Hardy. CFD modeling of natural gas engine combustion with a flame area evolution model. In *AIP Conference Proceedings*, volume 2191, page 020087. AIP Publishing LLC, 2019.

[44] Florian Goebel and Christian Mundt. Implementation of the P1 radiation model in the CFD solver NSMB and investigation of radiative heat transfer in the SSME main combustion chamber. In *17th AIAA international space planes and hypersonic systems and technologies conference*, page 2257, 2011.

[45] David G. Goodwin, Raymond L. Speth, Harry K. Moffat, and Bryan W. Weber. Cantera: An object-oriented software toolkit for chemical kinetics, thermodynamics, and transport processes. https://www.cantera.org, 2018. Version 2.4.0.

[46] J Goulier. *Comportements aux limites de flammes de prémélange hydrogène/air/diluants. Étude de la transition flamme laminaire-flamme turbulente*. PhD thesis, Thesis, University of Orléans, 2015.

[47] J. Goulier, A. Comandini, F. Halter, and N. Chaumeix. Experimental study on turbulent expanding flames of lean hydrogen/air mixtures. *Proceedings of the Combustion Institute*, 36(2):2823–2832, 2017. doi: 10.1016/j.proci.2016.06.074.

[48] J Goulier, K N'Guessan, M Idir, and N Chaumeix. Tomographic visualization of thermo-diffusive instabilities of lean hydrogen/air mixtures. *Proc. 26th ICDERS*, 2017.

[49] William L Grosshandler. RADCAL: a Narrow-Band Model for radiation. *Calculations in a Combustion Environment, NIST Technical Note*, 1402, 1993.

[50] Carlo Gualtieri, Athanasios Angeloudis, Fabian Bombardelli, Sanjeev Jha, and Thorsten Stoesser. On the values for the turbulent Schmidt number in environmental flows. *Fluids*, 2 (2):17, 2017.

[51] Ömer L Gülder. Correlations of laminar combustion data for alternative si engine fuels. Technical report, SAE Technical Paper, 1984.

[52] Ömer L Gülder. Turbulent premixed flame propagation models for different combustion regimes. In *Symposium (International) on Combustion*, volume 23, pages 743–750. Elsevier, 1991.

[53] Sanjeev Gupta. Experimental investigations relevant for hydrogen and fission product issues raised by the Fukushima accident. *Nuclear Engineering and Technology*, 47:11–25, 01 2015. doi: 10.1016/j.net.2015.01.002.

[54] Y Halouane and A Dehbi. CFD simulations of premixed hydrogen combustion using the Eddy Dissipation and the Turbulent Flame Closure models. *International journal of hydrogen energy*, 42(34):21990–22004, 2017.

[55] Basim O Hasan. Turbulent Prandtl number and its use in prediction of heat transfer coefficient for liquids. *Al-Nahrain Journal for Engineering Sciences*, 10(1):53–64, 2007.

[56] Josef Hasslberger, Lorenz R Boeck, and Thomas Sattelmayer. Numerical simulation of deflagration-to-detonation transition in large confined volumes. *Journal of Loss Prevention in the Process Industries*, 36:371–379, 2015.

[57] Josef Hasslberger, Hyoung Ki Kim, Byung Jo Kim, In Chul Ryu, and Thomas Sattelmayer. Three-dimensional CFD analysis of hydrogen-air-steam explosions in APR1400 containment. *Nuclear Engineering and Design*, 320:386–399, 2017.

[58] Daniel Connell Haworth and TJ Poinsot. Numerical simulations of Lewis number effects in turbulent premixed flames. *Journal of fluid mechanics*, 244:405–436, 1992.

[59] Chen Huang and Andrei N Lipatnikov. Comparison of presumed PDF models of turbulent flames. *Journal of Combustion*, 2012, 2012.

[60] Chen Huang, Andrei N Lipatnikov, and Ken Nessvi. Unsteady 3-D RANS simulations of dust explosion in a fan stirred explosion vessel using an open source code. *Journal of Loss Prevention in the Process Industries*, 67:104237, 2020.

[61] LL Humphries, RK Cole, DL Louie, VG Figueroa, and MF Young. Melcor computer code manuals vol. 2: Reference manual. *Version*, 2:6840, 2015.

[62] International Atomic Energy Agency. *Mitigation of Hydrogen Hazards in Severe Accidents in Nuclear Power Plants*. Number 1661 in TECDOC Series. International Atomic Energy Agency, 2011. ISBN 978-92-0-116510-7.

[63] International Atomic Energy Agency. *Nuclear power reactors in the world*. International Atomic Energy Agency, 2018. ISBN 92-0-101418-X. Page 12.

[64] Dmytro Iurashev, Giovanni Campa, Vyacheslav Anisimov, Andrea Di Vita, Ezio Cosatto, Federico Daccà, and Alp Albayrak. Turbulent flame models for prediction of pressure oscillations in gas turbine burners. In *Proceedings of the 22nd International Congress on Sound and Vibration, Florence, Italy*, pages 12–16, 2015.

[65] Peter Janas. *Large eddy simulation of in-cylinder phenomena in spark ignition engines*. PhD thesis, University of Duisburg-Essen, 2017.

[66] Hrvoje Jasak. *Error analysis and estimation for the finite volume method with applications to fluid flows*. PhD thesis, Imperial College London (University of London), 1996.

[67] Hrvoje Jasak. Dynamic mesh handling in openfoam. In *47th AIAA aerospace sciences meeting including the new horizons forum and aerospace exposition*, page 341, 2009.

[68] Hrvoje Jasak, Aleksandar Jemcov, and Zeljko Tukovic. OpenFOAM: A C++ library for complex physics simulations. In *International workshop on coupled methods in numerical dynamics*, volume 1000, pages 1–20. IUC Dubrovnik Croatia, 2007.

[69] Hyung Seok Kang, Jongtae Kim, Seong Wan Hong, and Sang Baik Kim. Numerical analysis for hydrogen flame acceleration during a severe accident in the apr1400 containment using a multi-dimensional hydrogen analysis system. *Energies*, 13(22):6151, 2020.

[70] T Kanzleiter and G Langer. Hydrogen deflagration tests in the THAI test facility. Technical report, Eschborn, Germany: Becker Technologies GmbH, 2010.

[71] T Kanzleiter, S Gupta, K Fischer, G Ahrens, G Langer, A Kühnel, G Poss, G Langrock, and F Funke. Hydrogen and fission product issues relevant for containment safety assessment under severe accident conditions. *Final Report, OECD-NEA THAI Project, Reactor Safety Research Project*, 150:1326, 2010.

[72] Vladimir Karpov, Andrei Lipatnikov, et al. A test of an engineering model of premixed turbulent combustion. In *Symposium (International) on Combustion*, volume 26, pages 249–257. Elsevier, 1996.

[73] VP Karpov and ES Severin. Effects of molecular-transport coefficients on the rate of turbulent combustion. *Combustion, explosion and shock waves*, 16(1):41–46, 1980.

[74] Wiliam M Kays. Turbulent Prandtl number. Where are we? *ATJHT*, 116(2):284–295, 1994.

[75] John F Keays. *Large Eddy simulation of premixed combustion*. PhD thesis, Imperial College London, 2007.

[76] D Kim and J Kim. Numerical method to simulate detonative combustion of hydrogen-air mixture in a containment. *Engineering Applications of Computational Fluid Mechanics*, 13(1):938–953, 2019.

[77] W Klein-Hessling and B Schwinges. ASTEC v0 CPA module, program reference manual, rev. 0. *ASTECV00DOC001-34, ASTEC*, 1006, 1998.

[78] Andrey Nikolaevich Kolmogorov. The local structure of turbulence in incompressible viscous fluid for very large Reynolds numbers. *Cr Acad. Sci. URSS*, 30:301–305, 1941.

[79] Thomas Komarek and Wolfgang Polifke. Impact of swirl fluctuations on the flame response of a perfectly premixed swirl burner. *Journal of Engineering for Gas Turbines and Power*, 132(6), 2010.

[80] Ed MJ Komen, Dirk C Visser, Ferry Roelofs, and Jos GT Te Lintelo. The role of CFD computer analyses in hydrogen safety management. *Atw. Internationale Zeitschrift fuer Kernenergie*, 60 (11):660–665, 2015.

[81] AS Kotchourko, SB Dorofeev, and W Breitung. Test of extended Eddy Break Up model in simulations of turbulent H2-air combustion. In *17-th Int. Colloq. on the Dynamics of Explosions and Reactive Systems (ICDERS)*, 1999.

[82] Harmen Krediet. *Prediction of limit cycle pressure oscillations in gas turbine combustion systems using the flame describing function*. PhD thesis, University of Twente, Enschede, 2012.

[83] J. R. Lamarsh and A. J. Baratta. *Introduction to Nuclear Engineering*. Prentice Hall, 3rd edition, 2001. ISBN 978-0-201-82498-8. Pages 139-142.

[84] Caelan Lapointe, Nicholas T. Wimer, Jeffrey F. Glusman, Amanda S. Makowiecki, John W. Daily, Gregory B. Rieker, and Peter E. Hamlington. Efficient simulation of turbulent diffusion flames in OpenFOAM using adaptive mesh refinement. *Fire Safety Journal*, 111:102934, 2020-01. doi: 10.1016/j.firesaf.2019.102934.

[85] BE Launder. Advanced turbulence models for industrial applications. In *Turbulence and transition modelling*, pages 193–231. Springer, 1996.

[86] Brian Edward Launder and Dudley Brian Spalding. The numerical computation of turbulent flows. In *Numerical prediction of flow, heat transfer, turbulence and combustion*, pages 96–116. Elsevier, 1983.

[87] A. Liñán, A. Linan, and F.A. Williams. *Fundamental Aspects of Combustion*. Oxford engineering science series. Oxford University Press, 1993. ISBN 9780195076264.

[88] A. Lipatnikov. *Fundamentals of Premixed Turbulent Combustion*. CRC Press, 2012. ISBN 9781466510258.

[89] AN Lipatnikov and J Chomiak. Turbulent flame speed and thickness: phenomenology, evaluation, and application in multi-dimensional simulations. *Progress in energy and combustion science*, 28(1):1–74, 2002.

[90] AN Lipatnikov and Jerzy Chomiak. Molecular transport effects on turbulent flame propagation and structure. *Progress in energy and combustion science*, 31(1):1–73, 2005.

[91] AN Lipatnikov and Jerzy Chomiak. Self-similarly developing, premixed, turbulent flames: a theoretical study. *Physics of Fluids*, 17(6):065105, 2005.

[92] Andrei Lipatnikov and Jerzy Chomiak. A theoretical study of premixed turbulent flame development. *Proceedings of the Combustion Institute*, 30(1):843–850, 2005.

[93] Andrei N Lipatnikov. Stratified turbulent flames: Recent advances in understanding the influence of mixture inhomogeneities on premixed combustion and modeling challenges. *Progress in Energy and Combustion Science*, 62:87–132, 2017.

[94] Dave Lochbaum. Preventing fuel damage in Nuclear Reactors. `https://allthingsnuclear.org/dlochbaum/preventing-fuel-damage-in-nuclear-reactors`, 2014. [Online; accessed 1-April-2021].

[95] Xuefeng Lyu, Jian Cheng, Yang Feng, Tianfang Liu, and Xiong Huang. Effectiveness analysis of hydrogen control system in ap1000 nuclear power plant under lb-loca. *Annals of Nuclear Energy*, 147:107695, 2020.

[96] Dmitriy Makarov, F Verbecke, Vladimir Molkov, A Kotchourko, A Lelyakin, J Yanez, D Baraldi, M Heitsch, A Efimenko, and A Gavrikov. An intercomparison of CFD models to predict lean and non-uniform hydrogen mixture explosions. *International journal of hydrogen energy*, 35(11): 5754–5762, 2010.

[97] Thierry Mantel and Roland Borghi. A new model of premixed wrinkled flame propagation based on a scalar dissipation equation. *Combustion and Flame*, 96(4):443 – 457, 1994. ISSN 0010-2180.

[98] Frank E Marble and James E Broadwell. The coherent flame model for turbulent chemical reactions. Technical report, Purdue University Lafayette in project squidheadquarters, 1977.

[99] Moshe Matalon. Intrinsic flame instabilities in premixed and nonpremixed combustion. *Annu. Rev. Fluid Mech.*, 39:163–191, 2007.

[100] Neil McManus. *Safety and health in confined spaces*. Routledge, 2018.

[101] C Meneveau and T Poinsot. Stretching and quenching of flamelets in premixed turbulent combustion. *Combustion and Flame*, 86(4):311–332, 1991.

[102] Florian R Menter, Martin Kuntz, and Robin Langtry. Ten years of industrial experience with the sst turbulence model. *Turbulence, heat and mass transfer*, 4(1):625–632, 2003.

[103] M. F. Modest. *Radiative heat transfer*. Academic Press, third edition edition, 2013. ISBN 978-0-12-386944-9.

[104] Vladimir Molkov, Dmitriy Makarov, and Jonathan Puttock. The nature and large eddy simulation of coherent deflagrations in a vented enclosure-atmosphere system. *Journal of Loss Prevention in the Process Industries*, 19(2-3):121–129, 2006.

[105] Vincent Moreau. Progress in the self-similar turbulent flame premixed combustion model. *Applied mathematical modelling*, 34(12):4074–4088, 2010.

[106] Anderson Mossi, Marcelo M Galarça, Rogério Brittes, Horácio A Vielmo, and Francis HR França. Comparison of spectral models in the computation of radiative heat transfer in participating media composed of gases and soot. *Journal of the Brazilian Society of Mechanical Sciences and Engineering*, 34(2):112–119, 2012.

[107] Zakaria Movahedi. *An Investigation of Premixed Flame Propagation in a Straight Rectangular Duct*. PhD thesis, University of Windsor, 2017.

[108] Federico Municchi, Pranay P Nagrani, and Ivan C Christov. A two-fluid model for numerical simulation of shear-dominated suspension flows. *International Journal of Multiphase Flow*, 120: 103079, 2019.

[109] K.K. Murata, D.E. Carroll, K.E. Washington, F. Gelbard, G.D. Valdez, D.C. Williams, and K.D. Bergeron. User's manual for CONTAIN 1.1: A computer code for severe nuclear reactor accident containment analysis. Technical report, NUREG/CR–5026, 1989.

[110] Thommie Nilsson, Rixin Yu, Nguyen Anh Khoa Doan, Ivan Langella, Nedunchezhian Swaminathan, and Xue-Song Bai. Filtered reaction rate modelling in moderate and high Karlovitz number flames: an a priori analysis. *Flow, Turbulence and Combustion*, 103(3):643–665, 2019.

[111] Dipal Patel and Martin Agelin-Chaab. DNS for Turbulent Premixed Combustion. In *An Introduction to Direct Numerical Simulations of Turbulent Flows*. IntechOpen, 2020.

[112] Lars Magnus Persson. *Presumed and transported PDF methods applied to turbulent premixed flames*. PhD thesis, Imperial College London, 2011.

[113] Norbert Peters. *Turbulent Combustion*. Cambridge Monographs on Mechanics. Cambridge University Press, 2000. doi: 10.1017/CBO9780511612701.

[114] Thierry Poinsot and Denis Veynante. *Theoretical and Numerical Combustion*. RT Edwards, Inc., 2005. ISBN 9781930217102.

[115] Stephen B Pope. PDF methods for turbulent reactive flows. *Progress in energy and combustion science*, 11(2):119–192, 1985.

[116] Stephen B. Pope. *Turbulent Flows*. Cambridge University Press, 2000.

[117] A Cutrono Rakhimov, DC Visser, T Holler, and EMJ Komen. The role of CFD combustion modelling in hydrogen safety management VI: Validation for slow deflagration in homogeneous hydrogen-air-steam experiments. *Nuclear Engineering and Design*, 311:142–155, 2017.

[118] Sankaranarayanan Ravi and Eric L Petersen. Laminar flame speed correlations for pure-hydrogen and high-hydrogen content syngas blends with various diluents. *International journal of hydrogen energy*, 37(24):19177–19189, 2012.

[119] W Rehm, M Gerndt, W Jahn, F Semler, and I Jones. CFD simulation of deflagration–detonation processes using vector-and parallel computing systems. *Applied mathematical modelling*, 22 (10):811–822, 1998.

[120] Daniel Rettenmaier, Daniel Deising, Yun Ouedraogo, Erion Gjonaj, Herbert De Gersem, Dieter Bothe, Cameron Tropea, and Holger Marschall. Load balanced 2d and 3d adaptive mesh refinement in openfoam. *SoftwareX*, 10:100317, 2019.

[121] Vladimir Sabel'nikov and Olivier Soulard. Rapidly decorrelating velocity-field model as a tool for solving one-point Fokker-Planck equations for probability density functions of turbulent reactive scalars. *Physical Review E*, 72(1):016301, 2005.

[122] Pratap Sathiah, Ed Komen, and Dirk Roekaerts. The role of CFD combustion modeling in hydrogen safety management—Part I: Validation based on small scale experiments. *Nuclear Engineering and Design*, 248:93–107, 2012.

[123] ZM Shapiro and TR Moffette. *Hydrogen flammability data and application to PWR loss-of-coolant accident*, volume 545. Office of Technical Services, Department of Commerce, 1957.

[124] Gregory P. Smith, David M. Golden, Michael Frenklach, Nigel W. Moriarty, Boris Eiteneer, Mikhail Goldenberg, C. Thomas Bowman, Ronald K. Hanson, Soonho Song, William C. Gardiner Jr., Vitali V. Lissianski, , and Zhiwei Q. Gri-mech 3.0. `http://combustion.berkeley.edu/gri-mech/`, 2007. [Online; accessed 21-April-2021].

[125] TF Smith, ZF Shen, and JN Friedman. Evaluation of coefficients for the weighted sum of gray gases model. *ASME. Journal Heat Transfer*, 1982.

[126] Gary A Sod. A survey of several finite difference methods for systems of nonlinear hyperbolic conservation laws. *Journal of computational physics*, 27(1):1–31, 1978.

[127] Marek M. Stempniewicz. Steady-state and accident analyses of PBMR with the computer code SPECTRA. Technical report, International Atomic Energy Agency (IAEA), 2002. INIS-XA–524.

[128] Peter K Sweby. High resolution schemes using flux limiters for hyperbolic conservation laws. *SIAM journal on numerical analysis*, 21(5):995–1011, 1984.

[129] Ryan Taylor, Clinton PT Groth, Zhe Rita Liang, and Lucian Ivan. Mesh-independent large-eddy simulation with anisotropic adaptive mesh refinement for hydrogen deflagration prediction in closed vessels. *Hydrogen Knowledge Centre*, 2019.

[130] Luis Valino. A field Monte Carlo formulation for calculating the probability density function of a single scalar in a turbulent flow. *Flow, turbulence and combustion*, 60(2):157–172, 1998.

[131] A Velikorodny, E Studer, S Kudriakov, and A Beccantini. Combustion modeling in large scale volumes using EUROPLEXUS code. *Journal of Loss Prevention in the Process Industries*, 35: 104–116, 2015.

[132] Rajasekhar Venuturumilli and Lea-Der Chen. Numerical simulation using adaptive mesh refinement for laminar jet diffusion flames. *Numerical Heat Transfer, Part B: Fundamentals*, 46(2): 101–120, 2004.

[133] H. K. Versteeg and W. Malalasekera. *An introduction to Computational Fluid Dynamics: the finite volume method*. Pearson Education Ltd, 2nd ed edition, 2007. ISBN 978-0-13-127498-3.

[134] Denis Veynante and Luc Vervisch. Turbulent combustion modeling. *Progress in energy and combustion science*, 28(3):193–266, 2002.

[135] Babkin V.S. Baric, thermal and overall thermokinetic indexes for H2-air laminar burning velocity. private communication, 2003.

[136] J. Samuel Walker. *Three Mile Island: a nuclear crisis in historical perspective*. University of California Press, 2004. ISBN 978-0-520-23940-1. Issue: v. 41; v. 88; pages 73-74.

[137] Johan Wallesten. *Modeling of Flame Propagation in Spark Ignition Engines*. Chalmers University of Technology, 2003.

[138] H G Weller. The development of a new flame area combustion model using conditional averaging. *Thermo-fluids section report TF 9307*, page 60, 1993.

[139] H.G. Weller, G. Tabor, A.D. Gosman, and C. Fureby. Application of a flame-wrinkling LES combustion model to a turbulent mixing layer. *Symposium (International) on Combustion*, 27(1): 899–907, 1998. doi: 10.1016/S0082-0784(98)80487-6.

[140] David C Wilcox. Reassessment of the scale-determining equation for advanced turbulence models. *AIAA journal*, 26(11):1299–1310, 1988.

[141] FA Williams. Some recent studies in turbulent combustion. In *Smart control of turbulent combustion*, pages 1–11. Springer, 2001.

[142] Jianjun Xiao and Thomas Jordan. Numerical investigation of downward-propagating hydrogen flame in THAI HD-23 test using CFD code GASFLOW-MPI. In *CFD4NRS-7: OECD/NEA & IAEA Workshop Application of CFD/CMFD Codes to Nuclear Reactor Safety and Design and their Experimental Validation*, 09 2018.

[143] Jianjun Xiao, Wolfgang Breitung, Mike Kuznetsov, Han Zhang, John R Travis, Reinhard Redlinger, and Thomas Jordan. GASFLOW-MPI: A new 3-D parallel all-speed CFD code for turbulent dispersion and combustion simulations: Part I: Models, verification and validation. *international journal of hydrogen energy*, 42(12):8346–8368, 2017.

[144] Ehsan Yasari. Modification of the temperature calculation library for premixed turbulent combustion simulation. In *6th OpenFOAM Workshop, Pennsylvania, USA*, 2011.

[145] Ehsan Yasari. *Extension of OpenFOAM library for RANS simulation of premixed turbulent combustion*. PhD thesis, Chalmers University of Technology, 2013.

[146] Shuai Ye, Yufei Lin, Liyang Xu, and Jiaming Wu. Improving initial guess for the iterative solution of linear equation systems in incompressible flow. *Mathematics*, 8(1):119, 2020.

[147] Chungen Yin, Lasse A Rosendahl, and Søren K Kær. Chemistry and radiation in oxy-fuel combustion: a computational fluid dynamics modeling study. *Fuel*, 90(7):2519–2529, 2011.

[148] Dennis A Yoder. Comparison of turbulent thermal diffusivity and scalar variance models. In *54th AIAA Aerospace Sciences Meeting*, page 1561, 2016.

[149] Y.B. Zel'dovich, G.I. Barenblatt, Akademiia nauk SSSR., D.H. McNeill, V.B. Librovich, and G.M. Makhviladze. *The Mathematical Theory of Combustion and Explosions*. Consultants Bureau, 1985. ISBN 9780306109744.

[150] V. L. Zimont. Theory of turbulent combustion of a homogeneous fuel mixture at high Reynolds numbers. *Combustion, Explosion, and Shock Waves*, 15(3):305–311, 1979. doi: 10.1007/BF00785062.

[151] Vladimir Zimont, Wolfgang Polifke, Marco Bettelini, and Wolfgang Weisenstein. An efficient computational model for premixed turbulent combustion at high Reynolds numbers based on a turbulent flame speed closure. *Journal of Engineering for Gas Turbines and Power*, 1998.

[152] Vladimir L Zimont. A compatibility principle, analytical formulation, and the G and σ-equations in the theory of turbulent premixed combustion. *Physics of Fluids*, 31(10):105113, 2019.

[153] Vladimir L Zimont and Fernando Biagioli. Gradient, counter-gradient transport and their transition in turbulent premixed flames. *Combustion Theory and Modelling*, 6(1):79–101, 2002.